

Modeling and Inversion of airborne Full Tensor Magnetic Gradiometry Data in the Thuringian Basin and Forest

Dissertation

zur Erlangung des akademischen Grades doctor rerum naturalium
(Dr. rer. nat.)

vorgelegt dem Rat der Chemisch-Geowissenschaftlichen Fakultät der
Friedrich-Schiller-Universität Jena

von Dipl.-Geophys. Matthias Queitsch
geboren am 01.05.1986 in Wippra

Gutachter:

1. Prof. Dr. Nina Kukowski
Lehrstuhl für Allgemeine Geophysik
Institut für Geowissenschaften
Friedrich-Schiller-Universität Jena
2. Prof. Dr. Jörg Ebbing
Lehrstuhl für Geophysik und Geoinformation
Institut für Geowissenschaften
Christian-Albrechts-Universität zu Kiel
3. Dr. Ronny Stolz
Abteilung Quantendetektion
Leibniz-Institut für Photonische Technologien Jena

Tag der Verteidigung: 10.02.2016

Zusammenfassung

Die Vermessung des Magnetfeldes ist eines der Standardverfahren in der geophysikalischen Exploration. Traditionell werden dabei Totalfeld-Magnetometer eingesetzt, welche die Intensität des Magnetfeldvektors am Beobachtungsort ermitteln, jedoch nicht seine Richtung. Diese ist hilfreich, wenn die magnetischen Eigenschaften, wie beispielsweise die Remanenz geologischer Strukturen im Untergrund im Detail erkundet werden sollen. Die Erfassung von gerichteten Informationen mittels vektorieller Magnetometer ist aufgrund technischer Hürden derzeit schwierig zu realisieren. Dieses Problem kann jedoch umgangen werden, indem die räumlichen Ableitungen der Komponenten des Magnetfeldvektors gemessen werden. Dazu werden in dieser Arbeit planare Gradiometer erster Ordnung zum Einsatz gebracht, welche auf supraleitenden Quanteninterferenzdetektoren (SQUIDs) basieren. Diese Sensoren zeichnen sich durch ein sehr niedriges Eigenrauschen aus und ermöglichen so hochgenaue Messungen der räumlichen Gradienten des Magnetfeldvektors. Durch die Kombination mehrerer Gradiometer ist es möglich, den vollständigen Gradiententensor des Erdmagnetfeldes (Full Tensor Magnetic Gradiometry, FTMG) zu erfassen. Dieser bietet eine Reihe von Vorteilen im Vergleich zu der konventionell gemessenen Totalintensität. Dazu gehören unter anderem eine höhere örtliche Auflösung und zusätzliche gerichtete Informationen. Diese können dazu beitragen, die Magnetisierung, Geometrie und Lage von Störkörpern im Untergrund besser zu ermitteln.

Ein solches Volltensor-System wurde im Rahmen des multidisziplinären Projektes INFLUINS (Integrierte Fluidodynamik in Sedimentbecken) eingesetzt. Ziel dieses Projektes war es, die Bewegung von Fluiden auf unterschiedlichen zeitlichen und örtlichen Skalen besser zu verstehen. Beim Einsatz des magnetischen Volltensor-System wurden dabei unterschiedliche Ziele verfolgt, wie zum Beispiel die Kartierung von magnetischen Anomalien entlang von Störungssystemen in Sedimentbecken. Des weiteren sollten die Vorteile des gemessenen magnetischen Gradiententensors an geeigneten Strukturen gezeigt werden. Zu diesem Zweck wurde in fünf unterschiedlichen Fluggebieten im Thüringer Becken, dem Thüringer Wald und dem Thüringer Schiefergebirge luftgestützt der komplette Gradiententensor des Erdmagnetfeldes gemessen. Diese Datensätze zeichnen sich durch sehr niedriges Rauschen von lediglich 60 (pT/m)_{PP} in einigen der Fluggebieten aus.

In dieser Arbeit werden zwei unterschiedliche Fallstudien präsentiert: In der ersten Fallstudie werden die Vorteile von magnetischen Volltensorsystemen bei der Ermittlung der Magnetisierungsvektoren im Vergleich zu konventionellen Totalfelddaten beleuchtet. Als Untersuchungsgebiet dient der Intrusivkörper des *Dolerits der Höhenberge* im Zentrum des Thüringer Waldes. In diesem Gebiet wurde eine starke magnetische Anomalie detektiert, welche deutliche Anzeichen einer remanenten Magnetisierung zeigt. Die gemessenen aeromagnetischen Daten korrelieren bei erster Betrachtung sehr gut mit den bekannten geologischen Karten. In dieser Studie wird ein Vergleich zwischen der inversen Modellierung von Volltensor- und Totalfelddaten präsentiert. Die Ergebnisse dieser Inversionen werden anhand vorliegender geologischer Informationen und paläomagnetischer Messungen evaluiert. Beide Modelle zeigen vergleichbare Strukturen. Der in östliche Richtung einfallende Intrusivkörper wurde in beiden Modellen abgebildet, wobei sowohl der Einfallswinkel als auch die ungefähre Mächtigkeit rekonstruiert werden konnten. Das Modell, welches auf den Gradientendaten beruht, zeigt kompaktere Strukturen, schärfere Kontraste und höhere Magnetisierungen. Zudem konnten selbst schwächere Strukturen identifiziert werden,

welche in Verbindung mit Apophysen der Dolerit-Intrusion stehen. Diese Strukturen konnten nicht in den Modellen beobachtet werden, welche auf den Totalfelddaten basieren. Zur Evaluierung der rekonstruierten Magnetisierungsrichtungen wurden Bereiche in den Modellen ausgewählt, welche die stärksten Amplituden zeigen. Der Vergleich der Magnetisierungsvektoren mit den gemessenen Vektoren an den Probenahmestellen zeigt deutliche Übereinstimmungen, wobei das Modell, welches auf den Gradientendaten basiert, deutlich bessere Ergebnisse zeigt als das Totalfeld-Modell. Der remanente Anteil der rekonstruierten Magnetisierungsrichtungen wurde mit Hilfe der gemessenen Suszeptibilitäten von der totalen Magnetisierung getrennt. Auch dabei zeigte das Modell beruhend auf den Gradientendaten wesentlich bessere Ergebnisse. Für eine umfassendere Trennung beider Magnetisierungsarten ist jedoch eine genauere Kenntnis der Suszeptibilitäten im Untersuchungsgebiet vonnöten.

In der zweiten Fallstudie wird eine kombinierte Untersuchung einer kleinskaligen magnetischen Anomalie mit deutlich schwächerer Amplitude präsentiert. Diese Struktur wurde im Rahmen der Kartierung einer der wichtigsten Störungszonen des Thüringer Beckens, der Eichenberg-Gotha-Saalfeld-Störungszone, detektiert. Die Anomalie stellt dabei die einzige signifikante magnetische Struktur entlang der Störungszone im Untersuchungsgebiet dar. Ihre genaue Lage wirft jedoch einige Fragen auf, denn die Anomalie verläuft sich subparallel zu einer der Hauptstörungsflächen. Zur genaueren Untersuchung dieser Struktur wurden geoelektrische Messungen, sowie verfügbare geologische Modelle herangezogen. Die Inversion der magnetischen Volltensordaten zeigt, dass eine steil einfallende Magnetisierung ohne remanente Anteile zu erwarten ist. Dieses Einfallen steht im Widerspruch zur erwarteten geologischen Struktur. Die Lage der Hauptstörungsfläche der Eichenberg-Gotha-Saalfeld Störungszone konnte mit Hilfe der geoelektrischen Profile bestätigt werden. Die Unterschiede zwischen den erhobenen geophysikalischen Datensätzen und den geologischen Randinformationen werden in dieser Arbeit mit Hilfe von konzeptionellen Modellen erklärt. Dabei werden verschiedene Prozesse, welche zur erhöhten Magnetisierung in diesem Bereich führen könnten, diskutiert.

Abstract

The recent development of airborne full tensor magnetic gradiometer (FTMG) systems, based on superconducting quantum interference devices (SQUID), allows to obtain the full magnetic gradient tensor of Earth's magnetic field of large areas (10×10 km) in a few days of operation. This system applies planar-type first-order gradiometers in order to acquire all components of the magnetic gradient tensor. This tensor exhibits some advantages over conventional airborne magnetic field data, e.g. a higher spatial resolution and additional directional sensitivity. Thus, it should provide additional information useful for the interpretation of the geological structures.

In this work a FTMG system was applied in the framework of the multidisciplinary INFLUINS project (Integrated fluid dynamics in sedimentary basins) in order investigate different areas in the Thuringian Basin and the neighboring highlands. Main goal was to map magnetic lineaments along major fault zones and to demonstrate some general advantages of airborne FTMG data in direct comparison to conventional total field anomaly data. Full tensor data sets have been acquired in five survey areas in Thuringia with very low system noise of only $60 \text{ (pT/m)}_{\text{PP}}$ in some of them.

In the framework of this study, two different case studies are presented: In the first case study a strong magnetic anomaly in the center of the Thuringian Forest, caused by the magmatic intrusion of the *Höhenberger dolerite*, is analyzed. The acquired airborne magnetic data in this area shows a general agreement with the known geological information. Furthermore, the intrusive body exhibits indications of a significant remanent magnetization. In order to demonstrate the potential benefits of full tensor magnetic gradiometry, in terms of the determination of the geometry and magnetization direction of a target, this data set was intensively studied. Multiple magnetization vector inversions were performed using either the full magnetic gradient tensor or only the total field anomaly data. The inversion results are evaluated using magnetization directions acquired by paleomagnetic sampling and available geological information of the dolerite intrusion. Both inversion results show comparable results, with an eastward dipping structure. The dipping angle and the thickness of this particular structure are in accordance with the available geological information. However, the inversion result obtained from the gradiometry data features much sharper contacts with higher magnetization amplitudes and even very small and faint structures, which can be correlated with the apophysis of the intrusive body. The model based on the total field data is much smoother and does not show these small and weak signatures. A volume within both models was selected in order to compare the reconstructed magnetization vectors with the measured direction of the paleomagnetic rock samples. The model based on the gradiometry data shows a much better agreement in the magnetization vector directions. The remanent contribution of this total magnetization vector has been separated using the measured susceptibility. The remanence in the model for this particular survey area using the gradiometry data is in good accordance with the results from the paleomagnetic analysis. The total field anomaly model however, shows some significant differences.

In the second case study, a small and weak intra-basinal magnetic anomaly was investigated. It was discovered while mapping expected magnetic anomalies along the Eichenberg-Gotha-Saalfeld fault zone, which is one of the major fault zones in the Thuringian Basin. The detected lineament is interpreted using the components of the mapped magnetic gradient tensor, additional ground based geo-electrical data and available geological information. The inversion of the magnetic gradients revealed

a steeply dipping zone of mostly induced magnetization. Despite the Quaternary coverage, which made classical geological mapping in this area challenging, the location of the main normal fault of the Eichenberg-Gotha-Saalfeld fault zone has been detected only by ground based electrical resistivity tomography. The magnetic anomaly is located sub-parallel to this fault branch and its location does not fit into the available geological models. The discrepancies between the observed data, the inversion results and the geological sections lead to the development of conceptual models in order to explain possible processes that are the source of the magnetic anomaly.

Contents

List of Abbreviations	VII
List of Symbols	IX
List of Figures	XI
List of Tables	XIII
1 Introduction	1
2 Basics of Magnetic Full Tensor Gradiometry	3
2.1 Description of Magnetic Phenomena	3
2.1.1 Fundamentals of Magnetics	3
2.1.2 The Magnetic Gradient Tensor	4
2.1.3 The Magnetic Dipole	5
2.2 Earth's magnetic field	6
2.2.1 Internal Field	6
2.2.2 External Field	8
2.2.3 Crustal Field	9
2.2.4 Coordinate Systems	17
3 Magnetic field sensors	19
3.1 Superconductivity and SQUID	19
3.2 Superconducting Magnetometers and Gradiometers	20
3.3 Airborne full tensor gradiometer system	22
3.3.1 Full Tensor Magnetic Gradiometry System	22
3.3.2 Data acquisition unit and Navigation system	23
3.3.3 The Airborne Setup	24
3.4 Kappameter	24
4 Processing and Inversion	27
4.1 Processing of full tensor gradiometry data	27
4.1.1 Calibration of Magnetometers	27
4.1.2 Balancing of Gradiometers	28
4.1.3 Decomposition and Rotation of Tensor components	28
4.1.4 Post-processing	29
4.1.5 Data interpolation on a regular grid	30
4.2 Inversion	30
4.2.1 Introduction to Inverse modeling	30
4.2.2 Model parametrization	32
4.2.3 Forward modeling	33
4.2.4 Regularization	33
4.2.5 Inversion strategy	34
5 Case studies applying full tensor magnetic gradiometry	37
5.1 Introduction	37
5.2 Geological overview	38
5.2.1 Geological development of Thuringia	38

5.2.2	Geological framework of the "Schmalwasser" survey area	41
5.2.3	Stratigraphy of the Thuringian Basin	42
5.2.4	Local geological setting of the "Siebleben" study site	43
5.3	Case study 1: Determining remanent and total magnetization on crystalline rocks in the Thuringian Forest	45
5.3.1	Motivation	45
5.3.2	Methods and Operations	46
5.3.3	Results	49
5.3.4	Interpretation	55
5.4	Case study 2: Exploring sedimentary rocks in the Thuringian Basin . .	60
5.4.1	Motivation	60
5.4.2	Methods and Operation	61
5.4.3	Susceptibility Measurements	62
5.4.4	Acquired FTMG data	63
5.4.5	Inversion results of FTMG and resistivity data	68
5.4.6	Interpretation	68
6	Discussion	77
6.1	Magnetization vector inversion on remanent structures in the Thuringian Forest	77
6.1.1	Discussion of the findings in the "Schmalwasser" survey area . .	77
6.1.2	Comparison with other studies regarding remanence determination	79
6.2	Discussion of FTMG and ERT interpretations in the Thuringian Basin	81
6.2.1	Discussion of the findings in the "Ohrdruf" survey area	81
6.2.2	Comparison with other studies investigating sedimentary rocks .	82
6.3	Advantages and future perspectives of airborne FTMG	83
7	Conclusions and Outlook	87
7.1	Modeling FTMG data affected by remanence in the Thuringian Forest .	87
7.2	FTMG in sedimentary basin exploration	88
7.3	Future directions for FTMG exploration	89
	Bibliography	91
A	Appendix: FTMG data and inversion results of the "Schmalwasser" area	105
B	Appendix: FTMG data and inversion results of the "Ohrdruf" area	123
C	Appendix: Susceptibility and Paleomagnetic Measurements	135
D	Appendix: Color maps	139
	Acknowledgements	141
	Selbständigkeitserklärung	143

List of Abbreviations

AINS	aided inertial navigation system
BIF	banded-iron formation
BMBF	Bundesministerium für Bildung und Forschung
CMRR	common-mode-rejection ratio
CRM	chemical remanent magnetization
DAS	data acquisition system
dGPS	differential global positioning system
DRM	depositional remanent magnetization
ECEF	earth-centered earth fixed
EGSFZ	Eichenberg-Gotha-Saalfeld fault zone
ERT	electrical resistivity tomography
FLL	flux-locked-loop
FTMG	full tensor magnetic gradiometry
GK25	geological map 1:25.000
HD	Höhenberger Dolerit
HDGM	high definition geomagnetic model
HTS	high temperature superconductor
IC	inner core
IGRF	international geomagnetic reference model
IMU	inertial measurement unit
INFLUINS	integrated fluid dynamics in sedimentary basins
IPHT	Leibniz-Institute für Photonische Technologien
JJ	Josephson junction
KIAS	knots indicated airspeed
ku	Lower Keuper
LIAG	Leibniz-Institute für Angewandte Geophysik
LTS	low temperature superconductor
MVI	magnetization vector inversion
NED	north, east, down - coordinate system
NES	Nesselgrund
NRM	natural remanent magnetization
OC	outer core
PDF	probability density function

RMS	root-mean-square
SI	Système international d'unités
SPIT	Spittergrund
SQUID	superconducting quantum interference device
TFA	total field anomaly
TLUG	Thüringer Landesanstalt für Umwelt und Geologie
TMI	total magnetic intensity
TRM	thermoremanent magnetization
UTM32N	Universal Transverse Mercator coordinate projection zone 32 north

List of Symbols

\mathbf{D}	displacement current
\mathbf{E}	electrical field
\mathbf{B}	magnetic induction
\mathbf{H}	magnetic field
\mathbf{j}	electrical current density
∇	nabla vector operator
ρ	electric charge
t	time
\mathbf{M}, \mathbf{J}	magnetization vector
μ_0, μ_r	vacuum and relative magnetic permeability
χ	susceptibility
$\hat{\mathbf{G}}$	magnetic gradient tensor
G_{ij}	elements of $\hat{\mathbf{G}}$, i.e. magnetic gradients
I_0, I_1, I_2	rotational invariants of $\hat{\mathbf{G}}$
$\lambda_1, \lambda_2, \lambda_3$	eigenvalues of $\hat{\mathbf{G}}$
μ_{NSS}	normalized source strength
\mathbf{r}, r	position vector of observation point
δ_{ij}	Kronecker delta
I, D	inclination, declination angles
W	potential of the magnetic field
P_n^m	Legendre-polynomial of degree m and order n
g_n^m, h_n^m	Gauss-Schmidt coefficients of degree m and order n
R	Earth's radius
ϕ, θ	latitude, longitude
X, Y, Z	components of Earth's magnetic field vector (north, east and down component)
Q	Königsberger ratio
$\hat{\mathbf{I}}$	identity matrix
$\hat{\mathbf{N}}$	demagnetization tensor
ϕ_0	magnetic flux quantum
\mathbf{F}	raw magnetometer readings used in FTMG processing
\mathbf{O}	Offset vector used in FTMG processing
\mathbf{S}	sensitivity matrix used in FTMG processing

\mathbf{D}_{dist}	distortion matrix used in FTMG processing
α_i	balancing coefficients
\mathbf{D}_{NED}^b	rotation matrix from body frame to NED system
$\Phi, \Theta, \Psi,$	roll, pitch and yaw angles
\mathbf{d}	data vector
\mathbf{A}	forward operator
\mathbf{A}^{-1}	inverse of operator \mathbf{A}
\mathbf{m}	model vector
$\delta\mathbf{m}$	model perturbation
$\delta\mathbf{d}$	infinitesimal data variation
\mathbf{F}_0	Frèchet matrix
$\mathbf{P}^\alpha(\mathbf{m})$	parametric functional
$\phi_d(\mathbf{m})$	misfit functional
$s(\mathbf{m})$	stabilizer functional
α	regularization parameter
β	focusing parameter
κ	step length of one inverse step
$\hat{\mathbf{l}}(\mathbf{m})$	direction of steepest decent

List of Figures

2.1	Illustration of different magnetic gradient tensor and field components .	7
2.2	Principle of diamagnetism	10
2.3	Principle of paramagnetism	11
2.4	Illustration of ferromagnetism	12
2.5	Ternary system of Fe-Ti oxides	13
2.6	Susceptibility ranges of various rocks	15
2.7	Illustration of self-demagnetization	16
2.8	Sketch of most common coordinate systems for Earth's magnetic field. .	17
3.1	Illustration of the dc-SQUID concept	20
3.2	Illustration of gradiometer types	21
3.3	Illustration of parasitic areas of planar gradiometers	22
3.4	Illustration of the airborne FTMG system	23
4.1	Schematics of the processing of FTMG data.	27
4.2	Illustration of model discretization.	32
4.3	Illustration of the regularization methods.	35
5.1	Location of study areas.	37
5.2	Simplified Basement structure of Central Europe	38
5.3	Geological Map of Thuringia	40
5.4	Geological Map of the "Schmalwasser" survey area	41
5.5	Geological map of the "Siebleben study site."	44
5.6	Measured Gyy of the western "Schmalwasser" area with picked magnetic lineaments.	51
5.7	Horizontal slices of the FTMG and TFA magnetization model of the "Schmalwasser" area.	52
5.8	3D magnetization model of the HD.	54
5.9	Paleomagnetic results from the HD samples.	55
5.10	Comparison of measured and inverted magnetization directions at the <i>Nesselgrund</i> location.	59
5.11	Susceptibility sampling sites	63
5.12	Gzz of the "Ohrdruf" area.	66
5.13	FTMG and TFA of the "Siebleben" area.	67
5.14	Horizontal slices (E, N) through magnetization model of "Siebleben" study site.	69
5.15	Horizontal slices (D, I) through magnetization model of "Siebleben" study site.	70
5.16	Joint interpretation of magnetization models, ERT and geological cross sections (west) of the "Siebleben" site.	72
5.17	Joint interpretation of magnetization models, ERT and geological cross sections (east) of the "Siebleben" site.	73
5.18	Conceptual models of the "Siebleben" site	75
6.1	Examples of equivalent models	78
A.1	Gxx of the "Schmalwasser" area.	106
A.2	Gxy of the "Schmalwasser" area.	107
A.3	Gxz of the "Schmalwasser" area.	108
A.4	Gyy of the "Schmalwasser" area.	109
A.5	Gyz of the "Schmalwasser" area.	110
A.6	Gzz of the "Schmalwasser" area.	111

A.7	TFA of the "Schmalwasser" area.	112
A.8	Topography and flight track of the "Schmalwasser" area.	113
A.9	Histogram of residuals of the FTMG inversion at the "Schmalwasser" area.	114
A.10	Histogram of residuals of the TFA inversion at the "Schmalwasser" area.	115
A.11	Horizontal slices of the FTMG and TFA magnetization model of the "Schmalwasser" area.	116
A.12	Vertical slices of the FTMG and TFA magnetization model of the "Schmalwasser" area (<i>Nesselgrund</i>).	117
A.13	Zoom into vertical slices of FTMG magnetization models.	118
A.14	Vertical slices of the FTMG and TFA magnetization model of the "Schmalwasser" area (<i>Spittergrund</i>).	119
A.15	Vertical slices through the FTMG model (total magnetization).	120
A.16	Comparison of measured and inverted magnetization directions at the <i>Nesselgrund</i> location.	121
A.17	Comparison of measured and inverted magnetization directions at the <i>Spittergrund</i> location.	122
B.1	Gxx of the "Ohrdruf" area.	124
B.2	Gxy of the "Ohrdruf" area.	125
B.3	Gxz of the "Ohrdruf" area.	126
B.4	Gyy of the "Ohrdruf" area.	127
B.5	Gyz of the "Ohrdruf" area.	128
B.6	Gzz of the "Ohrdruf" area.	129
B.7	TFA of the "Ohrdruf" area.	130
B.8	Topography and flight track of the "Ohrdruf" area.	131
B.9	TFA of the Thuringia area.	132
B.10	Histogram of residuals of the magnetic inversion at the "Siebleben" area.	133
B.11	Vertical slices though the magnetization model at the "Siebleben" area.	134
D.1	Color maps used in this study.	139

List of Tables

1	Parameters of starting model for "Schmalwasser" FTMG inversion . . .	48
2	Compilation of susceptibility values from Thuringia.	64
3	Measured susceptibilities and sampling sites in Thuringia	137
4	Susceptibility and NRM results of HD samples	138

1 Introduction

The measurement of magnetic field anomalies has a long history and is nowadays amongst the most frequently used geophysical methods. Often, the standard procedure applied in industry, is the acquisition of the scalar magnetic total field anomaly (TFA)¹ using optically pumped caesium or potassium vapor magnetometers. These systems are used for example in airborne surveys for mineral, hydrocarbon or geothermal exploration (*Hinze et al.*, 2013). A great advantage of airborne magnetic exploration is that it allows to conduct surveys over large areas in a reasonable amount of time and is still relatively cheap in comparison with other geophysical methods. Furthermore, like with other airborne method, areas that are inaccessible by foot can be explored as well. Magnetic surveys allow to delineate geological structures according to their magnetic signature, for instance linear magnetic anomalies caused by lateral magnetization contrasts across folds and fault zones. In ground based surveys, magnetometer systems are also often used to search for unexploded ordnance (UXO) or in archaeology in order to map and investigate buried ancient structures.

Within the past decade a new type of instruments has been developed for magnetic exploration, which allows to gather vectorized information. The direct acquisition of the magnetic field vector is still not possible with the desired accuracy due to hardware limitations. Thus, a vectorized measurement can be realized by using a gradiometer design based on Superconducting Quantum Interference Devices (SQUIDs). These SQUID gradiometers are used to acquire the complete magnetic gradient tensor of the Earth’s magnetic field (full tensor magnetic gradiometry, FTMG). Those instruments have been successfully deployed in ground based surveys in archaeology (*Linzen et al.*, 2009) and UXO detection as well as in airborne exploration to search for mineral deposits (*Stolz et al.*, 2006; *Rompel*, 2009). A directly acquired magnetic gradient tensor has some advantages compared to conventional magnetic exploration. It offers additional directional information, which allows to better constrain the modeling of magnetized sources in the subsurface. It is also more sensitive to shallow structures of magnetized material and allows a more well defined distinction between closely spaced anomalies (*Pedersen and Rasmussen*, 1990). Thus, the airborne FTMG system implements new opportunities in airborne magnetic exploration.

Such a system has been applied within the framework of the multidisciplinary project *INFLUINS* (INtegrated FLUId Dynamics IN Sedimentary basins)². This collaborative research initiative aimed towards a better understanding of fluid flow in sedimentary basins on various spatio-temporal scales. These often hold valuable resources, i.e. hydrocarbons. It is very likely, that sedimentary basins will gain more importance in the future in terms of underground storage of gas or to ensure fresh water supply. Thus, an in-depth understanding of fluid flow processes is essential.

Fault zones in sedimentary basins play a significant role for fluid flow (*Hooper*, 1991; *Bjørlykke*, 1993, 2015). They mainly influence fluid flow patterns in two ways: either due to increased permeability which can allow fluids from greater depths to interact with shallower aquifers, or in the opposite way as fluid barriers. The location and geometry of a fault zone derived from airborne magnetic surveys can be important to know for hydrogeological modeling (*Grauch*, 2001).

The study area of the *INFLUINS* project is the medium-sized Thuringian Basin

¹often also referred as total magnetic intensity (TMI)

²www.influins.uni-jena.de

in the center of Germany. Different geophysical, geochemical, geological, and other methods have been applied throughout the project. These studies included three seismic profiles of 76 km length in total acquired in 2011 (*Goepel et al.*, in prep.) and a scientific deep drilling campaign in 2013 with a total depth of 1179 m (*Kunkel et al.*, 2014). In addition, in 2012 and 2013, five airborne FTMG surveys have been conducted above various areas in the Thuringian Basin and the Thuringian Forest, which had several aims, e.g. the mapping of magnetic lineaments along faults in the sedimentary basin, the exploration of the transition zone between basement and sediments, and the analysis of the magnetic properties of some of the crystalline structures, that are exposed in the highlands to the south.

The scope of this thesis is to apply airborne full tensor magnetic gradiometry in different geological scenarios. This includes the interpretation of the mapped magnetic gradient tensor maps, magnetization vector inversion (MVI) of FTMG data and the combined interpretation with complimentary data sets, e.g. electrical resistivity tomography or paleomagnetic information.

Structure of this thesis: In section 2, an introduction into the basic principles of the magnetic gradient tensor and the origin of the magnetic fields is given. This section is followed by an in-depth description of the applied magnetic field sensors in section 3. Since the applied system is different from conventional airborne magnetic instruments, a more complex processing scheme has to be used, which is outlined in section 4. One major point of this study is to model the acquired FTMG data using a voxel-based magnetization vector inversion code (*Zhdanov*, 2002). The basic principle of this inversion algorithm is also given in this section. These three chapters are intended to create the basis necessary to understand the methods, which are applied in the two case studies presented herein.

The first case study described in section 5.3 focuses on the topic to reduce the inherent ambiguity of magnetization vector inversions by exploiting the increased directional sensitivity provided by the full magnetic gradient tensor. This can be especially valuable in areas with significant remanent magnetization. Often the complexity of modeling magnetic field data is reduced by only varying susceptibility distributions, and thus the remanent part of the magnetization vector is neglected. This, however, can lead to serious misinterpretations of the geological structures. In this case study, a data set with indications of remanent magnetization has been modeled using the FTMG and total magnetic field data. Both models are compared and the recovered magnetization directions are evaluated by paleomagnetic measurements on field samples.

The second case study in section 5.4 aims to investigate a small and weak intra-basinal magnetic anomaly, which is probably related to one of the major fault zones crossing the Thuringian Basin. The interpretation of the acquired FTMG data and the inversion results of this data set is aided by ground based geo-electrical and geological sections. Several explanations and models have been presented in this case study.

At the end, the results of the two case studies are discussed in detail in section 6. This section ends with some implications drawn from both case studies, which suggest further technical improvements of the airborne system. Also, some methodical improvements are discussed, which may have the potential to enhance the results of similar studies in the future.

2 Basics of Magnetic Full Tensor Gradiometry

A new generation of magnetic field gradiometers and magnetometers has been developed in the last decade, which allows for an advanced airborne geophysical exploration. Even though these systems allow for new airborne geophysical exploration, an introduction of the basic effects of magnetism is necessary and is given here. This includes the introduction of the basic effects of magnetism, a general description of basic formulae and the magnetic gradient tensor. At the end of the first section, the basic example of a magnetic dipole is used to illustrate these properties and to show the sensitivity of this methods. These basic formulae also provide the foundation to understand the measurement principle of the new sensors applied in this study, which will be explained in section 3.2.

The second section comprises the description of the Earth's magnetic field and the explanation of the used coordinate systems. At the end of this chapter, the magnetic properties of some material are explained. This includes a description of the most common two types (induced and remanent) of rock magnetization.

2.1 Description of Magnetic Phenomena

2.1.1 Fundamentals of Magnetics

Magnetic and electric fields are coupled by the four Maxwell equations:

$$\nabla \cdot \mathbf{D} = \rho \quad (2.1)$$

$$\nabla \cdot \mathbf{B} = 0 \quad (2.2)$$

$$\nabla \times \mathbf{E} + \frac{\partial \mathbf{B}}{\partial t} = 0 \quad (2.3)$$

$$\nabla \times \mathbf{H} = \mathbf{j} + \frac{\partial \mathbf{D}}{\partial t}. \quad (2.4)$$

Equation 2.1 corresponds to **Gauss' law**, which relates electrical charges (ρ) with an electrical displacement field \mathbf{D} . **Gauss' law for magnetism** (Equation 2.2) states that magnetic monopoles do not exist. The electrical field \mathbf{E} and the magnetic induction \mathbf{B} are coupled by **Faraday's law** (Equation 2.3). Equation 2.4 connects the rotation of the magnetic field \mathbf{H} with the electrical current density \mathbf{j} and the time derivative of displacements currents \mathbf{D} . Since in this work only static magnetic fields are considered, the time derivative of \mathbf{D} in (2.4) vanishes. Also, telluric currents are neglected, which leads to the simplification of Equation 2.4:

$$\nabla \times \mathbf{H} = 0 \quad (2.5)$$

The magnetic induction and the magnetic field are connected via a material equation

$$\mathbf{B} = \mu_0(\mathbf{H} + \mathbf{M}) = \mu\mathbf{H}, \quad (2.6)$$

where \mathbf{M} is the magnetization vector in A/m , $\mu = \mu_0\mu_r = \mu_0(1 + \chi)$ the magnetic permeability, μ_0 the vacuum magnetic permeability, μ_r the relative magnetic permeability, and χ the susceptibility of the material. The magnetic susceptibility χ is related to the magnetic permeability

$$\chi = \mu_r - 1 \quad (2.7)$$

Susceptibility is a scaling factor, describing the strength of induced magnetic fields. In general, χ is a tensor, which describes the anisotropic induced magnetization of a material. A more detailed description of induced magnetism can be found in section 2.2.3.

2.1.2 The Magnetic Gradient Tensor

The focus of this work is to measure, model and interpret magnetic anomalies caused by geological structures due to induced and remanent magnetization in the uppermost crust. In conventional magnetic surveys, the total field (*total magnetic intensity*, $TMI = |\mathbf{B}|$) is obtained. During the field experiments conducted in the framework of this study, the gradients of the three magnetic field components $\mathbf{B} = (B_x, B_y, B_z)^T$ are directly measured, which means that the tensors is a 3 x 3 matrix of their spatial derivatives:

$$\hat{\mathbf{G}} = \frac{\partial B_i}{\partial x_j} = \begin{pmatrix} G_{xx} & G_{xy} & G_{xz} \\ G_{yx} & G_{yy} & G_{yz} \\ G_{zx} & G_{zy} & G_{zz} \end{pmatrix}. \quad (2.8)$$

Since the magnetic field is free of divergence (see Equation 2.2), the gradient tensor is traceless

$$G_{xx} + G_{yy} + G_{zz} \equiv 0. \quad (2.9)$$

Because only static magnetic fields are considered (see Equation 2.5), the tensor is also symmetric, which means that only five linear independent components are necessary:

$$\hat{\mathbf{G}} = \frac{\partial B_i}{\partial x_j} = \begin{pmatrix} G_{xx} & G_{xy} & G_{xz} \\ G_{xy} & G_{yy} & G_{yz} \\ G_{xz} & G_{yz} & -G_{xx} - G_{yy} \end{pmatrix}. \quad (2.10)$$

In conventional airborne magnetic surveys, TMI is measured e.g. using optically pumped Caesium (or Potassium) vapour magnetometers. Often, the total field gradients are then calculated, using an array of these magnetometers, by differentiating the measured signals, or using specific kernels in the Fourier domain (*Blakely, 1996*). These total field gradients, i.e. $\partial|\mathbf{B}|/\partial x$, do not feature the properties of potential fields, because $|\mathbf{B}|$ is only the projection of the magnetic field vector onto the Earth's magnetic field direction. This is not the case for the components of the gradient tensor ($\partial B_i/\partial x_j$) (*Schmidt and Clark, 2006*).

Compared to TMI surveys, measuring the gradient tensor has several advantages: Since the tensor consists of the first derivatives, it allows for a better resolution of closely spaced anomalies caused by shallow sources. Also the effect of sources with a homogeneous response, i.e. deep sources with regional magnetic field gradients, are suppressed. Geomagnetic field variations are homogeneous, which results in very low differences in the sensing areas of a gradiometer, i.e. across the baseline. Thus, geomagnetic variations are neglected (see section 2.2.2) and the use of a base station is not necessary. The assumption of an ideal, i.e. perfectly balanced gradiometer (section 3.2), leads to a system which is relatively insensitive to rotational noise and therefore the preferable solution for airborne, vectorized magnetic surveys. In addition the technical advantages, there are several other positive aspects regarding structural resolution, Euler deconvolution, and gridding (*Schmidt and Clark, 2006; FitzGerald and Holstein, 2006*).

The gradient tensor has three rotational invariants (*Pedersen and Rasmussen, 1990*), which are insensitive to rotational noise, similar to the TMI. The first invariant I_0 is the trace of the tensor, i.e. (compare with Equation 2.9)

$$I_0 = G_{xx} + G_{yy} + G_{zz} = 0. \quad (2.11)$$

The second invariant I_1 is defined as the contraction of the tensors

$$I_1 = G_{xx}G_{yy} + G_{yy}G_{zz} + G_{zz}G_{xx} - G_{xy}^2 - G_{yz}^2 - G_{zx}^2 \quad (2.12)$$

and the third invariant I_2 is the determinant of the tensor

$$\begin{aligned} I_2 &= \det \mathbf{G} \\ &= G_{xx}(G_{yy}G_{zz} - G_{yz}^2) + G_{xy}(G_{yz}G_{xz} - G_{xy}G_{zz}) \\ &\quad + G_{xz}(G_{xy}G_{yz} - G_{xz}G_{yy}). \end{aligned} \quad (2.13)$$

I_1 and I_2 are characterized by a lower motion noise³ level than the individual tensor components (*Pedersen and Rasmussen, 1990*). Both invariants can be applied when interpreting magnetic maps. I_1 and I_2 can be associated with the analytic signal (*Nabighian, 1972, 1974, 1984; Roest et al., 1992*), which has been proven to be a very useful tool for interpretation of mapped magnetic fields during the last decades. By using a dimensionless quantity I formulated by *Pedersen and Rasmussen (1990)*:

$$0 \leq I = -\frac{(I_2/2)^2}{(I_1/3)^3} \leq 1, \quad (2.14)$$

a distinction between 2D and 3D structures can be made. If I is zero, the field will be invariant along a certain strike direction, which means that the source structure is 2D, whereas it would be 3D if it is close to 1. The eigenvalues of the gradient tensor can be determined using the following relation (*Pedersen and Rasmussen, 1990*):

$$\lambda_i^3 - I_0\lambda_i^2 + I_1\lambda_i - I_2 = 0 \quad I = 1, 2, 3, \quad (2.15)$$

whereas $\lambda_1 \geq \lambda_2 \geq \lambda_3$ are the three eigenvalues. These can also be used to construct the normalized source strength (NSS)

$$\mu_{NSS} = \sqrt{-\lambda_2^2 - \lambda_1\lambda_3}, \quad (2.16)$$

which is independent of the magnetization direction of simply shaped sources, e.g. spheres, compact dipoles, and pipes with axial magnetization. The application of the NSS for the interpretation of magnetic field data is subject of current research (*Clark, 2012, 2013; Beiki et al., 2012; Pilkington and Beiki, 2013*). Additionally, the usage of the horizontal gradients of the tensor and the visualization using ternary color-maps have been discussed recently (*Wedge et al., 2012*).

2.1.3 The Magnetic Dipole

To illustrate the properties of the magnetic induction \mathbf{B} and the magnetic gradient tensor $\hat{\mathbf{G}}$, the response of a magnetic dipole is shown in this section. The units for these two properties are Tesla for the magnetic induction and Tesla/m for the components of

³this does not apply to the intrinsic noise of the FTMG system.

the gradient tensor, respectively. It is common practice to use nT ($1 \text{ nT} \equiv 1 \times 10^{-9} \text{ T}$) and nT/m instead.

The magnetic inductions of a magnetic dipole can be derived by combining equations (2.5) and (2.2). This leads to:

$$\mathbf{B} = \frac{\mu_0}{4\pi} \left(\frac{3(\mathbf{M} \cdot \mathbf{r})\mathbf{r}}{r^5} - \frac{\mathbf{M}}{r^3} \right), \quad (2.17)$$

where \mathbf{r} is the vector pointing from the observation point to the dipole, μ_0 the vacuum magnetic permittivity, and $\mathbf{M} = (M_x, M_y, M_z)^T$ the magnetization vector of the dipole. The complete derivation of this formula is given in *Blakely* (1996). Following this approach, analytic formulae for simple bodies or 3D bodies of arbitrary shape can be derived (*Nettleton*, 1942; *Talwani*, 1965; *Pohanka*, 1988; *Götze and Lahmeyer*, 1988; *Holstein*, 2003), which are useful when modeling magnetized geological structures.

Similar to equation (2.17), the components of the magnetic gradient tensor caused by a dipole can be calculated by:

$$G_{ij} = \frac{\partial B_i}{\partial x_j} = -\frac{3\mu_0}{4\pi r^7} [\mathbf{M} \cdot \mathbf{r} (5r_i r_j - r^2 \delta_{ij}) - r^2 (r_i M_j + r_j M_i)]. \quad (2.18)$$

This equation describes the five elements of the magnetic gradient tensor $\hat{\mathbf{G}}$ of a dipole with the magnetization vector \mathbf{M} .

The response of a magnetic dipole is shown in Fig. 2.1 with the gradient tensor in the upper panel, the magnetic induction in the middle and the direction and location of the dipole in the lower panel. As expected, the gradients show a shorter wavelength compared to the magnetic field components. The components G_{xy} , G_{yz} and B_y are zero because the shown profile is at the $y = 0$ location, and no magnetization in y -directions is given, i.e. 0° declination.

Equation 2.18 provides the basis of the forward operator, which is used in the inversion process and described in section 4.2.

2.2 Earth's magnetic field

The Earth's magnetic field consists of three main parts: (i) the main field, which makes up about 95 % of the field strength. It originates from the Earth's outer core (OC). (ii) The second part with highly variable amplitudes and frequencies is caused by solar winds and ionospheric effects. (iii) The third part is caused by the different magnetic properties of structures within Earth's crust, caused by varying susceptibility and various forms of remanent magnetization. This part is generally referred to as crustal anomalies.

2.2.1 Internal Field

The main part of the Earth's magnetic field is a dipolar field, which reaches amplitudes of 60 000 nT at the magnetic poles and 20 000 nT at the magnetic equator. There are several effects, such as the westward drift of non-dipole parts or magnetic field reversals in the past, suggesting a more dynamic and complex source of the main field. The source of the internal magnetic field is located in the outer core (OC) in a depth of 2900 to 5150 km (*Lowrie*, 2007). Seismological studies show that the OC is liquid. Its chemical composition is still under debate, but it is expected to be an iron-alloy

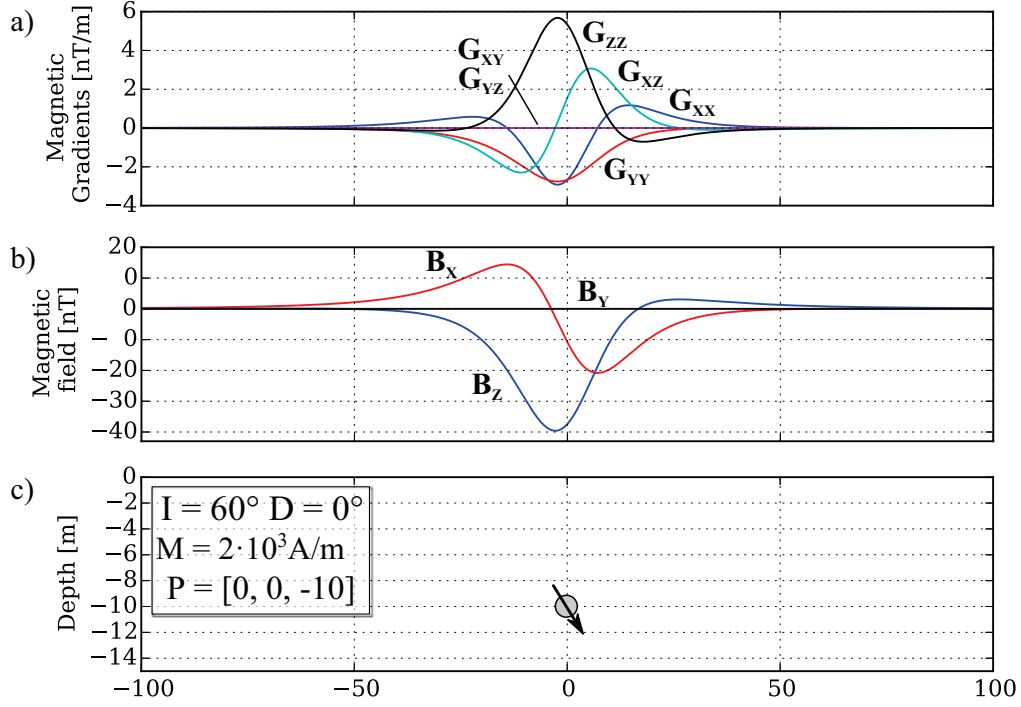


Figure 2.1: Magnetic field components (b) and gradients (a) of a magnetic dipole (c) with inclination of 60° and total magnetization of $2 \times 10^3 \text{ A/m}$ at a position (0,0,-10). Since $M_y = 0$, i.e. no declination, the components B_y , G_{xy} and G_{yz} are zero. Also note that gradients produce shorter wavelengths compared to the magnetic field components.

and often referred as FeX. Thereby, various different elements are discussed as the second component of the alloy (*Glatzmaier and Roberts, 1996*). Expected temperatures exceed 3000°C (*Campbell, 2003*), which is much higher than the Curie-temperature of iron and nickel of 770°C and 360°C , respectively. The Curie-temperature depends on pressure and the composition of the involved material. That means in the OC neither induced nor remanent magnetization is possible (section 2.2.3). Since iron and nickel are good electrical conductors, the internal magnetic field can be described using a model of a self-exciting dynamo (*Lowrie, 2007*).

Inside the OC convection cells are expected, which are driven by several different sources. The main contributors arise from sedimentation processes of heavier and the rising of lighter elements in the OC (*Lanza and Meloni, 2006*). Also heat production due to radioactive decay and latent heat provided by chemical reactions in the inner and outer core are considered to drive the convection current, however the amount of heat produced may not be sufficient. Because of Earth's motion and the Coriolis force, these convection currents are forced into flow rolls which are aligned parallel to the rotational axis. Convection of iron and nickel yields induction of strong currents inside the OC. To start this process, an initial \mathbf{B} -field is required. This field is then self-enhancing up to its saturation strength.

There are several attempts to model the geodynamo by using *magnetohydrodynamic* equations (*Priest and Forbes, 2000*), which link the magnetic field to particle velocities and the electrical conductivity. This is not an easy task, because many of the

parameters, such as temperature, chemical composition and viscosity of the OC are currently not sufficiently well known and assumptions have to be used (*Glatzmaier and Roberts, 1996; Roberts and Glatzmaier, 2000, 2001*).

Beside using dynamic models to understand the origin of Earth's magnetic field, there are ways to model the field itself in order to describe and to predict it. The most accurate approach to describe the potential of the magnetic field is by using spherical harmonic functions. The potential of the magnetic field is expressed by (*Lowrie, 2007*)

$$W = R \sum_{n=1}^{n=\infty} \sum_{m=1}^{m=\infty} \left(\frac{R}{r}\right)^{n+1} (g_n^m \cos m\phi + h_n^m \sin m\phi) P_n^m(\cos \theta), \quad (2.19)$$

with Legendre polynomials P_n^m of degree m and order n . The two constants g_n^m and h_n^m are called Gauss-Schmidt coefficients. These are derived from a world-wide network of geomagnetic observatories and several satellite missions. This is realized by finding a set of coefficients that fit the observed field. There are several global geomagnetic models available, which describe the Earth's magnetic field, e.g. the international geomagnetic reference field (IGRF) (*Finlay et al., 2010*) and the high definition geomagnetic model (HDGM) (*Maus et al., 2012*). Using Equation 2.19, the dipolar part of the field is expressed by the *Gauss-Schmidt* coefficients g_1^0 and h_1^0 . Coefficients of higher order and degree are used to describe the non-dipolar field, which only contributes 5% to the total field (*Lowrie, 2007*). Both, the IGRF and the HDGM, provide annual changes of the *Gauss-Schmidt* coefficients. Thus, future field values can be predicted. The IGRF coefficients are updated within a cycle of five years.

For modeling and inversion (see section 4) the field components are calculated using the IGRF. In order to calculate the magnetic field components from the full gradient tensor, knowledge of the background field is necessary.

2.2.2 External Field

The contribution of external magnetic field signals to the Earth's magnetic field are characterized by variable signal strength compared to the internal field, originated in the ionosphere. The ionosphere is part of the atmosphere between 60 and 1000 km (*Campbell, 2003*) altitude. It is characterized by a different chemistry due to intense ionization (*Kertz, 1992*). The main source of ionization is radiation excited by the sun. Due to the high variability of solar activity it is reasonable to distinguish between quiet and disturbed days. Days with low variations of the magnetic field associated with the solar activity are called solar quiet days (S_q) and they show predominantly variational cycles of 24 h, 12 h, 8 h and 6 h (*Campbell, 2003*). When the ionized gas of the ionosphere moves through the Earth's magnetic field electrical ring currents are induced. These electrical currents are the origin of the solar quiet variations and they usually reach amplitudes of 10 to 30 nT (*Lanza and Meloni, 2006*). These temporal variations can be explained by differences in ion concentration of the day and night sides of the Earth. In addition, the tidal interaction between the gravitational field of the moon and the ionosphere leads to a lunar variation. However, this effect is comparably small with only 1 – 2 nT.

Beside these regular changes associated with solar quiet days, also other irregular magnetic field variations based on different solar activity can be observed. Days characterized by solar magnetic storms are called solar disturbed days (S_D). Magnetic storms occur when a large number of charged particles, mainly protons and electrons,

are erupted from the sun, e.g. during a coronal mass ejection (CME). When a magnetic storm interacts with the magnetosphere of the Earth, amplitude changes of the external magnetic field can reach several tens to hundreds of nT (*Lanza and Meloni*, 2006). Such a storm can last for hours and up to several days. Particles trapped in the magnetosphere produce different ring currents, which are running in the equatorial plane. A magnetic storm can also be divided into several different phases (*Campbell*, 2003) with different duration and amplitudes, e.g. the *sudden storm commencement*, an *initial* phase and a *main* (or *growth*) phase. The intensity of magnetic storms varies within the 11-year cycle of the solar activity. A more comprehensive overview can be found in *Kertz* (1992); *Campbell* (2003); *Lanza and Meloni* (2006).

Conventional magnetometers are greatly affected by the temporal variations discussed earlier. In order to remove the effect of the external magnetic field variations, a correction has to be applied. Otherwise, the data will be noisy and magnetic anomalies with low amplitudes will not be detected. To correct for the daily variations a base station is used. The base station collects magnetic field data in a given time interval and therefore records the changes of the magnetic field. Since the internal field only shows very slow and low variations, all of the recorded changes are caused by variations in the external magnetic field. The data collected with a second magnetometer (often called "rover"), which has mapped the magnetic field of the investigation area, is then corrected with the variations recorded by the base station. Thus, the data of the rover is free of variations of the external magnetic field. Gradiometer setups are insensitive to small temporal changes, because they will affect both sensors at the same time. Thus, a base station for a gradiometer survey is unnecessary. Nevertheless, a magnetic survey will be suspended anyway if a strong magnetic storm is expected. The reason for that is, that the amplitude of the induced magnetization (see section 2.2.3) of the subsurface depends on the strength of the external field. Therefore, the temporal change of the external field will cause a varying induced magnetization strength. Additionally, the inclination and declination of the external magnetic field can also change, which leads to varying directions of the induced magnetization.

2.2.3 Crustal Field

The subject of this work is to analyze the magnetic field caused by magnetization variabilities in the uppermost crust. This comprises sources containing magnetized minerals that are below a specific temperature, called the Curie temperature T_C (*Blakely*, 1996). Thereby, only contrasts in the rock magnetization can be detected, which are referred as magnetic anomalies. An uniformly magnetized subsurface will not produce a magnetic anomaly.

In this section, a brief introduction to the effects that causes magnetic anomalies in the Earth's crust will be given. This includes the various types of induced and remanent magnetization, the most important magnetic minerals, and their occurrence in igneous, metamorphic and sedimentary rocks.

Induced Magnetism: There are three main types of induced magnetism, *diamagnetism*, *paramagnetism* and *ferromagnetism*. These different types each have different ranges of susceptibility values. *Paramagnetic* material are characterized by low positive susceptibilities and *diamagnetic* material by low negative values, respectively.

Diamagnetism (Fig. 2.2) occurs when the external \mathbf{H} -field interacts with electrons within matter. Since the electrons have a charge of $-e$ and are orbiting around the

atomic nucleus, they will cause a magnetic moment. When all orbitals are complete, the magnetic moments will compensate each other, and the resulting magnetization will be zero. If an external \mathbf{H} -field is present, the electrons will induce currents. By following Lenz's Law, these currents are directed in the opposite direction with respect to their source, i.e. the external field. Therefore, the resulting induced magnetization is anti-parallel to the external field. The susceptibility of diamagnetic material is negative and small compared to the other types of induced magnetism. Every material shows diamagnetic behavior, but usually it is superimposed by other, stronger magnetization.

A superconductor is a perfect diamagnet with a susceptibility of $\chi = -1$, which causes the magnetic field lines to be pushed out of the superconducting material. This effect is called *Meisner-Ochsenfeld effect*. Since the magnetometers used in this study are superconducting quantum interference devices, this effect is important to know in order to understand how such a system works (see section 3.2).

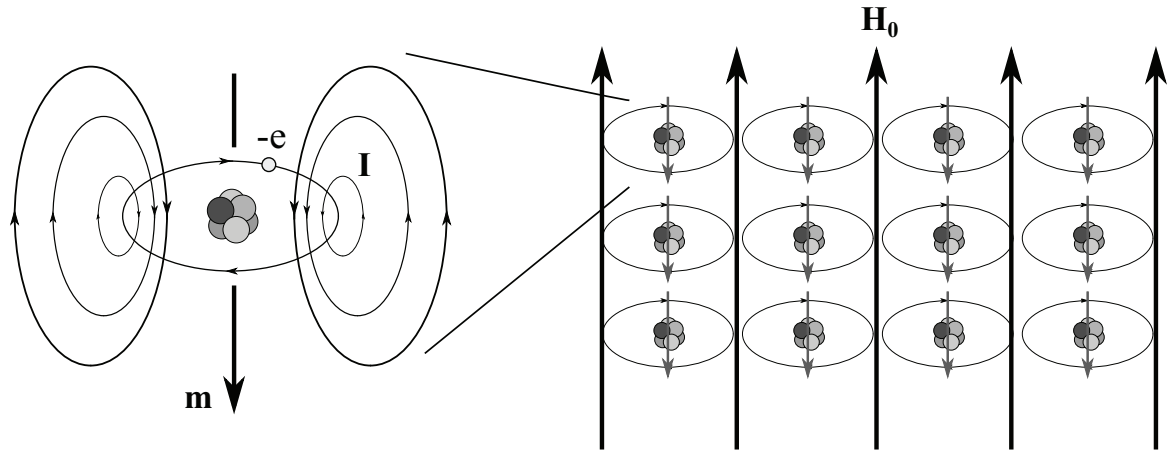


Figure 2.2: Principle of diamagnetism (Lowrie, 2007). The electron $-e$ is orbiting around the atomic nucleus and is inducing a current \mathbf{I} and magnetic moment \mathbf{m} opposite to the external field \mathbf{H}_0 .

Paramagnetism depends also on the strength of the external magnetic field. In contrast to diamagnetism, the induced magnetization vector is in-parallel to the external magnetic field. Paramagnetism occurs when molecules have a magnetic moment because of unpaired electrons and free orbitals. The spin directions of the unpaired electrons tend to align with the direction of the external field (Fig. 2.3). If no external field is present, spin directions are distributed randomly and the sum of the magnetic moments is zero. One important aspect of paramagnetic material is the temperature dependency of the susceptibility, which is inversely proportional. The susceptibility of paramagnetic material is positive and ranges from $0 < \chi < 1$.

Ferromagnetic material produce stronger induced fields than *paramagnetic* material. The main difference is that the interaction of atomic magnetic moments is negligible for para- and diamagnetism. In ferromagnetic metals, e.g. iron, nickel, and cobalt, atoms are arranged in a lattice which keeps the magnetic moments of adjacent atoms aligned and therefore creates a strong directional magnetization, which is called *ferromagnetism* (Lanza and Meloni, 2006). The induced magnetization of ferromagnetic material can be partially preserved after the external magnetic field disappears. This effect is known as *hysteresis* and the residual magnetization is called remanence, or more specific *isothermal remanence*. Remanent magnetization will be discussed later. Ferromagnetic behaviour depends on the temperature, too. Above the

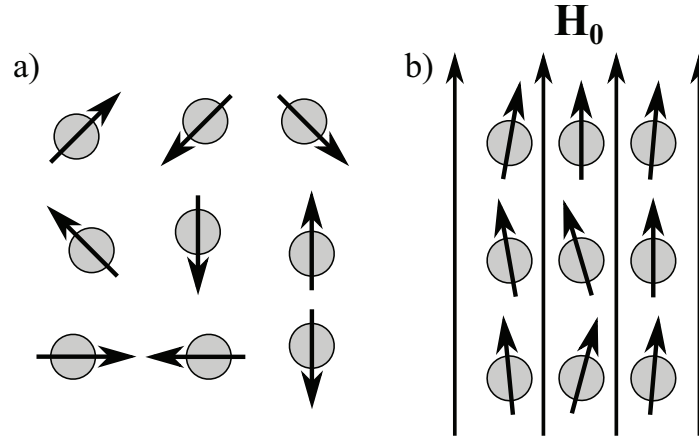


Figure 2.3: Principle of paramagnetism after Schön (2011). a) shows elementary dipole moments, without an external magnetic field. Thus, the dipole moments are orientated randomly. In the presence of an external field, these dipole moments are more or less aligned with the external field (b).

material-specific *Curie*-temperature, these material loose their ferromagnetic properties and become paramagnetic.

There are several subtypes of ferromagnetism such as **antiferromagnetism**, **ferrimagnetism**, or **canted (parasitic) antiferromagnetism** (Fig. 2.4). In these cases the direction of the magnetic spin moments is no longer parallel with respect to the magnetic field. In the case of **antiferromagnetism** the spin moments are aligned anti-parallel, resulting in a positive magnetization close to zero. The upper limit of antiferromagnetic behavior is given at the *Néel temperature*, defining the transition to paramagnetic behavior. **Canted (or parasitic) antiferromagnetic** material contain defects or vacancies in their lattice referred to as magnetic domains. Therefore, the anti-parallel magnetic moments are not perfectly paired and inclined to each other, resulting in a canted magnetization. The resulting magnetization will not necessarily point in the direction of the external applied magnetic field. Since defects are more or less randomly distributed in the lattice, very different magnetization directions can occur. **Ferrimagnetic** material (*ferrites*) are characterized by different ions occupying the gaps in the lattice. Depending on the lattice structure, e.g. tetrahedral or octahedral, and the type of ions in the gaps, sub-lattices with different magnetic moments are created. The magnetic moments are anti-parallel, similar to antiferromagnetic material, but the strength of the two types of magnetic moments is different. The most important magnetic minerals, that occur in nature (e.g. magnetite), show ferrimagnetic behavior.

Remanent Magnetization: *Remanent magnetization* or *remanence* is present in ferro- and ferrimagnetic material even without an external magnetic field. The ratio between remanent and induced magnetization is called *Königsberger ratio* Q :

$$Q = \frac{|\mathbf{M}_r|}{|\mathbf{M}_i|} \quad (2.20)$$

The most common type of remanence is **thermoremanent magnetization** (TRM). When igneous rocks are formed, their temperature often exceeds 1000°C , which is much more than the typical *Curie temperature* (T_C) of ferrimagnetic minerals

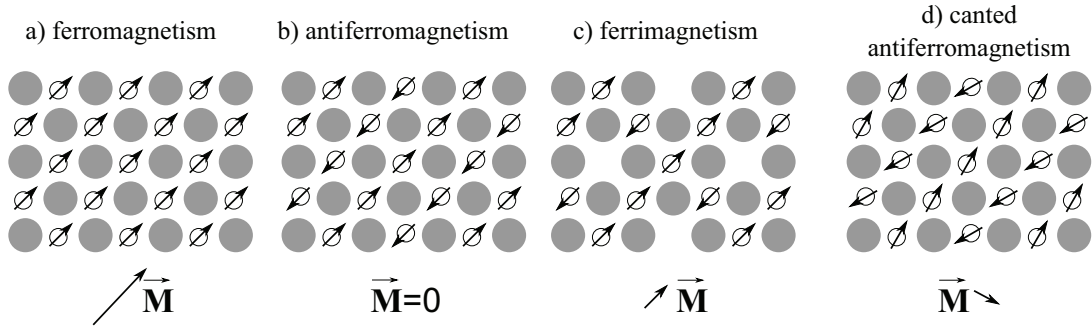


Figure 2.4: Illustration of forms of ferromagnetic material with the different orientation of the elemental dipoles in the lattice system. a) ferromagnetism, b) antiferromagnetism, c) ferrimagnetism, and d) canted (or parasitic) antiferromagnetism after *Lanza and Meloni* (2006). The resulting direction of the induced magnetization vector \vec{M} is indicated by the arrow.

(e.g. 578 °C for magnetite, 675 °C for hematite). Above T_C , minerals show paramagnetic behavior. When temperature drops below T_C , a statistically significant amount of magnetic moments remain aligned along the direction of the external field. Thus, TRM is usually very strong and stable as long as temperatures are well below T_C .

A second type of remanence is **depositional remanent magnetization** (DRM). DRM occurs during sedimentation of ferrimagnetic grains. These grains are oriented in the direction of the external magnetic field similar to a compass needle. DRM usually requires quiet depositional conditions, i.e. stable water temperatures and low water currents. When the sediments are compressed the orientation of the dipole moments might change, which leads to inclination and declination errors. This type of remanence is weaker and less stable compared to TRM.

Secondary remanence is found when existing ferrimagnetic grains are altered. When a magnetite grain, with existing remanence, becomes partially weathered, the weathering product, hematite, locks the magnetization of the present field. This magnetization might be different to the remanent magnetization of the magnetite. This process is also called **chemical remanent magnetization** (CRM).

TRM, DRM and CRM are the most important types of remanent magnetization. There are several other types which are explained in detail in *Lowrie* (2007).

Magnetic Properties of Rocks: The bulk susceptibility of rocks is controlled by their mineral composition. It is a highly variable rock property, which may vary over more than seven orders of magnitude. Already a small amount of mineral grains with high susceptibility is sufficient to increase bulk susceptibility. Thus, it is important to review the most important rock forming minerals and magnetic minerals.

The most common rock forming minerals like calcite, dolomite, quartz, and feldspar are diamagnetic with a susceptibility of around -1×10^{-5} SI. Pyroxenes and amphiboles, as well as clay minerals are paramagnetic with susceptibilities of 1×10^{-4} to 5×10^{-3} SI, depending on the variability of Fe-cations in the minerals (*Lanza and Meloni*, 2006). Therefore, these mineral groups do not contribute significantly to magnetic anomalies. Highest susceptibilities can be observed in ferrimagnetic iron-titanium oxides and iron-sulfides, e.g. magnetite, with susceptibilities ranging from 1 to 6 SI (*Clark and Emerson*, 1991). The iron-titanium oxides can be displayed in a ternary system of rutile (TiO_2), wüstite (FeO) and hematite (Fe_2O_3). This system is shown in Fig. 2.5

with the direction of increased oxidation indicated by dashed lines. The two solid lines

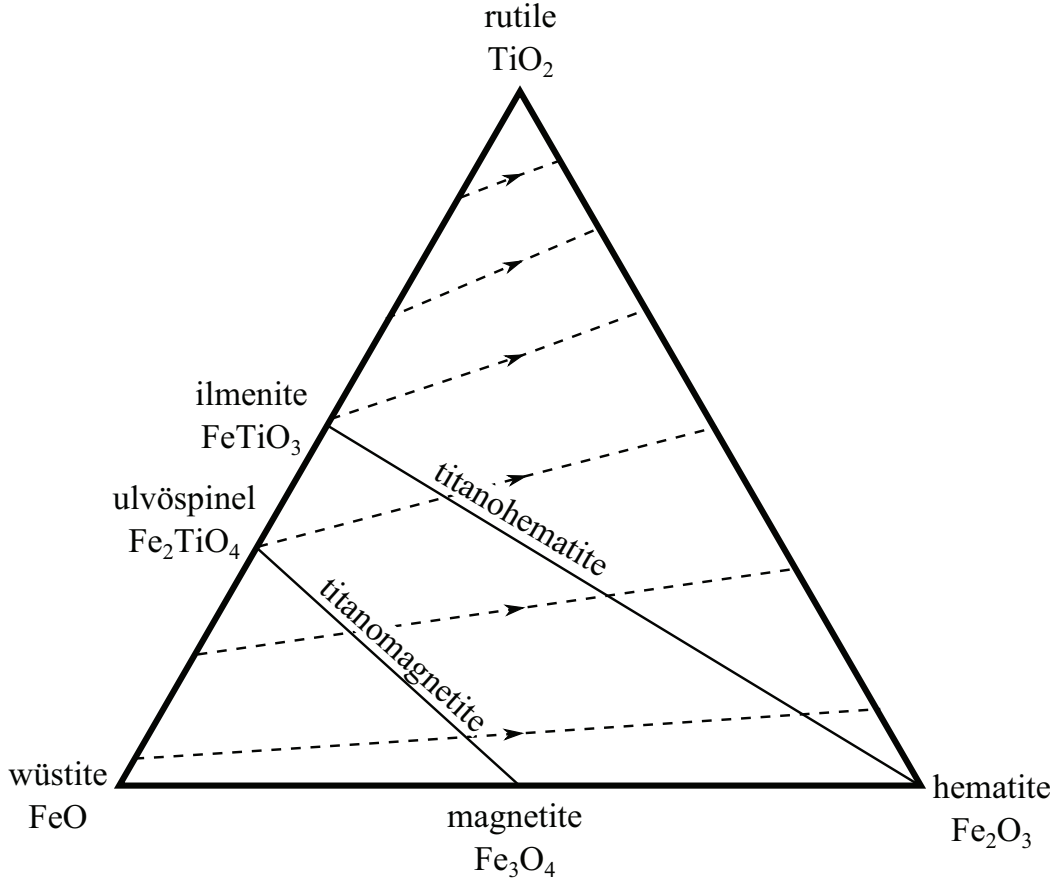


Figure 2.5: Ternary system of Fe-Ti oxides (after *Lowrie* (2007)) with the most important magnetic minerals. Dashed lines indicate increasing oxidation, solid lines represent the titanohematite and titanomagnetite series.

represent solid-solution series called **titanomagnetite** and **titanohematite** series, which comprise the most important magnetic minerals. The **titanomagnetite** is the iron-oxide family with the general formula $\text{Fe}_{2-x}\text{Ti}_x\text{O}_2$ with $0 \leq x \leq 1$ (*Lowrie*, 2007). Two end members of this series are ulvöspinel (Fe_2TiO_4) the already mentioned ferrimagnetic magnetite (Fe_3O_4). Due to the high susceptibility of magnetite, the bulk susceptibility of igneous and sedimentary rocks is proportional to the magnetite content.

The **titanohematite** series has the general formula $\text{Fe}_{2-x}\text{Ti}_x\text{O}_3$. The characteristics of this series are more complex and depend on the exact composition. Two important end members of this series are hematite (Fe_2O_3) and ilmenite (FeTiO_2). Hematite shows canted antiferromagnetism and thus exhibits an anisotropic induced magnetization. However, this mineral is important for paleomagnetic studies, since it is relatively stable in its magnetic and chemical properties. It is often a secondary mineral, formed by oxidation of other minerals like magnetite.

Fig. 2.6 gives an overview of susceptibility values of important igneous, metamorphic and sedimentary rocks, and their approximate content of magnetite. Since different processes are responsible for the formation of rocks, a more detailed look on magnetic properties of these rock types will be given subsequently.

Igneous rocks originate from the solidification of magma and take up a very large proportion of the crust. When cooled below the material specific Curie-temperature,

these rocks are a major source of magnetization. In general igneous rocks can be separated into felsic (acidic), mafic (basic) and ultramafic composition. Mafic rocks roughly have a iron-titanium content of 5 %, while felsic rocks only contain 1 % and thus are less magnetic (*Hinze et al.*, 2013). The cooling rate and the availability of oxygen controls which magnetic minerals will be in solid solution. The magnetic properties of igneous rocks are complex and depend on the chemical composition of the magma, cooling rate, mineralogy, and weathering state (*Clark*, 1999). A fast cooling rate will result in smaller grain sizes, and thus in lower bulk magnetization. However, this magnetization will be more stable, which is important for paleomagnetic studies. A higher availability will increase the oxidation state and reduce the susceptibility. Of course, when the magmatic composition contains a low amount of iron, only a few iron-titanium oxides will be solidified and thus the magnetization will be relatively low.

A large volume of continental crust consists of **metamorphic** rocks and is characterized by variable magnetic properties. The magnetization strongly depends on the source rock that has been undergoing metamorphism. Alteration, e.g. oxidation, is very common during this process, and thus it results mostly in a decreasing magnetization. Nevertheless, it has been shown that the magnetization can also increase, when under strong metamorphism iron-titanium oxides are recombined to magnetite and ilmenite (*Grant*, 1985). Strong metamorphism often leads to mineral growth and increasing grain sizes, which can also result in a higher magnetization. The hydrothermal alteration of ultramafic igneous rocks, also called serpentinization, can cause chemical remanent magnetization. At temperatures of 300 °C to 400 °C iron is released from paramagnetic olivine and pyroxene and is subsequently oxidized to magnetite (*Saad*, 1969), and thus the induced and remanent magnetization of the bulk rock will increase. The magnetic properties of metamorphic rocks depend on the educt. Sediments often contain far less magnetic minerals compared to igneous rocks and thus after metamorphism the magnetic properties will be lower than metamorphic rocks from iron-rich source rocks.

As mentioned earlier, **sediments** are often less magnetic. This rock type can be separated into chemical or detrital sediments. When the detritus of iron-rich igneous rocks is deposited, chances are much higher that this sediment will have a stronger magnetization because of the higher abundance of ferrimagnetic minerals. However, the minerals are likely to be weathered, i.e. oxidized, and therefore the magnetization will be lower compared to igneous rocks. As it is shown in Fig. 2.6, shales and sandstones, i.e. detrital sediments, feature higher magnetization than chemical sediments like limestones or dolomites. This is mainly caused by the higher content of magnetite grains in the sediments. Additionally, magnetization contrasts will only be detectable when sediments are folded or faulted (*Grauch and Hudson*, 2011). Horizontally layered structures do not create measurable magnetic anomalies using surface methods. In this case only borehole logging, i.e. borehole magnetometers and susceptibility logging, can be used to identify magnetized structures.

Self-demagnetization: Bodies with a very strong magnetization can exhibit an effect called *self-demagnetization*. When the elementary dipole moments within a grain are parallel (Fig. 2.7 a), they will compensate each other, except the north and south poles at the surface of the grain (Fig. 2.7 b). From outside, the grain behaves like a point dipole, with magnetic field lines going from the north to the south pole. Inside

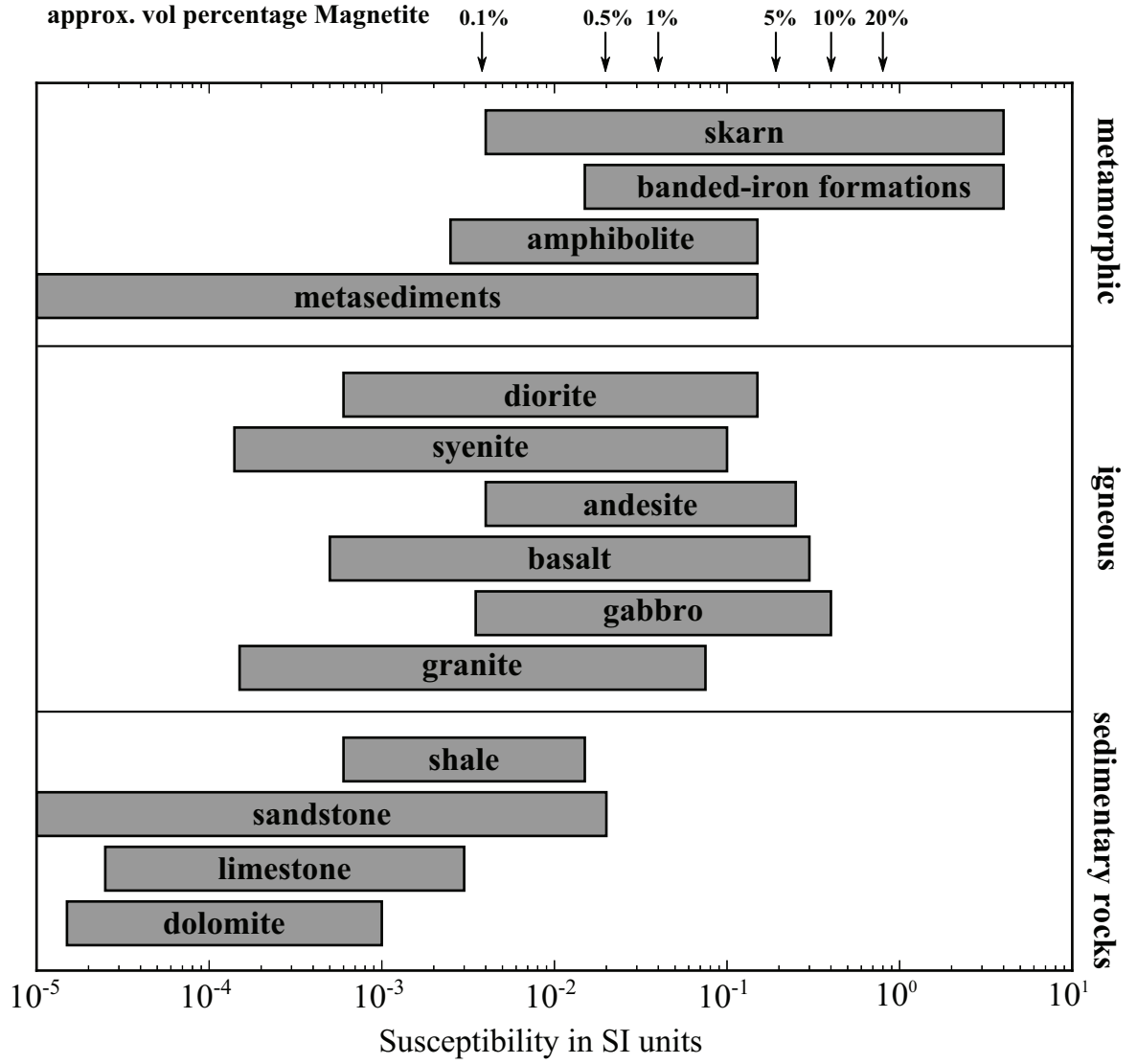


Figure 2.6: Overview of rock susceptibilities and related volume percentage of magnetite. Compiled after *Lowrie* (2007) and *Clark and Emerson* (1991).

the grain, there is a magnetic field, presented by the field lines, going from the north to the south pole (Fig. 2.7 c), and therefore pointing in the opposite direction. Thus, the field inside the grain will demagnetize the original field. Self-demagnetization is also influenced by the shape of a grain. Hence, a certain combination of shape and magnetization direction can cause a canted demagnetization field. This effect is mainly significant for material with susceptibilities higher than 0.1 SI (*Clark*, 2014). If a material shows self-demagnetization effects, the following correction can be applied:

$$\mathbf{M}' = \frac{\mathbf{M}_{NRM} + \hat{\chi} \mathbf{B}_0}{\hat{\mathbf{I}} + \hat{\chi} \hat{\mathbf{N}}}, \quad (2.21)$$

where \mathbf{M}' is the corrected magnetization, \mathbf{M}_{NRM} the uniform remanence, $\hat{\chi}$ the susceptibility tensor of the magnetized grain, \mathbf{B}_0 the external magnetic induction, $\hat{\mathbf{I}}$ the identity matrix, and $\hat{\mathbf{N}}$ the demagnetization tensor (*Clark et al.*, 1986). This is an analytic correction for an ellipsoidal source. *Clark* (2014) gave an expression to

correct scalar susceptibility readings from hand held devices (section 3.4):

$$\chi = \frac{\chi'}{(1 + \chi'/2)}, \quad (2.22)$$

where χ' is the susceptibility read of the device. This simple correction is, as mentioned above, a correction when the susceptibility is higher than 0.1 SI when self-demagnetization effects become significant.

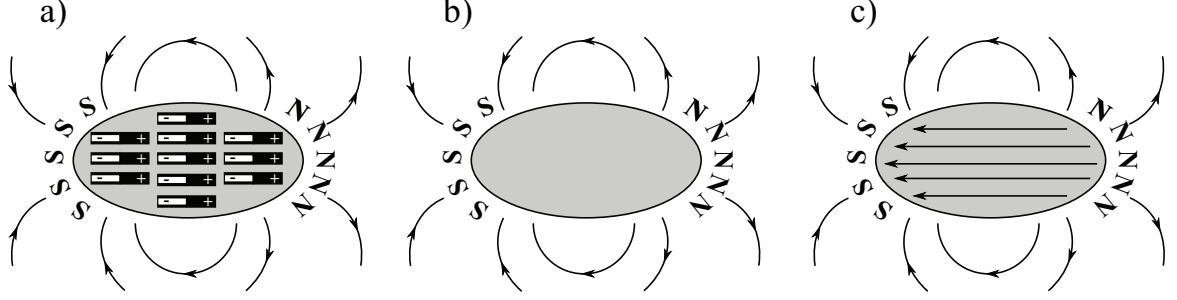


Figure 2.7: Illustration of self-demagnetization of a mineral grain with high susceptibility. a) mineral grain with elementary dipole moments. b) the internal dipole moments compensate each other and only the moments at the surface are left over. c) shows the internal demagnetization field of the mineral grain.

Because of the discussed effects, the susceptibility can no longer be referred to as a scalar value. Due to various reasons, susceptibility often is anisotropic and therefore has to be expressed as a tensor. The relationship between induced magnetization and the magnetic field is then given by

$$\mathbf{M}_i = \hat{\chi} \mathbf{H}, \quad (2.23)$$

where $\hat{\chi}$ is a tensor of second order presented by a symmetric 3×3 matrix. Its eigenvalues are representing the minimum, intermediate, and maximum susceptibility. Microscopically, anisotropy can result from the crystalline structure of a mineral, while macroscopically, anisotropy is controlled by the shape and orientation of mineral grains. For instance, small parallel rods of magnetite will produce a stronger induced field along their long axis. One important example for orientated ferromagnetic minerals are banded-iron formations (BIF).

The combination of remanent magnetization, self-demagnetization, and anisotropy of the susceptibility makes the interpretation of magnetic anomalies very complicated. Hence, the use of additional information, i.e. ground based susceptibility measurements on outcrops and paleomagnetic measurements on samples, is a necessity to avoid misleading interpretations. The measurement of rock susceptibility is fairly common, since it is easy to do in the field using hand-held devices (see section 3.4). More accurate measurements of rock susceptibility can be performed only in a laboratory. To gain information on remanent magnetization, orientated rock samples are necessary. These can be taken by measuring the drilling direction or the orientation of fixed markers on rock samples (section 5.3.2). Nevertheless, the analysis can only be done in the laboratory. There are also some methods available to estimate the remanent magnetization in the field (*Helbig, 1963; Breiner, 1973*), but they cannot replace laboratory measurements, since these methods are much more inaccurate.

2.2.4 Coordinate Systems

There are two main coordinate systems commonly used when describing magnetic data in geophysics: a spherical and a Cartesian system. While the Cartesian system is mostly used to describe the measured data and the modeled magnetization vector, the spherical system is mainly used for the global magnetic field and the magnetization direction of paleomagnetic samples. The different definitions of these systems is explained in this section.

The magnetic field in the spherical system is expressed by the angle between the field vector relative to Earth's surface (inclination, I), the direction towards the magnetic pole (declination, D) and the strength F (Fig. 2.8).

The Cartesian system uses the two horizontal magnetic field components X and Y and the vertical component Z . Throughout this dissertation, a north-east-down (NED) system is used, whereas X, Y, Z points towards the north, eastwards, and downward direction, respectively.

Both coordinate systems are related to each other in the following way (Lowrie, 2007):

$$\begin{aligned}
 X &= F \cos I \cos D \\
 Y &= F \cos I \sin D \\
 Z &= F \sin I \\
 F &= \sqrt{X^2 + Y^2 + Z^2} \\
 D &= \arctan \frac{Y}{X} \\
 I &= \arctan \frac{Z}{\sqrt{X^2 + Y^2}}
 \end{aligned} \tag{2.24}$$

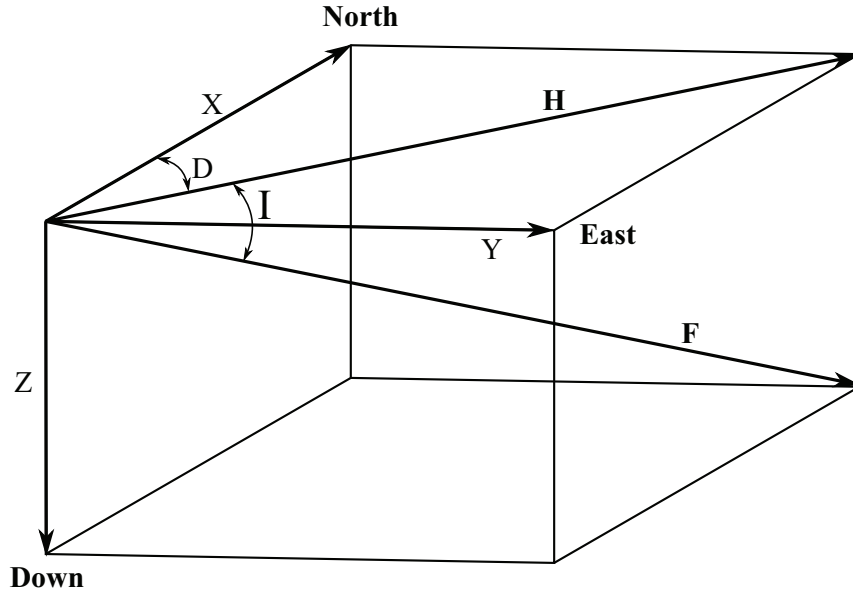


Figure 2.8: Coordinate systems for the description of Earth's magnetic field used in this study. Vector \mathbf{H} points towards magnetic north, F points along the magnetic field direction. X, Y, Z are the magnetic field components in a Cartesian coordinate system. The angles I and D are denoting inclination and declination, respectively.

3 Magnetic field sensors

Within the framework of this study, a gradiometer system based on SQUIDs was used to measure the complete gradient tensor of Earth's magnetic field. Therefore, in the following, a short introduction of the basic principle of SQUIDs and the design of the sensors is given. More details about SQUIDs can be found in *Clarke and Braginski (2005)*. In section 3.3, the airborne setup used during the field campaigns as well as the principle of a susceptibility meter is explained.

3.1 Superconductivity and SQUID

In 1911, the physicist Heike Kamerlingh Onnes observed that the resistance of mercury disappears at very low temperatures (*Kamerlingh Onnes, 1911a,b*), which was afterwards addressed to its superconducting properties. Since then, several other metallic superconductors with different low critical temperatures T_{Cr} (*low temperature superconductor*, LTS) were discovered. In the 1980's, *high-temperature superconductors* (HTS) based on ceramics were developed (*Bednorz and Müller, 1986*). Both types of superconducting materials can be used to build a SQUID sensor. The sensors, used in this work are LTS-SQUIDs based on niobium with a critical temperature T_{Cr} of 9.2 K.

A SQUID makes use of several quantum effects: At first, the magnetic flux through a closed superconducting ring is quantized (*Deaver and Fairbank, 1961*). Thus, the magnetic flux occurs as a multiple of the magnetic flux quantum $\Phi_0 = 2.07 \times 10^{-15}$ Vs. The second important effect is the tunneling of electron pairs through an isolating barrier. Electrons move as pairs inside a superconductor, and when a critical current I_C is exceeded they will tunnel through these isolating barriers, called *Josephson junctions* (JJ). This effect is called *Josephson-effect* (*Josephson, 1962*).

Here, dc-SQUIDs are used. The concept of these devices was first proposed by *Jaklevic et al. (1964)*. The dc-SQUID (see Fig. 3.1 a) consists of a superconducting ring, also called *washer*, and two *Josephson junctions* (marked by crosses in Fig. 3.1 a), which divide the ring into two halves. If a dc current is applied at both ends of the ring, the JJ will act as high-frequency⁴ oscillator, which is coupled with the inductance of the ring. When a variable magnetic flux through the ring is present, a phase shift of this coupling will occur. Therefore, an averaged voltage across the ring can be detected, which depends on the amplitude of the magnetic flux (see Fig. 3.1 c). The maximum voltage can be expected at a magnetic flux $\Phi_{ext} = n\Phi_0$ and the minimum at $\Phi_{ext} = n\Phi_0/2$ (see Fig. 3.1 b). Typically a voltage range of about 70×10^{-6} V across the ring can be expected.

As schematically shown in Fig. 3.1 c), the relation between magnetic flux and voltage is nonlinear and periodic. To use these sensors for geophysical applications low-noise and low-drift electronics are necessary in order to linearize the periodic relation. This linearization is realized using a feedback system called flux-locked-loop (FLL) (*Drung and Mück, 2004; Oukhanski et al., 2006*). The voltage of the SQUID is amplified, low-pass filtered, and fed back as flux to the SQUID by means of an inductively coupled feedback coil. Using this technique, the flux inside the loop of the SQUID is kept constant, i.e. the output voltage of the FLL becomes linear.

⁴ 1×10^{-6} V corresponds to 485 MHz oscillation frequency

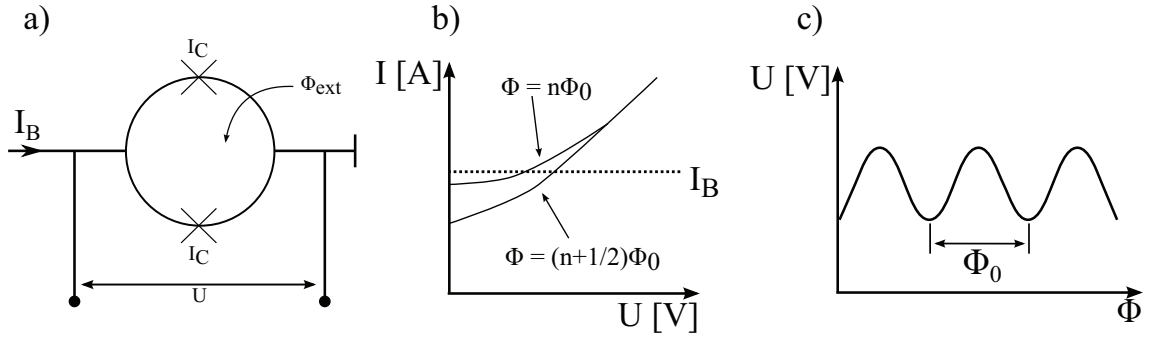


Figure 3.1: a) Illustration of the concept of a dc-SQUID with the critical currents I_C at the JJ (marked by the crosses), the external flux Φ_{ext} , the bias current I_B , and the voltage across the ring U . b) Schematic current-voltage diagram with both extrema. c) voltage-flux diagram at a constant bias current and the period of one magnetic flux quantum Φ_0 (after Clarke and Braginski (2004)).

3.2 Superconducting Magnetometers and Gradiometers

The principle of the SQUID magnetometer as described previously has to be optimized in terms of coupling of an external signal to a SQUID in order to achieve a high sensitivity. A larger area of the ring will increase the flux measured by the SQUID, but at the same time also increase the inductance. Four different types optimize the SQUID and increase its sensitivity: *washer*-, *multiloop*-, *transformer*-, and *galvanometer*-types (Zakosarenko *et al.*, 1996). In this study only transformer-type SQUIDs were applied (Stolz *et al.*, 2006).

SQUID magnetometers are vectorized sensors, which means that they are per se sensitive to rotation in an external magnetic field, while conventional total field magnetometers, like optically pumped caesium vapor or potassium magnetometers are insensitive to rotation. As an example: assuming a magnetic field of 50 000 nT, a rotation of the sensor of about 1° will result in an amplitude change of up to 1000 nT (Clem *et al.*, 1996). Even if a very good correction for rotation, by calculating the Euler angles from a highly accurate inertial measurement unit (IMU), is applied, the signal due to rotation is in the same order of magnitude as the magnetic anomalies of the geological target. Another point is, that if the accuracy of the magnetometer should be better than 100 pT, then the dynamic range has to cover about six orders of magnitude⁵.

To overcome these two problems, a first-order gradiometer can be used instead, because signals of a uniform field are compensated. Thus, unwanted signals from a rotating sensor and large dynamic ranges are not expected. Nevertheless, both effects depend on the construction and the layout of the gradiometer. There are two main types of gradiometric setups: *electronic* or *hardware* gradiometers and *intrinsic* gradiometers. Hardware gradiometers are using at least two individual sensors, e.g. fluxgate magnetometers, and the gradient is calculated by the electronics by calculating the difference of the measured values of both individual sensors. Intrinsic gradiometers directly measure the gradient. In this study, this last type of intrinsic gradiometers has been applied which consists of two antennas, so-called *pickup-coils*. The differences of the magnetic flux through both pick-up coils is measured via a SQUID, which is cross-connected with both antennas. When the magnetic flux in both coils is the same,

⁵This means more than 100 dB of dynamic range.

i.e. a uniform field is present, no signal is measured and the gradient therefore is zero. An advantage of this design is, that flux differences are perfectly linear over a large dynamic range (*Clem et al.*, 2005).

In both cases, the distance between the two sensors defines the *base length* of the gradiometer. Fig. 3.2 shows the two main types of sensor orientation of gradiometers, axial or planar. In this study, planar gradiometers were used, because they are

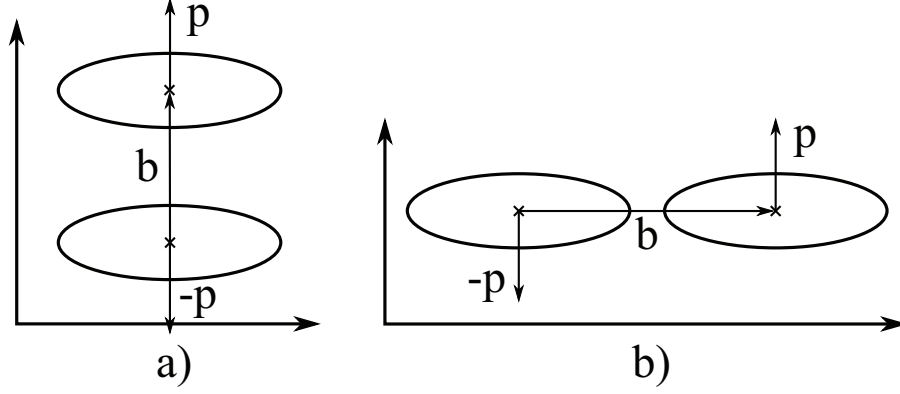


Figure 3.2: Schematics of the two main types of gradiometers: a) axial gradiometer b) planar gradiometer. The baseline is denoted by b and the sensing direction by p . For current SQUID-based gradiometers, the baseline b is in the range of mm to a few cm.

fabricated using a lithographic thin-film technology which offers a high intrinsic planarity. This is a very important aspect of the fabrication. If the two antennas deviate from the planarity, a magnetic response from the uniform magnetic field vector will be measured as well and not compensated as stated earlier. The areas of the antenna that are not in the plane are called parasitic areas. Fig. 3.3 illustrates a typical, called real gradiometer, as a combination of the three parasitic areas and the effective areas of the pick-up coils. These areas are caused by limited lithographic accuracy as well as non-planar substrates. Bending of the substrate can also be caused by differences in the thermal expansion coefficients of the material used, while cooling the sensor down to 4.2 K. Planarity is usually expressed as imbalance, the inverse of balance, or common-mode-rejection ratio (CMRR)⁶ with

$$CMRR_i = A_i/A_{eff} \quad i = x, y, z \quad (3.1)$$

and A_i and A_{eff} representing the parasitic and effective areas, respectively. The CMRR and the baseline define the balancing coefficients α_i

$$\alpha_i = CMRR_i/b \quad i = x, y, z, \quad (3.2)$$

where \mathbf{b} is the vector of the baseline. The balancing coefficients are used in the processing work flow (section 4.1.2) in order to increase the balance of the gradiometers and remove the effect of the parasitic areas. The gradiometers used for the field measurements conducted in the framework of this study have an imbalance of 1×10^6 CMRR and a base length of 3.5 cm (*Stolz et al.*, 2006; *Stolz*, 2006). To illustrate the effect of rotation of these gradiometers in an external magnetic field the same example as

⁶imbalance = $1/(CMRR \cdot \text{baselength})$

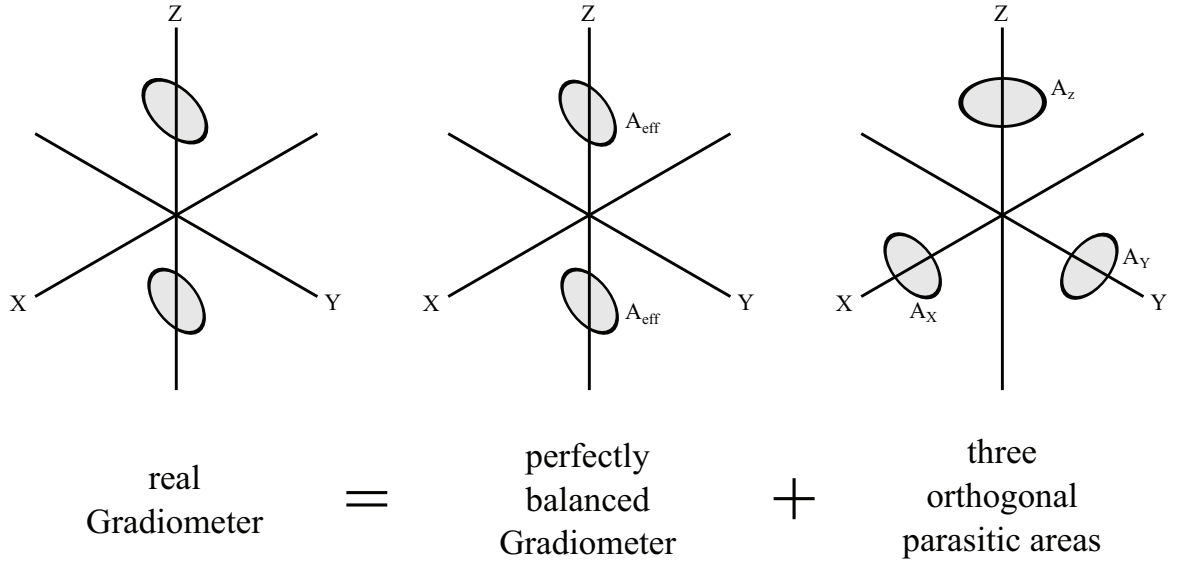


Figure 3.3: Illustration of the parasitic areas for a planar gradiometer (*Clem et al.*, 1996). The measured gradiometer signal (left) is a combination of the gradients of a perfectly balanced gradiometer (middle) and the magnetic field vector measured by three orthogonal parasitic areas (right).

above is used: The rotation of 1° of a gradiometer with this CMRR in a uniform magnetic background field of 50 000 nT will result in a gradient of about 30 pT/m. The imbalance of axial gradiometers is generally higher (*Döring*, 2013) and it is technically more challenging to fabricate such a sensor with a high intrinsic balance.

3.3 Airborne full tensor gradiometer system

In order to conduct an airborne survey a towed system is used, which was developed jointly by the IPHT and Supracon AG in Jena, Germany. This system incorporates the a planar gradiometer design based on SQUIDs, which is explained in section 3.3.1. For processing and interpretation, additional information is necessary, which is collected by several auxiliary sensors incorporated in the airborne system. These sensors are described in section 3.3.2. Finally, the complete system is shown and explained at the end of this chapter in section 3.3.3.

3.3.1 Full Tensor Magnetic Gradiometry System

In this section, a focus on the technical implementation in the airborne system is set. In Fig. 3.4 a 3D illustration of the bird that has been deployed during the airborne magnetic field surveys conducted in this study is presented. The cryostat (1), containing the SQUID gradiometers and magnetometers (2), is located close to the center of rotation of the bird. It is filled with liquid helium at a temperature of 4.2 K to maintain the superconductivity of the sensors (see section 3.2). In total, six planar-type gradiometers of first order and four vector magnetometers are mounted inside the cryostat. To measure the complete gradient tensor, a set of at least five gradiometers is necessary (section 2.1.2). The gradiometers are mounted in a certain⁷ way, so that any combination of five of these six gradiometers can be used to construct

⁷patent pending at IPHT

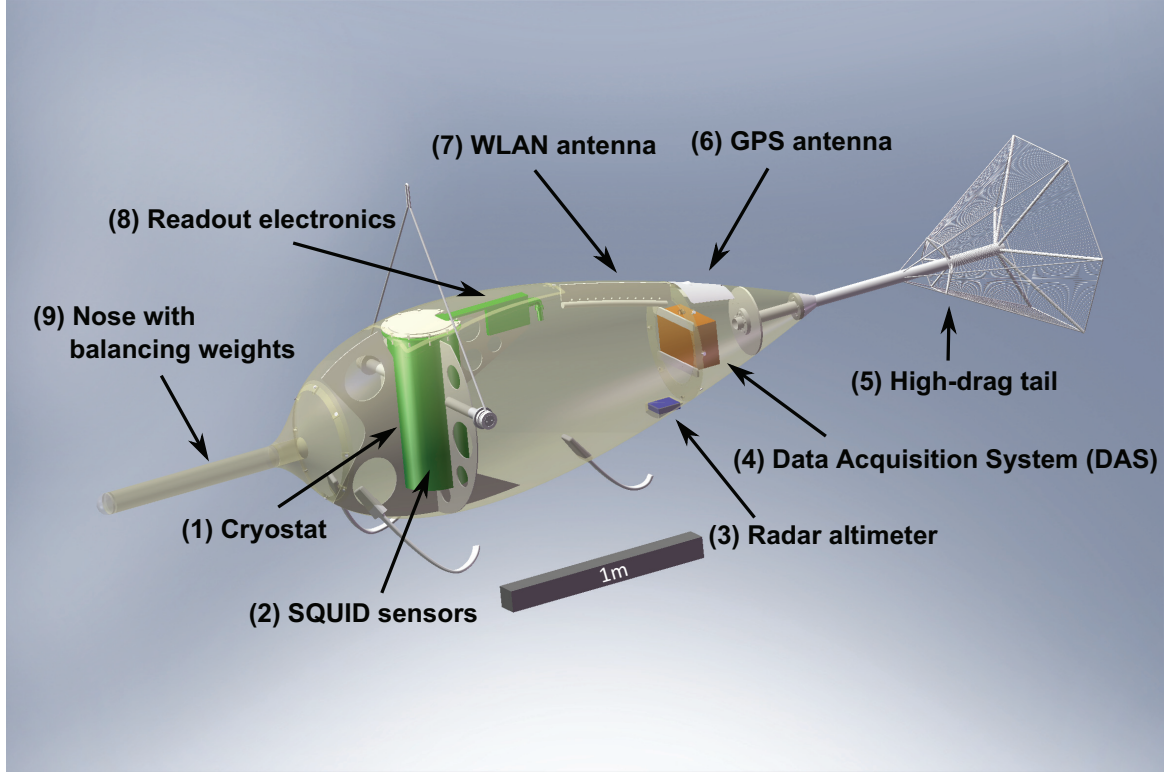


Figure 3.4: Illustration of the bird showing the most important parts of the airborne system. Further descriptions are given in section 3.3.

the full gradient tensor. The additional gradiometer is only there for redundancy to ensure operational reliability. Three magnetometers are needed for balancing of the gradiometer signals (see section 4.1). The fourth one is also for redundancy.

The readout electronics (Fig. 3.4 (8)) are placed away from the cryostat, on an approximately 30 cm long boom, to reduce the amplitude of disturbing electromagnetic signals at the location of the SQUIDS. Since SQUID sensors are sensitive in a broad bandwidth, the cryostat is wrapped in aluminium coated MylarTM foil in order to limit the bandwidth and therefore shield high frequencies. During construction, different electromagnetic shieldings have been tested (Stolz, 2006).

3.3.2 Data acquisition unit and Navigation system

The data acquisition system (Fig. 3.4 (4)) (DAS) is located at the back of the bird, distanced as far possible from the FTMG system. The DAS collects all data streams from the cryostat electronics (1,2), the GPS antenna (6), radar altimeter (3), and inertial measurement unit (IMU). Additionally, the DAS provides the power supply for the FTMG system. It also controls the helium pressure inside the cryostat by using a control valve to keep the pressure at a constant value of about 1036 mbar. This eliminates the influence of external pressure changes, e.g. when flying at changing altitudes.

The differential global positioning system (dGPS) placed in the bird is a commercial *Novatel OEM628* dGPS receiver (NovAtel Inc., 2010) with a lateral accuracy⁸ of 2 m to 5 m. As mentioned before, the DAS contains an IMU, which is custom built and

⁸The SBAS service (Satellite Based Augmentation System) was used to achieve higher accuracy.

uses a set of three accelerometers and three fiber optic gyroscopes. The IMU is used to compensate the motion of the systems and to transform the measured gradients into a georeferenced coordinate system (*Schiffler et al.*, 2016). After processing of the IMU data towards the Euler angles (see section 4.1), the root-mean-square (RMS) accuracy of these angles is $\sim 0.1^\circ$ for the heading and $\sim 0.05^\circ$ for roll and pitch.

The altitude of the bird is obtained using a radar altimeter (3) *UMRR Typ 30* by *smart microwave sensor GmbH* with high accuracy. According to the data sheet provided with the radar altimeter, the minimum and maximum range of detection is 4.6 m and 160 m, respectively. The sensors offers an accuracy of around 2.5 %, when measuring distances of up to 10 m and 5 % between 10 m and the maximum detection range.

All data streams collected by the DAS are transferred to a laptop via a 11 Mbit/s wireless LAN connection (7) on board of the helicopter which is used as the carrying platform of the system.

3.3.3 The Airborne Setup

The airborne system has been composed completely out of fiberglass and has a total weight of 125 kg. To compensate the mass of the DAS and the tail at the back of the bird, a balancing weight (9) of approximately 40 kg was placed inside the nose to shift the center of mass in front of the cryostat. The tail at the back of the bird is used to ensure a stable flight path, even at low velocities. This design is called "high-drag-tail" (5) and consists of an eight-sided pyramid with densely tied strings. An airflow through these strings results in negative pressure within the pyramid. Caused by the shape of the tail, the bird will automatically orientate itself in the direction of the air stream. To damp vibrations of the helicopter, a 30 cm long bungee rope was placed as damping element between the cargo hook and the towing rope. The towing rope is 8 mm thick and made out of DyneemaTM fibers. This material is non-magnetic, has nearly no elongation along the rope and offers a high breaking load of 33 kN.

During a flight, the survey speed was about 60 KIAS⁹. The most critical maneuvers are departure and arrival of the bird during survey operation. Strong winds can easily flip the bird over, in particular the *down wash*¹⁰ of the helicopter. Therefore, during these maneuvers, two people at the ground are required to assist and handle the bird to prevent uncontrolled behavior. Those two are also necessary to catch the bird in the landing phase. Survey operations are commonly done along parallel flight lines, with a line spacing of 50 m to 100 m, depending on the desired spatial resolution and ground clearance.

3.4 Kappameter

In order to constrain the inversion of potential field data, a priori information of some rock properties is essential. Usually, acquisition of magnetic field data is supported by susceptibility measurements either taken on outcrops in the laboratory or by conducting borehole measurements. For measurements in outcrops, a *Kappameter KM-7* (*SatisGeo*, 2012) by *SatisGeo* was used. This device creates a magnetic field by using a small ferrit-core coil and leads to magnetization of a sample, which is subsequently

⁹KIAS - knots (kt) indicated airspeed, 1 kt = 1.852 km/h

¹⁰strong, downward directed winds, generated by the main rotor of the helicopter

measured. Since susceptibility is a scaling factor between the magnetic field and the magnetization of the sample, it can be directly derived. The Kappameter KM-7 system has a sensitivity of 1×10^{-6} SI units. Hand-held susceptibility devices vary in accuracy and are mostly affected by temperature changes. Thus, a known standard should be carried in the field while conducting susceptibility readings on outcrop walls in order to correct the measurements (*Schmidt and Lackie, 2014*). Additionally, the correction for self-demagnetization (Equation 2.22) should be applied when the susceptibility exceeds 0.1 SI, as explained in section 2.2.3.

4 Processing and Inversion

This section gives a general overview of the processing techniques applied to FTMG data. Processing comprises some basic processing procedures of gradiometer signals, i.e. balancing of the gradiometers, calibration of magnetometers, and the rotation into an earth-fixed coordinate system. Also more advanced processing steps, i.e. tensor consistent leveling and the removal of unwanted signals, e.g. from power-lines, will be explained. At the end of this chapter, the inversion of potential field data with focus on magnetic data is briefly introduced.

4.1 Processing of full tensor gradiometry data

An advanced processing procedure is necessary for raw magnetic gradiometer data due to the special sensors that are used in the system. The most important steps of the processing scheme are presented in this section and are illustrated in Fig. 4.1.

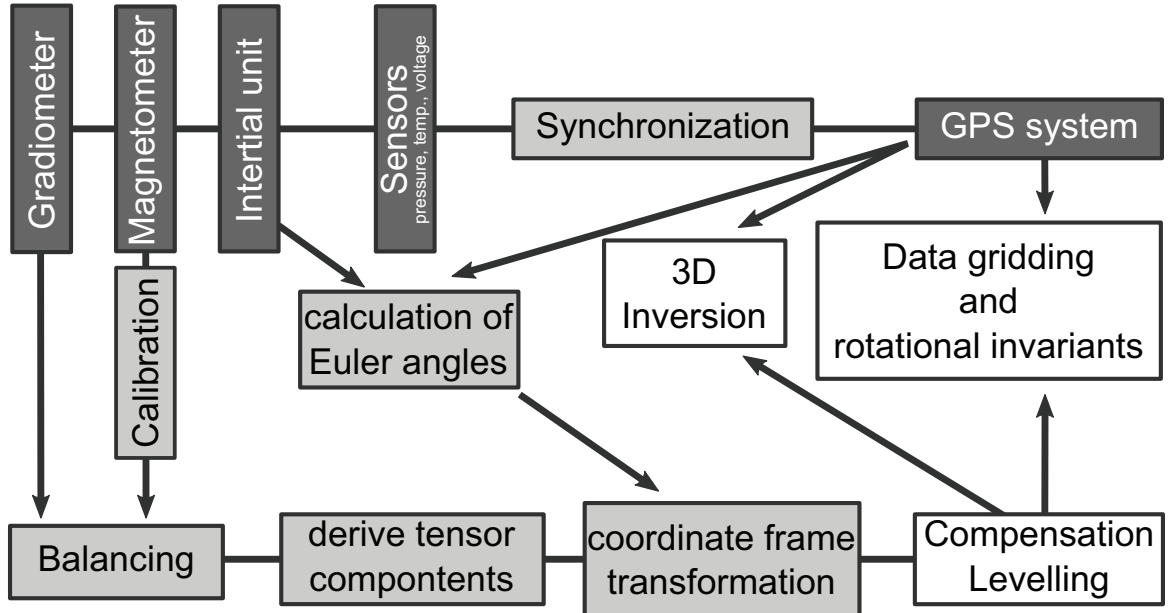


Figure 4.1: Illustration of processing scheme. Data streams are represented by dark grey, processing steps by light grey and post-processing and modeling by white boxes.

4.1.1 Calibration of Magnetometers

Magnetometer readings are necessary to balance the gradiometers. It may be beneficial to calibrate the magnetometer readings to achieve a higher accuracy (*Schiffler et al.*, 2014). It is necessary to correct for possible misalignments and arbitrary offsets of the magnetometers. The raw magnetometer data can be converted into magnetic field data using an error model which consists of three misalignment angles, three sensitivities and three arbitrary offsets. The raw readings of the magnetometers \mathbf{F} (voltages of the FLL) can be described by

$$\mathbf{F} = (F_x, F_y, F_z)^T = \mathbf{S} \cdot \mathbf{D}_{\text{dist}} \cdot \mathbf{B} + \mathbf{O}, \quad (4.1)$$

where \mathbf{B} is the magnetic field vector, \mathbf{S} is the sensitivity matrix

$$\mathbf{S} = \begin{pmatrix} S_x & 0 & 0 \\ 0 & S_y & 0 \\ 0 & 0 & S_z \end{pmatrix} \quad (4.2)$$

and $\mathbf{O} = (O_x, O_y, O_z)^T$ is the vector of three arbitrary offsets. \mathbf{D}_{dist} represents the distortion matrix which describes the transformation between the measured, non-orthogonal magnetic field sensors and an ideal, orthogonal set of sensors.

An optimization technique is used to minimize the standard deviation of the difference between measured magnetic field data and the expected data (*Schiffler et al.*, 2016), which originate from a global geomagnetic model, e.g. the IGRF (*Finlay et al.*, 2010).

4.1.2 Balancing of Gradiometers

As explained in section 3.2, the FTMG system uses planar-type first-order gradiometers, which are fabricated using lithographic thin-film technology. The ability to reject the uniform background field is one of the main reasons to use SQUID-based gradiometers. Therefore, the sensors must offer a high balance. To further enhance the balance, the effects of the parasitic areas have to be reduced. The measured gradiometer signal is a superposition of the gradient tensor component and the magnetic field vector measured by the parasitic areas. Fig. 3.3 illustrates this superposition of a single planar gradiometer (*Vrba*, 1996; *Clem et al.*, 1996).

The measured gradiometer signals g_k can be expressed as:

$$g_k = G_k + \sum_i \alpha_i B_i = \Delta G_k + \overline{G_k} + \sum_i \alpha_i B_i, \quad (4.3)$$

where ΔG_k is the balanced gradiometer signal and $\overline{G_k}$ gradiometer offsets. α_i represent three coefficients¹¹ (*Clarke and Braginski*, 2004; *Schiffler et al.*, 2014), and B_i are the magnetic field vector components. In order to balance the signals, the coefficients α_i are estimated by minimizing the residual signals ΔG_k . Since airborne FTMG surveys are conducted on parallel flight lines, this minimization is done on each individual line. Thereby, these sections along the survey line with a low starting value of ΔG_k are used to calculate the balancing coefficients α_i .

Equation 4.3 usually contains an additional, frequency dependent term (*Vrba*, 1996), which describes the effect of curl currents affecting the gradiometer signal. Here, this term is neglected, since only magnetic fields below 10 Hz are considered and the whole environment around the sensors is designed to be electrically non-conducting, in order to prevent the occurrence of curl currents.

4.1.3 Decomposition and Rotation of Tensor components

After the balancing of the six gradiometer data streams, a set of five gradiometer signals is used to calculate the five linear independent components of the gradient tensor. This decomposition requires knowledge of the mounting geometry of the planar gradiometers inside the cryostat (*Stolz et al.*, 2006). To ensure redundancy, any

¹¹parasitic areas A_i normalized by the effective volume V_{EFF} (*Stolz et al.*, 2006)

combination of five of the six sensor signals is possible. Usually the channels with the lowest standard deviation are selected since this will ensure the best signal to noise ratio. The decomposed gradient components are orientated with respect to the local coordinate frame of the airborne system called *body system*.

The transformation into an Earth-centered, Earth-fixed (ECEF) coordinate system requires knowledge of the orientation of the airborne system in terms of three Euler angles at any given moment in time. Therefore, the rotational information, i.e. acceleration and angular rates, of the inertial unit is used in combination with the GPS data to calculate an aided inertial system (AINS) (*Shin and El-Sheimy, 2004*). This provides the Euler angles roll (Φ), pitch (Θ) and yaw (Ψ), which are required to perform the rotation of the tensor, which can be described by:

$$\mathbf{G}_{NED} = (\mathbf{D}_{NED}^b)^T \cdot \mathbf{G}_b \cdot \mathbf{D}_{NED}^b, \quad (4.4)$$

where \mathbf{G}_b is the gradient tensor in the coordinate frame of the airborne system (body frame), \mathbf{G}_{NED} is the gradient tensor in the ECEF coordinate system and \mathbf{D}_{NED}^b is the rotation matrix from the body frame into the NED system

$$\mathbf{D}_{NED}^b = \mathbf{D}_{roll} \cdot \mathbf{D}_{pitch} \cdot \mathbf{D}_{yaw} = \begin{pmatrix} \cos \Theta \cos \Psi & \cos \Theta \sin \Psi & -\sin \Theta \\ \sin \Phi \sin \Theta \cos \Psi - \cos \Phi \sin \Psi & \sin \Phi \sin \Theta \sin \Psi + \cos \Phi \sin \Psi & \sin \Theta \cos \Psi \\ \cos \Phi \sin \Theta \cos \Psi + \sin \Phi \sin \Psi & \cos \Phi \sin \Theta \sin \Psi - \sin \Phi \sin \Psi & \cos \Theta \cos \Psi \end{pmatrix} \quad (4.5)$$

After the rotation the gradient tensor will be in an ECEF coordinate frame where x refers to the northward, y to eastward and z to the downward direction (NED).

4.1.4 Post-processing

After the basic processing steps, several post processing steps are carried out in order to remove artifacts in the data: At first, a semi-automatic step is performed, which removes data points affected by periodic noise sources, e.g. close to power lines or railway tracks. Secondly, noisy data points around man made sources, e.g. settlements are removed. Lastly, offsets between individual flight lines are removed using a leveling algorithm.

In the first step, data points with a significant amplitude at 50 Hz and 16 2/3 Hz are detected by a semi-automatic technique. These distortions are generated by the power grid and electrified rail way tracks, respectively. By calculating the spectrum of the recorded data at each flight line, areas with amplitudes at these specific frequencies above a threshold were masked. This threshold has to be empirically determined, since it controls the amount of data which is masked.

In order to remove man-made artifacts, operator notes in combination with aerial photographs were used to remove data points in the vicinity of settlements, buried water and gas pipelines, radio antennas as well as highways.

Airborne magnetic data is usually collected along parallel flight lines. Artifacts along the flight direction are visible in the data set by small offsets between the individual lines. In the case of SQUID-FTMG data, these offsets can be caused by slightly different altitudes from line to line and by varying balancing coefficients, since these are estimated for each flight line separately (see section 4.1.2). Commonly, the flight lines are leveled by using *tie lines* (*Urquhart, 1988; Luyendyk, 1997*), which are

orthogonal to the survey lines. Another method is *micro-leveling* (Mauring and Kihle, 2000; Mauring et al., 2002), which removes these offsets by using directional median filters. This technique does not require tie lines. The five linear independent tensor components can be leveled individually by these two techniques, but the consistency of the tensor, i.e. symmetry and tracelessness, could be spoiled. Thus, a leveling algorithm was used which preserves the consistency of the tensor (Schiffler, 2015). A major disadvantage of all leveling algorithms is that linear geological structures parallel to the flight direction could also be removed. Additionally, the directional information of FTMG data can be used during leveling to improve results (FitzGerald and Holstein, 2006).

4.1.5 Data interpolation on a regular grid

The final step of the processing sequence is the interpolation of the irregularly spaced data points on a regular grid, also called gridding. In this study, data points are approximately 3 m apart along the flight line. Depending on the survey area, the flight lines are 50 to 100 m apart. Thus, the data points are highly irregularly spaced.

To interpolate the data sets on a regular grid, a standard *ordinary kriging* algorithm (Krige, 1951; Oliver and Webster, 1990) is used. This algorithm is part of the *Geostatistical Toolbox* of the program package *ESRI ArcGIS*. The data sets in Appendix B are interpolated on a 50×50 m using a radial search radius of 150 m with four sectors. At each grid point 25 observation points are used for the interpolation.

The interpretation of magnetic field maps significantly depends on the color maps that are used. For the gradient data two different color maps have been selected, which allow to highlight also weak anomaly contrasts. The total field anomaly data is presented by using a rainbow color map. All of the used color maps offer a nearly constant color perception across the complete spectrum (Kovesi, 2015). To further enhance the structural features in the total field maps, sun shading of the data has been applied (Cooper, 2003). The different color maps used in this study are presented in Appendix B to highlight the perception.

4.2 Inversion

This chapter covers the basics of inverse modeling. This includes the general principle of inverse modeling, types of regularizations which are important for this work, and the inversion strategy. Finally, some advantages and disadvantages of the applied discretization and regularization technique are discussed.

4.2.1 Introduction to Inverse modeling

Geophysical methods are investigating physical fields which are interacting with subsurface materials. The most important fields are potential fields, i.e. gravity and magnetic fields, seismic wave fields and electromagnetic fields. In the framework of this study only magnetic fields are considered. The observed data \mathbf{d} contains the cumulative information of material properties. The aim is to reconstruct these material properties on a basis of a subsurface model by using the measured responses of the physical fields at the surface. The problem of reconstruction is called *inverse problem*. In the case of FTMG data, each element of the vector $\mathbf{d} = (d_1, \dots, d_n)^T$ contains the five linear independent components of the magnetic gradient tensor at each observation

point. This data vector can be calculated by applying a function \mathbf{A} to a model vector \mathbf{m} , which leads to the following relation:

$$\mathbf{d} = \mathbf{A}(\mathbf{m}). \quad (4.6)$$

Each element of the model vector \mathbf{m} contains the magnetization of the discretized model and the function \mathbf{A} describes the respective physical laws. This relation is also called *forward problem*. The aim of the *inverse problem* is to find a set of model parameters based on the observed data:

$$\mathbf{m} = \mathbf{A}^{-1}(\mathbf{d}). \quad (4.7)$$

Unfortunately, \mathbf{A}^{-1} is non-unique. To obtain a single solution of the inverse problem, the operator \mathbf{A}^{-1} can be locally linearized (Zhdanov, 2002, pg. 571, Appendix D) by the following relations:

$$\mathbf{d}_0 = \mathbf{F} \cdot \mathbf{m}_0, \quad (4.8)$$

where \mathbf{F} is the *Frèchet matrix* of \mathbf{A} and contains the derivatives with respect to the initial model \mathbf{m}_0 :

$$\mathbf{F} = \nabla_m \mathbf{A}(\mathbf{m}_0) \quad (4.9)$$

Equation 4.8 is always a linear relation. In the case of a infinitesimal small variation (perturbation) applied on the model:

$$\delta \mathbf{d} = \mathbf{F} \cdot \delta \mathbf{m} \quad (4.10)$$

the *Frèchet matrix* can be considered as invariant. The data perturbation $\delta \mathbf{d}$ can also be seen as the residual between observed \mathbf{d} and modeled data \mathbf{d}_0 . The elements F_{ij} are the sensitivities of observation d_j with respect to model parameter m_i . Due to the invariance of \mathbf{F} for small variations a single inverse operation can be performed:

$$\delta \mathbf{m} = \mathbf{F}^{-1} \cdot \delta \mathbf{d}. \quad (4.11)$$

Equation 4.11 provides a small model adjustment $\delta \mathbf{m}$ by a given data perturbation $\delta \mathbf{d}$. By performing multiple single inverse steps in an iterative process, the inverse relation of Equation 4.7 can be calculated. Thereby, the difference between modeled \mathbf{d}_0 and observed data \mathbf{d} is reduced and a set of model parameters \mathbf{m} is found that fits the observed data. By this process, the full inverse problem described with Equation 4.7 is approximated by local linearized inverse steps.

Unfortunately, the inverse of the *Frèchet matrix* does not exist, since the problem is *ill-posed*. This means, that it is underdetermined because the amount of modeling parameters is much higher than the observation points. To overcome this problem, a regularization has to be applied. The regularization techniques used in this work are discussed in section 4.2.4. There are different methods available to perform the iterative inverse process, e.g. a *least-squares* or *conjugated-gradient* (CG) method. These methods minimize the following parametric functional (Tikhonov and Arsenin, 1977)

$$P^\alpha(\mathbf{m}) = \phi_d(\mathbf{m}) + \alpha s(\mathbf{m}), \quad (4.12)$$

where $\phi_d(\mathbf{m})$ is the misfit functional and $s(\mathbf{m})$ the stabilizer. α is a regularization parameter, which controls the trade off between misfit and stabilizer. The misfit functional

$$\phi_d = \|\mathbf{d}_{pre} - \mathbf{d}_{obs}\|_2^2 \quad (4.13)$$

represents the L_2 -norm of the difference between the observed \mathbf{d}_{obs} and predicted \mathbf{d}_{pre} data vector. In this study, a variation of CG is used, which is briefly described in section 4.2.5.

4.2.2 Model parametrization

In order to calculate the magnetic field or the magnetic gradient tensor caused by a given distribution of rock magnetization, the model has to be parametrized or discretized in an appropriate way. In this work, the physical parameter is the magnetization vector, but the same discretization can be used to model the distribution of scalar values like density or susceptibility.

The classic approach, introduced by *Talwani* (1965), uses polygonal bodies with constant magnetization to calculate the magnetic field at a given location. This method was extended by multiple authors to allow for modeling of complex 3D polyhedral bodies of arbitrary shape (*Pohanka*, 1988; *Götze and Lahmeyer*, 1988; *Furness*, 1994; *Holstein*, 2003). Usually, a measured magnetic field can be matched by modifying the shape and magnetization of the polyhedrons. Fig. 4.2 a) shows the parametrization of the geological structure by a polygon of arbitrary shape.

A simple variation of this method is to discretize the model space into voxels, i.e. rectilinear prisms, with homogeneous magnetization (*Sharma*, 1966; *Bhattacharyya*, 1980). By using this parametrization, the geological structure can be constructed by only varying the physical parameters of multiple cells. An illustration of this discretization is shown in Fig. 4.2 b). Unfortunately, the exact analytic solution for prism are inefficient to implement, because several logarithms and arctangents functions are used. Therefore, in this work this method is simplified by only assuming one magnetic dipole at the center of each voxel. This will introduce a calculation error when the distance between the cell and the observation point is small compared to the size of the cell. For most cases this error is small enough to be neglected.

In comparison to the polyhedral-based parametrization technique, voxel-based discretization will create much more degrees of freedom for the model, making the problem highly underdetermined. This makes a strong regularization necessary, which is discussed in section 4.2.4.

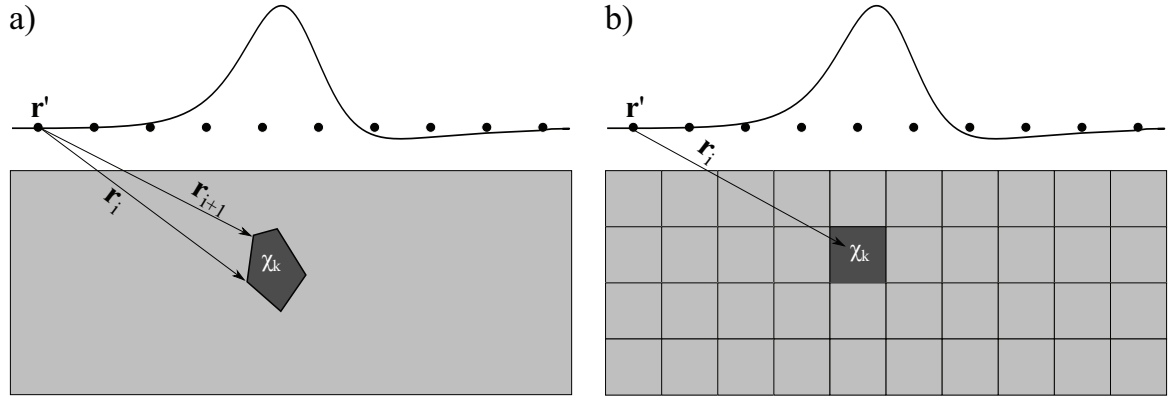


Figure 4.2: Illustration of the model discretization. a) shows the geological structure parameterized by a polygon (polyhedron in 3D) of arbitrary shape with a higher susceptibility than the host rock. The vectors \mathbf{r}_i and \mathbf{r}_{i+1} are representing the distance relation required for the line integral algorithm used in this parametrization method. In b) the model space is discretized by rectilinear cells with constant physical parameters, i.e. susceptibility. One cell with a higher susceptibility is marked by one cell shaded in dark grey. The resulting schematic magnetic anomaly and the observation points \mathbf{r}' are shown above in both figures.

4.2.3 Forward modeling

To perform the inverse process, forward calculation is necessary. This operator depends on the model parametrization shown in Fig. 4.2. Therefore, the geometry and the model parameters are included to calculate the response, i.e. the magnetic gradient tensor, of the model at any given location. To illustrate this example, the operator:

$$\mathbf{A}_{ik} = -\frac{H_0}{4\pi} \iiint_{D_k} \frac{1}{|\mathbf{r}_i - \mathbf{r}'|^3} \left[\mathbf{I} - \frac{3(\mathbf{l} \cdot (\mathbf{r}_i - \mathbf{r}'))(\mathbf{r}_i - \mathbf{r}')}{|\mathbf{r}_i - \mathbf{r}'|^2} \right] d\mathbf{r}, \quad (4.14)$$

is used to model the magnetic field vector at the observation point \mathbf{r}' . \mathbf{r}_i is the vector pointing to each model cell. H_0 denotes the intensity of the external magnetic field and the vector \mathbf{l} provides its direction. As shown in Fig. 4.2 b) the model space D is discretized in k rectilinear cells with a dipole source in the center. The response, i.e. magnetic field vector, at the i -th observation point \mathbf{d}_i is calculated by applying the forward operator to the model \mathbf{m}_k :

$$\mathbf{d}_i = \sum_k \mathbf{A}_{ik} \mathbf{m}_k, \quad (4.15)$$

where vector $\mathbf{m}_k = (\chi_1, \chi_2, \dots, \chi_k)^T$ contains the susceptibilities of k model cells. This formulation allows to model the magnetic field vector caused by a given susceptibility distribution. Formulations for the full gradient tensor are given in *Cai* (2012). The magnetization vector of this model points in the direction of the external field, therefore only the induced magnetization is modeled.

In this study, the total magnetization vector is modeled, therefore Equation 4.14 is modified to the following relation:

$$\mathbf{A}_{ik} = -\frac{1}{4\pi} \iiint_{D_k} \frac{1}{|\mathbf{r}_i - \mathbf{r}'|^3} \left[\mathbf{I} - \frac{3(\mathbf{r}_i - \mathbf{r}')(\mathbf{r}_i - \mathbf{r}')^T}{|\mathbf{r}_i - \mathbf{r}'|^2} \right] d\mathbf{r}, \quad (4.16)$$

where \mathbf{I} is the identity matrix. Similar to Equation 4.15:

$$\mathbf{d}_i = \sum_k \mathbf{A}_{ik} \mathbf{m}_k, \quad (4.17)$$

provides the magnetic field vectors at every observation point. In this case $\mathbf{m}_k = (\mathbf{J}_1, \mathbf{J}_2, \dots, \mathbf{J}_k)^T$ contains the total magnetization vectors of each cell with $\mathbf{J}_k = (J_{kx}, J_{ky}, J_{kz})^T$ the magnetization strength in each direction.

4.2.4 Regularization

In section 4.2.1, the *Fréchet matrix* was used to perform the inverse step. As stated there, the problem is ill-posed, since the amount of model parameters \mathbf{m} is generally higher than the number of observation points \mathbf{d} . To overcome this problem, a regularization has to be applied, which ensures that reasonable model parameters are chosen from the solution space. With Equation 4.12, the parametric functional of *Tikhonov and Arsenin* (1977) was introduced. It includes the misfit functional ϕ_d (4.13) and a stabilizing functional $s(\mathbf{m})$. A great variety of different stabilizers have been developed in the past and this is still subject of current research. Within the last years many different regularization techniques have been published (*Last and Kubik*, 1983; *Li and Oldenburg*, 1996; *Portniaguine and Zhdanov*, 1999; *Zhdanov*, 2002; *Li and Oldenburg*,

2003). The integration of geological constraints (*Lelièvre et al.*, 2009) should provide the best results, but only when additional information, such as borehole logging data, is available.

The choice of the stabilizer $s(\mathbf{m})$ is crucial because it will lead the inversion towards reasonable models. Therefore, a short overview of the two stabilizing functionals used in this study will be given here.

The first stabilizer is called *minimum-norm*:

$$s_{mn}(\mathbf{m}) = \int_V (\mathbf{m} - \mathbf{m}_{apr})^2 dv, \quad (4.18)$$

which reduces the difference between the model \mathbf{m} of the current inversion step and an a priori model \mathbf{m}_{apr} . Thus, the model change is penalized with respect to the a priori model, which means when \mathbf{m}_{apr} is smooth, the inversion will show a smoothing behavior.

Smooth models can explain the data in many cases and satisfy the fact that geophysical methods have a limited resolution. On the contrary, geological structures often exhibit sharp contrasts and discontinuities in the petrophysical parameters, e.g. magnetization or susceptibility contrasts of a dyke intrusion in a sediment layer. Therefore, the regularization can be used to force sharper transitions of compact structures. *Last and Kubik* (1983) and *Portniaguine and Zhdanov* (1999) introduced multiple stabilizers which will produce sharper contrasts in the models. Here, only one of these stabilizers will be discussed. The *minimum-support* stabilizer:

$$s_{MS}(\mathbf{m}) = \int_V \frac{(\mathbf{m} - \mathbf{m}_{apr})^2}{(\mathbf{m} - \mathbf{m}_{apr})^2 + \beta^2} dv, \quad (4.19)$$

increases the compactness of the recovered model \mathbf{m} by penalizing models with a smooth parameter distribution. β is a small positive number, also called *focusing parameter*, which prevents singularities if $\mathbf{m} = \mathbf{m}_{apr}$. This parameter can be used to control the smoothness or sharpness of the model. Using higher values of β will result in smoother models and vice versa for lower values. Therefore, this stabilizer penalizes smooth model distributions with small deviations from the a priori model and compact model distributions with sharper contrasts are penalized less. Both stabilizers are illustrated in Fig. 4.3.

4.2.5 Inversion strategy

As stated in section 4.2.1, the inversion has to be performed as an iterative process, because the forward operator \mathbf{A} in Equation 4.6 is nonlinear. At each iteration, a small model perturbation $\delta\mathbf{m}$ is applied to the model \mathbf{m}_i , which results in the updated model $\mathbf{m}_{i+1} = \mathbf{m}_i + \delta\mathbf{m}$, which should decrease the misfit and therefore also minimize the parametric functional (4.12). The algorithm which is used in this study is based on the *conjugated-gradient* approach.

The model update (perturbation) has to be selected in the direction of decreasing misfit. Thus, the descent direction must be determined. The model perturbation of the first iteration is:

$$\delta\mathbf{m} = -\kappa\tilde{\mathbf{l}}(\mathbf{m}), \quad (4.20)$$

where κ is the step length and $\tilde{\mathbf{l}}(\mathbf{m})$ is the direction of the steepest ascent. This is similar to the *steepest decent* method. For the following steps the direction is obtained

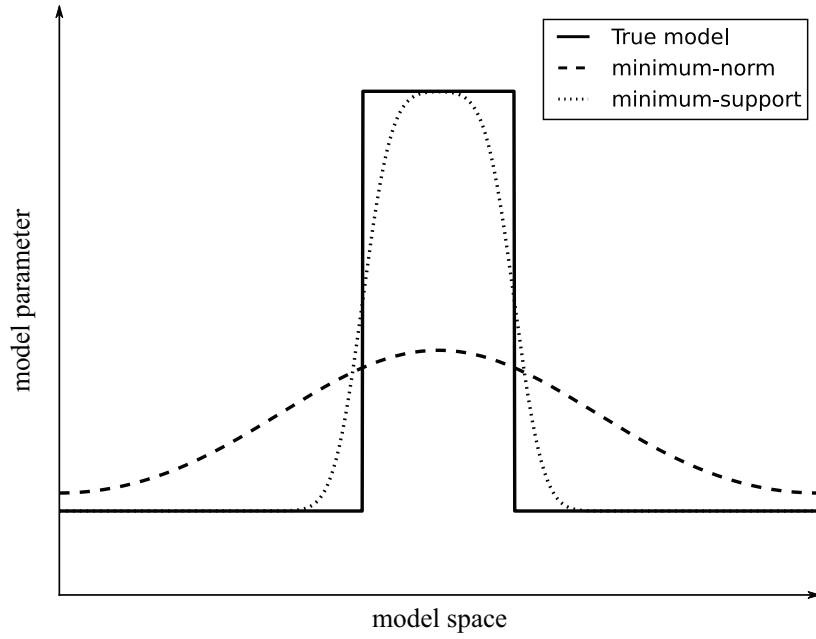


Figure 4.3: Illustration of the behavior of the minimum-norm and -support stabilizers (Zhdanov, 2002). The solid line represents the true model, the dashed line the inversion result using the mn, and the dotted line the MS stabilizer.

using the direction of the previous steps. The step length κ is determined by using a linear or parabolic line search approach (Zhdanov, 2002). Portniaguine and Zhdanov (1999) extended the CG approach by regularizing the determination of the descent direction and by applying weights to the parametric functional. Weighting is applied to the data and to the model.

The weighting of the model is important in order to account for the depth sensitivity of the methods. Thus, the weights are different for total magnetic field, magnetic gradient tensors or gravity inversions. The model is weighted by using the *Frèchet* derivative \mathbf{F} similar to the approach of Li and Oldenburg (2000). Model weighting also includes the regularization technique, in this case it could either be minimum-norm or minimum-support. This means that the model weighting matrix depends on the model of the previous iteration and has to be pre-computed at every iteration. This variation of the CG algorithm is called *regularized re-weighted conjugated gradients* (RRCG) (Zhdanov, 2002).

5 Case studies applying full tensor magnetic gradiometry

5.1 Introduction

Within the INFLUINS project, airborne FTMG data has been acquired in five survey areas, which are marked by white boxes in Fig. 5.1 (Kukowski and Totsche, 2015). In this chapter, two case studies of airborne exploration with a full tensor magnetic gradiometry system will be presented using data from the "Schmalwasser" and "Ohrdruf" areas ("S" and "O" in Fig. 5.1). As discussed in section 2.1.2, measuring the magnetic gradient tensor yields several advantages compared to conventional magnetic surveys, which may have the potential to improve interpretation.

The first study area (SWR in the box "S" in Fig. 5.1) is located in the central part of the *Thuringian Forest* within the "Schmalwasser" survey area (marked by "S" in Fig. 5.1). Conglomerates from the *Upper Rotliegend*, are discordantly overlaying crystalline rocks, which were formed during the *Variscan orogeny*. The aim of this investigation is to study the performance of the FTMG system and the ability to accurately model the total magnetization vector by using the complete information of the magnetic gradient tensor. This study includes the analysis of natural remanent magnetization (NRM) of orientated rock samples. The comparison of measured and predicted remanent magnetization is an important topic within the framework of this case study.

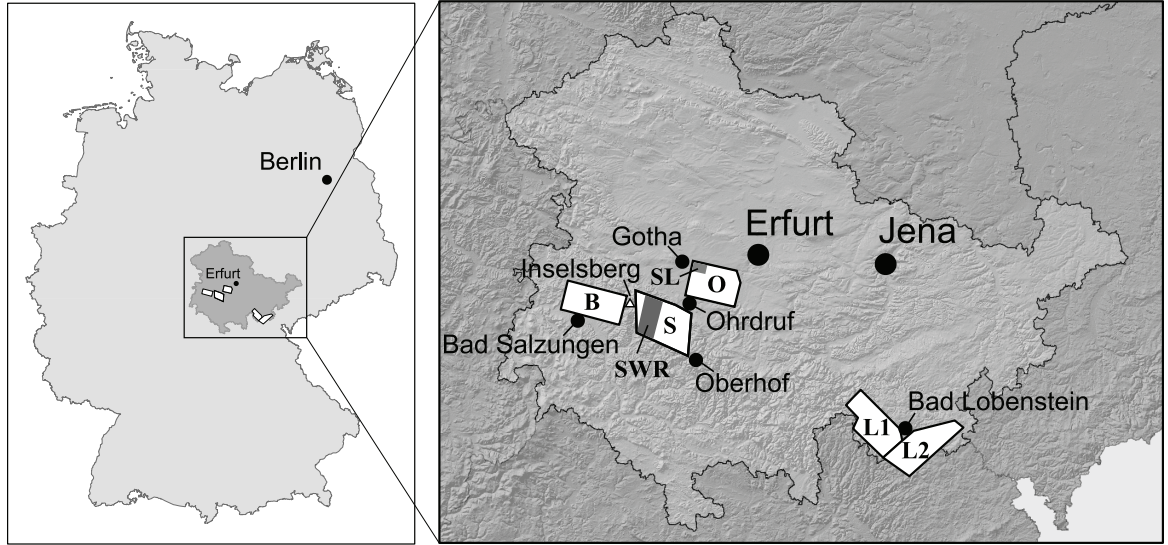


Figure 5.1: Location of the five survey areas and some larger settlements in Thuringia. The survey areas are called "Ohrdruf" (O), "Bad Salzungen" (B), "Schmalwasser" (S), "Lobenstein I" (L1), and "Lobenstein II" (L2). All of these areas are named after nearby towns or other landmarks, e.g. the "Schmalwasser" dam. The study areas of both case studies are marked by the dark gray rectangles SL and SWR for "Siebleben" and "Schmalwasser-Remanence".

In the second case study, a small-scale magnetic anomaly linked to a major fault zone in the *Thuringian Basin* is investigated. It includes the interpretation of the measured magnetic gradients, inversion of the complete gradient tensor and complementary ground based measurements, e.g. electrical resistivity tomography (ERT). In combination with an available geological model, implications on the source

of the magnetic anomaly are drawn. The survey area is part of the "*Ohrdruf*" area and is located near the small settlement named "*Siebleben*". The outline of the area, focussed on here, is marked by the dark gray rectangle (SL) in the "*Ohrdruf*" area, which is indicated by the white box named "O" in Fig. 5.1.

5.2 Geological overview

The five study areas are situated in the *Thuringian Basin*, the *Thuringian Forest* and *Thuringian Highlands*. The Thuringian Basin is part of the *North German Basin* (Littke, 2008) and is elongated in WNW-ESE direction with an extent of approximately 150×70 km. It holds *Late Permian* to *Triassic* sediments with a *Paleozoic* basement underneath. This basement, mainly *Cambrian* to *Early Carboniferous* units, is exposed in the *Harz Mountains*, the *Thuringian Forest* and the *Thuringian Highlands*. The development of the zones forming the basement (Fig. 5.2) is briefly described in the next section. The highlands define the northern, southern and eastern border of the *Thuringian Basin*. The western border is defined by the *Leinetal Graben*. The *Thuringian Forest* resembles a basement uplift with an extent of 70×20 km and strike direction (NW-SE) parallel to the *Thuringian Basin*. Fig. 5.3 shows a simplified overview of the chronostratigraphic units in Thuringia. In the following the geological development of the areas will be discussed in more detail.

5.2.1 Geological development of Thuringia

The Thuringian Forest and Highlands are part of the crystalline basement which consists of units related to the formation of *Pangaea* during the *Variscan Orogeny* in the *Devonian* and *Carboniferous* (Matte, 2001). This orogeny resulted from the

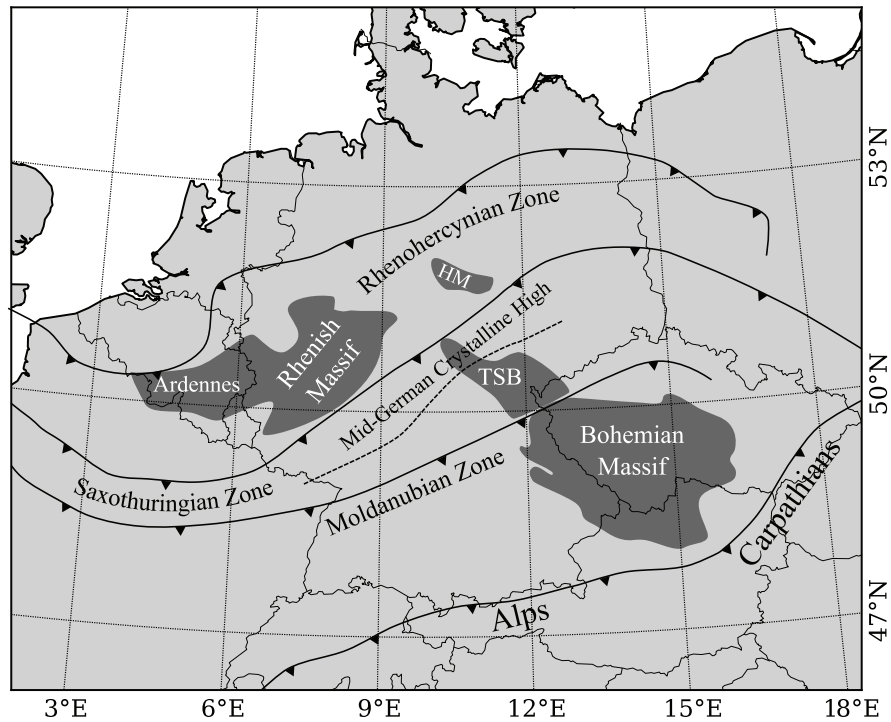


Figure 5.2: Basement structures of the Variscan Orogeny in Central Europe. This map is simplified after Winchester (2002) and Walter (1995). Abbreviations: HM - *Harz Mountains*; TSB - *Thuringian-Saxonian Basement* (also includes *Mönchberger Nappe*).

collision between *Gondwana* and *Laurussia* as well as the accretion of several smaller terranes. During the closure of at least three oceanic basins (*Matte*, 1991), sediments were deposited in *Early Carboniferous* time and folded during the subsequent orogeny, accompanied by granitic plutonism (*Ziegler*, 1990). In central Europe, remnants of the Variscan Orogen are subdivided from north to south into the *Rheno-Hercynian*, *Saxo-Thuringian* and *Moldanubian* zones following the definition of *Kossmat* (1927). These zones form the basement of central Europe and their present location is shown in Fig. 5.2. The "Schmalwasser" study area is located within the Saxothuringian zone, which is characterized by *Cambrian* to *Carboniferous* volcano-sediments folded during the *Variscan Orogeny* (*O'Brien and Carswell*, 1993). In post-variscan times granitic plutonism occurred followed by uplift and erosion (*Matte*, 1991).

From the *Late Carboniferous* until the *Early Permian* (*Rotliegend*), a basin-and-range type extension phase took place, with contemporaneous volcanism ("Rotliegend-volcanism"). Subsequent thermal subsidence led to the deposition of evaporites and shales during the *Late Permian* (*Ziegler*, 1990). In the *Triassic*, local graben systems established due to subsidence and E-W extension (*Kockel*, 2002). These were filled with clastic sediments, carbonates and evaporites. Regional extension from the *Late Jurassic* to the *Early Cretaceous* created NW-SE striking fault zone (e.g. the "Eichenberg-Gotha-Saalfeld" fault zone (EGSFZ), cf Fig. 5.3). The EGSFZ was most likely inverted during a compressional phase, which affected central Europe from *Late Cretaceous* to *Early Tertiary* (*Kley and Voigt*, 2008). This led to erosion of most of the *Mesozoic* sediments and the present day structure of the *Thuringian Basin* was established. This compression also led to the uplift of the *Thuringian Forest* and the *Harz-Mountains*.

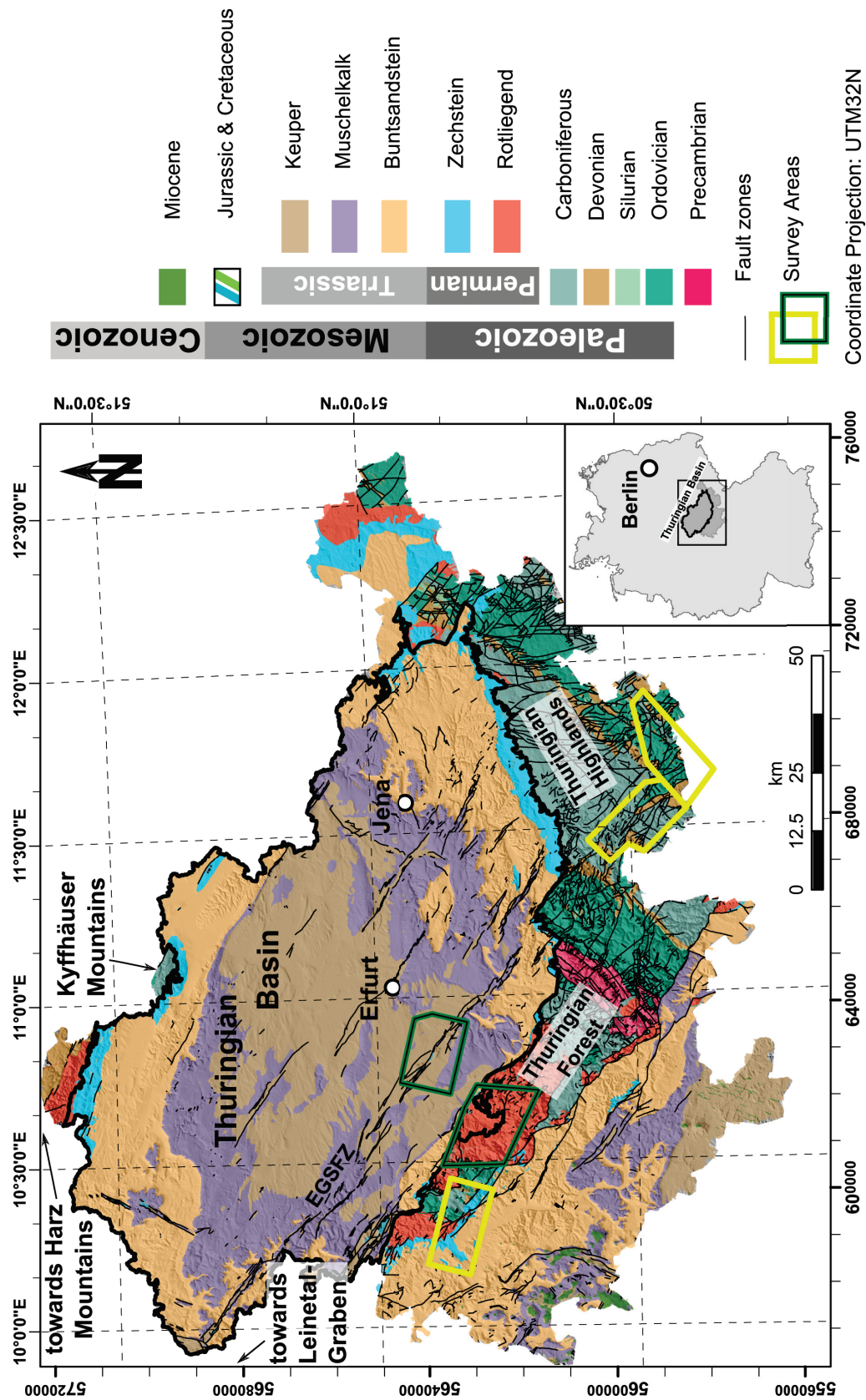


Figure 5.3: Geological Map of Thuringia, Germany, after *TLUG* (2003). Black lines indicate the location of known fault zones. The Eichenberg-Gotha-Saalfeld fault zone is marked by "EGSFZ". The Thuringian Basin is marked by the thick black outline. The major chronostratigraphic units are indicated by different colors in the legend on the right.

5.2.2 Geological framework of the "Schmalwasser" survey area

As mentioned earlier, the Thuringian Forest consists of *Cambrian to Carboniferous* volcano-sediments and plutonic intrusions. A short overview of the important units within the *Schmalwasser* survey area (see Fig. 5.1 and Fig. 5.4) is given hereafter.

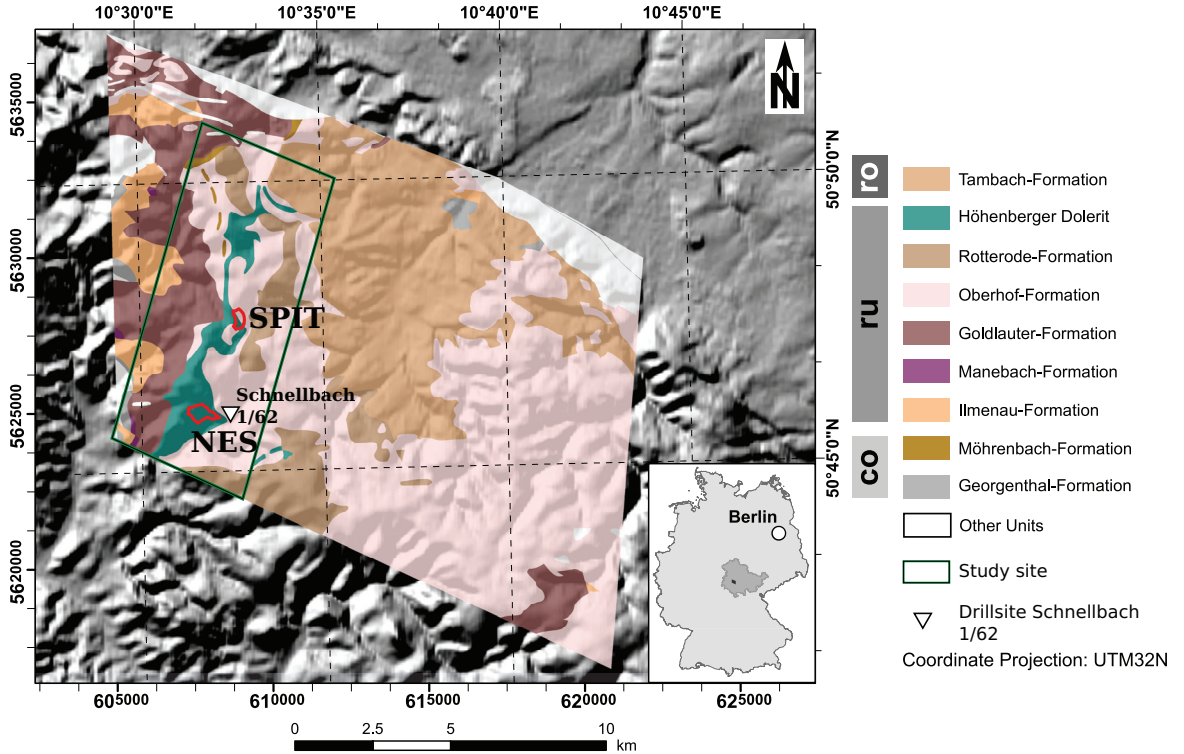


Figure 5.4: Geological Map of the "Schmalwasser" survey area *TLUG* (2003). Red polygons mark the location of two quarries *Nesselgrund* (NES, south) and *Spittergrund* (SPIT, north). In the following maps, the two quarries are always denoted by such red polygons. Units shown in color belong to the *Upper Carboniferous* (co), *Lower Rotliegend* (ru) and *Upper Rotliegend* (ro).

The most important geological formations in and around the study area are the *Möhrenbach*-, *Goldlauter*-, *Oberhof*-, *Rotterode*-, and *Tambach*-formation (Fig. 5.4). A more detailed description of those and older formations is given in *Lützner et al.* (2003), *Lützner et al.* (2012) or *Andreas and Lützner* (2009).

The *Möhrenbach* formation (*Upper Carboniferous*) only crops out in a few locations in the north-western part of the study area. This formation is dominated by a great variety of different intrusive and effusive magmatic rocks including rhyolites, trachytes, ignimbrites, and tuff (*Lützner et al.*, 2003). Some very local deposits of trachytes are located in the north-western part of the study area. The *Goldlauter* formation (*Lower Rotliegend*) mainly consists of conglomerates, lacustrine sand and silt stones with pelitic and pyroclastic intercalations (*Andreas and Lützner*, 2009). The conglomerates contain volcanic material originating from the *Manebach*- and *Ilmenau* formation (both *Lower Rotliegend*) (*Lützner et al.*, 2003). Other components of the conglomerates are various metamorphic rocks (schist and quartzite), flysch sediments, andesite, and rhyolite in varying portions and grain sizes (*Lützner et al.*, 2003). The *Oberhof* formation (*Lower Rotliegend*) mainly consists of rhyolites and pyroclastic material with local interbeddings of clay sediments. This material mainly originates from intrusive and effusive magmatism along WNW-ESE striking faults

(Andreas, 2013). Conglomerates containing mainly rhyolitic material are also present within this formation (Andreas and Lützner, 2009). Within the *Rotterode* formation (*Lower Rotliegend*) three different conglomerates are present: a sandy one, one with an increased amount of volcano-clastic material and a porphyritic conglomerate (Andreas and Lützner, 2009). A mafic intrusion cuts through the entire Thuringian Forest and is known as the *Höhenberger-Dolerite* (HD). This N-S striking structure has several smaller apophyses located east of the main intrusive body (Lützner et al., 2003). Its dip angle is about 30° to 40° and becomes steeper at greater depth. Lützner et al. (2012) described this as a steep feeder conduit at greater depth, which follows the layered sediments closer to the surface of the *Oberhof* formation. This intrusion was drilled at the drill site "Schnellbach 1/62" (Andreas and Volland, 2010) (Fig. 5.4). At the lower and upper contacts of the intrusion, hornfels is present, due to local metamorphosis. Indications for multiple intrusion phases have been found at the "Spittergrund" quarry (Mädler, 2009) and in the drilled cores (Andreas and Volland, 2010): As a result different magnetic properties might be present. The *Tambach* formation (*Upper Rotliegend*) consists of gravelly conglomerate with a large amount of rhyolitic material from the *Oberhof* formation. This unit is followed by a reddish sandstone with silty-clay interbeddings and finally, a conglomerate with a large amount (70 %) of volcanic material (Lützner et al., 2003).

5.2.3 Stratigraphy of the Thuringian Basin

The stratigraphy of the Thuringian Basin, will be briefly outlined with the focus on important formations. The crystalline basement of the Thuringian Basin is characterized by *Rheno-Hercynian* rocks in the north and *Saxo-Thuringian* rocks in the south. They are separated by the *Mid-German Crystalline High*. The basement is discordantly overlain by sedimentary rocks of *Permian* (*Zechstein*) age. These sediments are up to 700 m thick and contain shales, carbonates and evaporites. The upper part of the *Zechstein* sequence is predominantly shaly according to Langbein and Seidel (2003a).

The *Zechstein* layers are overlain by the *Triassic Buntsandstein*. The *Lower* and *Middle Buntsandstein* consists of sandstones with a thickness of roughly 500 m and shaly and silty intercalations (Puff and Langbein, 2003). The *Upper Buntsandstein* is characterized by strong thickness variations between 50 to 150 m. It consists mainly of shaly rocks and evaporites, which can reach a thickness of up to 90 m. The *Buntsandstein* groups are followed by the *Muschelkalk* formations. The *Lower Muschelkalk* consists of 100 m thick marine carbonates. The *Middle Muschelkalk* is dominated by marls and evaporites with a total thickness of about 100 m. The *Upper Muschelkalk* consists of thick-bedded limestones at the bottom and thin-bedded limestones with shaly intercalations at the top. In total, the *Upper Muschelkalk* has a thickness of 80 m and is overlain by *Keuper* formations (Langbein and Seidel, 2003b). The *Lower Keuper* mainly consists of marine sandstones and shales with a total thickness of 50 m. The *Middle Keuper* is characterized by shaly and marly sediments. The *Upper Keuper* predominantly comprises light gray to yellow sandstones with reddish clay stones (Dockter and Langbein, 2003). A small deposit of silt- and clay stones from the *Lower Jurassic* (*Lias*) can be found close to the EGSFZ. Units from both times (*Upper Keuper* and *Lower Jurassic*) are mostly eroded within the center of the basin. The *Upper Keuper* as well as very local deposits of *Jurassic* rocks are only present along major tectonic lines, e.g. the EGSFZ.

5.2.4 Local geological setting of the "Siebleben" study site

Similar to section 5.2.2 a brief overview of the geological setting of the "Siebleben" study site will be given here. The location of this site is marked by the gray area "SL" in Fig. 5.1. A detailed geologic map is shown in Fig. 5.5.

The area is characterized by a flat topography, except for a range of hills crossing from NW to SE. Parts of this ridge are the two hills "Kleiner Seeberg" and "Großer Seeberg". Directly north of these hills is a geographic low, which originally had no natural outflow. It was artificially drained in the 18th century and only a small pond, the "Sieblebener Teich" is left today. The "Sieblebener Teich" is in the central part of the study area marked by the red polygon in Fig. 5.5.

The study area is characterized by a *Mesozoic* sedimentary succession of *Middle* to *Upper Triassic* strata, i.e. *Muschelkalk* and *Keuper*. The *Middle Keuper* is exposed in most locations of the study area. The ridge is formed by *Middle* and *Upper Muschelkalk* strata. Units that are stratigraphically younger than the *Middle Keuper* (*Upper Keuper* and *Jurassic*) are preserved in the central part of this area, between the different branches of the previously mentioned EGSFZ, which crosses the study area from NW to SE. The northern normal fault dips southwards, while the southern fault planes feature a northward dip direction. The southernmost fault branch is a reactivated reverse fault. In general, this structure is a reactivated graben system, which has been normal faulted due to extension during the *Late Jurassic* to *Early Cretaceous* and reverse faulted, i.e. reactivated, in the *Late Cretaceous* to *Early Tertiary* (Kley and Voigt, 2008).

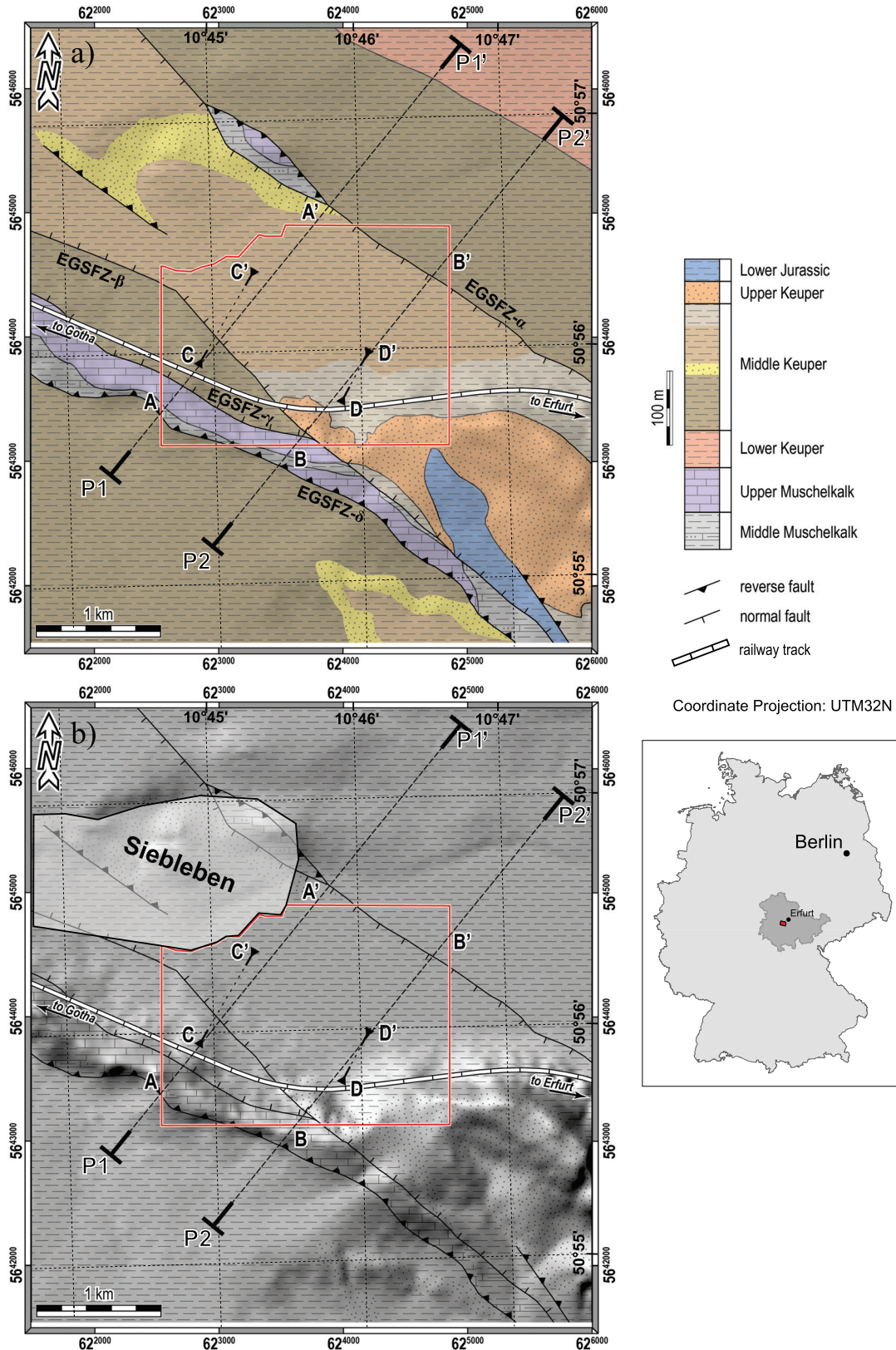


Figure 5.5: a) Geological map of the "Siebleben" study site based on *TLUG* (2010).
 b) Topography of the study area with overlain fault zones and stratigraphic units. The red polygon marks the location of the airborne FTMG data set. The outline of the nearby village "Siebleben" is shown in the lower map. The different branches of the EGSFZ are marked by EGSFZ- α to EGSFZ- δ . For the regional framework of the study area see Fig. 5.1.

5.3 Case study 1: Determining remanent and total magnetization on crystalline rocks in the Thuringian Forest

5.3.1 Motivation

In conventional airborne magnetic surveys, mostly only the total magnetic intensity (TMI) or total field gradients are measured. By subtracting the IGRF background field from the TMI, the total field anomaly (TFA) is obtained, which is generally used for interpretation. Since the sources of the anomalous magnetic field are not only affected by induced magnetization but can also show a significant remanent contribution, a directional information in the data is necessary for a better reconstruction of the shape, orientation and magnetization direction of the source. Even though the TFA does contain some sensitivity regarding the magnetization vector, the magnetic gradient tensor offers a higher sensitivity (*Foss, 2006a*). Historically, mostly the induced magnetization was modeled due to the higher computational effort when remanence was included. Additionally, paleomagnetic information on the modeled sources is not as often available as susceptibility values. Also it is much easier to interpret a 3D susceptibility distribution rather than magnetization vectors. However, the assumption that only induced magnetization is present can result in misleading interpretations. This problem becomes very apparent when the dip direction of a structure versus the magnetization direction is modeled (*Clark, 2014*).

So far two different types of methods for estimating the magnetization direction from airborne magnetic data have been suggested: Analytical methods and approaches based on the inversion of magnetic data. The inversion approach can be further sub-divided into algorithms using discrete body or a voxel-based discretization. One of the first analytical approaches is based on a set of integrals introduced by *Helbig (1963)*, which allows to infer the magnetization direction from measured TFA maps. *Phillips (2005)* re-evaluated Helbig's approach by testing various windows-sizes during scanning TFA maps. *Foss (2006b)* and *Foss and McKenzie (2009)* showed examples how Helbig's method compares to inversions of shape and magnetization of discrete bodies. *Roest and Pilkington (1993)* presented a work flow which involves the cross correlation of pseudo-gravity and the analytic signal in order to estimate the remanence of vertical sources. An extended variation of this approach was developed by *Dannemiller and Li (2006)*. Another method was proposed by *Medeiros and Silva (1995)*, where multiple magnetic multipole moments were used to approximate the source magnetization amplitude and directions. Since the magnetic gradient tensor has a higher sensitivity regarding the magnetization direction as stated by *Foss (2006a)*, methods have been developed that only rely on the analysis of the magnetic gradient tensor. *Beiki et al. (2012)* presented the normalized source strength (NSS), which allows for a better localization of magnetic source moments and their respective magnetization direction.

Modeling and inversion algorithms have also been modified to account for remanence in the following ways: Due to higher ambiguity caused by two additional degrees of freedom when including remanence in the modeling process, many approaches are based on inversion of discrete geometric bodies. Various case studies show the benefit of a staged-inversion approach, which means that at first the induced component of a discrete body is modeled and in consecutive steps the remanent part is taken into account in order to achieve a better data fit (*Foss, 2006b; Foss and McKenzie, 2009; Foss et al., 2012, 2015*). Some of these studies evaluate their results not only using Helbig's method but also paleomagnetic data. One example that is extensively

studied by means of remanence information extraction from airborne magnetic data is the *Black Hill Norite* in Australia (*Schmidt et al.*, 1993; *Rajagopalan et al.*, 1993, 1995; *Foss and McKenzie*, 2011). *Pratt et al.* (2014) extended the staged-inversion approach by using polar wander paths known from paleomagnetic data bases in order to remotely find the most reasonable remanent magnetization direction. All these studies show a great agreement in modeled magnetization directions, magnetic-moment based methods and measured paleomagnetic samples.

Voxel-based methods have been tested with regard to their ability to reconstruct the magnetization vector and therefore remanent magnetization. Since this approach has much more degrees of freedom, a strong regularization and geological constraints are necessary in order to derive reasonable results. *Kubota and Uchiyama* (2005) applied the magnetization vector inversion to ship-borne TFA data of a seamount. The inversion applied in this study uses a simplified discretization of cells within only a few layers. The results showed good agreement with previous paleomagnetic studies. *Li et al.* (2010) presented an algorithm where the amplitude of the magnetic anomaly vector was inverted. By using a wavelet based method the direction of the resulting vector was then reconstructed. *Lelièvre and Oldenburg* (2009) implemented voxel-based 3D magnetization vector inversion, which is very similar to the method used in this study. *Ellis et al.* (2012) presented a voxel-based inversion algorithm for TFA data, which allows to reconstruct the full magnetization vector. This algorithm was also used to invert the magnetization direction of the *Black Hill Norite* study site (*MacLeod and Ellis*, 2013). Even though it showed a general agreement in the direction and amplitude, the accuracy was not as good as the previously mentioned examples using discrete bodies. *Fullagar and Pears* (2015) presented a voxel-based inversion algorithm too, which allows to treat volumes within the model as bodies with remanent properties. Self-magnetization of these sources is also supported. As shown earlier by *Fullagar and Pears* (2013), self-demagnetization and interaction between different magnetized bodies can lead to serious differences when these effects are neglected. However, these effects are mostly relevant in extreme scenarios like the one presented by *Clark et al.* (2015). Nevertheless, a directly measured magnetic gradient tensor would undeniably support the presented work flow positively. A review on the various mentioned methods, their advantages and disadvantages is given in *Clark* (2014). Up to now, only one example of voxel-based FTMG inversion was published (*Zhdanov et al.*, 2011). In this example, only the susceptibility distribution was modeled and remanence was neglected, which means that the full capacity of the FTMG inversions, as proposed by *Foss* (2006a), have not been demonstrated so far.

The main focus of this case study is the inversion of a FTMG and a TFA data set using a voxel-based inversion code in order to reconstruct the complete magnetization vector. The data sets are part of the "Schmalwasser" survey area (section 5.2.2), in which a significant remanent magnetization is expected in some of the geological units. The reconstructed magnetization vector is separated into an induced and remanent part, which is then compared to the measured rock properties obtained from paleomagnetic samples. Thereby, the differences between the TFA and FTMG inversion will be discussed.

5.3.2 Methods and Operations

Airborne FTMG survey operation: The "Schmalwasser" data sets (Fig. 5.1) were collected during two campaigns between the 11th and the 29th of September

2012 and the 15th to 16th of May 2013. The study area covers an area of 12.5×18 km. Line spacing of 100 m resulted in 121 flight lines and 2200 line kilometers. The data sampling rate was 1 kHz during the survey, which was decimated down to 10 Hz during processing. Thus, in flight direction a reading was taken about every 3 m, considering the approximate survey speed of 60 KIAS¹². Weather conditions during this survey varied strongly, including survey days with higher wind speeds of up to 15 kt and local turbulences in narrow valleys. This resulted in challenging flight conditions and probably higher noise in the processed data.

The measured gradient tensor components of the complete "Schmalwasser" area as well as the TFA map are shown in Appendix A interpolated onto 50×50 m grids. This is a viable grid size, because of the highly anisotropically spaced data points and the SE-NW flight direction. A subset showing the G_{yy} component of the eastern part of the area is presented in Fig. 5.6. The further investigations are focused on this area. The color scale is clipped to a range of ± 1 nT/m for the gradient maps and -100 to 200 nT for the TFA. Here, a gray scale color map is used, which offers a better color perception when faint and strong anomalies are close to each other.

Inversion of FTMG and TFA data: The data set used for the FTMG and TFA inversion is shown in Fig. 5.6, covering an area of approximately 4.8×10.3 km. Because of the rough topography and strongly varying ground clearance of the airborne system, a very fine discretization of the uppermost cells is necessary to reduce calculation errors (section 4.2.2). Since the area is quite large, this leads to a model size of $348 \times 542 \times 60$ cells, including padding cells of 1000 m at all sides to reduce side effects. The horizontal cell size of this model is 25×25 m². In vertical direction, the cell thickness varies from 12.5 m for the uppermost 40 cells and 50 m for the lowermost 20 cells. Discretization was chosen like this to reduce the amount of cells and calculation time. To further reduce the inversion time the data set was decimated by the factor of 10 down to 13840 data points.

Multiple inversions were performed following a certain procedure: At first, an unconstrained inversion with a homogeneous starting model was performed including the tensor components G_{zz} , G_{xz} , G_{yz} , G_{xy} , and G_{yy} . Thereby, the following regularization strategy was chosen: For the first ten iterations, the mn stabilizer was applied. For the following iteration steps, the MS regularization was used (section 4.2.4). The application of the first stabilizer results in a relatively smooth model. The second stabilizer sharpens the structures in the smooth model in order to generate more compact structures. The inverse process was stopped after 50 iterations because the relative model change was very low. Therefore, more inverse steps would not lead towards a better data fit.

For the second inversion run, two polyhedral bodies were used as a starting model. The anomaly of interest in this area can be roughly separated into a northern and southern part. One polyhedron was located at the northern part of the main anomaly, the other one at the southern anomaly (compare Fig. 5.6). Both bodies are very simplistic dipping plates. The geometry and magnetization of these bodies was optimized using the inversion code of *Schneider et al.* (2014) before using them as starting models in the voxel-based inversion. The data fit of this parameter optimization is bad, since the variation of the shape is very limited and the magnetization is constant

¹²KIAS - knots indicated airspeed. The true ground speed depends on the wind conditions. Without wind the survey speed was therefore about 110 km/h

within the plate. The top plane of the plates is flat. Thus, the plate has to always be below the surface, which means that it is not possible to account for strongly varying topography. Nevertheless, the basic shape of the anomaly in all gradient tensor components can be reconstructed. The parameters of these two polyhedral bodies are listed in Table 1. The starting model was then constructed using the same

Table 1: Optimized parameters of the two dipping plates. The location of each plates is chosen to provide the best fit.

Body	Dip angle	Width	Top	Depth extent	Magnetization in A/m (M_x, M_y, M_z)
body North	75°	215 m	640 m a.s.l.	280 m	-0.127 -0.399 0.419
body South	80°	165 m	710 m a.s.l.	535 m	-0.304 -1.436 1.758

discretization as for the first inversion run by representing the polyhedral bodies by multiple voxels. All other parameters, i.e. regularization, decimation factor, and gradient components, are kept the same.

The third inversion run was done using only the TFA data. At first, the same model discretization and regularization strategy was applied. Even though the inversion converged, the resulting model was very blocky, thus indicating that the data was heavily overfitted. These models featured a lot of small volumes with very high magnetization amplitudes, often concentrated at the surface. For additional inversion runs the iteration number, at which the regularization scheme is changed from *mn* to *MS*, was changed. This resulted in very inconsistent magnetization models. Therefore, an inversion run only using the *mn* stabilizer was used. It was stopped after 75 iterations, again because of a low relative model change. The final inversion run was performed with a starting regularization parameter $\alpha = 1e-3$, which was automatically terminated after seven iterations because of a low misfit. Thus, the TFA inversion model is much smoother than the FTMG models and this model is used for further interpretation. The use of the previously described starting model did not lead to a significant improvement of the inversion result and thus it was not used for this inversion run. The two final models are presented in Fig. 5.7.

Paleomagnetic sampling: The main goal of this case study is to compare the measured natural remanence (NRM) with the magnetization direction recovered by the inversion of the airborne FTMG data. Thus, a brief description of the paleomagnetic sampling methodology, i.e. the collection of orientated rock samples and the processing in the laboratory is required.

The rock samples were collected in two quarries, denoted by red polygons in Fig. 5.4, where the intrusive rocks of the HD (see section 5.2.2) are exposed. The collection of the rock samples followed the methodology explained by *Butler* (1992). At the southern quarry, *Nesselgrund*, small cores were drilled using a portable gasoline-powered and water-cooled drill with diamond drilling bit. The collected cores are approximately 7 cm long with a diameter of 2.5 cm. After drilling, an orientation stage was placed in the drill hole. This device consists of a magnetic compass, an inclinometer and a bubble level, which allows to measure the azimuth and dip of the drilling direction. The upper side of the core is marked by a thin white line and arrow indicating the direction of the drill hole.

At the northern location, *Spittergrund*, the drilling of rock cylinders failed due to small fractures in the outcrop. Thus, all the cores broke out before a measurement of the orientation could be done. Therefore, orientated block samples were collected. Planar markers were created using gypsum and a 5×5 cm plate on top of the rock sample. An orientation arrow was carved into the gypsum and the direction of this arrow was measured using a geological compass. After hardening of the gypsum, the rock sample was carefully quarried out.

Both methods have some advantages and disadvantages: The drilling of rock cylinders provides a more accurate orientation measurement of $\pm 2^\circ$ compared to block sampling. While drilling is fast and many different sites can be sampled in a short time, only up to two specimen can be taken from one sample. Block sampling on the other hand provides a higher amount of specimens per sample. Usually, these samples have to be collected on joint blocks, which means that the rocks are more likely to be more weathered. Due to weathering, magnetite may be already oxidized to hematite, which might lead to a different NRM determination.

Processing of the collected samples was performed in the magnetic laboratory of the *Leibniz-Institute of Applied Geophysics* in Grubenhagen, Germany. The first step was the cutting of 2.5 cm long sections from the cores. From the block samples, similar cores were drilled and also cut in to 2.5 cm long sections. The second step was to measure the volumetric susceptibility using the *AGICO Minikappabridge* (AGICO Brno, Czech Republic). The NRM was then measured using the three-axis cryogenic magnetometer (2G Enterprises, California, USA) (*Rolf*, 2000). The measurement is performed in the coordinate system of the sample. The reorientation into the global coordinate frame with inclination, declination and magnetization amplitude using the orientation of the sample noted in the field is done afterwards. By using the information gained by the susceptibility measurements it is also possible to calculate the *Königsberger ratio* Q of each sample.

Separation of induced and remanent magnetization: In order to evaluate the magnetization direction in the inversion results, volumes within the models containing multiple cells are selected and compared to the measured magnetization directions. These volumes are depicted by black boxes in Fig. 5.10 c) and d). These locations were chosen because they are almost in the center of the highest absolute magnetization (see Fig. A.15) and at the same time still close to the two sampling sites.

In order to compare not only the total magnetization, but rather the remanence, it is necessary to separate the induced and the remanent contributions. By using the assumption that the magnetization which is parallel to the Earth's magnetic field belongs to the induced magnetization, the remanent part can be separated. This however leads to the limitation that the extracted remanence is always perpendicular to the induced magnetization. In other words, when the remanence is parallel to the Earth's field direction it is counted as induced magnetization. Thus, the length of the induced magnetization vector is required for scaling. In this case study, the mean value of the measured susceptibility of 0.86 A/m was used to scale the assumed induced magnetization vector.

5.3.3 Results

Mapped magnetic gradients: The mapped gradients and the TFA are shown in Appendix A for the complete survey area. A zoomed map of the western part of this

map is presented in Fig. 5.6, which contains only the G_{yy} component with and without interpreted lineaments. The topography and the flight track can be seen in Fig. A.8.

In the survey area, there are only two settlements. Therefore, the data set has only a few gaps at the locations of the settlements. About 1.3 km west of the area, a high-frequency DVB-T transmitter with an output power between 50 to 100 kW is located on top of the *Inselberg*. Flying close to this antenna led to jumps in the SQUID signals, depending on the approach angle towards the antenna, the distance and the topography. These jumps occurred within a distance of 3 to 4 km.

The minimum and maximum values of the gradient maps reach values of -15.2 to 17.6 nT/m and for the TFA maps -389.1 to 464.7 nT. Overall, the magnetic signatures in this area can be separated into three distinct regions: In the east, a large amount of high frequency anomalies can be seen. Most of them have a wavelength of 200 to 300 m and an amplitude of ± 0.5 nT/m. The central part of the survey area is characterized by no significant magnetic anomalies in the gradient maps. The TFA map shows variations of 50 nT and anomaly wavelength of more than 1.5 km. The western part is dominated by a strong north-south striking magnetic anomaly which is between 700 m and more than 2 km wide and can be tracked through the complete survey area from north to south. Here, the highest magnetic amplitudes of up to ± 10 nT/m for the gradients and up to 300 nT variation of the TFA were detected.

The strong magnetic anomaly in the western part of the survey area is best visible in the gradient tensor component G_{yy} and is depicted in Fig. 5.6 with a more detailed view. Please note, that the map was rotated and the north direction is indicated by the north arrow. The two red polygons indicate the location of the *Nesselgrund* quarry in the south and the *Spittergrund* (compare Fig. 5.4) in the north which are both actively exploited for building material, e.g. for railway constructions. Thus, man-made noise can be expected in this area. The large anomaly can be separated into two parts: the northern part shows lower amplitudes of ± 2 nT/m and forms a well defined E-W dipole. The southern part features the higher amplitudes, and has a more complex internal structure. This complex anomaly pattern is especially visible around the southern quarry, where the anomaly spans the largest area.

The main anomaly is accompanied by several smaller linear anomalies with a similar strike direction but lower amplitudes. At the northern end of the anomaly lineaments diverge in NW and NE directions. The width of these lineaments is mostly around 200 m and the amplitudes are around ± 0.5 nT/m. These smaller lineaments are also visible in the TFA, but they are much better defined spatially in the gradient tensor components, especially in G_{yy} .

By examining the various gradient components, the main anomaly as well as the smaller lineaments have the highest amplitudes in the vertical and eastern components (G_{yy} , G_{yz} , G_{zz} in Appendix A Fig. A.4, Fig. A.5 and Fig. A.6). In the other components, the northern part of the main anomaly nearly disappears. Considering the E-W dipole in TFA and higher amplitudes in these gradient components, this anomaly indicates a significant remanent magnetization.

Inversion results: The FTMG and TFA data sets have been inverted using the parameters outlined earlier in section 5.3.2. Multiple slices through the FTMG and TFA inversion result can be found in Appendix A Fig. A.11 to Fig. A.15. Horizontal slices through both models at an elevation of 400 m^{13} are presented in Fig. 5.7. The

¹³The elevation is given with respect to the mean sea level [m.s.l.]

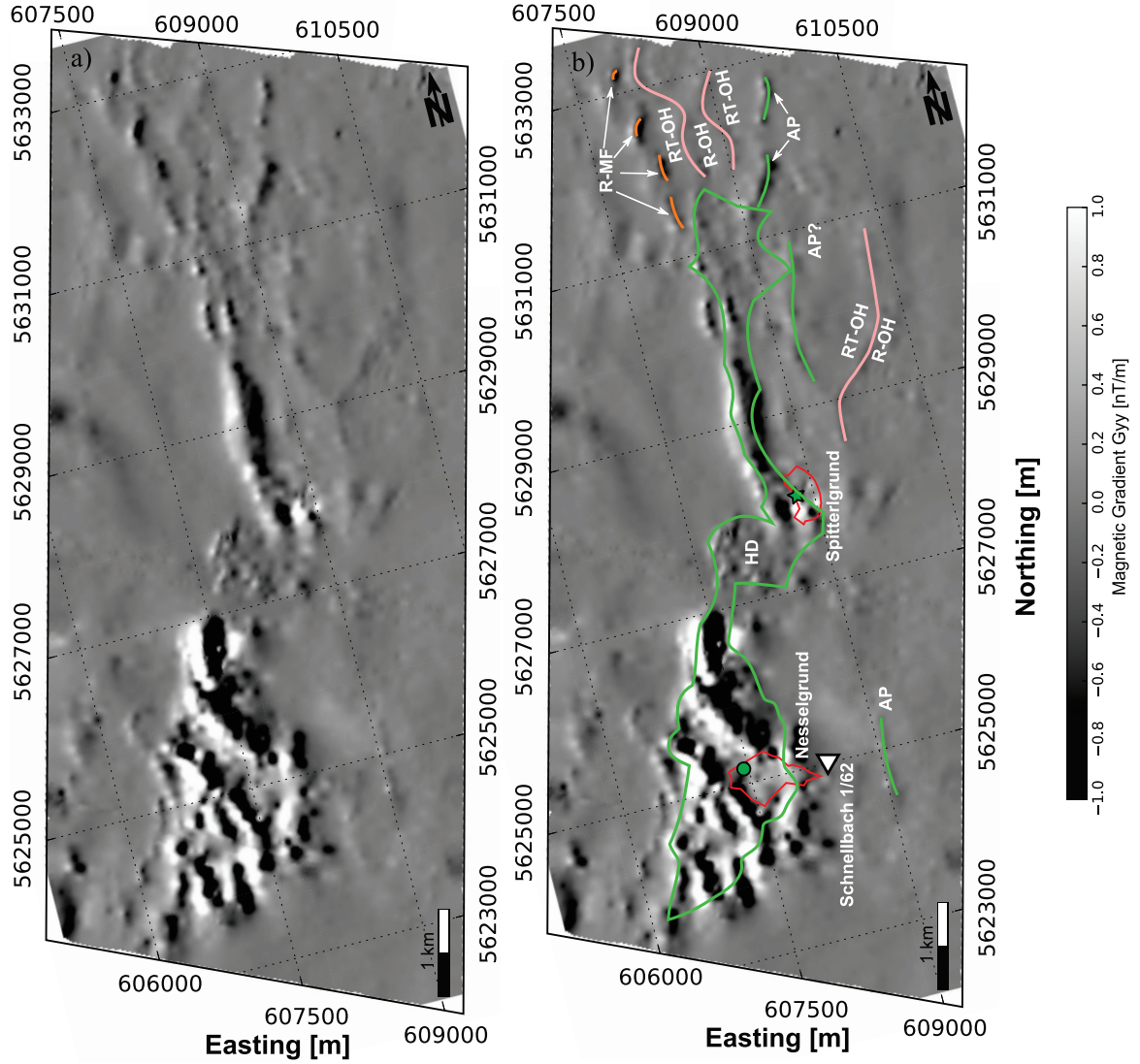


Figure 5.6: Detailed map of the magnetic gradient component G_{yy} . The two quarries "Nesselgrund" (south) and "Spittergrund" (north) are marked by the red polygons. Paleomagnetic sampling sites are shown by the green dot and star. Map (b) also includes picked lineaments that can be correlated with several apophyses (AP) of the *Höhenberger Dolerite* (HD) in green, rhyolites of the *Möhrenbach* formation (R-MF) in orange and transitions of rhyolites (R-OH) to rhyolite-tuffs (RT-OH) of the *Oberhof* formation in pink (compare Fig. 5.4). The triangle marks the location of the drill site "Schnellbach 1/62". Coordinates are given in the UTM32N projection.

paleomagnetic sampling sites are denoted by white dots and the outlines of both quarries are marked by red polygons. The black lines in this figure indicate the two locations of the vertical slices shown in Fig. A.12 across the *Nesselgrund* (NES-NES') and in Fig. A.14 at the *Spittergrund* quarry (SPIT-SPIT'). All slices are scaled to a range of -0.5 to 1.0 A/m. The vertical slices also include the location of the paleomagnetic sampling sites at the surface marked by triangles and black boxes, which indicate the volumes used later in this case study to compare the magnetization vectors of the inversion results and the paleomagnetic samples.

The strongest magnetization amplitudes can be found in the vertical and eastwards pointing components ranging from -1.0 to 2.0 A/m. The northern extension of the

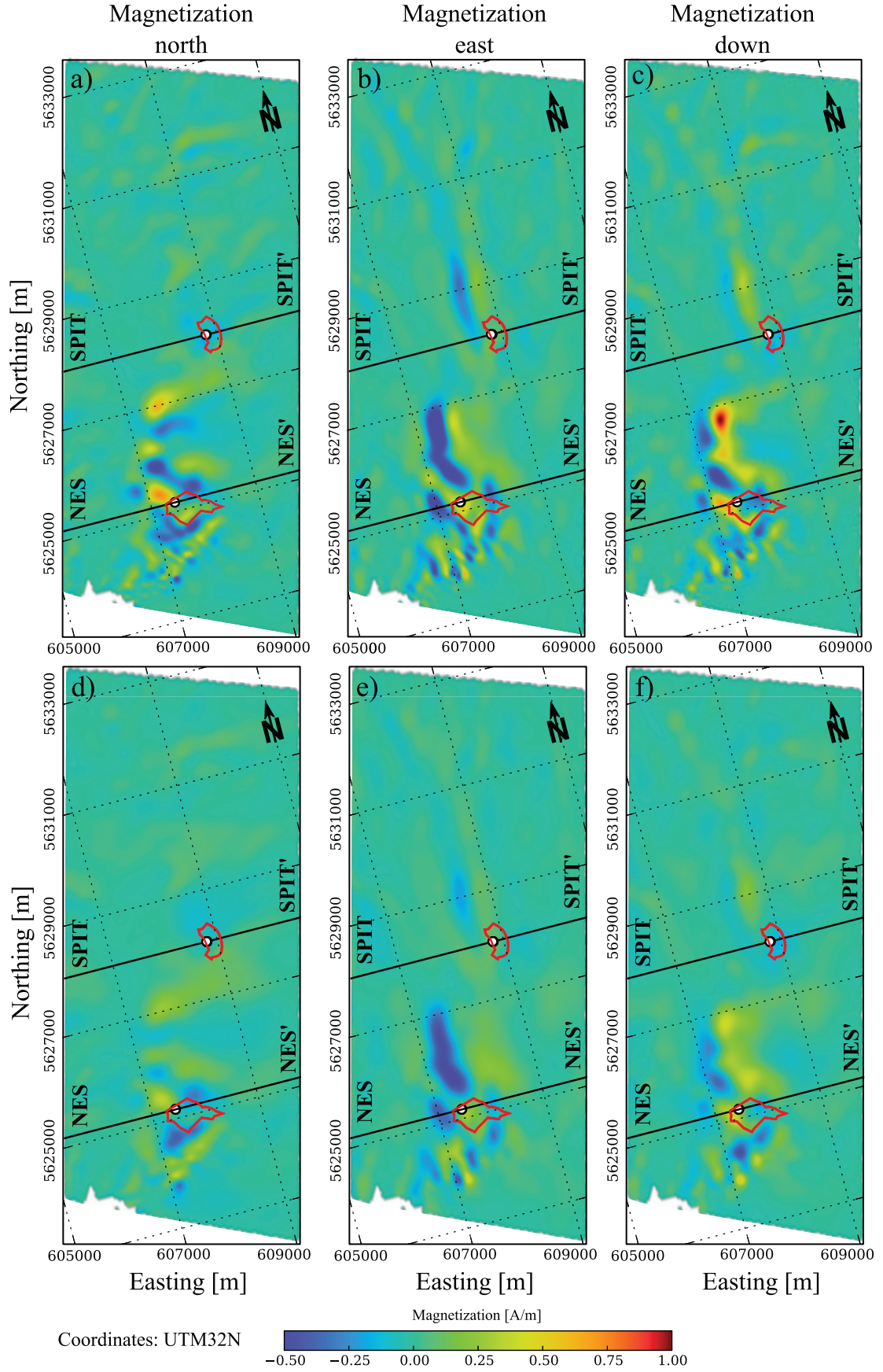


Figure 5.7: Horizontal slices at an elevation of 400 m through the final models of the FTMG (a-c) and TFA inversions (d-f). The red outline marks the location of the two quarries *Spittergrund* (north) and *Nesselgrund* (south). Paleomagnetic sampling locations are denoted by the white dots within the quarries. The location of the vertical slices are illustrated by the solid lines SPIT-SPIT' and NES-NES'.

southern anomaly, around 5 626 000 m northing, shows the highest magnetization within the model. By comparing the FTMG and TFA inversion results, it is obvious that the FTMG model features a much more compact and thereby also stronger magnetization.

As earlier mentioned, the magnetization anomaly can be divided into a northern and southern part. In the north, between 5 628 000 to 5 632 000 m northing, the magnetization is much lower around -0.25 to 0.25 A/m. However, the N-S striking structure is still very clearly defined. Similar to the structures visible in the gradient maps, this magnetization anomaly diverges in NNW and NNE branches beginning at 5 630 500 m northing. The southern anomaly is much stronger and, since it covers a greater area, divided into several positively and negatively magnetized regions. A general E-W dipole can be observed in the vertical and eastern magnetization components in both, FTMG and TFA, inversion results (Fig. 5.7). The northward magnetization in both models does not show a continuous structure.

The structure of the magnetization anomaly can be clearly seen along the southern profile (NES-NES') in Fig. A.12, crossing the *Nesselgrund* quarry. In both models, FTMG and TFA, the eastwards dipping structure is visible, especially in the eastern and vertical magnetization components. The upper slice in Fig. A.15 shows the same section through the FTMG model displaying the total magnetization, i.e. the norm of the magnetization vector, scaled between 0.0 to 1.0 A/m. The total magnetization highlights the complete magnetization anomaly, but it removes the directional information. Nevertheless, it should be easier to point out the area where the material with different magnetic properties is located using this visualization. In comparison, the TFA model shows a stronger vertical smearing, especially in the lowermost parts, but in general shows the same structures. The dip direction of the magnetization anomaly can be estimated to be around 40 to 45° .

A zoomed view into the eastern section of this slice, indicated by the dashed outline is presented in Fig. A.13. In this area, the FTMG model shows some faint structures that are enhanced due to a clipped color range of 0.05 to 0.125 A/m. At least two shallow magnetization anomalies are visible in this slice. The thickness of these structure is less than 100 m and they can be traced into depths of about 150 m beneath the surface. Similar to the main magnetization anomaly, the northward component of the magnetization vector does not show this structure.

Along the northern section (SPIT-SPIT') in Fig. A.14 a weaker magnetization is present, as expected from the mapped gradients and the horizontal slices. Nevertheless, steeply dipping structures are visible in the model slices, although they do not have the same depth extent as in the southern section.

A 3D view of the high-magnetized region in the FTMG inversion result striking in N-S direction is shown in Fig. 5.8 viewing from south to north. The isovolume includes all the model cells with a total magnetization higher than 0.6 A/m. As expected from the slices, the compact volume of higher magnetization dips eastwards and includes a greater volume at depth.

Paleomagnetic results: In Fig. 5.9 a), the direction of the NRM is shown in blue dots and the direction of the total magnetization with red dots, respectively. The total magnetization has been calculated by summing up the amplitude of the measured susceptibility and the direction of the current background field to the measured NRM. Values from both sampling locations are very similar. A probability density function

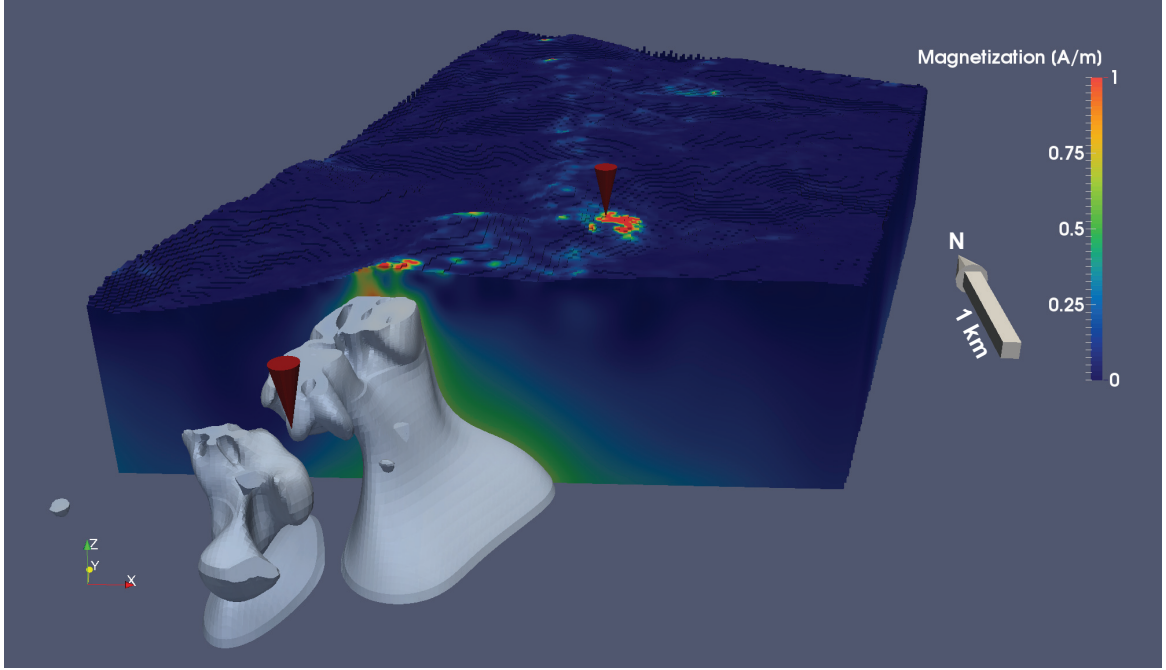


Figure 5.8: 3D view from south to north of the magnetized area of the *Höhenberger Dolerite* (compare Fig. 5.4). The isovolume (gray body) includes the volume with a total magnetization amplitude higher than 0.6 A/m in the FTMG inversion result. The locations of the *Spittergrund* (north) and *Nesselgrund* quarries (south) are marked with red arrow heads.

(PDF) was estimated by using a Gaussian kernel density estimation¹⁴ in order to illustrate the highest density of measured directions. The dashed line encircles one sigma of the data (95 %) and the solid line represents the median. This means that 50 % of the PDF should be inside the encircled area and the rest outside of this isoline. The data set is plotted in the lower (southern) hemisphere of a polar azimuthal equidistant projection.

The histogram in Fig. 5.9 b) shows the strength of the NRM (blue), the induced magnetization (green) and the total magnetization in red of all measured samples. Susceptibility was converted to magnetization in A/m by scaling it with the background field magnetization of 39 A/m.

The measured directions are mostly pointing into a SW direction between 190° to 210° declination and with an inclination of 30° to 50°. When the induced and remanent magnetization is combined, the resulting magnetization vector points nearly vertical downwards. The induced magnetization is about twice as strong as the remanence, resulting in a mean Q-factor of around 0.5. Therefore, the remanence of the HD can be considered to be significant and cannot be neglected. The scattering of the measured values, in direction and amplitude, is within normal standards. Less weathered samples might lead to a lower variance, but such samples are more difficult to obtain.

The results of each specimen are listed in Table 4 including the susceptibility values. The mean susceptibility of the samples is about $21.90 \times 10^{-3} \pm 13.61 \times 10^{-3}$ SI, which is much higher than any other rock formation that has been sampled in Thuringia within the framework of this study.

¹⁴http://docs.scipy.org/doc/scipy-0.14.0/reference/generated/scipy.stats.gaussian_kde.html

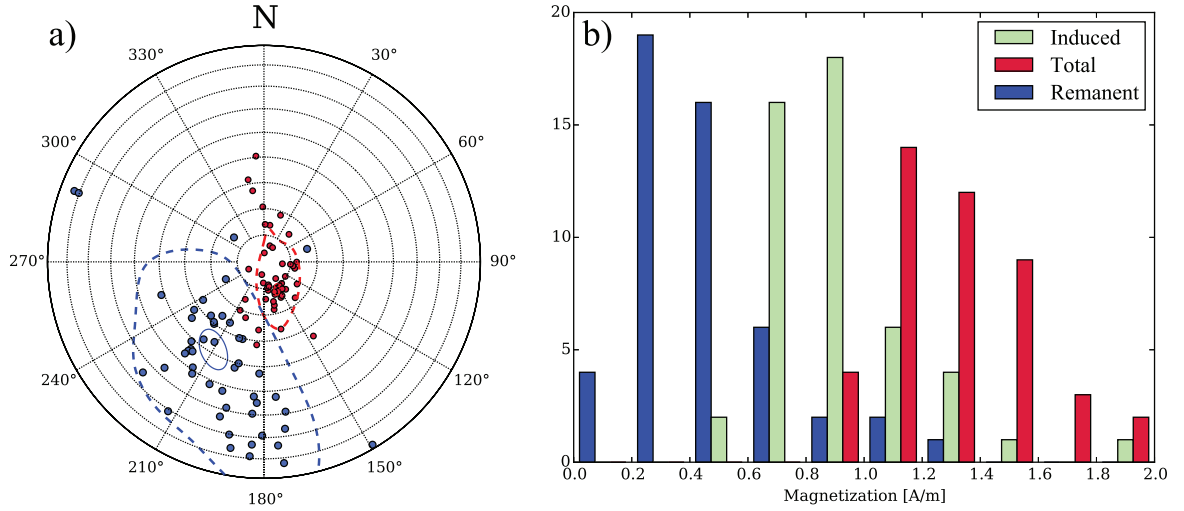


Figure 5.9: Results of the paleomagnetic measurements at both sampling sites. a) shows the magnetization directions of the NRM (blue) and the total magnetization (red) on polar azimuthal equidistant projection. The isolines represent the probability density function of the remanent and total magnetization at one sigma (dashed) and the median (solid). The histogram b) shows the distribution of the magnetization amplitudes including also the measured induced magnetization. The inducing field strength was assumed to be 39 A/m.

5.3.4 Interpretation

Data and inversion quality: The data set of the "Schmalwasser" area shows a noise level of about $0.2 \text{ (nT/m)}_{PP}^{15}$, mainly due to rough topography and windy conditions including turbulences in steep and narrow valleys. The signal-to-noise ratio, however, is acceptable, simply because the magnetic anomalies have high amplitudes. Additionally, the study area is nearly free of man-made noise sources, i.e. settlements or power lines. The effect of the DVB-T antenna at the *Inselsberg* was only present in close approaches and on a few flight lines. The jumps caused by this transmitter were removed by offset corrections during post-processing (*Schönau et al., 2013*) so that the processed data is not affected by this noise source any more.

The inversion results of the FTMG data set showed consistent results during the inversion process, which means similar models when different inversion parameters were chosen. The combination of *mn* and *MS* provided the best inversion results over all. Also, the variation of the iteration number on which the regularization was changed had only a minor impact on the final result, especially when a later iteration number was chosen. Considering the low misfit, displayed for the five gradient tensor components in Fig. A.9, of better than $\pm 0.1 \text{ nT/m}$, the final model can be seen as a very reasonable magnetization model.

The TFA inversions, however, were less consistent when applying different regularization parameters. Nevertheless, the final model also features a low misfit of $\pm 10 \text{ nT}$, as seen in Fig. A.10. As previously mentioned, the different regularization leads, as expected, to less compact and well defined structures.

The paleomagnetic analysis of the orientated rock samples shows a scattering in the magnetization directions, susceptibility and NRM. Even though two different sampling methods had to be applied, including the less accurate block sampling, the orientation error should only have a minor influence on data quality. More important are the

¹⁵ Assuming a conversion factor from RMS to peak-to-peak value (*Crest-factor*) of 4.

conditions of the rocks at the outcrop wall. Weathering can be a significant factor concerning the magnetization direction. Both sampling locations are close to the contact zone of the HD to the host rock of the *Oberhof* formation (see section 5.2). This might have a negative influence on the accuracy of the NRM determination, due to alteration and local metamorphism. Nevertheless, scattering is still in the acceptable range.

Interpretation of FTMG and TFA maps: The central part of the survey area can be correlated with the occurrence of the *Tambach* formation, which shows long wavelength magnetic anomalies and only low amplitudes. This can be explained by the structure of the *Tambach Basin*, which is filled with more or less horizontally layered conglomerates (*Andreas and Lützner, 2009*).

The western part of the survey area is dominated by the *Höhenberger dolerite* HD, which produces the strong N-S striking magnetic anomaly. Due to the E-W dipole structure in the TFA, and by examining the different gradient tensor components, a significant remanent magnetization is likely to be present. The difference in the magnetic signature in the northern and southern part of the HD anomaly is probably caused by the fact that the intrusion has been built by several phases of magma injection (*Lützner et al., 2012*). This implies that the intrusion might have a different petrology locally and thereby also varying magnetic properties.

The picked lineaments (Fig. 5.6, b)) provide a possible interpretation of some of the smaller anomalies and lineaments. The green outline represents the location of the HD after *TLUG (2010)*. Several apophyses, as described by *Andreas and Lützner (2009)* and *Lützner et al. (2012)* can be seen as faint lineaments marked by green lines (AP) in the map. In the northwest of the study area, similar lineaments can be observed striking in NNW-SSE direction. Those are related to rhyolithes of the *Möhrenbach* formation. On two locations, north and east of the dolerite intrusion, the transitions of rhyolithe tuffs to rhyolithes of the *Oberhof* formation (RT-OH, R-OH) can be seen by faint structures. Compared to the other lineaments, these anomalies have a longer wavelength probably related to the magnetization contrast and the structure of the transition. The apophyses are cutting more steeply through the sediment and thus the anomaly is much clearer defined and sharper.

The interpretation of the other lineaments visible in the map is difficult, due to the strongly varying topography and ground clearance of the airborne system. In this subset of the area, the minimum altitude was about 20 m over a mountain ridge, and the maximum 200 m over a valley. This leads to a topography effect, and thus some lineaments are very sharp and well defined, while others might not be detected at all. This makes the interpretation of some anomalies, especially the smaller ones, very challenging.

Interpretation of Inversion Results: The slices through the magnetization models (Fig. 5.7 and Fig. A.12) for both inversion runs, FTMG and TFA, are compiled in Fig. 5.10 for better comparison. In this figure only the horizontal slice at an elevation of 400 m and the vertical slices along the NES-NES' profile are depicted. Only the vertical magnetization component is displayed, since it is the strongest and easiest to interpret. Additionally the total magnetization, i.e. the norm of the magnetization vector, of the FTMG model along the NES-NES' and SPIT-SPIT' sections are shown in Fig. A.15.

In the horizontal slices, the principle location and strike direction of the HD is represented by the change from a negative magnetization in the west to a positive magnetization towards the east. The northern part of the HD can be traced up to the northernmost area of the study area. However, the previous interpretation of the mapped gradients suggests that the lineaments in the NNW are related to the *Möhrenbach* formation and not to the HD. Since both signals are caused by intrusive material it might be possible that the HD used the same intrusion pathways as the rhyolites of the R-MF in Fig. 5.6. This hypothesis, however, is only supported by this inversion result and it is not constrained by geological or drilling information. Thus, it is just a suggestion in order to explain the seamless transition between the two structures in the magnetization model.

In the vertical slices the principle structure of the HD intrusion is, as suggested by *Andreas and Lützner* (2009) and *Lützner et al.* (2012), very clearly defined. In comparison to geological profiles (*Andreas and Lützner*, 2009), the dip in the upper part is about 5° steeper. The transition from host rocks to the dolerite is defined by the change from a negative to positive downward magnetization. In other words, the dolerite is located between 607 000 m and 608 000 m easting at the NES-NES' section (see Fig. 5.10). This can also be observed by looking at the total magnetization in Fig. A.15. This correlates well with the occurrence of the intrusive material at the surface of this location. Within this area, some smaller structures close to the surface can be seen which might be related to the mining activity, i.e. man-made signals caused by technical equipment.

The TFA inversion result shows a similar picture, but the eastern and western transitions are less well defined. The smaller structures at the surface are not visible. As pointed out earlier, the reason for this is mainly the different regularization strategy used for the TFA inversion. As expected from the different mapped gradients, the east- and downward magnetization components are the strongest in both models, and thus a significant remanence is present.

Since the FTMG model shows smaller and fainter structures, some of the apophyses marked in Fig. 5.6 can be detected in the magnetization model as well. To enhance these structures, a zoom in of the eastern part of Fig. A.12 marked by the dashed box is shown in Fig. A.13. Close to the surface up to three structures are visible, that correlate well with the lineament and are most probably caused by one of the apophyses of the HD. Due to the fact that the structure might be less than 50 m thick it is too strongly smoothed out to be traced into greater depth. The thicker appearance of the magnetization anomalies in the model, with a thickness of about 100 m, is also caused by the smoothing behavior of the voxel-based inversion. The amplitude of the magnetization is much lower than the HD itself. Again, this is probably caused by the smoothing of the inversion. Since it is too narrow, the contact metamorphism might also have an impact on the strength of the magnetization. Unfortunately, no information on the susceptibility of the host rock is available. In the TFA model, this structure is not detectable.

Comparison of paleomagnetic and inverted magnetization: As explained in section 5.3.2 the magnetization at selected locations within the final magnetization models was separated into an induced and remanent part. To compare the measured with the inverted directions, both results were plotted together in Fig. 5.10. The directions are shown in the polar plots c) and f). These plots also contain the isolines

of the PDF of the measured directions from Fig. 5.9 in order to relate both directions to each other. Here, only the results from the NES-NES' profile are depicted because it has a higher magnetization and thus a more clearly defined structure compared to the *Spittergrund* location. A similar comparison at the northern location is shown at Fig. A.17.

For the FTMG inversion, the remanent and total magnetization are very close to the measured directions. However, the declination of the remanent part does scatter over a range of more than 45° . The TFA inversion shows a similar result, but the declination of the recovered remanence points more to the west than expected. The scattering of the declination is also present. This can be explained for both inversions by the smoothing of the voxel-based inversion. In magnetization vector inversions (MVI), this usually leads to the effect that the vectors on the edge of a certain structure do not change their direction abruptly, but rather "sweeping" over a range of directions.

The amplitudes of the FTMG and TFA inversions, as well as the measured magnetizations are shown in Fig. 5.10 g-i). The recovered amplitudes are about 0.8 to 1.0 A/m for both FTMG and TFA inversion. Compared to the measured amplitudes this is significantly lower, but it can be also explained by the smoothing of the inversion process, which results in a larger volume of higher magnetization relative to the background. The effect of the different regularization schemes is also apparent, because the FTMG inversion shows a bit higher amplitudes due to the more compact structure. Nevertheless, due to the small volume within the magnetization model that has been selected for the comparison, this effect might be different for other locations. Q-factors at the *Nesselgrund* location are about 1.3 and 1.1 for the FTMG and TFA inversion, respectively. At the *Spittergrund* the Q-factors are around 0.6 for the FTMG and 0.3 for the TFA inversion results. The Q-factor of the paleomagnetic samples at both sampling locations is 0.53. Nevertheless, as visible in the histogram h), these values scatter also quite a lot and some samples even show Q factors > 1.0 . In general, the ratio between the induced and remanent parts of the magnetization models differ from the measured values, which might be caused either by the smoothing of the inversion or by the assumptions made for the separation process.

The consensus in the magnetization direction and the eastward dip angle of 45° of the structure increases the confidence in the FTMG inversion results. The TFA inversion also features similar structures and magnetization directions, but, due to inconsistent behavior during the inversion process, this model is less assured. A major factor is most probably directional information of the five gradient tensor components used during the inversion, which offers better constraints compared to the TFA data set. This confirms the proposed higher sensitivity of magnetic gradient tensor data regarding the magnetization direction (*Foss, 2006a*). Nevertheless, the impact of the different regularization should not be underestimated. The discussion of the different results is given in section 6.1.1.

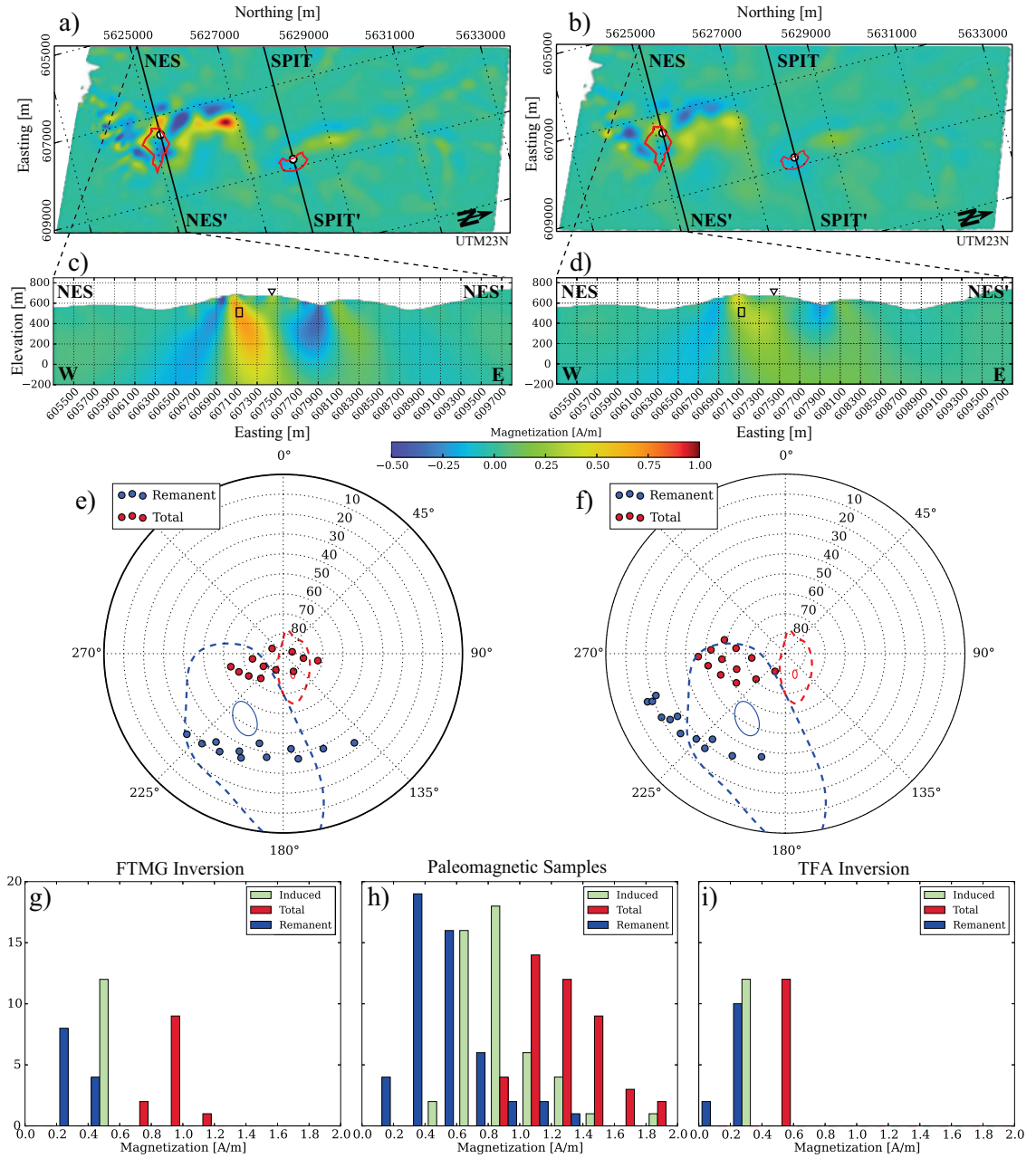


Figure 5.10: Comparison of FTMG and TFA inversion results with measured paleomagnetic data. The upper row shows horizontal slices of the downward magnetization at an elevation of 400 m through the final model of the FTMG inversion (a) and TFA inversion (b). The red polygons marks the location of the *Nesselgrund* quarry (south) and *Spittergrund* quarry (north). Paleomagnetic sampling locations are noted by white dots within the quarries. c) and d) show vertical slices along the profile NES-NES'. The paleomagnetic sampling site at the *Nesselgrund* quarry is marked here by the white triangle at the surface. Slices of the second profile SPIT-SPIT' and the other magnetization components of both models are shown in Fig. A. These rotated maps are also shown in Fig. 5.7 c) and f). The magnetization direction within the black boxes in c) and d) are shown in the polar plots e) and f) using the polar azimuthal equidistant projection, and their appropriate magnetization in the histograms g) and i). The blue and red isolines in e) and f) refer to the probability density function of the measured magnetization directions from the paleomagnetic samples shown in Fig. 5.9. The dashed isolines encircle 95 % of the data and the solid isoline represents the median. Each bin in the histograms g), h) and i) includes a range of 0.2 A/m. Further explanations can be found in the text. Coordinates in a-d) are given in the UTM32N projection.

5.4 Case study 2: Exploring sedimentary rocks in the Thuringian Basin

5.4.1 Motivation

The survey area "Ohrdruf" (Fig. 5.1) covers the central part of the Eichenberg-Gotha-Saalfeld fault zone (EGSFZ) (Fig. 5.3). The intention of this study was to map magnetic lineaments along the EGSFZ. This particular fault zone was intensively studied in the framework of the INFLUINS project (*Goepel et al.*, in prep.; *Malz*, 2014; *Kukowski and Totsche*, 2015). Magnetic anomalies were expected due to different petrophysical properties of the sedimentary layers close to faults with vertical offsets. However, only one weak small-scale magnetic lineament was detected in the north-west of this survey area, close to the small village "Siebleben" (compare Fig. 5.1 and Fig. 5.5). This structure is elongated in NW to SE direction and thus, sub-parallel to the EGSFZ. Due to the rural character of the wider area, only a few outcrops are available. Most of the study area is also covered by Quaternary sediments. Thus, the exact location of the fault planes cannot be easily deduced by analyzing geomorphological features or using geological methods.

In general, sedimentary rocks are less magnetized than crystalline basement (see Fig. 2.6). Thus, often faulted basement causes more prominent magnetic anomalies, i.e. lineaments even underneath a thick sedimentary coverage. Therefore, potential field methods are mostly used in these settings to analyze the basement structures below sediments (*de Castro et al.*, 2014). However, magnetic gradients usually do not provide the sensitivity to map deep structures under a thick coverage and therefore only magnetic structures within the sediments can be detected.

Most magnetic anomalies within sedimentary basins are caused by faulted layers. A sub-vertical offset of magnetized layers will produce magnetic lineaments in the strike direction of the fault (*Grauch and Hudson*, 2011). In specific cases, this can be used to derive structural information of intra-basinal faults in a hydrogeological context (*Grauch*, 2001).

The investigation of faults in sedimentary basins using various geophysical methods can be a valuable tool to evaluate their geothermal potential (*Egger et al.*, 2014). Geothermal fluids often cause magnetization contrasts, e.g. due to precipitation of magnetic minerals, in the vicinity of highly permeable zones, such as fault zones.

Most studies use conventional total field anomaly data sets. Studies using FTMG systems are rare, because of the limited availability of these systems. *Rompel* (2009) presented the first application of an airborne FTMG instrument with a focus on comparing this system with conventional magnetic survey methods. The study site presented in this publication comprises a great variety of different geological units ranging from layered sediments to volcanic dyke complexes. Even though, no detailed interpretation of the data was presented.

Besides regional magnetic studies, small and shallow structures, some hundreds of meters in width and depth, are mostly investigated by applying complementary ground based methods, i.e. the analysis of electrical or seismic properties (*Villani et al.*, 2015). Even though, the investigation of small scale structures using airborne magnetic data is very uncommon, mainly because of greater flight line separation and altitudes of most conducted surveys. In most studies, only the TFA maps or principle 2D models are discussed. The application of 3D inversion is also very uncommon, especially for small scale studies with multiple geophysical data sets. Thus, in this case study the

interpretation of mapped magnetic gradients, accompanied by 3D inversion of airborne FTMG data, ground based ERT sections, and available geological information at the "Siebleben" site is presented. The main goal is to explain the occurrence of this small-scale, intra-basinal magnetic anomaly and provide possible explanations for the processes that caused this structure.

5.4.2 Methods and Operation

FTMG data acquisition: The *Ohrdruf* data set ("O" in Fig. 5.1) was acquired from the 2nd to 11th of July and also on the 23rd and 24th of July 2012. This survey operation covers an area of 11×16 km. Line spacing of 50 m resulted in 242 flight lines and 2874 line kilometers. The mean flight altitude of the bird was 46.6 m above ground in a terrain-following flight. The speed was roughly around 60 KIAS. Originally, it was planned to keep an altitude of 30 m above ground, but because of topography, large trees and buildings, the mean flight altitude was somewhat higher.

Weather during this operation was mostly sunny with a few days with light rain. Wind conditions were calm with wind speeds not exceeding 10 kt. Occasionally, jumps in the raw SQUID data caused by remote lightning strikes could be observed. When the jumps occurred too frequently, the flight was suspended until thunderstorm activity was reduced. These jumps were also removed during processing (*Schönau et al.*, 2013). The measured FTMG data are presented in the following section 5.4.4.

FTMG data inversion: A subset of 2×2 km of the FTMG data (compare red polygon in Fig. 5.5), which covers the most prominent magnetic anomaly of the study area, was inverted using the voxel-based discretization and the algorithm outlined in section 4.2.5. The model space was discretized by 110×132×92 cells with a volume of 25×25×12.5 m³. Prior to the inversion, the data subset was decimated down by a factor of 15 to 1630 data points. This results in a data density of only one or two data points per cell at the surface. A higher data density does not increase model resolution but enlarges the computation time. For the inversion, the following five tensor components were used: G_{zz} , G_{xz} , G_{yz} , G_{xy} , and G_{yy} . A homogeneous starting model with a susceptibility of zero was used. In this case, this is a reasonable assumption, because of the low susceptibilities in this area. Susceptibility measurements were conducted prior to data acquisition. An overview of the magnetic properties of the most important formations in the Thuringian Basin, as well as the position of all sampling locations, is given in section 5.4.3.

The regularization strategy involves two different stabilizing functionals, that were introduced in section 4.2.4. For the first ten iterations the *minimum-norm* (*mn*) stabilizer was chosen. In combination with the homogeneous starting model this results in a smooth magnetization distribution after ten iterations. For the following inversion steps, the *minimum-support* (*MS*) stabilizer was applied, which produces a more compact structure as illustrated in Fig. 4.3. Various combinations of these inversion parameters, i.e. the iteration at which the regularization scheme is changed as well as pure *mn* or *MS* regularization, have been tested. But, the strategy presented above has shown the best and most consistent results. In total, the inversion was carried out for 50 iterations. For an easier interpretation of the final model, the projection of the magnetization vector parallel to Earth magnetic field is treated as induced magnetization, even though it could also contain remanent magnetization pointing in the same direction. By using the field parameters from the IGRF (48 890 nT total intensity,

66.323° inclination, 2.076° declination) the magnetization strength was converted to SI susceptibility units. It should be pointed out, that remanent magnetization in parallel to the Earth's magnetic field will be represented as a susceptibility variation. This means that depending on the direction of the remanent magnetization, susceptibility can either be increased (remanence parallel to induced magnetization) or decreased (anti-parallel to induced magnetization). Nevertheless, remanent magnetization is not expected in this area.

Resistivity data acquisition and inversion: In addition to the airborne FTMG data, ground based resistivity data was acquired across the main magnetic anomaly along two parallel profiles. They are marked as profiles C and D in Fig. 5.5. Data acquisition took place in October 2013. Multiple readings of each electrode configuration were taken in order to increase the reliability of the data set. A simple averaging of the measured potentials was automatically performed by the software in order to increase the signal-to-noise ratio. Both profiles were orientated perpendicular to the strike direction of the magnetic anomaly. Profile C is 900 m long and profile D 500 m. Electrode spacing for both profiles was 5 m using 100 electrodes for each profile. A Wenner- α array was chosen, since it provides a greater depth of investigation (Lowrie, 2007). The length of profile C was achieved by re-positioning 100 m long sections. Thus, the investigation depth of this profile is about the same as in profile D.

The inversion of the two data sets was performed using the program package *BERT* (boundless electrical resistivity tomography). Here, the model space is discretized by triangular cells and the algorithm uses a finite element approach (Rücker *et al.*, 2006) for forward modeling. This inversion algorithm applies a *conjugated-gradient* approach, similar to the one outlined in section 4.2.5, in order to minimize the objective function (Günther *et al.*, 2006). Again, the two profiles were inverted with a homogeneous starting model, since only little information of the subsurface in this area was available. The starting model is automatically constructed using the median of the apparent resistivity. Since the study area is more or less flat, only a minor impact of the topography on the model is expected. Nevertheless, topography was also included in the inversion.

5.4.3 Susceptibility Measurements

In order to support the interpretation of the magnetization models, susceptibility measurements in various outcrops in Thuringia were conducted. Fig. 5.11 provides an overview of the sampling locations. The hand-held device *Kappameter KM-7*, which was described in section 3.4, was used to undertake these measurements. More reliable susceptibility values are ensured by taking multiple readings (minimum of five) at each sampling site. A compilation of susceptibility values are given in Table 2. Samples were taken from the entire *Thuringian Basin*. Most of the units are only exposed at the margin of the basin. Thus, some of them are not accessible directly in the survey area. Therefore, the assumption was made, that the susceptibility values of the different units are more or less the same throughout the entire basin. This assumption is supported by the fact that the measurements at the northern margin and those close to the "Ohrdruf" area show nearly the same susceptibility values (Table 3). Nevertheless, some geological units can feature local mineral concretions, e.g. of iron-rich minerals (Seidel, 2003). These can lead to locally increased susceptibilities.

This compilation reveals that within the sedimentary units low susceptibility values are dominant. The main unit with a significantly higher susceptibility is the *Lower Keuper* (ku). This unit is only exposed at few locations in Thuringia and is very diverse in terms of iron-rich minerals (*Seidel, 2003*). The standard deviations (Table 2) of the other units are overlapping, which means that it will be impossible to distinguish the different units only by using magnetization models, especially considering the more or less layered structure in the study area.

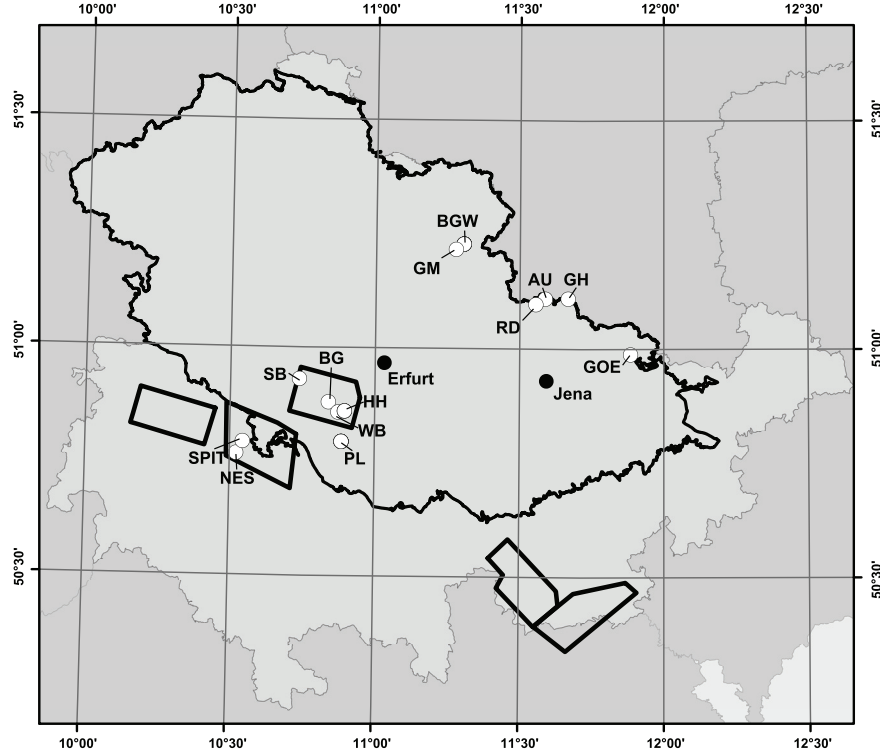


Figure 5.11: Location of sampling sites of susceptibility measurements in Thuringia performed during this study. Abbreviations of the different sites (white circles) are given in Table 3.

5.4.4 Acquired FTMG data

Ohrdruf survey: The derived tensor component G_{zz} of the complete survey area "Ohrdruf" interpolated onto a 50×50 m grid (see section 4.1.5 for interpolation details) is shown in Fig. 5.12. Maps of the other four tensor components, the total magnetic intensity and topography with flight lines are available in Appendix B. To visually enhance the faint signals in this area, the color range of the gradient maps was clipped to ± 0.125 nT/m using a linear scale. Minimum and maximum values of the measured gradients reach -2.8 and 8.8 nT/m, respectively. White areas are gaps in the data coverage, usually due to settlements or industrial areas, which were spared out during surveying. Other disturbances, e.g. power-lines, highways and railways, were removed during post-processing (see section 4.1.4). These gaps are usually smaller and therefore do not appear in the map because of the interpolation radius of 150 m. The southern part of the survey area shows only low signal variations, whereas in the northern part some faint structures become visible. The black lines in Fig. 5.12 represent the location of known faults (*TLUG, 2003*) of the *Eichenberg-Gotha-Saalfeld* fault zone. A correlation of the location of faults and structures in the mapped magnetic

Table 2: Susceptibility values from selected units in Thuringia. The Upper Buntsandstein (*) values were taken from *Scheibe et al.* (2010). The sample locations are scattered around the complete Thuringian Basin, assuming only little variations in magnetite content within the same geological unit between different locations. A more detailed overview of the different measurements is given in Table 3. The locations of the sampling sites are given in Fig. 5.11.

Geological Unit	Samples	Sampling sites	Median [SI]	σ [SI]
Middle Keuper	112	13	0.60×10^{-4}	0.57×10^{-4}
Lower Keuper	22	2	3.25×10^{-4}	2.78×10^{-4}
Upper Muschelkalk	16	2	0.35×10^{-4}	0.50×10^{-4}
Middle Muschelkalk	46	6	0.55×10^{-4}	0.28×10^{-4}
Lower Muschelkalk	123	16	0.40×10^{-4}	0.18×10^{-4}
Upper Buntsandstein*	2	n.a.	1.10×10^{-4}	n.a.
Middle Buntsandstein	11	1	0.30×10^{-4}	0.23×10^{-4}
Lower Buntsandstein	7	1	0.40×10^{-4}	0.13×10^{-4}
Zechstein	5	1	0.30×10^{-4}	0.04×10^{-4}

gradients, i.e. lineaments, is almost nonexistent. In the southern part, the standard deviation of the measured gradient along lines with no visual magnetic signal is about $60 \text{ (pT/m)}_{\text{PP}}$, which can be interpreted as average noise floor for this operation. Thus, most of the detected magnetic signals are close to the estimated noise level of the data set. Stronger anomalies with longer wavelengths are visible in the north-west of the survey area. This study focuses on the anomaly in the green box in Fig. 5.12. The full gradient tensor and the total field anomaly (TFA) of this subset are shown in Fig. 5.13.

Fig. B.7 in Appendix B shows the TFA of the "Ohrdruf" area interpolated on a $50 \times 50 \text{ m}$ grid (see section 4.1.5). The comparison of the TFA map of Thuringia (Fig. B.9) (*Scheibe et al.*, 2010) and the TFA of "Ohrdruf" does not show any clear correlation. Most structures in the total field map of Thuringia are caused by the magnetized basement, i.e. the Mid German Crystalline High (*Gabriel et al.*, 2011). Magnetic anomalies along the EGSFZ are not visible in both maps. However, in Fig. B.7 a general trend towards slightly higher values north of the fault zone is visible. Smaller features are not visible, since the TFA map of Thuringia is interpolated on a $250 \times 250 \text{ m}$ grid.

Siebleben study site: Fig. 5.13 shows the measured FTMG and the TFA data set of the "Siebleben" study site interpolated on a $20 \times 20 \text{ m}$ grid. The shown anomaly is the most prominent magnetic feature in the complete "Ohrdruf" area. The color range in Fig. 5.13 was clipped to $\pm 0.25 \text{ nT/m}$ for the magnetic gradients and -20 to 40 nT for the total field anomaly. The main magnetic anomaly is striking from NNW to SSE parallel to the *Eichenberg-Gotha-Saalfeld* fault zone (Fig. 5.5), but approximately 500 m north of the mapped main normal fault (EGSFZ- β in Fig. 5.5). The anomaly covers about 1.5 km in strike direction and is approximately 750 m wide. The strongest amplitudes ($|G| = 2 \text{ nT/m}$) were observed in the G_{zz} , G_{xz} and G_{yz} components. The

horizontal components G_{yy} and G_{xy} show the lowest signal amplitudes, which indicates a magnetization mainly parallel to Earth's magnetic field direction. Inclination and declination values of the survey area during the acquisition time were approximately 66° and 2° , respectively. A smaller magnetic anomaly and a shorter wavelength, with a high signal amplitude is located at the southern end of the main anomaly. The north-western part of the area is spared out due to the small village "Siebleben" (gray area in Fig. 5.13), after which the study site was named.

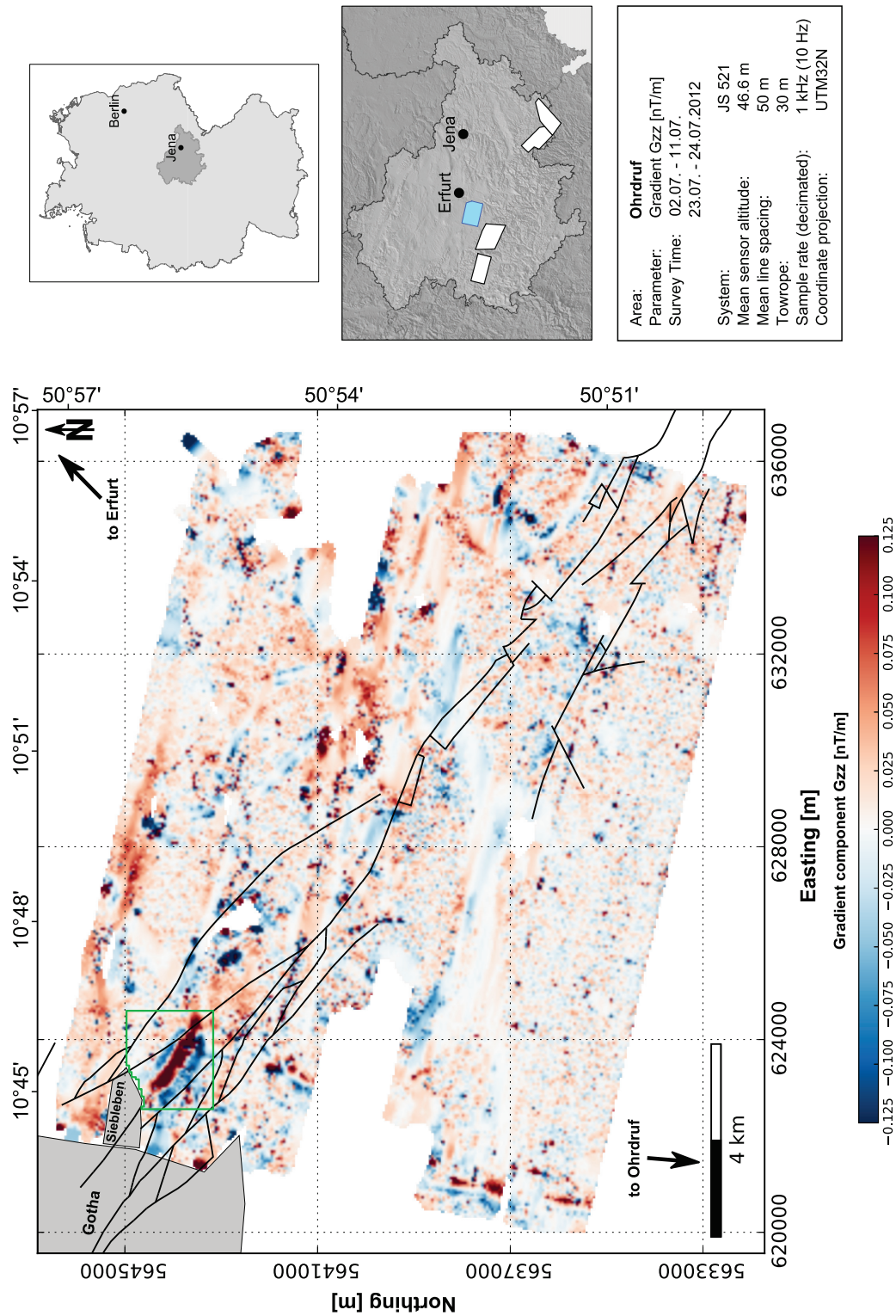


Figure 5.12: Gradient component Gzz of the "Ohrdruf" area. Black lines indicate the location of the EGSFZ in the published geological map (TLUG, 2003). The green polygon in the north-west marks the detailed investigation area "Siebleben" (see Fig. 5.13). The village "Siebleben" and town "Gotha" are denoted by gray areas in the north west.

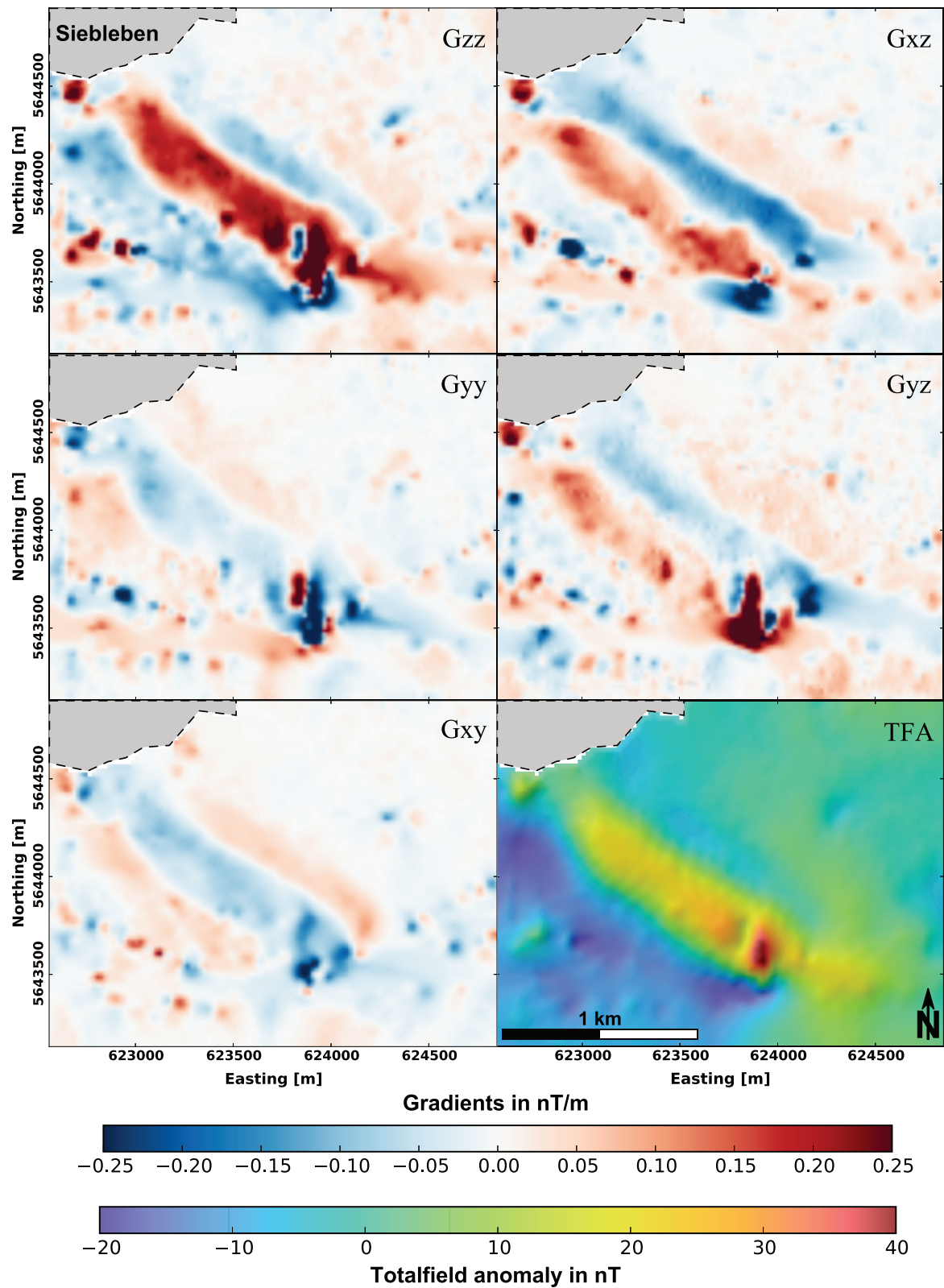


Figure 5.13: Full magnetic gradient tensor (G_{zz} , G_{xz} , G_{yy} , G_{yz} and G_{xy}) and total field anomaly of the "Siebleben" study area. The outline of the village "Siebleben" is marked by the gray area. Coordinates are given in the UTM32N projection.

5.4.5 Inversion results of FTMG and resistivity data

FTMG Inversion: Horizontal slices through the final magnetization model are depicted in Fig. 5.14 (eastward and northward magnetization) and in Fig. 5.15 (downward and induced magnetization). Vertical slices in north-south direction are shown in Fig. B.11. The scale for all the figures is clipped to ± 0.05 A/m and 0 to 15×10^{-3} SI units for the calculated induced magnetization. The eastward component of the magnetization vector shows the lowest amplitude, whereas the downward and northward components show similar, but somewhat higher, values. The maximum of magnetization is located in an elevation of approximately -50 m, i.e. about 200 m beneath the surface. Below -200 m the strength of the magnetization decreases, but a vertical smearing to greater depth is still visible. As expected from the mapped magnetic gradients, the zone of higher magnetization is elongated in NW-SE direction. The main zone is in its center approximately 100 m wide. But because of the used inversion method and discretization, the exact extent can only be estimated. The strong positive magnetization in the downward component is accompanied by two weak negative zones. This behavior was observed for all models and is strongly depended on the regularization technique. Using the combination of minimum-norm (*mn*) and minimum-support (*MS*), as explained in section 5.4.2, reduces the amplitudes of these negative magnetized zones. However, different combinations of these inversion parameters have been tested, with mostly similar results, i.e. magnetization amplitudes and recovered structures. Thus, the presented model is considered to be robust.

The vertical slices shown in Fig. B.11 also reveal that the zone of higher magnetization is more or less vertical with a slight dip towards north east. Additional slices perpendicular to the anomaly and along geological cross sections are shown in Fig. 5.16 and Fig. 5.17 in panel RIII.

ERT sections: The inversion results of both ERT profiles C and D can be found in Fig. 5.16 and Fig. 5.17 (RIV). Both profiles show low electric resistivities ranging from 10 to 75Ω m. Up to an elevation of approximately 200 m resistivities lower than 25Ω m are dominant. At greater depth, higher resistivities are present, but also a stronger lateral variation. Both profiles show a zone where the lower resistivities extent to greater depths. In profile C, this zone is around profile meter 1600 m to 1900 m and in profile D between 1550 m to 1700 m. The location of the main normal fault of the EGSFZ (EGSFZ- β), marked by the black lines in Fig. 5.5 and in the map RI of Fig. 5.16, coincides with the shallow lateral resistivity variation at the location (1) in profile C (Fig. 5.16 RIV). The lower parts of both ERT sections shown in Fig. 5.16 and Fig. 5.17 are overlain by the coverage of the ERT measurements in order to represent deeper regions with less reliability due to lower model resolution. Therefore, one should be careful with interpreting the lowermost part of the model.

5.4.6 Interpretation

Data and inversion quality: As stated earlier, the FTMG data set features very low noise values of about 60 (pT/m)_{PP}. This value was estimated by flying one survey line at a higher altitude, where geological and man-made signals are negligible. Due to the low magnetization of geological structures in the study area, the signal-to-noise ratio is not as good as expected. Nevertheless, the detected magnetic anomaly in the *Siebleben* area is significant, especially in the vertical and northern gradient components

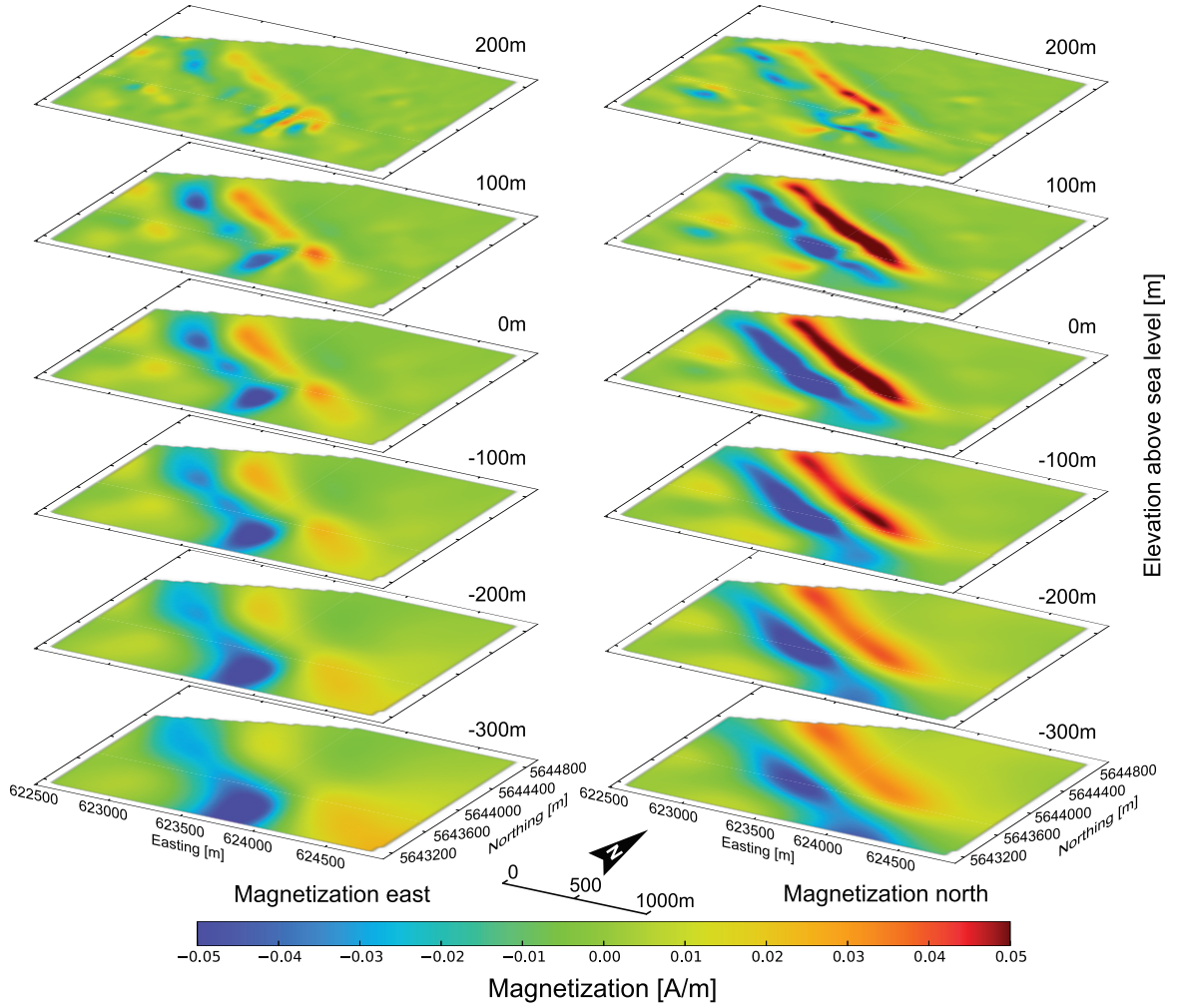


Figure 5.14: Horizontal slices through the final model of the FTMG data inversion. Left side shows the eastward magnetization and the right side the northward magnetization. The color scale is clipped to ± 0.05 A/m. Coordinates are given in the UTM32N projection.

(G_{zz} and G_{xz} in Fig. 5.13) as well as the TFA. Most distortions, characterized by large amplitudes and short wavelengths, were caused by man-made structures. While the majority of these signals were removed during processing, some of these signals are still observable in the data set. For example, the strong and shallow anomaly at grid location 623900/5643500 in Fig. 5.13 is probably caused by underground water pipelines, which could not be recognized by the flight operator or by examining aerial photographs. Remainders of these man-made magnetic anomalies are fairly easily visible across the complete data set, which is shown in Fig. 5.12 and in Appendix B.

The quality of the FTMG inversion was evaluated by comparing the observed magnetic gradient components and the calculated gradients at each observation point using the final inversion result. The differences between the observed and calculated gradient tensor components are shown in multiple histograms in Fig. B.10. It is clearly visible that misfits are below the estimated peak-to-peak noise of the observed data set. Thus, the data fit is of good quality and, despite the fact that a homogeneous starting model was used, the final model can be considered as a valid model.

The ERT data set shows very good signal-to-noise ratios, mainly because of the good coupling of each individual electrode with the ground due to the very low resistivities at the surface. The two models shown in Fig. 5.16 and Fig. 5.17 (RIV) have a relative

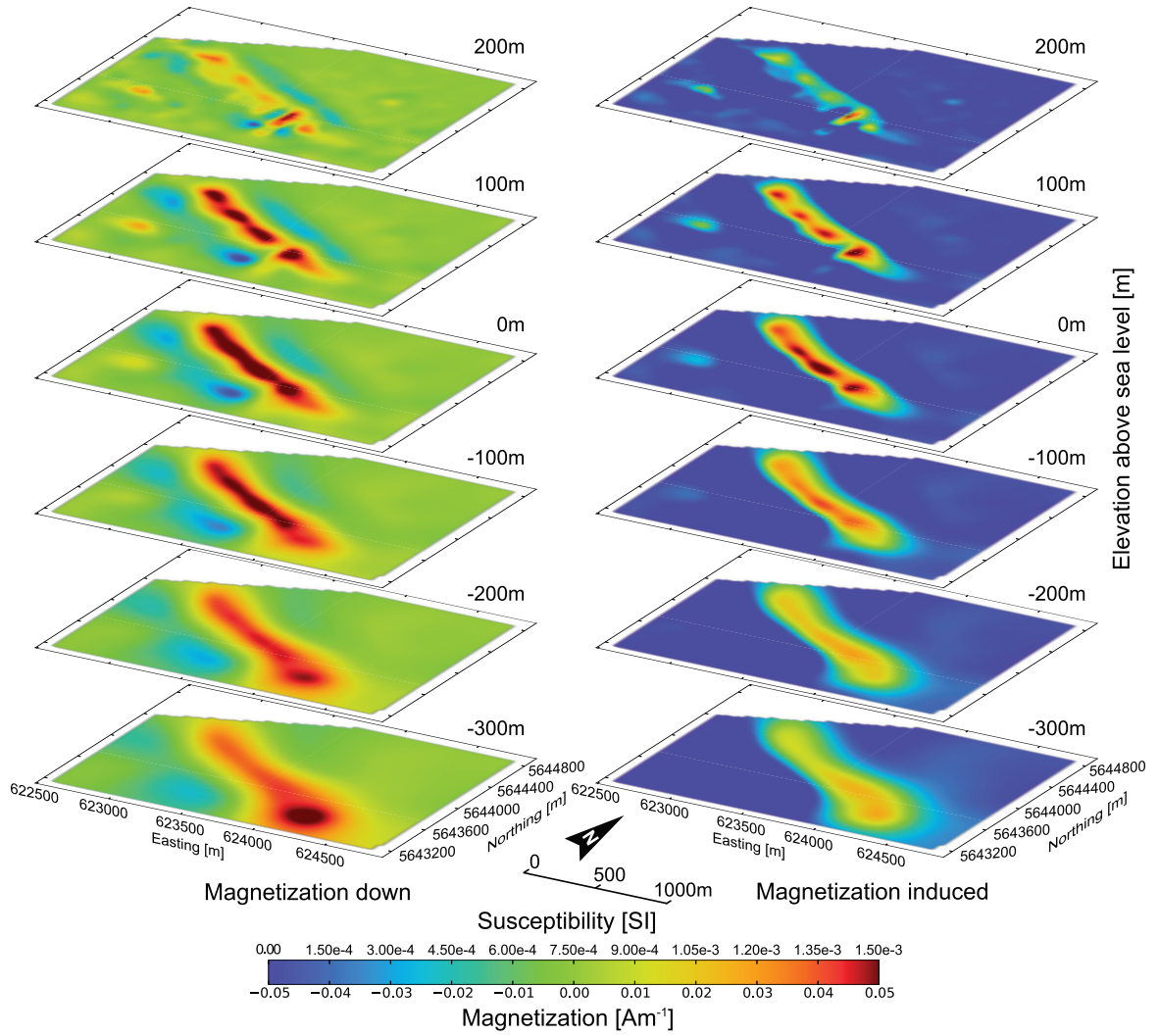


Figure 5.15: Horizontal slices through the final model of the FTMG data inversion. Left side shows the downward magnetization and the right side the calculated induced magnetization. The color scale is clipped to ± 0.05 A/m and 0 to 15×10^{-3} SI units for the calculated induced magnetization. Coordinates are given in the UTM32N projection.

root-mean-square misfit of 3.9 % for profile C and 4.7 % for profile D. Considering the length of the profiles and the number of electrodes used in this survey, these misfit values are very low. Hence, it can be concluded, that these two models are of good quality, even though only homogeneous starting models were used here as well.

Interpretation of FTMG Maps: The magnetic anomaly at the *Siebleben* study site is more than likely linked to the EGSFZ. This can be deduced from the coinciding strike direction of the anomaly and the fault zone as well as its location in the direct vicinity 500 m north of the main normal fault (EGSFZ- β).

From the wavelength of the magnetic anomaly, the source depth can be estimated to be around 100 m beneath the surface, with a possible greater extension in depth. Most smaller anomalies, especially those ones with a higher amplitude, are linked to man-made structures.

By examining the different gradient tensor components, a strong induced magnetization component is expected, or at least a magnetization in parallel to the Earth

magnetic field. Considering the fact, that mostly carbonate sediments with a low magnetite or hematite content are present, the only expected type of remanent magnetization could be depositional remanence (DRM). However, due to the dominant induced part, the remanence is either very weak or non-existent. Thus, possible remanent magnetization of the rocks in this area can be neglected.

Interpretation of FTMG inversion model and ERT sections: In order to jointly interpret the results of the ERT sections and the magnetization model two geological cross sections¹⁶ (*Malz et al.*, in prep.) are presented in relation to the other data sets in Fig. 5.16 and Fig. 5.17. The geological sections are derived from cross section balancing using drilling information from outside the study area as well as surface geology from published geological maps (*TLUG*, 2010). The combination of the results from the FTMG inversion, the ERT sections and geological cross sections lead to the following interpretations:

I. Due to *Quaternary* coverage and no available drilling information in the study area, the deeper structure of these geological models is not well supported. Nevertheless, the location of the main normal fault (EGSFZ- β) seems to be detected by the ERT profile C (see Fig. 5.16 R IV) at location (1). No magnetic anomaly has been detected at this location. The main magnetization anomaly however is located about 200 to 400 m north of EGSFZ- β . Hence, the source of the magnetization cannot be found in the fault plane of EGSFZ- β .

II. The inversion of the FTMG data set supports the initial observation of a dominant induced magnetization and negligible remanence. The estimated depth of the magnetization anomaly fits the initial estimation of approximately 150 m beneath the surface, too. Comparing the susceptibility of the induced magnetization of up to 1.5×10^{-3} SI units with the measured values of sediments in the study area (see Table 2), this structure cannot be caused by one of these geological units. Additionally, the steep dipping angle of the magnetized structure in the model and the proposed layered geology in the geological cross sections as shown in row RII in Fig. 5.16 reveals fundamental discrepancies. The only geological unit, which has a higher average susceptibility is the *Lower Keuper* (*ku*). As mentioned in section 5.4.3, this unit is known to have local iron-rich concretions (*Seidel*, 2003). Unfortunately, the *Lower Keuper* is only partially exposed at a few locations. Thus, the structure, amplitude and depth of the anomaly can possibly be explained by a locally higher magnetization in the *Lower Keuper*. This explanation however demands steep dipping angle of the *Lower Keuper*, or a process that leads to a more or less vertical enrichment of the higher magnetized minerals.

III. Both ERT sections (C and D) also reveal lateral variation in resistivities at location (2) and (3) in Fig. 5.16 and Fig. 5.17 (RIV). The location of the magnetization anomaly coincides with these lateral resistivity variations.

These three interpretations: **I.** confirmation of the EGSFZ- β location, **II.** structure and possible properties of the magnetization source and **III.** correlation of deep resistivity variations and the occurrence of the higher magnetization lead to several conceptual models, which will be outlined in the following.

¹⁶personal communication A. Malz

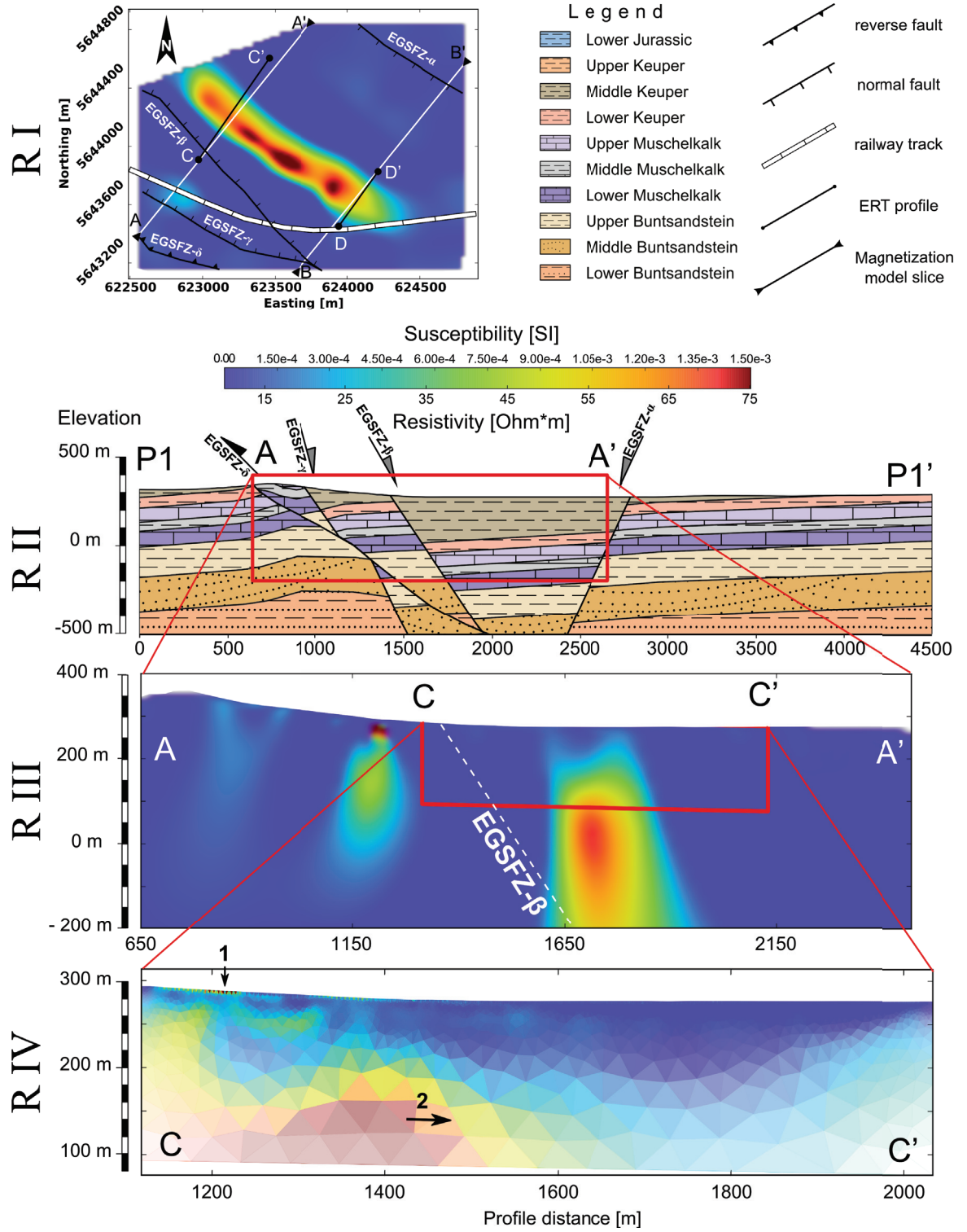


Figure 5.16: Position of magnetization anomaly in relation to the ERT profiles and the given geological cross sections (pers. comm. A. Malz). RI: Depth slice at elevation 0m through the susceptibility model with overlain fault locations and the railway track from Fig. 5.5 for better orientation. Coordinates in this map are given in the UTM32N projection. RII: western geological section along the white line in the map. The full extent of this profile (P1-P1') is marked in Fig. 5.5. RIII: Vertical slice through the susceptibility model along profile A-A'. RIV: ERT section C-C'. The different branches of the EGSFZ are marked by EGSFZ- α to EGSFZ- δ in the vertical slices and the map.

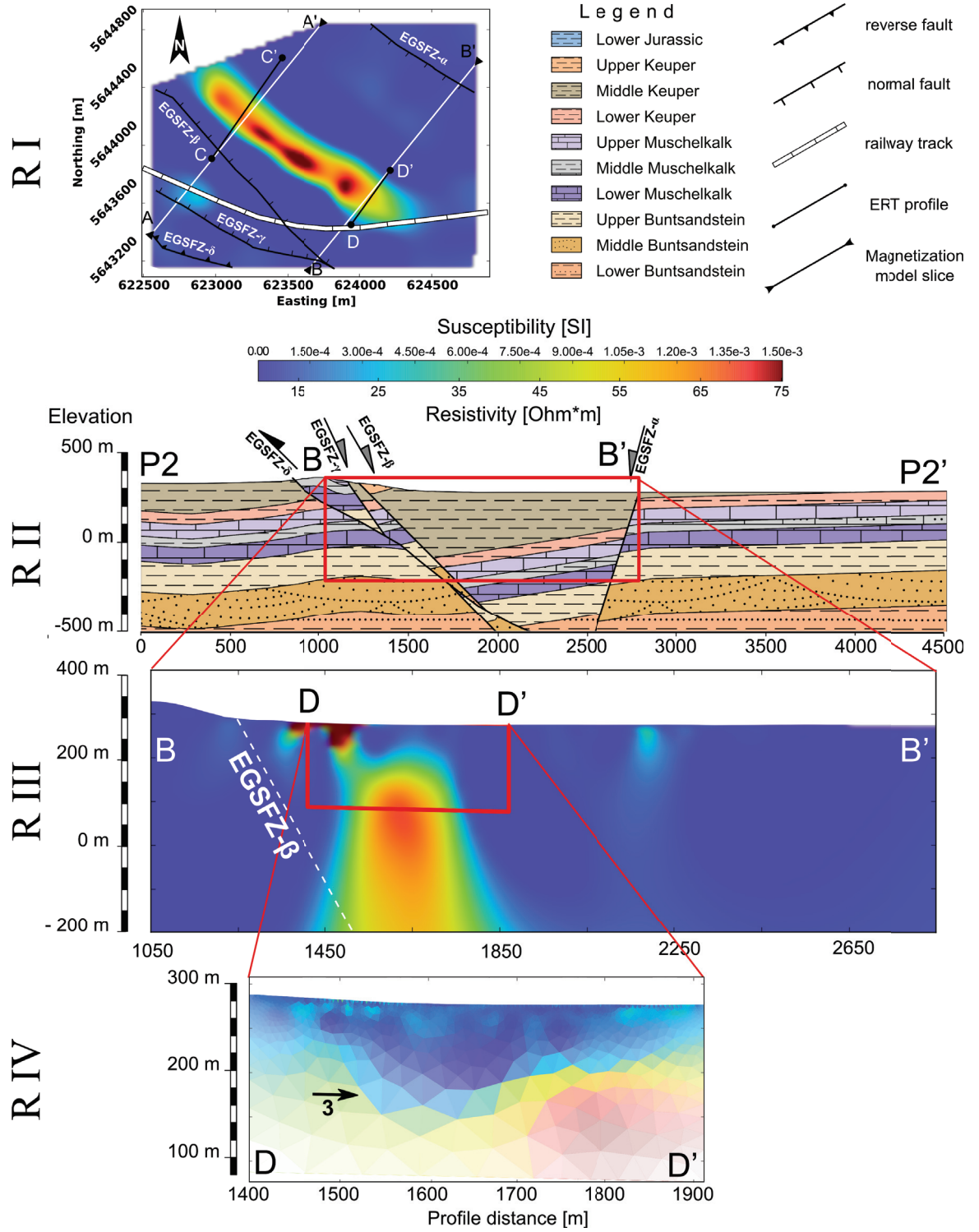


Figure 5.17: Position of magnetization anomaly in relation to the ERT profiles and the given geological cross sections (pers. comm. A. Malz). RI: Depth slice at elevation 0 m through the susceptibility model with overlain fault locations and the railway track from Fig. 5.5 for better orientation. Coordinates in this map are given in the UTM32N projection. RII: eastern geological section along the white line in the map. The full extent of this profile (P2-P2') is marked in Fig. 5.5. RIII: Vertical slice through the susceptibility model along profile B-B'. RIV: ERT section D-D'. The different branches of the EGSFZ are marked by EGSFZ- α to EGSFZ- δ in the vertical slices and the map.

Conceptual Models In the initial state of the study, different options for the cause of the magnetic anomaly were discussed: One of the first explanations was an old man-made drainage system. This however cannot explain the width of the magnetic anomaly of several hundreds of meters. Furthermore, it is more reasonable to assume that a drainage system would be most effective if it would lead towards the nearby creek in the north-west. Thus, the location and strike direction of the magnetic lineament is unlikely. Secondly, due to the drainage of the lake the occurrence of placer ores at the old shores as a possible source of the magnetization have been discussed. By careful consideration of the topography in Fig. 5.5 it is quite obvious that an old shoreline probably had a different shape than the magnetic lineament. Additionally, all the other areas in the vicinity that may belong to the shoreline do not show any anomalies. Therefore, these two models have been rejected at an early stage and have not been investigated in full detail.

The combination of the three interpretations I-III from the previous section revealed several discrepancies between the geophysical findings and the geological sections (see Fig. 5.16 and Fig. 5.17 RII). Thus, new conceptual models have been developed in order to explain the different aspects that do not fit into the initial expectations of layered sediments between EGSFZ- α and - β . To illustrate these concepts, profile A (Fig. 5.16 RII) is used as a reference and the suggested subsequent models are based on this simplified structure. The *Lower Keuper* is used as a reference layer and it is marked in all conceptual models in gray for a better orientation. The four conceptual models are presented in Fig. 5.18.

The first model in Fig. 5.18 ("reference model") illustrates the main problem with the given geological section. The *Lower Keuper* is by far the geological unit with the highest susceptibility and has the potential of localized, small scale enrichment of iron-rich minerals (Seidel, 2003). It is known that the *Lower Keuper* is rather shallow in the north and the south of the EGSFZ despite the *Quaternary* coverage in this area. Thus, a magnetic anomaly at the faults, where the *Lower Keuper* is shallow should be detectable. The measured anomaly is roughly at the position, where the *Lower Keuper* is the deepest. This means, that the *Lower Keuper* should have a significant lower susceptibility in this area, otherwise magnetic anomalies at the northern and southern normal faults would be present. On top of this, another source of the magnetization anomaly has to be identified.

The second conceptual model shown in Fig. 5.18 introduces an additional reverse fault including a higher magnetized zone at the location of the magnetic anomaly. Thereby, the *Lower Keuper* is lifted up to explain the depth and the steep dipping angle of the magnetization structure. In this model the *Lower Keuper* does not have a significant higher susceptibility. The source of the magnetization is explained by an enrichment of magnetic minerals around the newly introduced reverse fault. Thus, only a local magnetic anomaly is present. This would also explain that the anomaly ends rather abrupt in the north-west and south-east and does not continue along the other fault planes. Both applied geophysical methods do not provide information of depths greater than 300 m beneath the surface. Also, the process of mineral enrichment cannot be explained by the data. Hence, this model cannot finally be confirmed with the data available.

The third conceptual model shown in Fig. 5.18 contains multiple smaller fractures at the location of the higher magnetized zone ("model fractures"). These fractures could be formed during the compression phase during the *Late Cretaceous* up to the

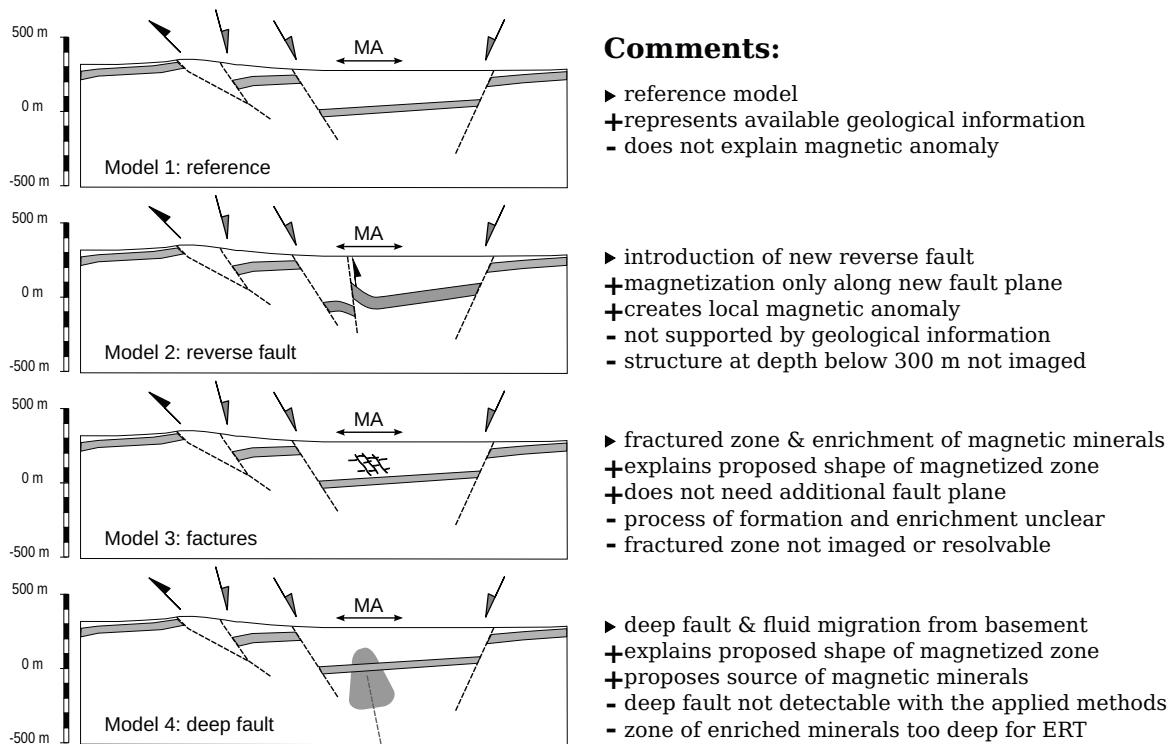


Figure 5.18: Illustration of conceptual models explaining the geophysical and geological findings at the "Siebleben" study site. The location of the measured magnetic anomaly is indicated by the arrow at "MA". **Model 1** ("reference model") shows the expected location of the *Lower Keuper* and the fault system simplified after the geological section in Fig. 5.16 (profile P1-P1' in Fig. 5.5). **Model 2** introduces a new reverse fault in order to explain the magnetic anomaly. **Model 3** uses a fractured zone to explain the geophysical data. **Model 4** is a combination of model 2 and 3 and introduces a deep fault which allows for fluid migration originating in the basement. The gray shaded area on top of the indicated fault plane illustrates the area of enriched high susceptibility minerals. On the right side, comments on the different models are given, including the main difference to the reference model (black triangle), the advantages (+) and disadvantages (-).

early *Paleogene* time (see section 5.2). Within the fractured area it is possible that minerals with higher susceptibility have been enriched, either by the solution of other material leaving these minerals behind, or due to precipitation of mineralized fluids. Due to the fact that a larger area can be affected by these fractures, the source of the anomaly signal can be expected closer to the surface. Thus, the shape of the measured magnetic anomaly and the resistivity variation can be explained. The benefit of this model is, that no new fault plane has to be introduced, which can hardly be explained by known geological cross sections. On the other hand, the available data sets provide no evidence for the mentioned processes for the creation of the fractures as well as enrichment of suitable magnetic minerals.

The fourth model ("model deep fault") proposes a fault in the basement, which also cuts through most of the sediments. The fault plane is sealed in its upper part, e.g. by re-mineralization of dissolved carbonates. In this model, mineralized fluids from the basement have migrated through most of the sediments and through fractures in the *Permian* to *Triassic* sediments, resulting in an enrichment of magnetic minerals in the upper part. Therefore, this model is a combination of model two and three. Due to the proposed migration of mineralized fluids through fractures and the sealing of

the fault plane in the upper part, a larger area (depending on the depth, of several meters to tens of meters) should be affected, similar to model three. Because of the fact, that the fault is deeper and reaches down to the basement, it is not possible to detect it with both applied geophysical methods. In this area the top of the basement is at a depth of more than one kilometer. This fault also does not need a lot of throw and therefore is easy to justify within the expected tectonic setting. It is also possible that one fault plane of the EGSFZ, e.g. EGSFZ- β , reaches into the basement and provides fluid pathways. In this case, no extra fault plane is needed to explain the model. The zone with increased content of magnetic minerals due to mineralization might also be too deep for the ERT sections and thus has not been detected. Due to the generally very low resistivities, it might also be hard to detect a zone of even better electrical conductivity.

Since no drilling information in this area is available up to date it is not possible with the acquired geophysical data to finally explain the magnetic anomaly in the study area. A future seismic study would provide more structural information and could clarify the exact location of fault planes at depth. Even though, the proposed models do provide some explanations of the discrepancies. The criteria that led to the different presented models are discussed in detail in section 6.2.1.

6 Discussion

Two different case studies were performed using an airborne FTMG instrument within the framework of the INFLUINS project, which had different research foci. These case studies were reported in detail in section 5.3 and section 5.4. In the first case study, the potential of airborne FTMG data to model structures with significant remanent magnetization using magnetization vector inversion was investigated. The used data set is from the center of the Thuringian Forest and featured clearly defined signals. The applied inversion technique is compared with other approaches in section 6.1.2. The second case study dealt with the interpretation of a shallow and weakly magnetized anomaly in combination with ERT data and geological cross sections obtained from geological maps, which supported interpretation. This data set is from south of the center of the Thuringian Basin and is dominated by low signal amplitudes, which made the interpretation challenging.

In this section, the findings from the two case studies are discussed. This includes a review of the advantages that are provided by the magnetic gradient tensor for magnetization vector modeling in the first case study, as well as a discussion of the various conceptual models presented in the second case study. At the end, the performance of the applied FTMG system is reviewed and various potential future improvements are considered. This includes technical aspects of integrating complementary methods as well as methodical improvements of the processing and inversion procedure.

6.1 Magnetization vector inversion on remanent structures in the Thuringian Forest

6.1.1 Discussion of the findings in the "Schmalwasser" survey area

In magnetic exploration, the combination of the magnetization direction and the orientation of the structure itself has to be modeled. In the past, mostly the susceptibility, treated as a scalar value, has been used in modeling and inversion to simplify this problem. Thereby, only induced magnetization was considered. In many cases this can be a viable assumption. However, when remanent magnetization is present, this approach can lead to significant misinterpretations.

It has been shown, e.g. by *Foss* (2006a), that the full magnetic gradient tensor has an increased sensitivity regarding the magnetization direction in comparison to the total field anomaly. Other studies have applied magnetization vector inversion in order to recover remanence, using either discrete bodies (*Pratt et al.*, 2014) or a voxel-based approach (*Lelièvre and Oldenburg*, 2009). Due to the limited availability of FTMG systems, mostly total field anomaly data has been used so far. In this study, remanent magnetization has been modeled using FTMG as well as TFA data sets in combination with a voxel-based inversion approach. The reconstructed magnetization models have been evaluated by paleomagnetic measurements on orientated rock samples. Even though, this modeling technique is easier to use than discrete body modeling, it has a significant disadvantage because of the very high amount of degrees of freedom. Hence, it makes the inversion highly under-determined. In addition, variations of the orientation and magnetization direction, can result in similar magnetic anomalies, which is often referred as equivalence principle. Fig. 6.1 shows some examples of magnetized structures, which result in equivalent anomalies. This also highlights

the relation between geometry and magnetization direction of an exploration target. Thus, it would be ideal if either the orientation of the structure or the magnetization direction is known prior to the inversion.

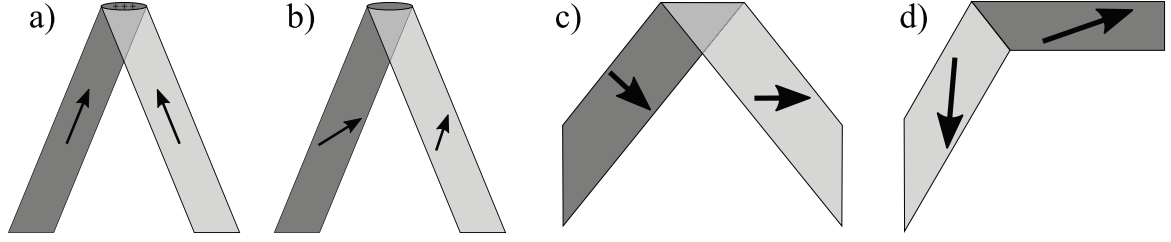


Figure 6.1: Simplified models representing equivalent magnetic sources. a) Infinite plugs, e.g. kimberlites, with axial magnetization. The light and dark gray plug will result in the same magnetic anomaly. b) Non-equivalent plugs. Similar geometry as in example a), but with tilted magnetization vector. Resulting magnetic anomaly of b) is not identical. c) and d) equivalent dipping 2D beds. The sheets in a) have an infinite depth extent, whereas in f) the dark gray bed extends infinitely towards the right. Examples a) and b) after *Clark* (2014); c) and d) after *Radhakrishna Murthy* (1985)

The mapped magnetic gradients in the survey area "Schmalwasser" show a very good agreement with the published geological maps. Different geological units can be easily distinguished only using the acquired FTMG data. The largest magnetic anomaly in the western part of the study area is related to a magmatic intrusive body (HD) and shows indications of remanent magnetization. This structure has been drilled in 1962 (*Andreas and Voland*, 2010) and therefore the thickness of 350 m and eastward dip direction of 30° to 45° are known. Besides the general structure, some smaller apophyses have been drilled, which are also mapped by the FTMG system. Some implications were made whether this structure has seen multiple intrusive phases (*Mädler*, 2009), which may have led to varying magnetic rock properties.

The inversion of FTMG data with five linear independent tensor components showed much better results than the TFA data inversion. The structures recovered in the FTMG model are much more compact and show very well defined contacts in direct comparison with the TFA model. In both models, the general dip direction of the HD has been reconstructed and the dipping angle correlates well with the known geological information. The FTMG model also showed signatures of very small structures less than 50 m wide, like the apophysis east of the HD. Since the apophyses are expected to be very thin, they are only represented by weak and shallow magnetizations in the model because of the smoothing behavior of the voxel-based inversion code.

Throughout the different inversion runs, it became very obvious that the FTMG inversion is characterized by much more consistent results, whereas the different resulting TFA models were strongly dependent on the regularization scheme. The usage of the same inversion strategy, namely the two stabilizing functionals mn and MS , led to strongly overfitted results for the model based on the TFA data. Thus, only mn regularization was used to avoid over-interpretations of the recovered structures. This choice may explain the difference in the compactness of the final TFA and FTMG inversion result. Due to the much smoother appearance of the TFA model, a body of larger volume represents the magnetized structure. This leads to the fact that the amplitude of magnetization of the main structure is lower in the TFA model compared to the FTMG result.

In order to evaluate the magnetization directions of the two models, paleomagnetic samples have been collected in two quarries in the study area. The measured magnetization directions scatter over a quite large range. This could have two reasons: As stated earlier, the HD may have been affected by multiple magma injections during formation, and therefore different magnetic rock properties may be present. The amount of acquired and investigated samples is still quite low. Due to sampling issues at one location, some samples had to be collected by using the block sampling method. This leads to a large number of specimens from one sample and therefore may bias the statistics.

However, the magnetization directions obtained from the FTMG model are in very good agreement with those of paleomagnetic measurements. The TFA model also shows nearly the same directions, but not as close as the FTMG model. The variation of the magnetization direction in these models can have several reasons. The main reason is the smoothing of the voxel-based inversion algorithm at sharp discontinuities. Thus, the magnetization directions in these zones sweep over a range of values. In order to get a reasonable comparison, volumes within the models close to the paleomagnetic sampling locations have been selected. The size and location of these volumes have been chosen purely empirically at the area with the highest magnetization in the models. This does not correlate exactly with the sampling locations and the results may change when a different volume is selected.

The separation of the NRM direction and induced magnetization is based on the basic assumption that the induced magnetization is in-parallel to the Earth's magnetic field. Additionally, the amplitude of the induced magnetization in the volume selected for comparison was assumed to be 0.86 A/m. This value was derived from the mean value of the rock samples. It is well possible that susceptibility varies within the dolerite intrusion. For a better separation of the two types of magnetization more susceptibility measurements at various locations or from borehole logging will be necessary. The more or less accurate fit to the NRM direction is caused by the fact that the induced and remanent magnetization of the HD structure are already almost perpendicular, as it can be seen in the paleomagnetic results (Fig. 5.9). Furthermore, it should be noted that this approach may fail in general, when anisotropic induced magnetization or demagnetization effects are present, because these directions will be treated as remanence instead. For this particular example, self-demagnetization effects can be neglected, since the measured samples are simply not sufficiently strong magnetized (*Clark, 2014*).

Nevertheless, the results presented show that voxel-based FTMG inversion yields much more consistent results, even when a very simple starting model is applied. The same structure may have been recovered solely using TFA data, but more constraints are necessary, i.e. a more detailed and complex starting model. This confirms the higher sensitivity of FTMG data for remanent modeling (*Foss, 2006a*).

6.1.2 Comparison with other studies regarding remanence determination

In section 5.3.1 an overview of different approaches for remanence determination from airborne magnetic data was given. Here, the results from the first case study in the framework of this thesis project are put in relation to those studies.

The application of 3D magnetization vector inversion (MVI) of TFA data started with the combination of different methods which aided a scalar-like inversion (*Li et al., 2010*). The inversion only using the amplitude of the measured TFA data alone showed

poor results in recovering the dip of a structure. It should be noted, that in the study of *Li et al.* (2010) the direction was assumed to be uniform in the magnetized volume. The dip information is mostly encoded in the phase information of the TFA data (*Li et al.*, 2010). Thus, the increased directional sensitivity (*Foss*, 2006a) of the magnetic gradient tensors can be beneficial, especially when the magnetization direction and the dip of a target structure is unknown.

One of the first voxel-based inversion algorithms used for MVI was presented by *Zhdanov* (2002). The code used in the framework of this thesis is based on that approach. Even though this code is capable of inverting the magnetization vector and using FTMG data, only examples showing susceptibility inversions have been presented (*Čuma et al.*, 2012). *Lelièvre and Oldenburg* (2009) presented a completely free magnetization vector inversion for TFA data. These authors also mentioned that an implementation of magnetic gradient tensor data sets would be easy to realize. They demonstrated the successful application of this inversion approach. For interpretation purposes, only the effective susceptibility, which is defined as the amplitude of the total magnetization normalized by the intensity of the Earth's field strength, was presented. This is a common way to illustrate MVI inversion results, since a compact geological structure is much harder to visualize using the three magnetization vector components. The scope of the study by *Lelièvre and Oldenburg* (2009) was to present a new implementation of MVI for data sets affected by strong remanence. Unlike the case study presented in this thesis, no detailed interpretation of the results and evaluation of the obtained magnetization directions by paleomagnetic studies was given.

The inversion code presented by *Ellis et al.* (2012) has been applied by *MacLeod and Ellis* (2013) to two study areas: The first one in Brazil with challenging conditions concerning the low magnetic latitude and background field strength. Thus, the induced magnetization is weak and the remanent part cannot be neglected. MVI showed a more reasonable result, even though the evaluation of the amplitude and directions was not presented. The second example is the very well studied *Black Hill Norite* in Australia. The MVI results showed a reasonable agreement with previously published values for inclination and declination. However, it is not always clear whether the total magnetization direction or the remanent contribution is presented in the study by *MacLeod and Ellis* (2013). Also, no information on the accuracy of the results was provided by these authors. One reason is, that their approach suffers from the same effects as the inversion results in this thesis (section 5.3.3), meaning the "sweeping" of magnetization directions at the edges of the magnetized bodies when the direction should change abruptly.

As mentioned before, the staged-inversion approach of *Foss and McKenzie* (2011) and the advanced approach of *Pratt et al.* (2014) offer the highest accuracy when the remanent direction is extracted from the total magnetization direction. These two studies show the best agreement between the recovered magnetization vectors in the models and the paleomagnetic results (*Schmidt et al.*, 1993; *Rajagopalan et al.*, 1993).

The combined approach of discrete body and voxel-based inversion presented by *Fullagar and Pears* (2015) showed promising results. Again, an inversion of FTMG data sets using this algorithm could provide additional sensitivity to recover the shape of the body and the magnetization direction. Unfortunately, FTMG data sets are still rarely available and thus most authors use TFA data sets. An important feature of this method is the possibility to include self-demagnetization effects, which can have a

great impact on the interpretation (*Clark et al.*, 2015). Including self-demagnetization and interactions between magnetized structures will however make the problem set highly non-linear and therefore increase the computational effort (*Fullagar and Pears*, 2013). The performance of FTMG data in scenarios with very high magnetization should be evaluated in the future.

In comparison of the approaches mentioned above, the case study presented in the framework of this thesis showed that the FTMG inversion provides better results compared to TFA inversions, mainly because the latter one showed more inconsistent results during the various inversions that have been done in order to find a reasonable magnetization model. This confirms that the increased directional information content of five linear independent magnetic gradient tensor components does help to recover shape, orientation and the magnetization vector of geological structures (*Foss*, 2006a). The evaluation of the inversion results with paleomagnetic measurements has shown acceptable agreements, even though the variance in directions and amplitudes of the modeled and measured magnetization vectors was relatively high.

6.2 Discussion of FTMG and ERT interpretations in the Thuringian Basin

6.2.1 Discussion of the findings in the "Ohrdruf" survey area

The presented "Ohrdruf" data set showed that the applied airborne FTMG system section 3.3, in combination with the introduced processing work-flow section 4.1, produces high quality magnetic gradient data with a low peak-to-peak noise of 60 (pT/m)_{PP}. The semi-automatic removal of man-made signals, e.g. 50 Hz from power lines, further significantly increases the quality of the data set and allows interpretation of anomalies close to densely populated areas.

In general, the "Ohrdruf" area is characterized by only weak magnetic anomalies, mainly due to the more or less horizontally layered strata and overall low magnetic rock susceptibilities in the Thuringian Basin. It can clearly be seen, that the complete area has almost no significant magnetic lineaments along the mapped EGSFZ, which means that only low susceptibility contrasts are present in the area. Nevertheless, the good data quality and performance of the FTMG system led to the discovery of low amplitude magnetic anomalies, for instance the most prominent anomaly in the NW of the "Ohrdruf" survey area at the "Siebleben" site.

This particular magnetic anomaly, represented by a lineament, is sub-parallel to the EGSFZ and was rather unexpected. It was investigated using the combined approach of interpreting the measured gradient maps, a voxel-based FTMG magnetization vector inversion, electrical resistivity tomography, and available geological cross sections (*Malz et al.*, in prep.). The ERT data set was acquired with the intention to image fault planes in the center of the investigation area, represented by varying resistivities. These could either be caused by local mineralization or due to increased porosity, both resulting in local change of resistivities. However, the ERT sections verified the location of the main normal fault of the EGSFZ (EGSFZ- β), which is hard to map at the surface due to the Quaternary coverage.

In order to explain the magnetic anomaly and the ERT data, four different conceptual models have been proposed in section 5.4.6. The first concept represents the available geological model, with the *Lower Keuper* as the geological unit with the highest susceptibility, as one possible source of the magnetization anomaly. Magnetized

layers with a vertical offset may produce magnetic lineaments in strike direction of the a fault zone (*Grauch and Hudson, 2011*). Since no magnetic lineaments were detected directly at the other fault planes, the *Lower Keuper* is most likely not the source of magnetization.

Due to the short wavelength of the anomaly, the depth is expected to be quite shallow, probably around 100 to 150 m below the surface. By suggesting an additional reverse fault, the *Lower Keuper* is lifted and becomes shallower. However, this model is highly unlikely, mainly because of two reasons: First, there is no geological evidence for an additional fault and second, the problem of the first model remains, which demands that magnetic lineaments should be present at the northern and southern fault planes as well. Thus, the "new" fault plane can only allow for an increased fluid flow and mineralization of magnetized minerals in its direct vicinity. Again, this is highly unlikely, because this process and the resulting magnetic signatures should be also observable at the other fault planes.

The third and fourth model offer more realistic explanations, even though they are speculative since no strong evidence can be derived from the available data. The third model explains the magnetic anomaly with a zone of smaller fractures filled with magnetic minerals. This may have the potential to create a relatively shallow magnetization anomaly, and spread out over a few tens of meters, thus creating a magnetic zone with the right dimensions to explain the detected anomaly. To create smaller fractures, either the pore fluid pressure has to be high caused by influx of fluids, or due to decreased lithostatic pressure by erosion. Since the area of interest is small, about a few hundreds of meters wide, the first option is much more reasonable. When a more widespread zone is affected, minerals with a lower susceptibility are sufficient to create the magnetic anomaly, which may fit the observed susceptibility values. Nevertheless, this conceptual model has the flaw that the source of the magnetic minerals or mineralized fluids is unclear. Because of the generally low resistivities in the study area and the limited resolution of the ERT methods applied, it is not possible to image individual fractures.

In the fourth model, the source of the mineralized fluids is located at greater depth. In this model a deep fault is suggested, which allows fluids to migrate from the basement, assuming that these are highly mineralized and contain magnetic minerals. It is reasonable to assume that the upper part of the fault plane is sealed by carbonates and does not allow for fluids to migrate. Thus, the zone around the fault plane is impregnated by magnetic minerals precipitated from these fluids. Now again, this is highly speculative, since neither the fault plane nor the source of the magnetization is clear. However, this model eliminates the problems of models one and two.

At this point, no clear explanation of the magnetic anomaly, the dipping magnetized structure or the lateral variation of the resistivity in greater depth can explain the available geological model, or vice versa. Thus, additional data are necessary. Most beneficial would be reflection seismic profiles across the anomaly, to get a structural image. Furthermore, the volume of increased magnetization can be directly sampled by conducting a drilling campaign in this area. This may provide insight in the processes that caused the magnetic anomaly.

6.2.2 Comparison with other studies investigating sedimentary rocks

In section 5.4.1 an overview of different studies using magnetic exploration and other geophysical methods in order to investigate sedimentary rocks on various different

spatial scales was given. Here, some of these studies are compared to the findings of the case study presented in section 5.4.

In contrast to regional magnetic investigations in sedimentary basins, where faults within the basement (*de Castro et al.*, 2014) or intra-basinal faults (*Grauch*, 2001) are analyzed, is this thesis focused on a much smaller scale (tens to hundreds of meters). Thus, a zone of increased magnetization within the sediments must be present. Two different processes can be considered in order to explain the occurrence of this anomaly: Either, a magnetization contrast caused by a sub-vertical offset of sediment layers with different magnetic properties (*Villani et al.*, 2015) or enrichment of minerals with higher susceptibility or remanence. However, remanent magnetization has been ruled out as a possible source in this particular study area.

The study by *Villani et al.* (2015) analyzes a structure which can be described by the simplified models of *Grauch and Hudson* (2011), which means a vertical offset of a layer with a higher susceptibility. The magnetic anomaly presented in the "Siebleben" case study of this thesis is probably caused by another geometry. As pointed out earlier, the main reason for this is the lack of magnetic lineaments at the other fault branches of the EGSFZ north and south of the detected magnetic anomaly. The most favored explanations are the conceptual models three ("fractures") and four ("deep fault"), discussed earlier in section 6.2.1. Both models propose a zone of enriched magnetic minerals as a possible magnetization source for this local magnetic anomaly. Unfortunately, there exist only a few studies, analyzing magnetic anomalies caused by shallow enrichment of magnetic minerals. *Egger et al.* (2014) interpreted magnetic data sets, mainly along profiles, in the vicinity of active hot springs. These authors make more effort in applying electromagnetic methods, which are probably a better tool in order to investigate active fluid movement along fault planes. However, active processes like hot geothermal fluids are not actually present in the "Siebleben" area. Additionally, no such process has been reported in the literature for the southern part of the Thuringian Basin.

Without a proper understanding of the basic subsurface structure in the "Siebleben" area, a final explanation of the magnetic anomaly cannot be given without major speculation. Thus, the presented joint interpretation of FTMG inversion and ERT sections should be re-evaluated when a seismic study has been conducted in the future. A seismic survey should be designed to image the upper 1000 m on a N-S profile perpendicular to the magnetic anomaly. Furthermore, it should cover the faults EGSFZ- α , β and $-\gamma$. A reflection seismic profile would provide reliable information on the fault locations and layered structure in the central part of this study area.

6.3 Advantages and future perspectives of airborne FTMG

It has been shown in both case studies, that the applied airborne FTMG system is capable of detecting very weak magnetic anomalies and yields several benefits in terms of remanence modeling and mapping. However, FTMG systems are up to date rarely used in airborne geophysical exploration, mainly due to the limited availability of these systems (*Rompel*, 2009). For most purposes, conventional total field magnetometers are used. These are often also mounted in a hardware-gradient setup, like the commercially

available systems from *Geometrics*¹⁷, *GEMSystems*¹⁸, *NRG*¹⁹ and *XCalibur*²⁰. Up to now, only one comparable airborne magnetic full tensor gradiometer was developed at CSIRO in Australia (*Leslie et al.*, 2007). Unfortunately, there is no real in depth comparison of the two FTMG systems yet. Only a few data samples along single flight lines of the CSIRO FTMG system have been published, thus a real evaluation is not possible.

Besides the presented advantages, it has been shown by several other authors that FTMG also yields potential benefits regarding interpolation between flight lines (*FitzGerald and Holstein*, 2006) and source localization methods like the normalized source strength approach (*Beiki et al.*, 2012). Both methods benefit from the directional information provided by the magnetic gradient tensor components. Most of the published examples involve the transformation from measured TFA data into the magnetic gradient tensor, which is not necessary with the availability of the FTMG instruments. This also applies to the special case reported by *Clark et al.* (2015) where the measured total field anomaly has to be corrected and a directly measured magnetic gradient tensor would be valuable.

Basically, most of the advantages of the FTMG system should also be available when the magnetic field vector \mathbf{B} is measured directly. As pointed out in section 3.2, this is not possible with the current generation of analogue-to-digital converters and the limited accuracy of the inertial units. If it would be possible however, the only advantages provided by the magnetic gradient tensor are the better spatial resolution of shallow and closely spaced anomalies due to the signal amplitude decay with distance of $1/r^4$ for a magnetic dipole. Hence, a desirable magnetometer system should acquire the magnetic field vector \mathbf{B} as well as the magnetic gradient tensor $\hat{\mathbf{G}}$. In this case, the balancing of the gradiometers during the processing will also benefit from the added magnetometers (section 4.1.2).

The second case study (section 5.4) showed that the investigation of basin structures with the FTMG instrument is not beneficial, mainly because of the generally lower magnetization contrasts and the more or less horizontally layered structures. In this scenario, a combination of electrical and magnetic methods has been shown to be more valuable. Thus, future improvement of the FTMG system can lay in the integration of electromagnetic measurements. This can be realized in various ways:

I The first option is to measure magnetic fields at a high sampling rate. Signals below 10 Hz are considered to be static, similar to the measurements performed during this study. Above 10 Hz, the measurements are within the inductive regime, thus the electrical conductivity of the subsurface can be explored. One method that is using these effects is called audio frequency magnetics (AFMAG²¹) (*Ward*, 1959; *Lo and Zang*, 2008).

II The second option is to incorporate an active electromagnetic (EM) transmitter and possibly an EM receiver. If integrated correctly, both systems can be operated in parallel and do not interfere with each other.

¹⁷www.geometrics.com

¹⁸www.gemsys.ca

¹⁹www.nrgex.co.za

²⁰www.xagsa.com

²¹often also referred as ZTEM (Z tipper axis electromagnetic)

III When EM and magnetic data sets are available, a joint inversion of these two data sets will lead to combined conductivity and magnetization models of the exploration target. This approach also yields the option to be used as an "active source magnetics" system as suggested by *Clark (2014)*. It offers the possibility to directly infer susceptibility values up to a certain depth depending of the conductivity of the subsurface. It has already been shown that susceptibility information can be gained from classical airborne electromagnetic measurements (*Zhang and Oldenburg, 1999; Zhdanov and Pavlov, 2001*).

The last option can provide the constraints necessary for a more accurate remanence modeling, which has been presented in the first case study (section 5.3). It should be noted, that the implementation of an active electromagnetic system may also be sensitive for induced polarization effects (*Kratzer and Macnae, 2012*). This can introduce further opportunities and challenges for the system, but this topic goes beyond the scope of this study.

Another lesson that has been learned from the two case studies is the need for complex 3D starting models. In both inversion processes, only very simple models were used. Considering the impact of the different regularization schemes, which take the starting model directly into account, the importance of a well defined model should not be underestimated. This highlights that an easy to use 3D model generator, similar to commercially available products like *IGMAS+*, *GoCAD* or *Intrepid GeoModeller*, should be used in order to generate more sophisticated and complex 3D magnetization models based on available geological maps and cross sections. Thereby, more strong constraints can be applied, i.e. paleomagnetic measurements or susceptibility values. *Lelièvre et al. (2012)* extended this idea and suggested that a shared model discretization for geophysical, geological and geochemical models should be used in order to get the best constrained joint interpretation of the exploration target. This requires a more complex discretization of the model, for instance the usage of tetrahedrons (*Furness, 1994; Holstein, 2003*). It results in some positive side effects: Firstly, the topography can be better implemented in the model and the error introduced by the dipole approximation in this study (see section 4.2.2) can be avoided. Secondly, the number of cells can be reduced by increasing the cell size with depth, which can speed up the inversion process significantly without losing model resolution.

In the "Schmalwasser" case study, it became evident that more paleomagnetic measurements or more susceptibility values are necessary to properly constrain the starting model. Samples from deeper units are hard to acquire and paleomagnetic samples are expensive and time consuming to collect. Thus, the following methods should be evaluated for their feasibility to estimate the magnetization direction: In order to measure the magnetization direction in the field, *Schmidt and Lackie (2014)* presented a device based on the methods suggested by *Breiner (1973)*. This device consists of a fluxgate magnetometer and a pendulum arrangement, where the rock sample is placed. By swinging the pendulum with the sample, a transient signal is measured with the fluxgate magnetometer. When this method is repeated with the rock sample in the reversed position, the magnetic moment of this sample can be calculated and the induced and remanent contributions of the total magnetization are separated. Even though it is less accurate than classical paleomagnetic analysis, it allows to quickly measure many samples directly in the field. An analytical approach to deduce the magnetization direction from mapped magnetic field data was proposed by *Helbig*

(1963). This may not be as accurate, but it would provide an independent estimation of the direction from units at greater depth, that can otherwise only be sampled by using borehole geophysical methods. However, this method can be improved using paleomagnetic data bases, e.g. pole wander tracks (*Merrill et al.*, 1998), in order to constrain the estimate of the magnetization direction (*Pratt et al.*, 2014). Thus, the application of these approaches for the evaluation of the recovered magnetization directions or for constraining the inversion might be beneficial and should be considered in future.

7 Conclusions and Outlook

In this thesis, the application of a newly developed airborne full tensor magnetic gradiometry system in two different geological scenarios was presented. The data sets used throughout the study were acquired in 2012 and 2013 within the framework of the multidisciplinary project INFLUINS. In total, airborne FTMG data was collected in five survey areas in the Thuringian Basin, Forest and Highlands. The main goal was to detect magnetic lineaments along fault zones within the sedimentary basin, to investigate the transition zone of sediments and crystalline basement as well as to analyze the exposed basement in selected areas. Prior to these airborne surveys, susceptibility values from a representative selection of geological units were collected. These measurements suggested a general low magnetization in the Thuringian Basin. Nevertheless, magnetic anomalies along the major fault zone EGSFZ were expected.

Processing of the data sets led to low noise 2D maps of the five linear independent magnetic gradient tensor components, the magnetic field vector components and total field anomaly data. Post-processing included semi-automatic removal of man-made noise sources. Depending on the survey area, this processing step was essential to get a high-quality data set. Noise values of about $60 \text{ (pT/m)}_{\text{PP}}$ were achieved for the data used in this thesis.

Two different case studies of airborne FTMG surveys were presented: In the first case study, the advantages of FTMG over conventional TFA data sets in areas with significant remanent magnetization were investigated. Both data sets were inverted using the voxel-based magnetization vector inversion algorithm introduced in section 4.2. The results were evaluated using paleomagnetic samples from an intrusive body that exhibits the remanence. In the second study, the FTMG data was applied in sedimentary basin exploration to map fault related magnetic lineaments. The unexpected discovery of a small scale intra-basinal magnetic anomaly was investigated further using complimentary ground based ERT data sets and other available geological information.

7.1 Modeling FTMG data affected by remanence in the Thuringian Forest

The main purpose of this case study was to compare conventional TFA and FTMG data in the inversion process. The focus was to highlight potential benefits of FTMG data in magnetization vector inversion, when the target exhibits a significant remanence. The data set was part of the "Schmalwasser" survey area in the center of the Thuringian Forest. The acquired data was characterized by relatively high noise due to tough environmental conditions, i.e. windy days and rough topography. The magnetic anomalies detected during this survey are much stronger than in the second case study and they correlate quite well with the known geological information. To evaluate the quality of the inversion results the geometry and magnetization direction of the target had to be recovered properly. The findings of this case study are summed up subsequently:

- a) The mapped magnetic gradient tensor components showed clearly defined anomalies. Most of these anomalies are in good agreement with available geological maps of the study area.

- b) The majority of the lineaments are caused by transitions between intrusive rocks in the surrounding rhyolites and conglomerates in the study area. Some of the smaller magnetic anomalies were correlated with apophyses of the dolerite intrusive body (HD).
- c) HD intrusion shows clear indications of remanent magnetization, e.g. EW dipole in the TFA maps. The magnetization direction can be estimated from the five magnetic gradient tensor components. The magnetization vectors are pointing roughly in SW direction and are dipping steeply downwards.
- d) Paleomagnetic samples from two locations in the study area confirm significant remanence with a direction approximately perpendicular to the Earth's magnetic field and with a mean Königsberger ratio of 0.5.
- e) Inversion of FTMG and TFA data of the HD anomaly confirms geological information, i.e. the geometry of the intrusion with an eastward dipping direction and an approximate thickness of 350 m.
- f) The FTMG inversions produced more reasonable results with sharper contacts compared to the models based on the TFA data.
- g) Magnetization directions in the two inversion results coincide with the results from the paleomagnetic analysis. However, the FTMG inversion results are closer to the determined paleomagnetic directions.
- h) Differences in both models can either be caused by differences in the applied regularization or due to the higher directional sensitivity of the FTMG data set.

The reconstruction of the geometry and magnetization direction using the FTMG data set in this case study was successful. Only minor differences in the model and the geological information were observed. Throughout the various inversion runs, the FTMG data set resulted in more consistent models compared to the TFA data. Additional paleomagnetic samples might be necessary for a better evaluation, due to the relatively strong scattering of the magnetization directions obtained from the orientated rock samples.

7.2 FTMG in sedimentary basin exploration

The survey area "Ohrdruf", located near the center of the Thuringian Basin, showed the lowest noise values, but also only a few weak magnetic structures. Expected magnetic lineaments along the EGSFZ were not detected. This data set was strongly affected by man-made noise sources. The investigation in this area focused on the weak magnetic lineament in the "Siebleben" area. At this study site, ground based ERT data was obtained to support the interpretation. The analysis of these data sets led to the following findings:

- a) The magnetic anomaly is sub-parallel to the EGSFZ- β , which represents the main normal fault of the EGSFZ.
- b) The expected fault branches of the EGSFZ have not been detected by the airborne FTMG data. The interpretation of ground based ERT sections was necessary to confirm the location of EGSFZ- β , which was indicated in the ERT data by a shallow lateral resistivity variation.

- c) The mapped magnetic gradient tensor components suggest that the source of the anomaly is mainly due to induced magnetization. The inversion results of the FTMG data in this area supports this observation.
- d) The magnetization in the inversion result reached amplitudes of about 1.5×10^{-3} SI, which is much higher than that of the present geological units. Also, the structure suggested by the available geological cross sections does not explain the magnetic anomaly.

The significant discrepancies between the geophysical data and the geological information led to the development of four conceptual models. While none of these models can explain all the findings, models three and four are considered to be the most reasonable. Nevertheless, without further data these models are speculative. Thus, seismic studies and a drilling campaign will be necessary to give a final answer on the nature of the source of the magnetic anomaly.

7.3 Future directions for FTMG exploration

The successful application of the FTMG instrument and the interpretation of the case study data provides a basis of future investigations. The "Ohrdruf" data set showed that magnetic gradients are not always suitable for sedimentary basin exploration, especially on a larger, basin-sized scale. This is caused mainly due to low magnetization contrasts in horizontally layered media and the limited sensitivity at depth. This shows that the instrument noise level has to be reduced further in order to map structures in sedimentary basins and underneath the sedimentary coverage. This requires the development of more sensitive SQUID gradiometers. A good alternative is the application of electromagnetic methods. Airborne EM systems are widely used for hydrogeophysical studies (*Siemon et al.*, 2009), but usually lack the required depth of investigation. For ground based exploration, magnetotellurics (MT) or controlled-source electromagnetics (CSEM, CSAMT) were successfully applied in sedimentary basins (*Megbel et al.*, 2013). These methods do not only allow to infer information on the fault geometry, but also provide insight in hydrogeophysical properties of the fault zones (*Becken and Ritter*, 2012). Thus, it can also be used for monitoring of underground gas storage (*Grayver et al.*, 2014) or for geothermal exploration (*Egger et al.*, 2014). This means, that the investigation of a sedimentary basin, like in the INFLUINS project, can benefit from the combination of EM and magnetic methods.

The estimation of the remanence properties using FTMG and TFA data sets was the main goal of the "Schmalwasser" study (section 5.3). Some alternative methods have been presented in section 5.3.1, which were not applied in this study. However, most of these methods were originally used only in combination with conventional TFA data. Thus, the potential benefits of FTMG data should be re-evaluated using the presented data sets. Other approaches already implicate the theoretical advantages of the full magnetic gradient tensor and might provide additional aspects:

- a) The traditional Euler deconvolution (*Reid et al.*, 1990) is a common interpretation technique applied on airborne magnetic data sets. This method should provide better results when applied on full tensor magnetic gradiometry data, due to the higher directional sensitivity.

- b) A very promising approach for the estimation of source parameters using the normalized source strengths was proposed by *Beiki et al.* (2012). The implementation and subsequent application of this algorithm is subject of future research. It is worth to test this method on the presented magnetic gradient tensor data sets.
- c) The interpretation of 2D maps of the two rotational invariants (see section 2.1.2) and the eigenvalues of the tensor should be further investigated. These approaches may provide a better interpretation of the mapped magnetic structures.
- d) Helbig's method (*Helbig*, 1963) and some more advanced applications of these integrals (*Phillips*, 2005) might provide independent information on the magnetization direction of the exploration targets.
- e) The staged inversion approach of *Foss and McKenzie* (2011) has proven to be very robust when the geometry is more or less known. It also eliminates the smoothing effect of the voxel-based inversion at discontinuities and thus, this method should be compared to the results of the magnetization models presented in the "Schmalwasser" case study.

The paleomagnetic evaluation data set exhibits some scattering in the directions and amplitudes of the magnetization vector. Thus, more samples of the HD intrusion should be collected and analyzed. In the cores from the *Schnellbach 1/62* borehole, seven different facies of the HD have been reported (*Andreas and Volland*, 2010). Paleomagnetic information of each facies might be useful to clarify the scattering in the magnetization directions and therefore improve the interpretation of the inversion result.

In future also the application of the "active-source magnetics" method suggested by *Clark* (2014) might be beneficial to increase the accuracy of the remanence estimation by directly measuring the susceptibility. By using this approach some of the simple assumptions of the magnetization directions in this study may become unnecessary.

In the case of the "Siebleben" study site (section 5.4), the application of the ground-based EM methods are not advantageous. The ERT sections already provided information on the resistivity distribution in the subsurface. Additionally, EM methods might be of limited use in this area due to the electrified railway track that runs through the investigation area and may cause to much electromagnetic noise. The only methods that can provide further data for this case study would be a small seismic survey to accurately locate the different fault branches and a drilling campaign to clarify the source of the magnetic anomaly. The seismic study should at least cover the two fault branches EGSFZ- α and - β in order to image the central part up to a depth of 1000 m. This would probably allow to confirm or rule out some of the conceptual models suggested in this case study.

Bibliography

- Andreas, D., *Der Thüringer Wald im Zeitraum der Stefan-Unterperm-Entwicklung - ein Abschnitt der Zentraleuropäischen N-S-Riftzone innerhalb des Mitteleuropäischen Großschollenscharniers: Dissertation*, Jena, 2013.
- Andreas, D., and H. Lützner, Schichtenfolge und Paläotektonik der Rotliegend im mittleren Thüringer Wald zwischen Friedrichroda und Steinbach-Hallenberg, *Geowissenschaftliche Mitteilungen von Thüringen*, (13), 141–161, 2009.
- Andreas, D., and B. Volland, Der Dolerit der Höhenberge - Teil eines eigenständigen Höhenberg-Intrusionsintervalls - sein Gesamtprofil in der Bohrung Schnellbach 1/62 und die Einordnung der Intrusion in den Ablauf der Rotliegendentwicklung des Thüringer Waldes, *Beitr. Geol. Thüringen*, (17), 23–82, 2010.
- Becken, M., and O. Ritter, Magnetotelluric studies at the San Andreas fault zone: Implications for the role of fluids, *Surveys in Geophysics*, 33(1), 65–105, doi:10.1007/s10712-011-9144-0, 2012.
- Bednorz, J. G., and K. A. Müller, Possible high T_c superconductivity in the Ba-La-Cu-O system, *Z. Physik B - Condensed Matter (Zeitschrift für Physik B Condensed Matter)*, 64(2), 189–193, doi:10.1007/BF01303701, 1986.
- Beiki, M., D. A. Clark, J. R. Austin, and C. A. Foss, Estimating source location using normalized magnetic source strength calculated from magnetic gradient tensor data, *Geophysics*, 77(6), J23–J37, doi:10.1190/GEO2011-0437.1, 2012.
- Bhattacharyya, B. K., A generalized multibody model for inversion of magnetic anomalies, *Geophysics*, 45(2), 255–270, doi:10.1190/1.1441081, 1980.
- Bjørlykke, K., Fluid flow in sedimentary basins, *Sedimentary Geology*, 86(1-2), 137–158, doi:10.1016/0037-0738(93)90137-T, 1993.
- Bjørlykke, K., Subsurface water and fluid flow in sedimentary basins, in *Petroleum Geoscience*, edited by K. Bjørlykke, pp. 279–300, Springer Berlin Heidelberg, Berlin, Heidelberg, doi:10.1007/978-3-642-34132-8_10, 2015.
- Blakely, R. J., *Potential theory in gravity and magnetic applications*, Stanford-Cambridge program, 1st paperback ed., Cambridge University Press, Cambridge, 1996.
- Breiner, S., Applications manual for portable magnetometers: Geometrics, 1973.
- Butler, R. F., *Paleomagnetism: Magnetic domains to geologic terranes*, Blackwell Scientific Publications, Boston, 1992.
- Cai, H., *Migration and inversion of magnetic and magnetic gradiometry data: Master Thesis*, University of Utah, Salt Lake City, 2012.
- Campbell, W. H., *Introduction to geomagnetic fields*, 2nd ed., Cambridge University Press, Cambridge and New York, 2003.

- Clark, D. A., Magnetic petrology of igneous intrusions: implications for exploration and magnetic interpretation, *Exploration Geophysics*, 30(2), 5, doi:10.1071/EG999005, 1999.
- Clark, D. A., New methods for interpretation of magnetic vector and gradient tensor data I: eigenvector analysis and the normalised source strength, *Exploration Geophysics*, doi:10.1071/EG12020, 2012.
- Clark, D. A., New methods for interpretation of magnetic vector and gradient tensor data II: application to the Mount Leyshon anomaly, Queensland, Australia, *Exploration Geophysics*, 44(2), 114, doi:10.1071/EG12066, 2013.
- Clark, D. A., Methods for determining remanent and total magnetisations of magnetic sources – a review, *Exploration Geophysics*, 45(4), 271, doi:10.1071/EG14013, 2014.
- Clark, D. A., and D. W. Emerson, Notes on rock magnetization characteristics in applied geophysical studies, *Exploration Geophysics*, 22(3), 547, doi:10.1071/EG991547, 1991.
- Clark, D. A., S. J. Saul, and D. W. Emerson, Magnetic and gravity anomalies of a triaxial ellipsoid, *Exploration Geophysics*, 17(4), 189, doi:10.1071/EG986189, 1986.
- Clark, D. A., C. A. Foss, J. R. Austin, and D. Hillan, Three-dimensional mapping of magnetite and hematite concentrations from reprocessing of detailed aeromagnetic data: Iron Ore Conference 2015 Perth, West Australia, *The Australasian Institute of Mining and Metallurgy Publication Series*, (5), 229–240, 2015.
- Clarke, J., and A. I. Braginski, *The SQUID Handbook, Vol.1: Fundamentals and Technology of SQUIDS and SQUID Systems*, Wiley-VCH, Weinheim and Cambridge, 2004.
- Clarke, J., and A. I. Braginski (Eds.), *The SQUID Handbook, Vol.2: Applications of SQUIDS and SQUID Systems*, Wiley-VCH and John Wiley [distributor], Weinheim and Chichester, 2005.
- Clem, T. R., G. J. Kekelis, J. D. Lathrop, D. J. Overway, and W. M. Wynn, Superconducting magnetic gradiometers for mobile applications with an emphasis on ordnance detection, in *SQUID Sensors: Fundamentals, Fabrication and Applications*, edited by H. Weinstock, pp. 517–568, Springer Netherlands, Dordrecht, doi:10.1007/978-94-011-5674-5_13, 1996.
- Clem, T. R., C. Foley, and M. N. Keene, SQUIDS for geophysical survey and magnetic anomaly detection, in *The SQUID Handbook, Vol.2*, edited by J. Clarke and A. I. Braginski, pp. 482–543, Wiley-VCH and John Wiley [distributor], Weinheim and Chichester, 2005.
- Cooper, G., Feature detection using sun shading, *Computers & Geosciences*, 29(8), 941–948, doi:10.1016/S0098-3004(03)00091-8, 2003.
- Čuma, M., G. A. Wilson, and M. S. Zhdanov, Large-scale 3D inversion of potential field data, *Geophysical Prospecting*, 60(6), 1186–1199, doi:10.1111/j.1365-2478.2011.01052.x, 2012.

- Dannemiller, N., and Y. Li, A new method for determination of magnetization direction, *Geophysics*, *71*(6), L69–L73, doi:10.1190/1.2356116, 2006.
- de Castro, D. L., R. A. Fuck, J. D. Phillips, R. M. Vidotti, F. H. Bezerra, and E. L. Dantas, Crustal structure beneath the Paleozoic Parnaíba Basin revealed by airborne gravity and magnetic data, Brazil, *Tectonophysics*, *614*, 128–145, doi:10.1016/j.tecto.2013.12.009, 2014.
- Deaver, B., and W. Fairbank, Experimental evidence for quantized flux in superconducting cylinders, *Physical Review Letters*, *7*(2), 43–46, doi:10.1103/PhysRevLett.7.43, 1961.
- Dockter, J., and R. Langbein, Keuper, in *Geologie von Thüringen*, edited by G. Seidel, pp. 332–362, Schweizerbart, Stuttgart, 2003.
- Döring, M., Entwicklung und Messung axialer TTS Gradiometer: diploma thesis (unpublished): Friedrich-Schiller-Universität Jena, 2013.
- Drung, D., and M. Mück, SQUID Electronics, in *The SQUID Handbook*, edited by J. Clarke and A. I. Braginski, pp. 127–170, Wiley-VCH Verlag GmbH & Co. KGaA, Weinheim, FRG, doi:10.1002/3527603646.ch4, 2004.
- Egger, A. E., Glen, J. M. G., and D. K. McPhee, Structural controls on geothermal circulation in Surprise Valley, California: A re-evaluation of the Lake City fault zone, *Geological Society of America Bulletin*, *126*(3-4), 523–531, doi:10.1130/B30785.1, 2014.
- Ellis, R. G., B. d. Wet, and I. N MacLeod, Inversion of magnetic data for remanent and induced sources, *ASEG Extended Abstracts*, *2012*(1), 1, doi:10.1071/ASEG2012ab117, 2012.
- Finlay, C. C., S. Maus, C. D. Beggan, T. N. Bondar, A. Chambodut, T. A. Chernova, A. Chulliat, V. P. Golovkov, B. Hamilton, M. Hamoudi, R. Holme, G. Hulot, W. Kuang, B. Langlais, V. Lesur, F. J. Lowes, H. Lühr, S. Macmillan, M. Manda, S. McLean, C. Manoj, M. Menvielle, I. Michaelis, N. Olsen, J. Rauberg, M. Rother, T. J. Sabaka, A. Tangborn, L. Tøffner-Clausen, E. Thébaud, Thomson, A. W. P., I. Wardinski, Z. Wei, and T. I. Zvereva, International Geomagnetic Reference Field: the eleventh generation, *Geophysical Journal International*, *183*(3), 1216–1230, doi:10.1111/j.1365-246X.2010.04804.x, 2010.
- FitzGerald, D. J., and H. Holstein, Innovative data processing methods for gradient airborne geophysical data sets, *The Leading Edge*, *25*(1), 87–94, doi:10.1190/1.2164762, 2006.
- Foss, C., Improvements in source resolution that can be expected from inversion of magnetic field tensor data, *The Leading Edge*, *25*(1), 81–84, doi:10.1190/1.2164761, 2006a.
- Foss, C. A., Evaluation of strategies to manage remanent magnetization effects in magnetic field inversion, in *SEG Technical Program Expanded Abstracts 2006*, pp. 938–942, doi:10.1190/1.2370410, 2006b.

- Foss, C. A., and B. McKenzie, Inversion of anomalies due to remanent magnetisation: an example from the Black Hill Norite of South Australia, *Australian Journal of Earth Sciences*, 58(4), 391–405, doi:10.1080/08120099.2011.581310, 2011.
- Foss, C. A., and K. B. McKenzie, Strategies to invert a suite of magnetic field anomalies due to remanent magnetization: an example from the Georgetown area of Queensland, *ASEG Extended Abstracts*, 2009(1), 1, doi:10.1071/ASEG2009ab112, 2009.
- Foss, C. A., K. B. McKenzie, and D. Hillan, A robust approach to estimation of magnetization direction from interpretation of magnetic field data, *SEG Technical Program Expanded Abstracts*, pp. 1–5, doi:10.1190/segam2012-1550.1, 2012.
- Foss, C. A., G. Reed, T. Keeping, and P. Heath, Geoscientific investigation of a remanent anomaly - Teetulpa, South Australia, *ASEG Extended Abstracts*, 2015(1), 1, doi:10.1071/ASEG2015ab205, 2015.
- Fullagar, P. K., and G. Pears, 3D magnetic modelling and inversion incorporating self-demagnetisation and interactions, *ASEG Extended Abstracts*, 2013(1), 1, doi:10.1071/ASEG2013ab239, 2013.
- Fullagar, P. K., and G. A. Pears, Remanent magnetisation inversion, *ASEG Extended Abstracts*, 2015(1), 1, doi:10.1071/ASEG2015ab188, 2015.
- Furness, P., A physical approach to computing magnetic fields, *Geophysical Prospecting*, 42(5), 405–416, doi:10.1111/j.1365-2478.1994.tb00218.x, 1994.
- Gabriel, G., D. Vogel, R. Scheibe, H. Lindner, R. Pucher, T. Wonik, and C. M. Krawczyk, Anomalies of the Earth’s total magnetic field in Germany - the first complete homogenous data set reveals new opportunities for multiscale geoscientific studies, *Geophysical Journal International*, 184(3), 1113–1118, doi:10.1111/j.1365-246X.2010.04924.x, 2011.
- Glatzmaier, G. A., and P. H. Roberts, Rotation and magnetism of Earth’s inner core, *Science*, 274(5294), 1887–1891, doi:10.1126/science.274.5294.1887, 1996.
- Goepel, A., N. Kukowski, M. Krause, T. Karp, J. Kley, K. U. Totsche, and L. Katzschnmann, Reflection-seismic imaging of the central Thuringian Basin, Germany., in prep.
- Götze, H. J., and B. Lahmeyer, Application of three-dimensional interactive modeling in gravity and magnetics, *Geophysics*, 53(8), 1096–1108, doi:10.1190/1.1442546, 1988.
- Grant, F. S., Aeromagnetism, geology and ore environments, i. magnetite in igneous, sedimentary and metamorphic rocks: An overview, *Geoexploration*, 23(3), 303–333, doi:10.1016/0016-7142(85)90001-8, 1985.
- Grauch, V. J. S., Using high-resolution aeromagnetic surveys to map subsurface hydrogeology in sediment-filled basins: A case study over the Rio Grande rift, central New Mexico, USA, *Exploration Geophysics*, 32(4), 209, doi:10.1071/EG01209, 2001.

- Grauch, V. J. S., and M. R. Hudson, Aeromagnetic anomalies over faulted strata, *The Leading Edge*, 30(11), 1242–1252, doi:10.1190/1.3663396, 2011.
- Grayver, A. V., R. Streich, and O. Ritter, 3D inversion and resolution analysis of land-based CSEM data from the Ketzin CO₂ storage formation, *Geophysics*, 79(2), E101–E114, doi:10.1190/geo2013-0184.1, 2014.
- Günther, T., C. Rücker, and K. Spitzer, Three-dimensional modelling and inversion of dc resistivity data incorporating topography - II. Inversion, *Geophysical Journal International*, 166(2), 506–517, doi:10.1111/j.1365-246X.2006.03011.x, 2006.
- Helbig, K., Some integrals of magnetic anomalies and their relation to the parameters of the disturbing body, *Zeitschrift für Geophysik*, (29), 83–96, 1963.
- Hinze, W. J., R. v. Frese, and A. H. Saad, *Gravity and magnetic exploration: Principles, practices, and applications*, 2013.
- Holstein, H., Gravimagnetic anomaly formulas for polyhedra of spatially linear media, *Geophysics*, 68(1), 157–167, doi:10.1190/1.1543203, 2003.
- Hooper, E. C. D., Fluid migration along growth faults in compacting sediments, *Journal of Petroleum Geology*, 14, 161–180, doi:10.1111/j.1747-5457.1991.tb00360.x, 1991.
- Jaklevic, R., J. Lambe, A. Silver, and J. Mercereau, Quantum interference effects in Josephson tunneling, *Physical Review Letters*, 12(7), 159–160, doi:10.1103/PhysRevLett.12.159, 1964.
- Josephson, B. D., Possible new effects in superconductive tunnelling, *Physics Letters*, 1(7), 251–253, doi:10.1016/0031-9163(62)91369-0, 1962.
- Kamerlingh Onnes, H., Further experiments with liquid helium. C. on the change of electric resistance of pure metals at very low temperatures, etc. IV. the resistance of pure mercury at helium temperatures., *Comm. Phys. Lab. Univ. Leiden*, (120b), 1911a.
- Kamerlingh Onnes, H., Further experiments with liquid helium. D. on the change of electric resistance of pure metals at very low temperatures, etc. V. the disappearance of the resistance of mercury., *Comm. Phys. Lab. Univ. Leiden*, (122b), 1911b.
- Kertz, W., *Einführung in die Geophysik*, *BI-Hochschultaschenbuch*, vol. Bd. 535, BI-Wiss.-Verl., Mannheim and Leipzig and Wien and Zürich, 1992.
- Kley, J., and T. Voigt, Late Cretaceous intraplate thrusting in central Europe: Effect of Africa-Iberia-Europe convergence, not Alpine collision, *Geology*, 36(11), 839, doi:10.1130/G24930A.1, 2008.
- Kockel, F., Rifting processes in NW-Germany and the German North Sea Sector, *Netherlands Journal of Geosciences*, 81(2), 149–158, 2002.
- Kossmat, F., Gliederung des varistischen Gebirgsbaues, *Abhandlungen des Sächsischen Geologischen Landesamtes*, (1), 1–39, 1927.

- Kovesi, P., Bad colour maps hide big features and create false anomalies, *ASEG Extended Abstracts*, 2015(1), 1, doi:10.1071/ASEG2015ab107, 2015.
- Kratzer, T., and J. C. Macnae, Induced polarization in airborne EM, *Geophysics*, 77(5), E317–E327, doi:10.1190/geo2011-0492.1, 2012.
- Krige, D. G., A statistical approach to some basic mine valuation problems on the Witwatersrand, *Journal of the Chemical, Metallurgical and Mining Society of South Africa*, 52(6), 119–139, 1951.
- Kubota, R., and A. Uchiyama, Three-dimensional magnetization vector inversion of a seamount, *Earth, Planets and Space*, 57(8), 691–699, doi:10.1186/BF03351849, 2005.
- Kukowski, N., and K. U. Totsche (Eds.), *Schlussbericht zum BMBF-Verbundvorhaben : INFLUINS - Integrierte Fluidodynamik in Sedimentbecken: Laufzeit des Vorhabens: 01.01.2010 - 31.12.2014*, Jena, 2015.
- Kunkel, C., M. Abratis, B. Müller, J. Hofmann, T. Tiepner, M. Aehnelt, T. Voigt, R. Gaupp, N. Kukowski, K. U. Totsche, and the INLFUINS scientific drilling Team, Die INFLUINS-Forschungsbohrung EF-FB 1/12: Einführung und erste stratigraphische Ergebnisse zur neuen Tiefbohrung im Herzen der Thüringer Mulde, *Beitr. Geol. Thüringen*, (21), 67–83, 2014.
- Langbein, R., and G. Seidel, Zechstein, in *Geologie von Thüringen*, edited by G. Seidel, pp. 277–302, Schweizerbart, Stuttgart, 2003a.
- Langbein, R., and G. Seidel, Muschelkalk, in *Geologie von Thüringen*, edited by G. Seidel, pp. 277–302, Schweizerbart, Stuttgart, 2003b.
- Lanza, R., and A. Meloni, *The earth's magnetism: An introduction for geologists*, Springer, Berlin and New York, 2006.
- Last, B. J., and K. Kubik, Compact gravity inversion, *Geophysics*, 48(6), 713–721, doi:10.1190/1.1441501, 1983.
- Lelièvre, P. G., and D. W. Oldenburg, A 3D total magnetization inversion applicable when significant, complicated remanence is present, *Geophysics*, 74(3), L21–L30, doi:10.1190/1.3103249, 2009.
- Lelièvre, P. G., D. W. Oldenburg, and N. C. Williams, Integrating geological and geophysical data through advanced constrained inversions, *Exploration Geophysics*, 40(4), 334, doi:10.1071/EG09012, 2009.
- Lelièvre, P. G., A. Carter-McAuslan, C. Farquharson, and C. Hurich, Unified geophysical and geological 3D Earth models, *The Leading Edge*, 31(3), 322–328, doi:10.1190/1.3694900, 2012.
- Leslie, K., K. Blay, D. Clark, P. Schmidt, D. Tilbrook, M. Bick, C. Foley, and R. Binks, Helicopter trial of magnetic tensor gradiometer, *ASEG Extended Abstracts*, 2007(1), 1, doi:10.1071/ASEG2007ab128, 2007.
- Li, Y., and D. W. Oldenburg, 3-D inversion of magnetic data, *Geophysics*, 61(2), 394–408, doi:10.1190/1.1443968, 1996.

- Li, Y., and D. W. Oldenburg, Joint inversion of surface and three-component borehole magnetic data, *Geophysics*, 65(2), 540–552, doi:10.1190/1.1444749, 2000.
- Li, Y., and D. W. Oldenburg, Fast inversion of large-scale magnetic data using wavelet transforms and a logarithmic barrier method, *Geophysical Journal International*, 152(2), 251–265, doi:10.1046/j.1365-246X.2003.01766.x, 2003.
- Li, Y., S. E. Shearer, M. M. Haney, and N. Dannemiller, Comprehensive approaches to 3D inversion of magnetic data affected by remanent magnetization, *Geophysics*, 75(1), L1–L11, doi:10.1190/1.3294766, 2010.
- Linzen, S., V. Schultze, A. Chwala, T. Schüller, M. Schulz, R. Stolz, and H.-G. Meyer, Quantum detection meets archaeology – Magnetic prospection with SQUIDs, highly sensitive and fast, in *New Technologies for Archaeology*, edited by M. Reindel and G. A. Wagner, Natural Science in Archaeology, pp. 71–85, Springer Berlin Heidelberg, Berlin, Heidelberg, doi:10.1007/978-3-540-87438-6\textunderscore5, 2009.
- Littke, R., *Dynamics of Complex Intracontinental Basins: The Central European Basin System*, Springer-Verlag, Berlin, 2008.
- Lo, B., and M. Zang, Numerical modeling of Z-TEM (airborne AFMAG) responses to guide exploration strategies, *SEG Technical Program Expanded Abstracts*, pp. 1098–1102, doi:10.1190/1.3059115, 2008.
- Lowrie, W., *Fundamentals of Geophysics*, 2nd ed., Cambridge University Press, Cambridge, 2007.
- Lützner, H., D. Andreas, J. Mädler, J. Michael, H. Voigt, R. Werneburg, G. Judersleben, and J. Jungwirth, Siles und Rotliegend, in *Geologie von Thüringen*, edited by G. Seidel, Schweizerbart, Stuttgart, 2003.
- Lützner, H., D. Andreas, J. Schneider, S. Voigt, and R. Werneburg, Stefan und Rotliegend im Thüringer Wald und seiner Umgebung, *Schriftenreihe der Deutschen Gesellschaft für Geowissenschaften*, (61), 418–487, 2012.
- Luyendyk, A. P. J., Processing of airborne magnetic data, *Journal of Australian Geology and Geophysics*, (17), 31–38, 1997.
- MacLeod, I. N., and R. G. Ellis, Magnetic Vector Inversion, a simple approach to the challenge of varying direction of rock magnetization: A forum on the application of remanent magnetisation and self- demagnetisation estimation to mineral exploration, *23rd ASEG Conference and Exhibition, Melbourne*, 2013.
- Mädler, J., Der Lagergang des basischen bis intermediären Höhenberg-Gesteins im Thüringer Wald – ein geologisch-petrographischer Überblick, *Geowissenschaftliche Mitteilungen von Thüringen*, (13), 69–98, 2009.
- Malz, A., *Inversionsstrukturen und abgescherzte Überschiebungssysteme: Strukturinventar und strukturelle Analyse einengender Deformation in Mitteleuropa am Beispiel der Thüringer Mulde und des Schweizer Faltenjura*, Dissertation, Jena, 2014.

- Malz, A., P. Navabpour, T. Voigt, and J. Kley, Along-strike structural segmentation of a reactivated fault zone controlled by stratigraphy variations - a case study from central germany, in prep.
- Matte, P., Accretionary history and crustal evolution of the Variscan belt in Western Europe, *Tectonophysics*, 196(3-4), 309–337, doi:10.1016/0040-1951(91)90328-P, 1991.
- Matte, P., The Variscan collage and orogeny (480-290 ma) and the tectonic definition of the Armorica microplate: a review, *Terra Nova*, 13(2), 122–128, doi:10.1046/j.1365-3121.2001.00327.x, 2001.
- Mauring, E., and O. Kihle, Micro-levelling of aeromagnetic data using a moving differential median filter: Report 2000.053 Geological Survey of Norway, 2000.
- Mauring, E., L. P. Beard, O. Kihle, and M. A. Smethurst, A comparison of aeromagnetic levelling techniques with an introduction to median levelling, *Geophysical Prospecting*, 50(1), 43–54, doi:10.1046/j.1365-2478.2002.00300.x, 2002.
- Maus, S., M. C. Nair, B. Poedjono, S. Okewunmi, D. Fairhaid, U. Barckhausen, P. R. Milligan, and J. Matzka, High-Definition Geomagnetic Models: A new perspective for improved wellbore positioning, in *IADC/SPE Drilling Conference and Exhibition*, doi:10.2118/151436-MS, 2012.
- Medeiros, W. E., and J. B. Silva, Simultaneous estimation of total magnetization direction and 3-D spatial orientation, *Geophysics*, 60(5), 1365–1377, doi:10.1190/1.1443872, 1995.
- Meqbel, N., O. Ritter, and DESIRE Group, A magnetotelluric transect across the Dead Sea Basin: electrical properties of geological and hydrological units of the upper crust, *Geophysical Journal International*, 193(3), 1415–1431, doi:10.1093/gji/ggt051, 2013.
- Merrill, R. T., M. W. McElhinny, and P. L. McFadden, *The magnetic field of the Earth: Paleomagnetism, the core, and the deep mantle*, This is volume 63 in the International geophysics series, Academic Press, San Diego, 1998.
- Nabighian, M. N., The Analytic Signal of two-dimensional magnetic bodies with polygonal cross-section: Its properties and use for automated anomaly interpretation, *Geophysics*, 37(3), 507–517, doi:10.1190/1.1440276, 1972.
- Nabighian, M. N., Additional comments on the analytic signal of two-dimensional magnetic bodies with polygonal cross-section, *Geophysics*, 39(1), 85–92, doi:10.1190/1.1440416, 1974.
- Nabighian, M. N., Toward a three-dimensional automatic interpretation of potential field data via generalized Hilbert transforms: Fundamental relations, *Geophysics*, 49(6), 780–786, doi:10.1190/1.1441706, 1984.
- Nettleton, L. L., Gravity and Magnetic Calculations, *Geophysics*, 7(3), 293–310, doi:10.1190/1.1445015, 1942.
- NovAtel Inc., Novatel OEM628TM GNSS Receiver Datasheet, 2010.

- O'Brien, P. J., and D. A. Carswell, Tectonometamorphic evolution of the Bohemian Massif: evidence from high pressure metamorphic rocks, *Geologische Rundschau*, 82(3), 531–555, doi:10.1007/BF00212415, 1993.
- Oliver, M. A., and R. Webster, Kriging: a method of interpolation for geographical information systems, *International journal of geographical information systems*, 4(3), 313–332, doi:10.1080/026937990008941549, 1990.
- Oukhanski, N., R. Stolz, and H.-G. Meyer, High slew rate, ultrastable direct-coupled readout for dc superconducting quantum interference devices, *Applied Physics Letters*, 89(6), 063,502, doi:10.1063/1.2335630, 2006.
- Pedersen, L. B., and T. M. Rasmussen, The gradient tensor of potential field anomalies: Some implications on data collection and data processing of maps, *Geophysics*, 55(12), 1558–1566, doi:10.1190/1.1442807, 1990.
- Phillips, J. D., Can we estimate total magnetization directions from aeromagnetic data using Helbig's integrals?, *Earth, Planets and Space*, 57(8), 681–689, doi:10.1186/BF03351848, 2005.
- Pilkington, M., and M. Beiki, Mitigating remanent magnetization effects in magnetic data using the normalized source strength, *Geophysics*, 78(3), J25–J32, doi:10.1190/geo2012-0225.1, 2013.
- Pohanka, V., Optimum expression for computation of the gravity field of a homogeneous polyhedral body, *Geophysical Prospecting*, 36(7), 733–751, doi:10.1111/j.1365-2478.1988.tb02190.x, 1988.
- Portniaguine, O., and M. S. Zhdanov, Focusing geophysical inversion images, *Geophysics*, 64(3), 874–887, doi:10.1190/1.1444596, 1999.
- Pratt, D. A., K. B. McKenzie, and T. S. White, Remote remanence estimation (RRE), *Exploration Geophysics*, 45(4), 314, doi:10.1071/EG14031, 2014.
- Priest, E. R., and T. Forbes, *Magnetic reconnection: MHD theory and applications*, Cambridge University Press, Cambridge and New York, 2000.
- Puff, P., and R. Langbein, Buntsandstein, in *Geologie von Thüringen*, edited by G. Seidel, pp. 326–341, Schweizerbart, Stuttgart, 2003.
- Radhakrishna Murthy, I. V., Magnetic equivalence of dipping beds, faults and anticlines, *Pure and Applied Geophysics PAGEOPH*, 123(6), 893–901, doi:10.1007/BF00876977, 1985.
- Rajagopalan, S., P. Schmidt, and D. A. Clark, Rock magnetism and geophysical interpretation of the Black Hill Norite, South Australia, *Exploration Geophysics*, 24(2), 209, doi:10.1071/EG993209, 1993.
- Rajagopalan, S., D. A. Clark, and P. W. Schmidt, Magnetic mineralogy of the Black Hill Norite and its aeromagnetic and palaeomagnetic implications, *Exploration Geophysics*, 26(3), 215, doi:10.1071/EG995215, 1995.

- Reid, A. B., J. M. Allsop, H. Granser, A. J. Millett, and I. W. Somerton, Magnetic interpretation in three dimensions using Euler deconvolution, *Geophysics*, 55(1), 80–91, doi:10.1190/1.1442774, 1990.
- Roberts, P., and G. Glatzmaier, Geodynamo theory and simulations, *Reviews of Modern Physics*, 72(4), 1081–1123, doi:10.1103/RevModPhys.72.1081, 2000.
- Roberts, P. H., and G. A. Glatzmaier, The geodynamo, past, present and future, *Geophysical & Astrophysical Fluid Dynamics*, 94(1-2), 47–84, doi:10.1080/03091920108204131, 2001.
- Roest, W. R., and M. Pilkington, Identifying remanent magnetization effects in magnetic data, *Geophysics*, 58(5), 653–659, doi:10.1190/1.1443449, 1993.
- Roest, W. R., J. Verhoef, and M. Pilkington, Magnetic interpretation using the 3-D analytic signal, *Geophysics*, 57(1), 116–125, doi:10.1190/1.1443174, 1992.
- Rolf, C., Das Kryogenmagnetometer im Magnetiklabor Grubenhagen, in *Angewandte Geophysik - neue Geräte und ihre Anwendungen, Geologisches Jahrbuch Reihe E, Geophysik*, vol. 52, edited by R. Schulz, pp. 161–188, Schweizerbart, Stuttgart, 2000.
- Rompel, A. K. K., Geological Applications for FTMG, *11th SAGA Biennial Technical Meeting and Exhibition*, pp. 39–42, 2009.
- Rücker, C., T. Günther, and K. Spitzer, Three-dimensional modelling and inversion of dc resistivity data incorporating topography - I. Modelling, *Geophysical Journal International*, 166(2), 495–505, doi:10.1111/j.1365-246X.2006.03010.x, 2006.
- Saad, A. H., Magnetic properties of ultramafic rocks from Red Mountain, California, *Geophysics*, 34(6), 974–987, doi:10.1190/1.1440067, 1969.
- SatisGeo, Kappameter KM-7 Magnetic Susceptibility Meter data sheet, 2012.
- Scheibe, R., M. Bauer, G. Klimmer, D. Wein, J. Schwabe, and F. Zetsche, Ergebnisbericht - Forschungsvorhaben INFLUINS - Thüringer Becken - Aufarbeitung vorhandener Potentialfelddaten Gravimetrie/Magnetik - Recherche vorliegender oberflächenseismischer und bohrlochseismischer sowie petrophysikalischer Daten: Technical report, 2010.
- Schiffler, M., *Enhancements in Processing, Analysis and Inversion of Full Tensor Magnetic Gradiometry data. Dissertation*, Jena, 2015.
- Schiffler, M., M. Queitsch, R. Stolz, A. Chwala, W. Krech, H.-G. Meyer, and N. Kukowski, Calibration of SQUID vector magnetometers in full tensor gradiometry systems, *Geophysical Journal International*, 198(2), 954–964, doi:10.1093/gji/ggu173, 2014.
- Schiffler, M., M. Queitsch, R. Stolz, H.-G. Meyer, and N. Kukowski, Application of Hilbert transforms for enhanced processing of full tensor magnetic gradient data, *Geophysical Prospecting*, 2015(in review), 2016.
- Schmidt, P. W., and D. A. Clark, The magnetic gradient tensor: Its properties and uses in source characterization, *The Leading Edge*, 25(1), 75–78, doi:10.1190/1.2164759, 2006.

- Schmidt, P. W., and M. A. Lackie, Practical considerations: making measurements of susceptibility, remanence and Q in the field, *Exploration Geophysics*, 45(4), 305, doi:10.1071/EG14019, 2014.
- Schmidt, P. W., D. A. Clark, and S. Rajagopalan, An historical perspective of the early palaeozoic APWP of Gondwana: New results from the early Ordovician Black Hill Norite, South Australia, *Exploration Geophysics*, 24(2), 257, doi:10.1071/EG993257, 1993.
- Schneider, M., S. Linzen, M. Schiffler, E. Pohl, B. Ahrens, S. Dunkel, R. Stolz, J. Bemann, H.-G. Meyer, and D. Baumgarten, Inversion of geo-magnetic SQUID gradiometer prospection data using polyhedral model interpretation of elongated anomalies, *IEEE Transactions on Magnetics*, 50(11), 1–4, doi:10.1109/TMAG.2014.2320361, 2014.
- Schön, S. J., Magnetic properties, in *Physical Properties of Rocks - A Workbook, Handbook of Petroleum Exploration and Production*, vol. 8, pp. 373–391, Elsevier, doi:10.1016/S1567-8032(11)08010-4, 2011.
- Schönau, T., M. Schneider, M. Schiffler, M. Schmelz, R. Stolz, and H.-G. Meyer, Removal of step-edges and corresponding Gibbs ringing in SQUID-based geomagnetic data, *Measurement Science and Technology*, 24(12), 125,004, doi:10.1088/0957-0233/24/12/125004, 2013.
- Seidel, G., *Geologie von Thüringen*, 2., neubearb. Aufl ed., Schweizerbart, Stuttgart, 2003.
- Sharma, V. P., Rapid computation of magnetic anomalies and demagnetization effects caused by bodies of arbitrary shape, *Pure and Applied Geophysics PAGEOPH*, 64(1), 89–109, doi:10.1007/BF00875535, 1966.
- Shin, E. H., and N. El-Sheimy, Aided Inertial Navigation System (AINSTTM) Toolbox for MatLab\textregistered Software, *INS/GPS integration software, Mobile Multi-Sensors Systems (MMSS) research group, the University of Calgary. Available: <http://mms.geomatics.ucalgary.ca/Research/research.htm>*, 2004.
- Siemon, B., A. V. Christiansen, and E. Auken, A review of helicopter-borne electromagnetic methods for groundwater exploration, *Near Surface Geophysics*, 7(1303), doi:10.3997/1873-0604.2009043, 2009.
- Stolz, R., *Supraleitende Quanteninterferenzdetektor-Gradiometer-Systeme für den geophysikalischen Einsatz: Dissertation*, Isle, Ilmenau, 2006.
- Stolz, R., V. Zakosarenko, M. Schulz, A. Chwala, L. Fritzsche, H.-G. Meyer, and E. O. Köstlin, Magnetic full-tensor SQUID gradiometer system for geophysical applications, *The Leading Edge*, 25(2), 178–180, doi:10.1190/1.2172308, 2006.
- Talwani, M., Computation with the help of a digital computer of magnetic anomalies caused by bodies of arbitrary shape, *Geophysics*, 30(5), 797–817, doi:10.1190/1.1439654, 1965.

- Tikhonov, A. N., and V. I. A. Arsenin, *Solutions of ill-posed problems*, Scripta series in mathematics, Winston and Distributed solely by Halsted Press, Washington and New York, 1977.
- TLUG, Geologische Übersichtskarte von Thüringen 1:200.000, 2003.
- TLUG, Digitale Geologische Karte von Thüringen für den Maßstab 1:25000 - GK25digTH, 2010.
- Urquhart, T., Decorrugation of enhanced magnetic field maps, in *SEG Technical Program Expanded Abstracts*, pp. 371–372, doi:10.1190/1.1892383, 1988.
- Villani, F., S. Pucci, R. Civico, De Martini, P. M., I. Nicolosi, F. D’Ajello Caracciolo, R. Carluccio, G. Di Giulio, M. Vassallo, A. Smedile, and D. Pantosti, Imaging the structural style of an active normal fault through multidisciplinary geophysical investigation: a case study from the Mw 6.1, 2009 L’Aquila earthquake region (central Italy), *Geophysical Journal International*, 200(3), 1676–1691, doi:10.1093/gji/ggu462, 2015.
- Vrba, J., SQUID gradiometers in real environments // SQUID Sensors: Fundamentals, Fabrication and Applications, in *SQUID Sensors: Fundamentals, Fabrication and Applications*, NATO ASI Series, vol. 329, edited by H. Weinstock, pp. 117–178, Springer Netherlands, doi:10.1007/978-94-011-5674-5, 1996.
- Walter, R., *Geologie von Mitteleuropa: Mit 12 Tabellen*, 6. Aufl. ed., Schweizerbart, Stuttgart, 1995.
- Ward, S. H., AFMAG - Airborne and ground, *Geophysics*, 24(4), 761–787, doi:10.1190/1.1438657, 1959.
- Wedge, D., Y. Sivarajah, P. Johnston, C. Wijns, E.-J. Holden, and P. Kovesi, Visualising Full Tensor Gradient Gravity data using texture and colour cues, in *International Conference on Digital Image Computing: Techniques and Applications (DICTA)*, pp. 1–8, doi:10.1109/DICTA.2012.6411716, 2012.
- Winchester, J., Palaeozoic amalgamation of central europe: new results from recent geological and geophysical investigations, *Tectonophysics*, 360(1-4), 5–21, doi:10.1016/S0040-1951(02)00344-X, 2002.
- Zakosarenko, V., L. Warzemann, J. Schambach, K. Blüthner, K.-H. Berthel, G. Kirsch, P. Weber, and R. Stolz, Integrated LTS gradiometer SQUID systems for unshielded measurements in a disturbed environment, *Superconductor Science and Technology*, 9(4A), A112–A115, doi:10.1088/0953-2048/9/4A/029, 1996.
- Zhang, Z., and D. W. Oldenburg, Simultaneous reconstruction of 1-d susceptibility and conductivity from electromagnetic data, *Geophysics*, 64(1), 33–47, doi:10.1190/1.1444528, 1999.
- Zhdanov, M. S., *Geophysical inverse theory and regularization problems*, *Methods in geochemistry and geophysics*, vol. 36, Elsevier Science, Amsterdam and Oxford, 2002.

- Zhdanov, M. S., and D. A. Pavlov, Analysis and interpretation of anomalous conductivity and magnetic permeability effects in time domain electromagnetic data, *Journal of Applied Geophysics*, 46(4), 235–248, doi:10.1016/S0926-9851(01)00041-6, 2001.
- Zhdanov, M. S., H. Cai, and G. A. Wilson, 3d inversion of full tensor magnetic gradiometry (ftmg) data, *SEG Technical Program Expanded Abstracts*, pp. 791–795, doi:10.1190/1.3628195, 2011.
- Ziegler, P. A., *Geological atlas of Western and Central Europe*, 2nd and completely rev. ed., Shell Internationale Petroleum Maatschappij, The Hague, 1990.

A Appendix: FTMG data and inversion results of the "Schmalwasser" area

Here, the acquired magnetic gradient tensor maps of the "Schmalwasser" area are shown. Two additional maps of the calculated total field anomaly and the topography with flight lines are presented as well. Histograms of the residual magnetic gradient tensor components and the total field anomaly after the magnetization vector inversions are depicted in Fig. A.9 and Fig. A.10, respectively. Slices through the magnetization models are depicting the three magnetization vector components along the E-W plane at the two quarries (Fig. A.12 and Fig. A.14) in the study area and at an altitude of 400 m (Fig. A.11). Additionally, a zoom into a part of the FTMG inversion result along the slice in Fig. A.12 is given in Fig. A.13. In Fig. A.15 the norm of the magnetization vector of the FTMG inversion result along the two vertical slices is presented. The comparison of the magnetization directions and amplitudes at the *Nesselgrund* and *Spittergrund* sampling sites in the "Schmalwasser" survey area are given in Fig. A.16 and Fig. A.17, respectively. This includes vertical and horizontal slices through the magnetization models of the FTMG and TFA inversions similar to Fig. A.14 and Fig. A.11. Polar plots of the magnetization directions and histograms of the amplitudes, including the amplitudes from the paleomagnetic measurements on orientated rock samples, are illustrating the differences of both inversions.

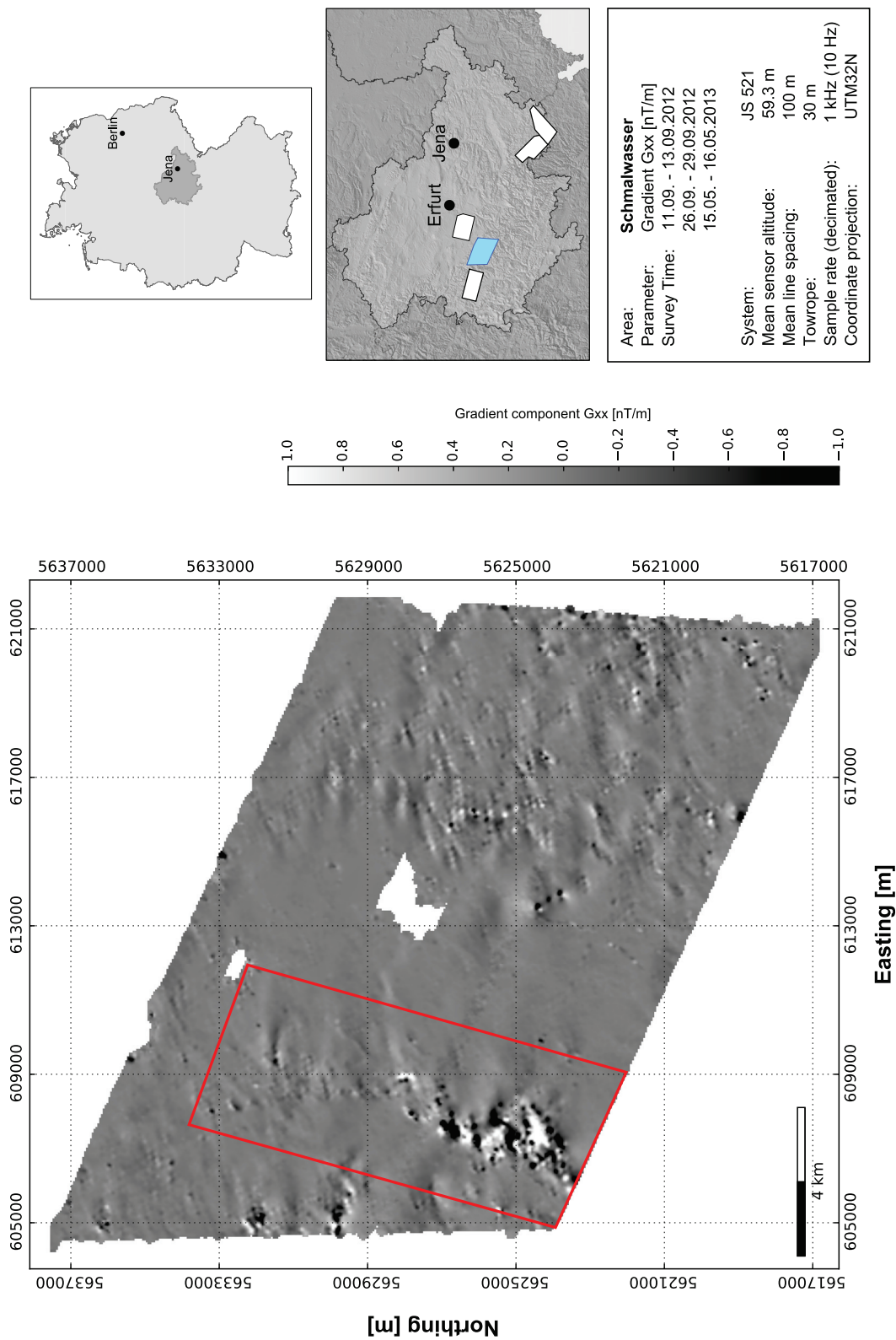


Figure A.1: Mapped magnetic gradient tensor component G_{xx} of the "Schmalwasser" area. The red box marks the outline of the "Schmalwasser-Remanence" study site. The main anomaly in this box is caused by the "Höhenberger" dolerite.

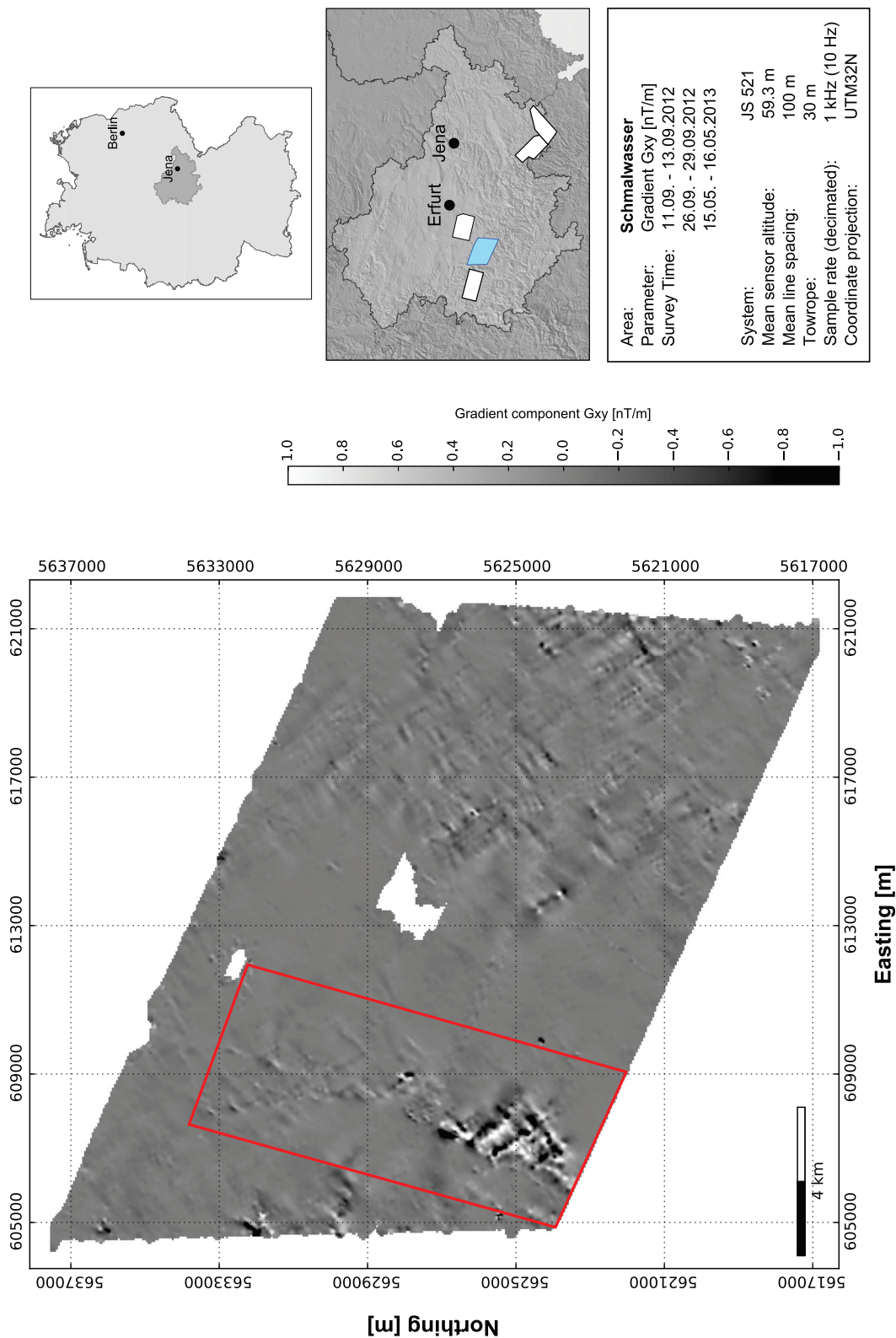


Figure A.2: Mapped magnetic gradient tensor component G_{xy} of the "Schmalwasser" area. The red box marks the outline of the "Schmalwasser-Remanence" study site. The main anomaly in this box is caused by the "Höhenberger" dolerite.

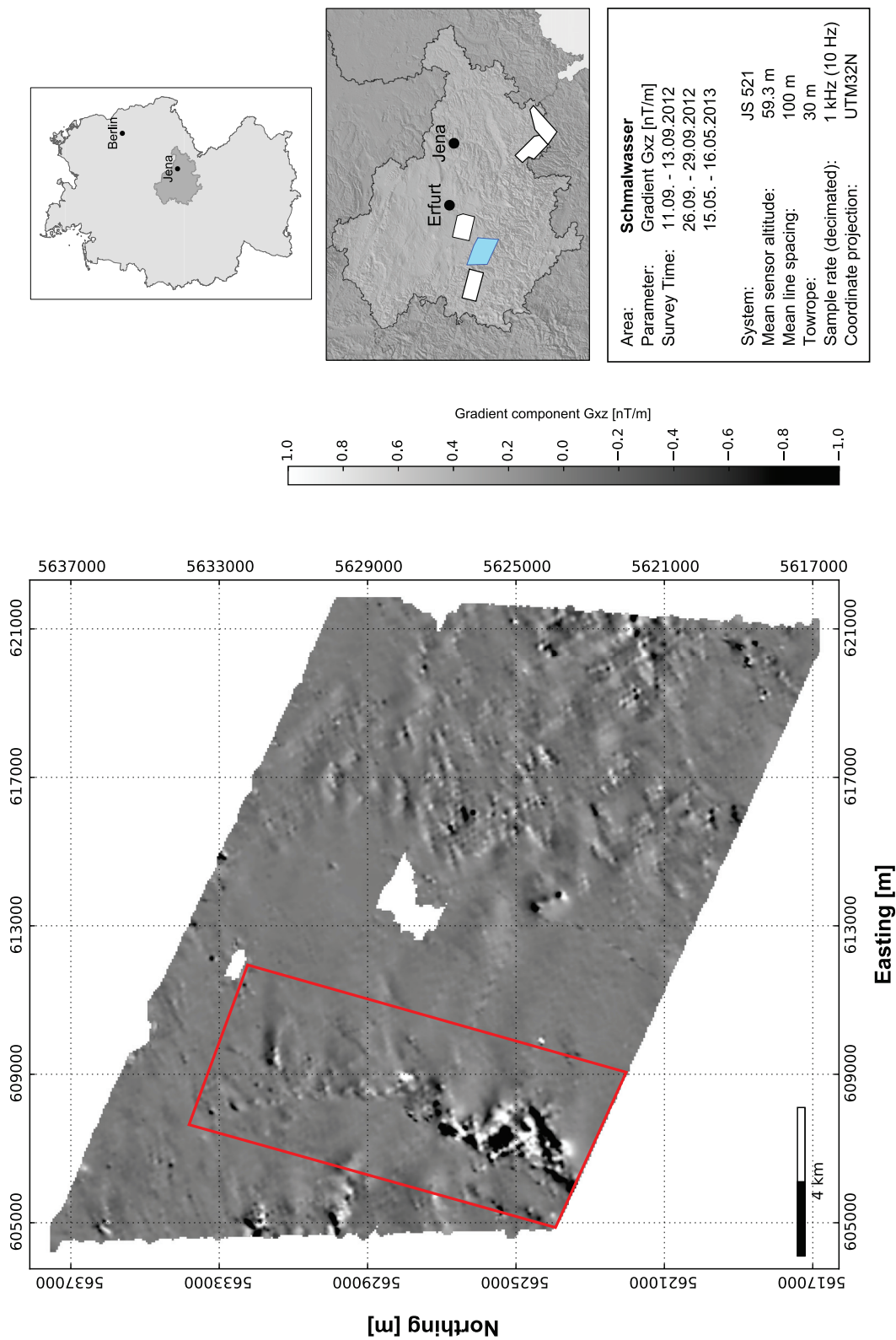


Figure A.3: Mapped magnetic gradient tensor component G_{xz} of the "Schmalwasser" area. The red box marks the outline of the "Schmalwasser-Remanence" study site. The main anomaly in this box is caused by the "Höhenberger" dolerite.

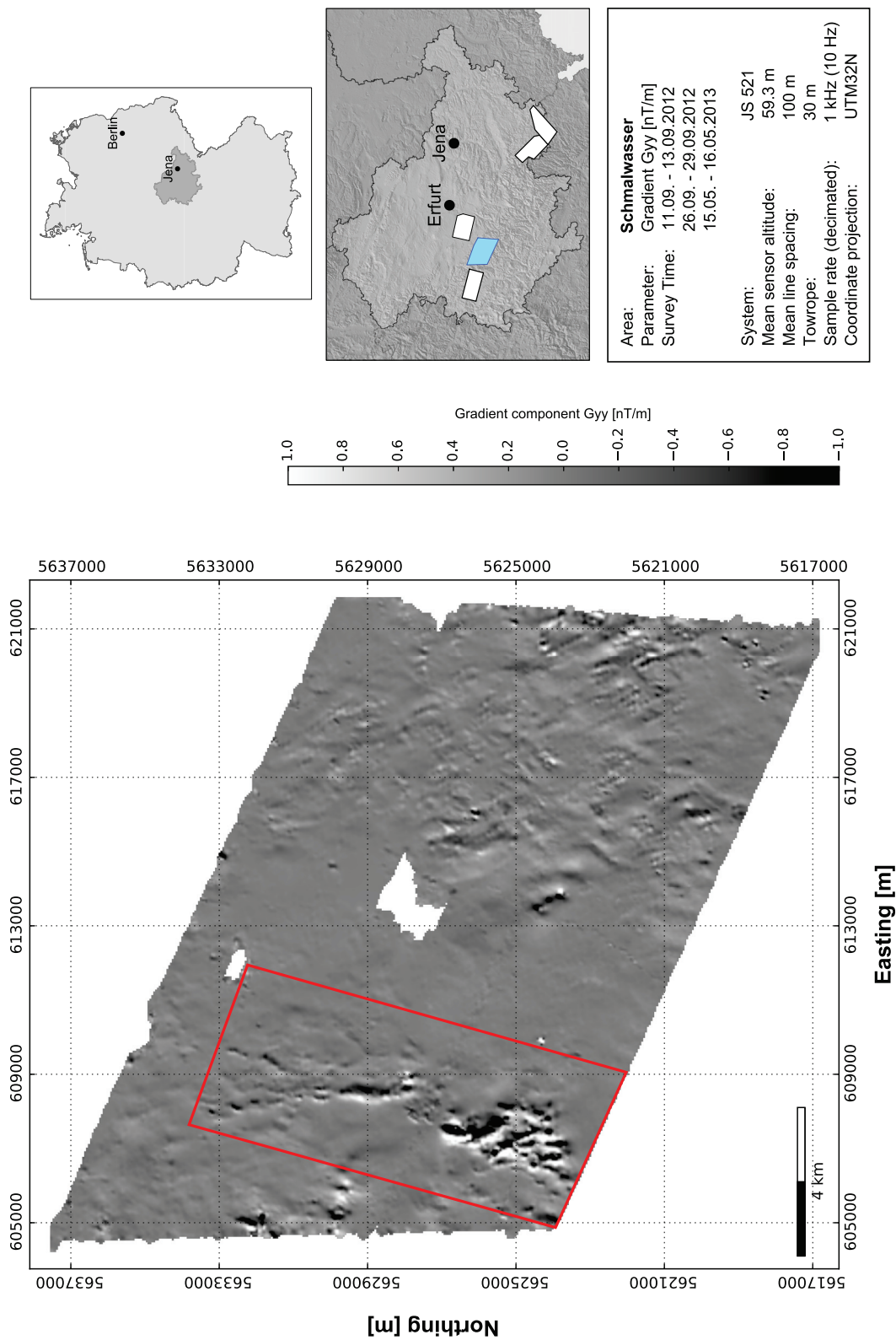


Figure A.4: Mapped magnetic gradient tensor component G_{yy} of the "Schmalwasser" area. The red box marks the outline of the "Schmalwasser-Remanence" study site. The main anomaly in this box is caused by the "Höhenberger" dolerite.

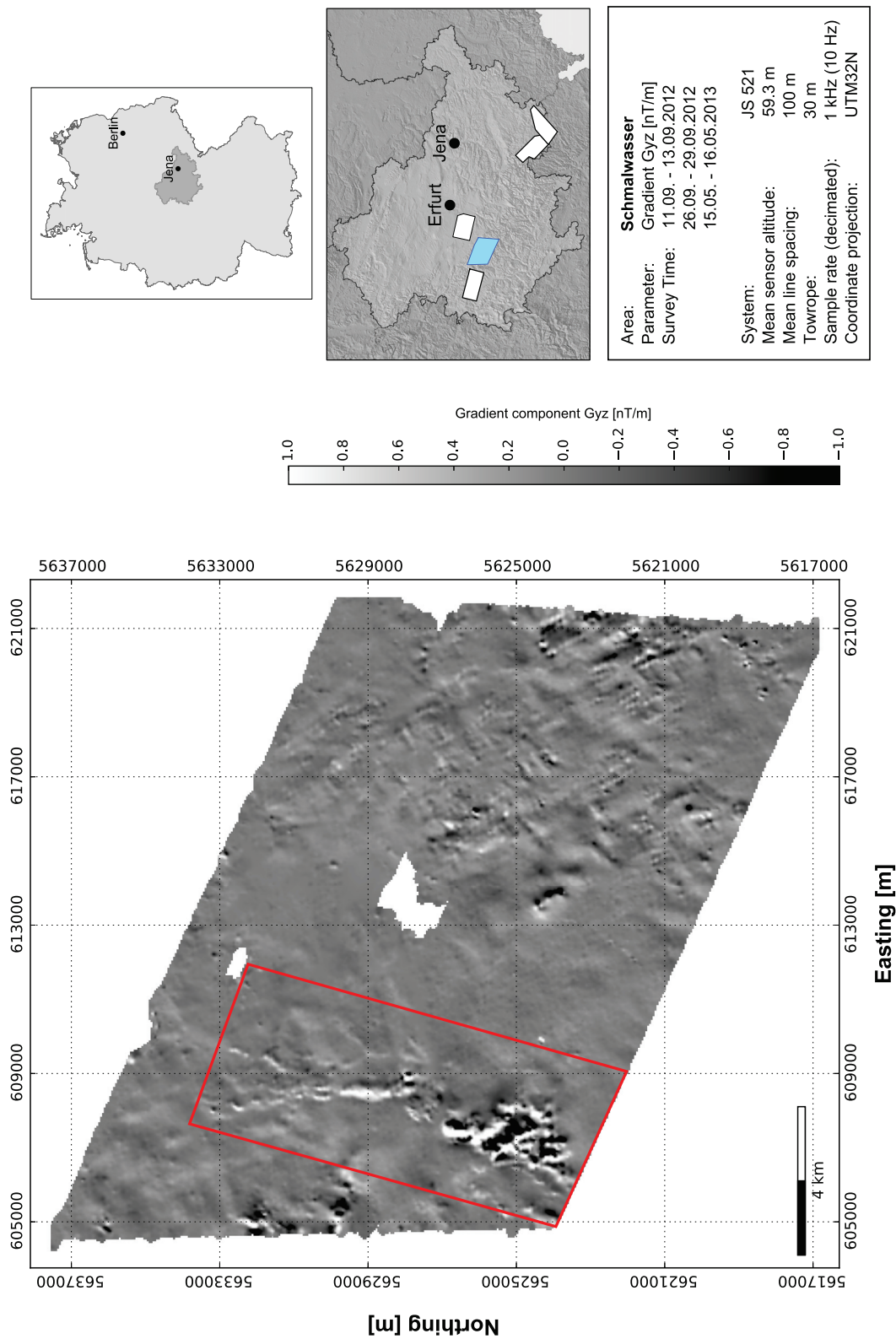


Figure A.5: Mapped magnetic gradient tensor component G_{yz} of the "Schmalwasser" area. The red box marks the outline of the "Schmalwasser-Remanence" study site. The main anomaly in this box is caused by the "Höhenberger" dolerite.

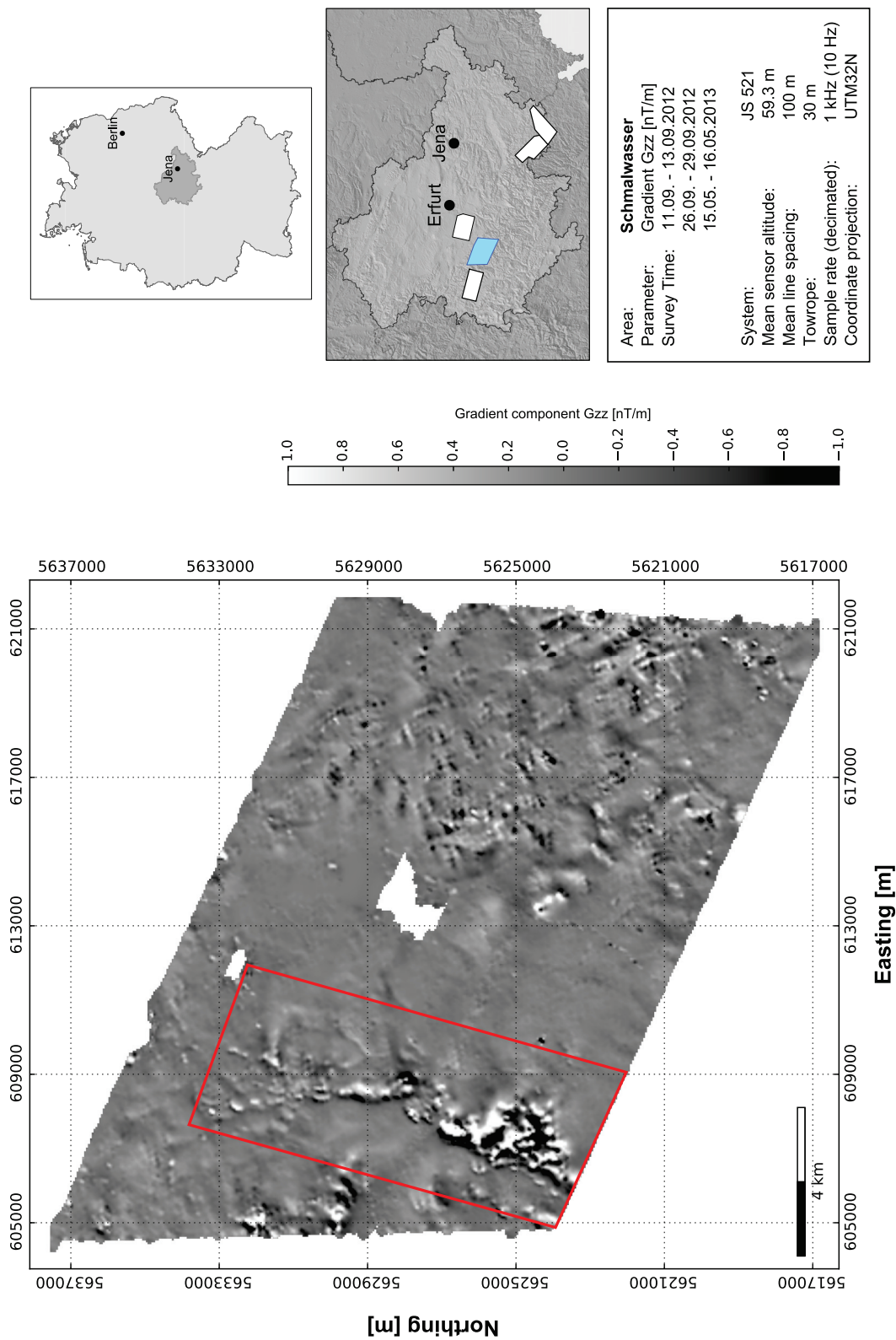


Figure A.6: Mapped magnetic gradient tensor component G_{zz} of the "Schmalwasser" area. The red box marks the outline of the "Schmalwasser-Remanence" study site. The main anomaly in this box is caused by the "Höhenberger" dolerite.

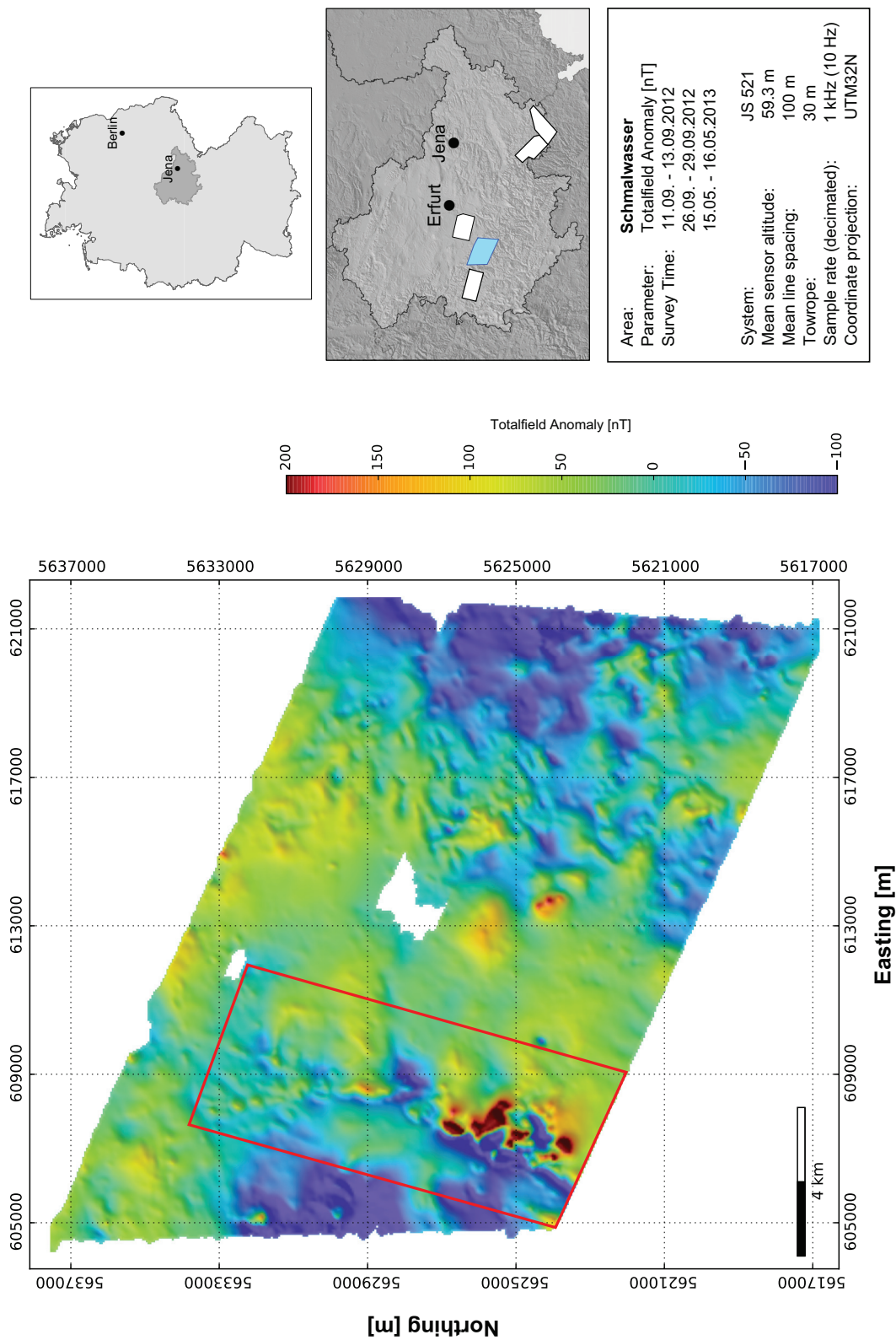


Figure A.7: Mapped total magnetic field anomaly of the "Schmalwasser" area. The red box marks the outline of the "Schmalwasser-Remanence" study site. The main anomaly in this box is caused by the "Höhenberger" dolerite.

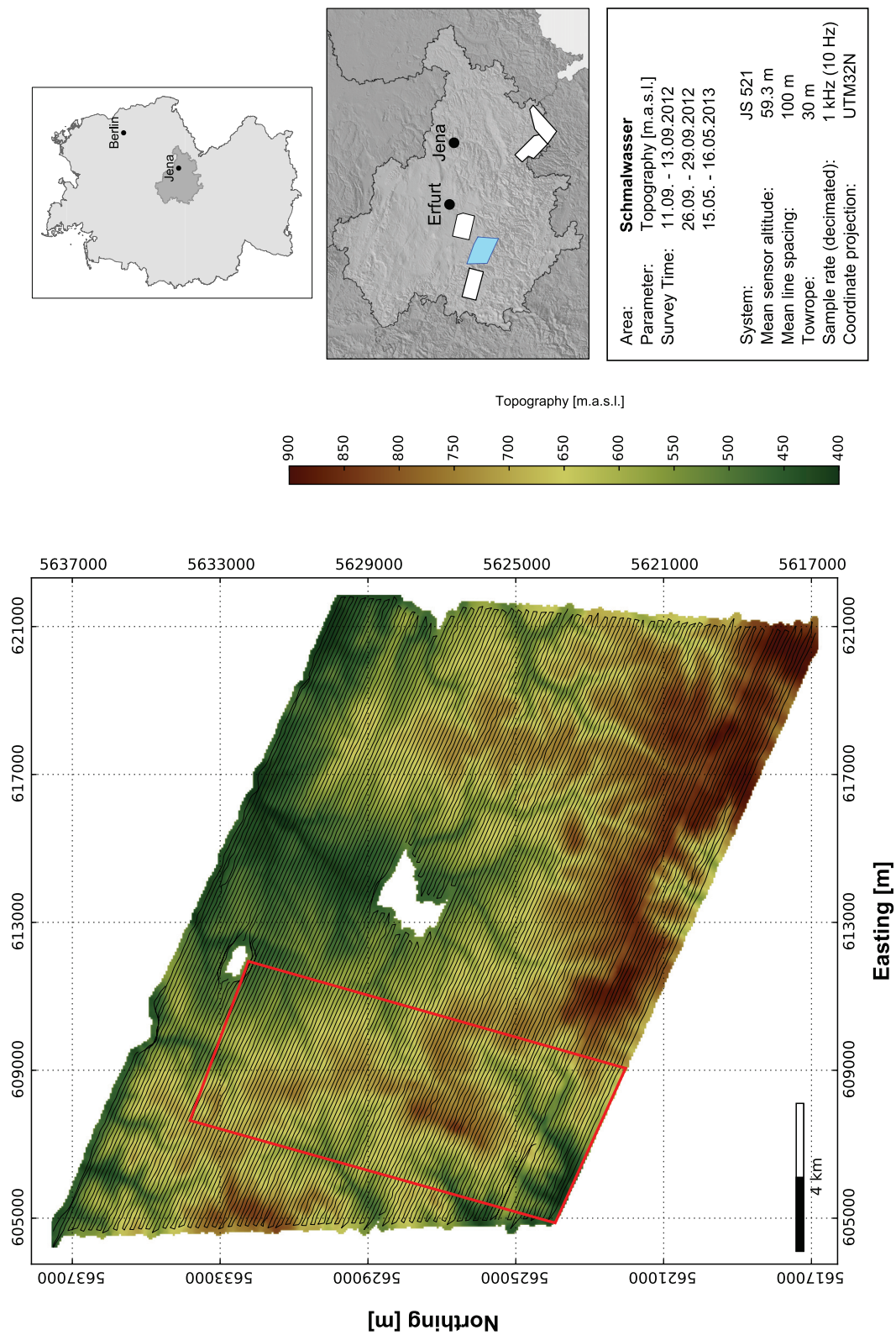


Figure A.8: Topography and flight track of the "Schmalwasser" area. The red box marks the outline of the "Schmalwasser-Remanence" study site.

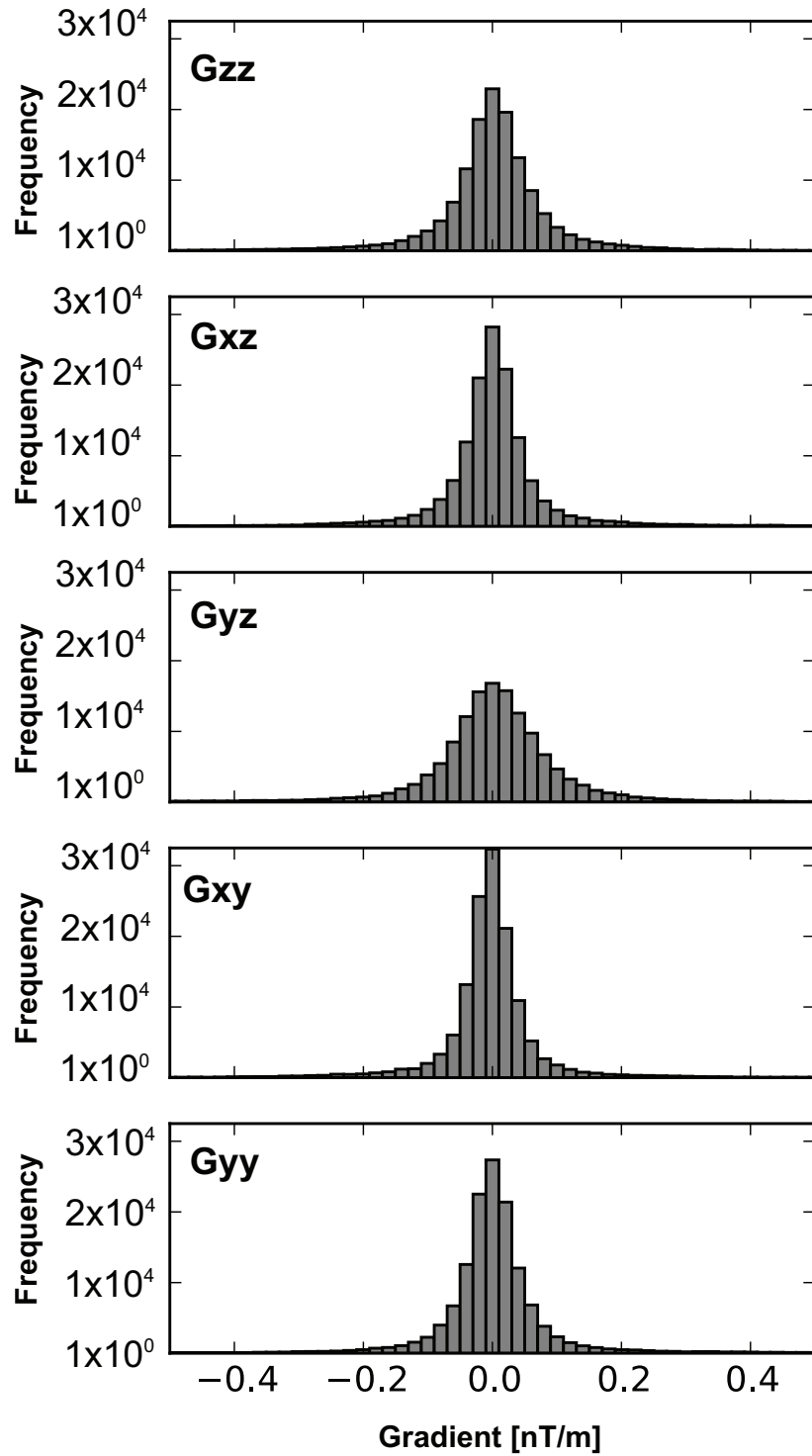


Figure A.9: Histogram of the residuals between the calculated magnetic gradient tensor components of the final model and the observed gradient tensor components.

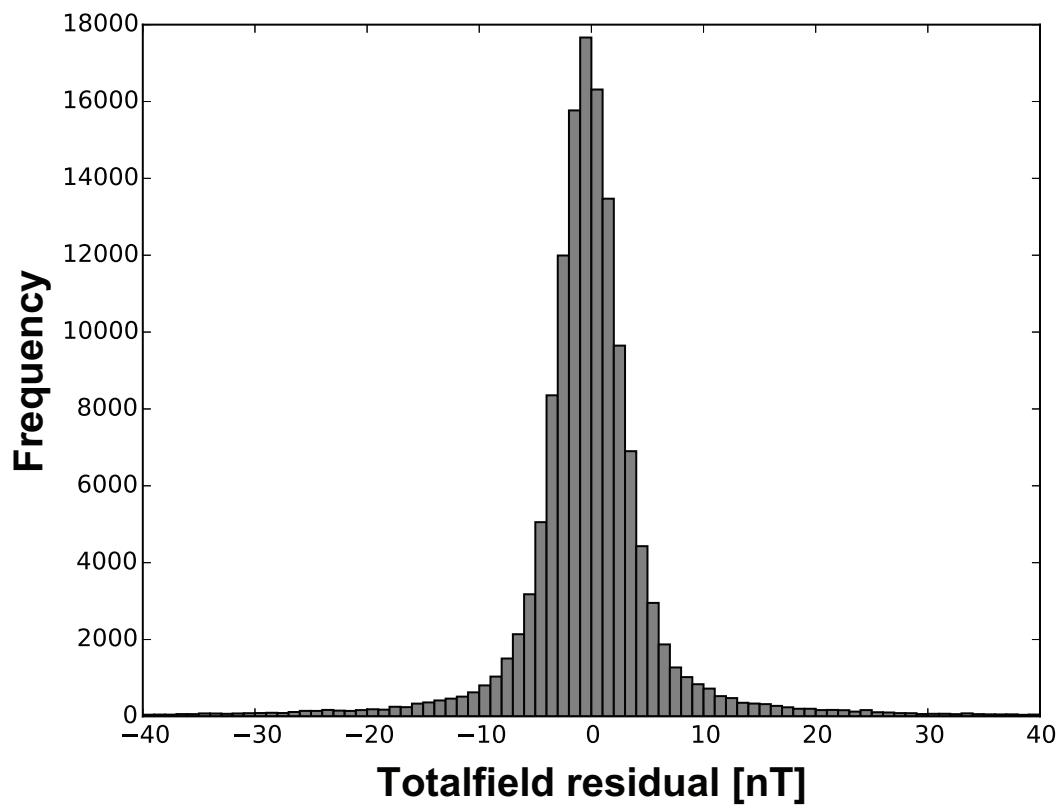


Figure A.10: Histogram of the residuals between calculated TFA of the final model and the observed total field anomaly.

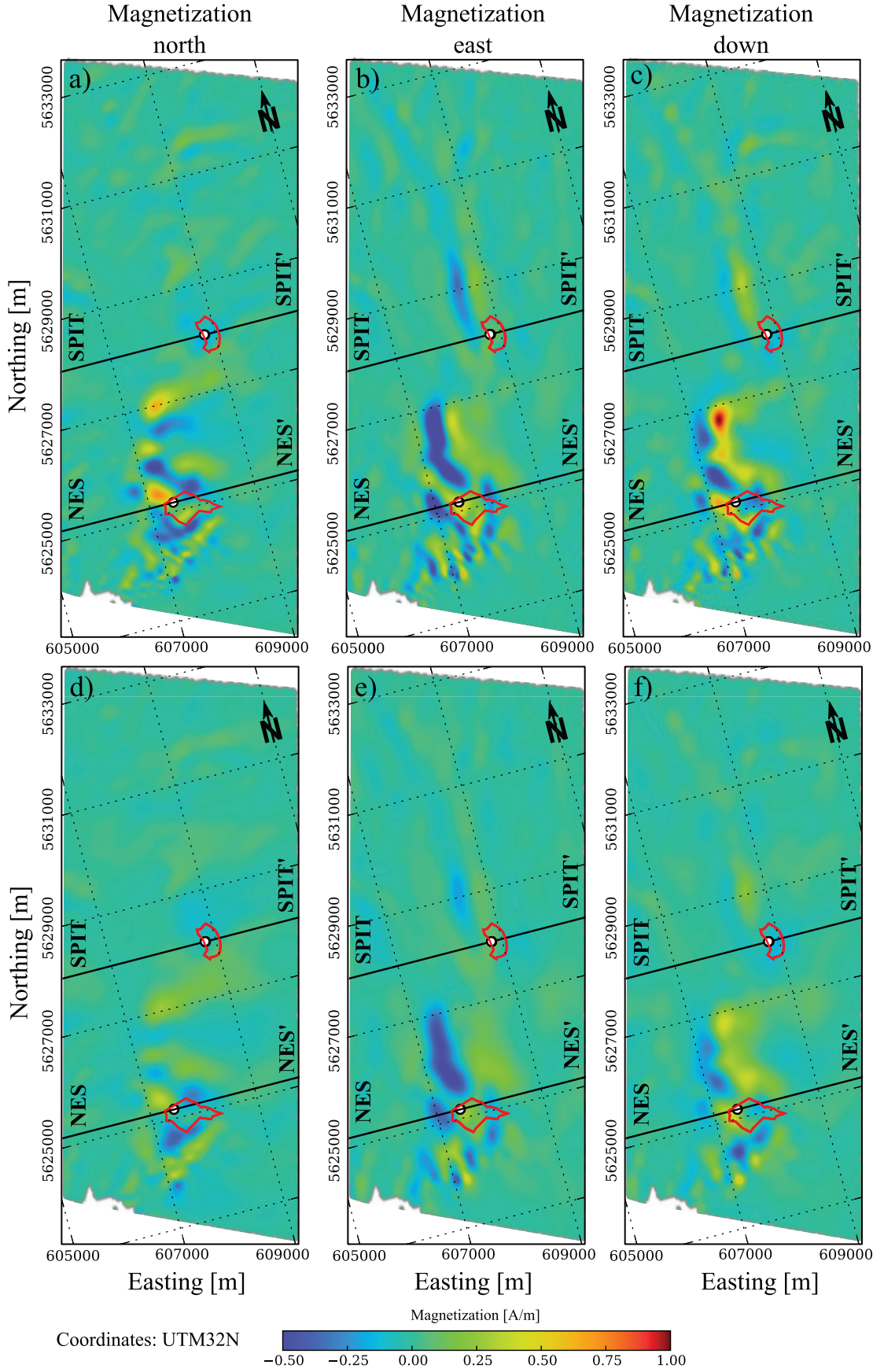


Figure A.11: Horizontal slices at an elevation of 400 m through the final models of the FTMG (a-c) and TFA inversions (d-f). The red outline marks the location of the two quarries *Spittergrund* (north) and *Nesselgrund* (south). Paleomagnetic sampling locations are denoted by the white dots within the quarries. The location of the vertical slices are illustrated by the solid lines SPIT-SPIT' and NES-NES'.

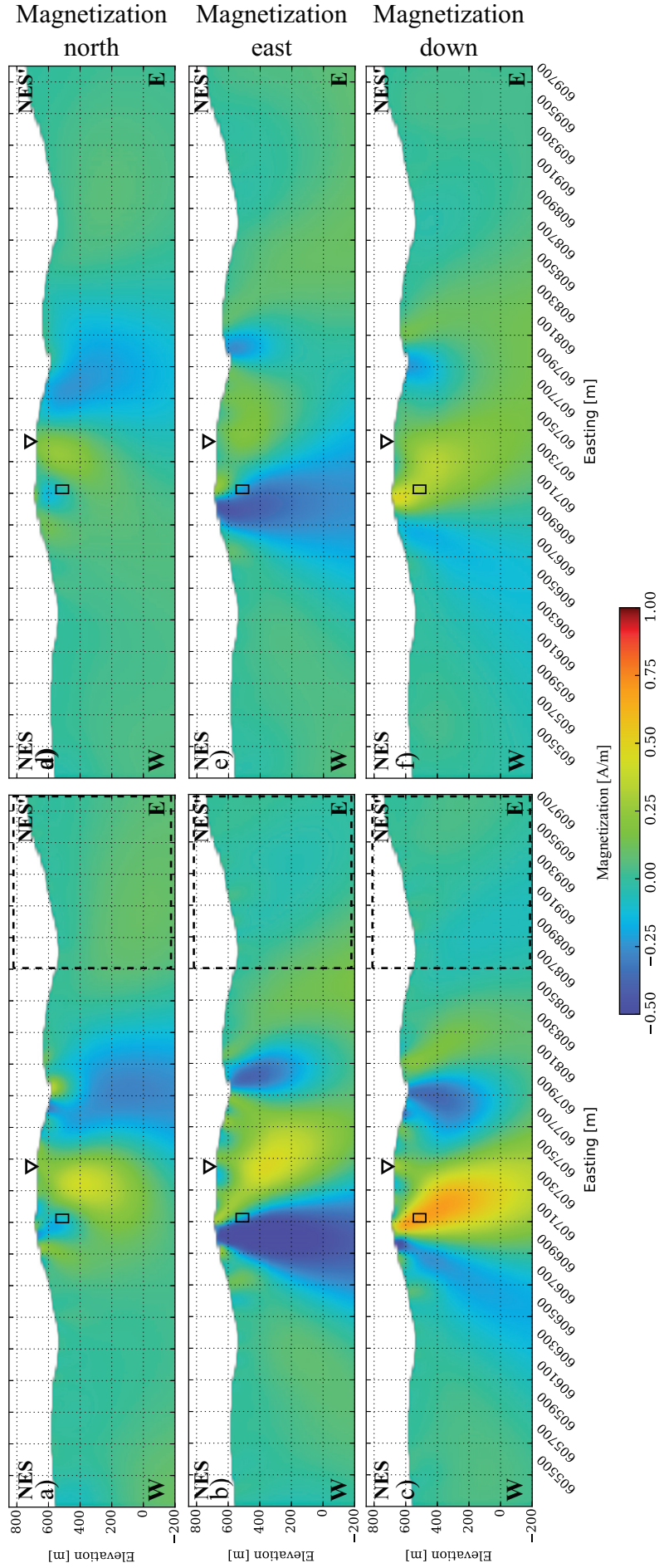


Figure A.12: Vertical slices through the final models of the FTMG (a-c) and TFA inversions (d-f) along the *Nesselgrund* transect. The paleomagnetic sampling site is marked by triangles at the surface. The black boxes represent the volume of the model which was used to check the reconstructed magnetization direction. The dashed box in the FTMG slices marks the location of the zoom slice in Fig. A.13.

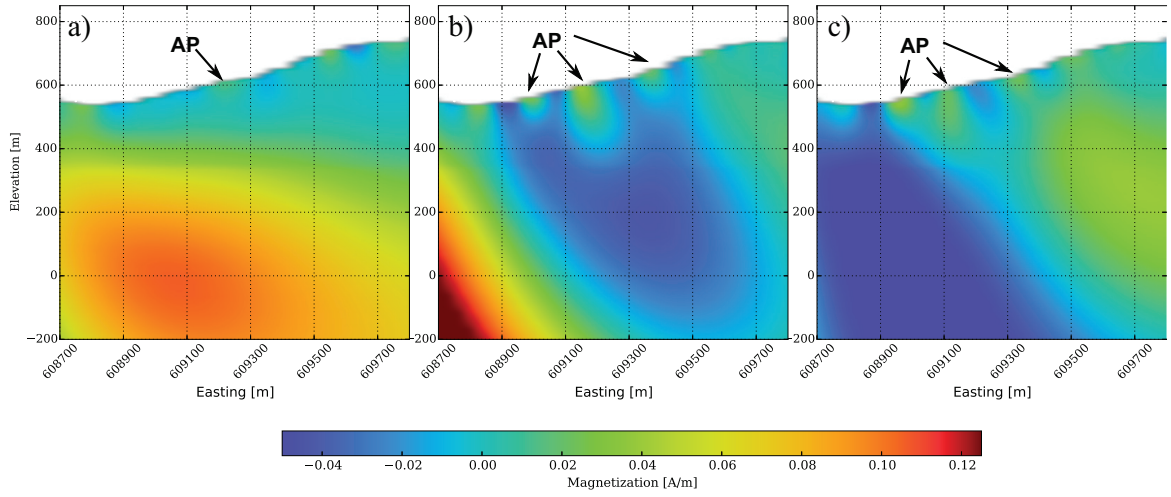


Figure A.13: Zoom into the area of the apophysis east of the Nesselgrund quarry. Figures a-c are showing the different magnetization directions north-, east- and downwards, respectively. This structure was also marked by a lineament in Fig. 5.6. At least two apophyses can be seen in the magnetization model. Since this structure has a thickness of approximately less than 50 m it cannot be traced into greater depth in this model and is represented by a much lower magnetization than the main intrusion.

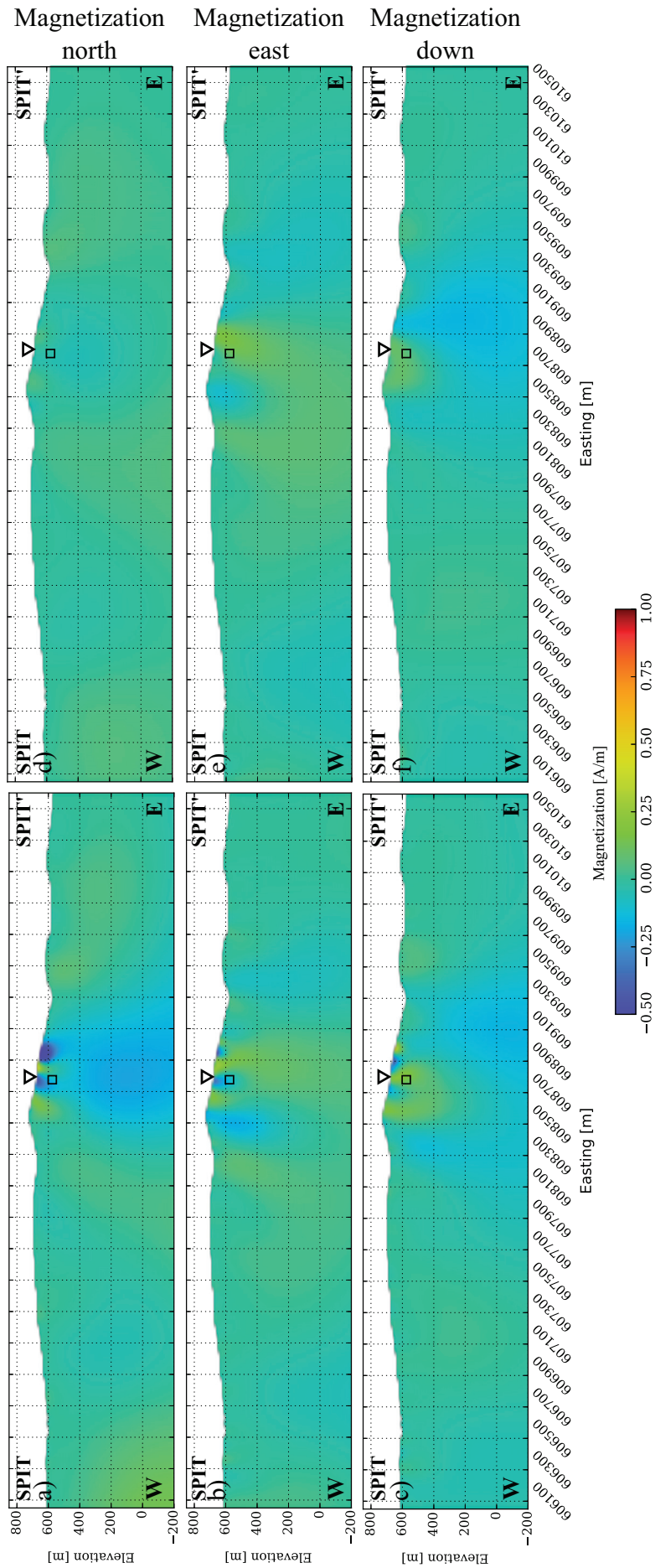


Figure A.14: Vertical slices through the final models of the FTMG (a-c) and TFA inversions (d-f) along the *Spittergrund* transect. The paleomagnetic sampling site is marked by triangles at the surface. The black boxes represent the volume of the model which was used to check the reconstructed magnetization direction.

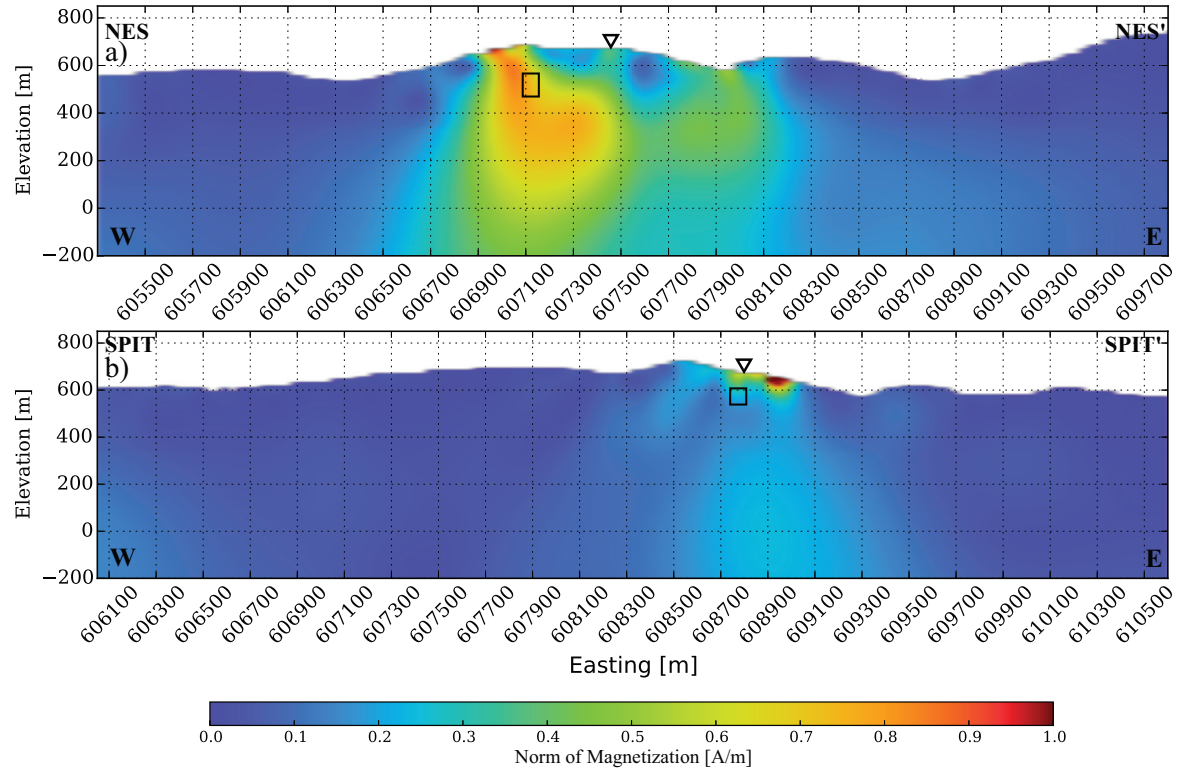


Figure A.15: Slices through the FTMG magnetization model along the NES-NES' (a) and SPIT-SPIT' section (b), showing the total magnetization (norm of magnetization vector). The paleomagnetic sampling sites are marked by triangles at the surface. The volume selected for the comparison of the measured and modeled MV is marked by black boxes in each slice.

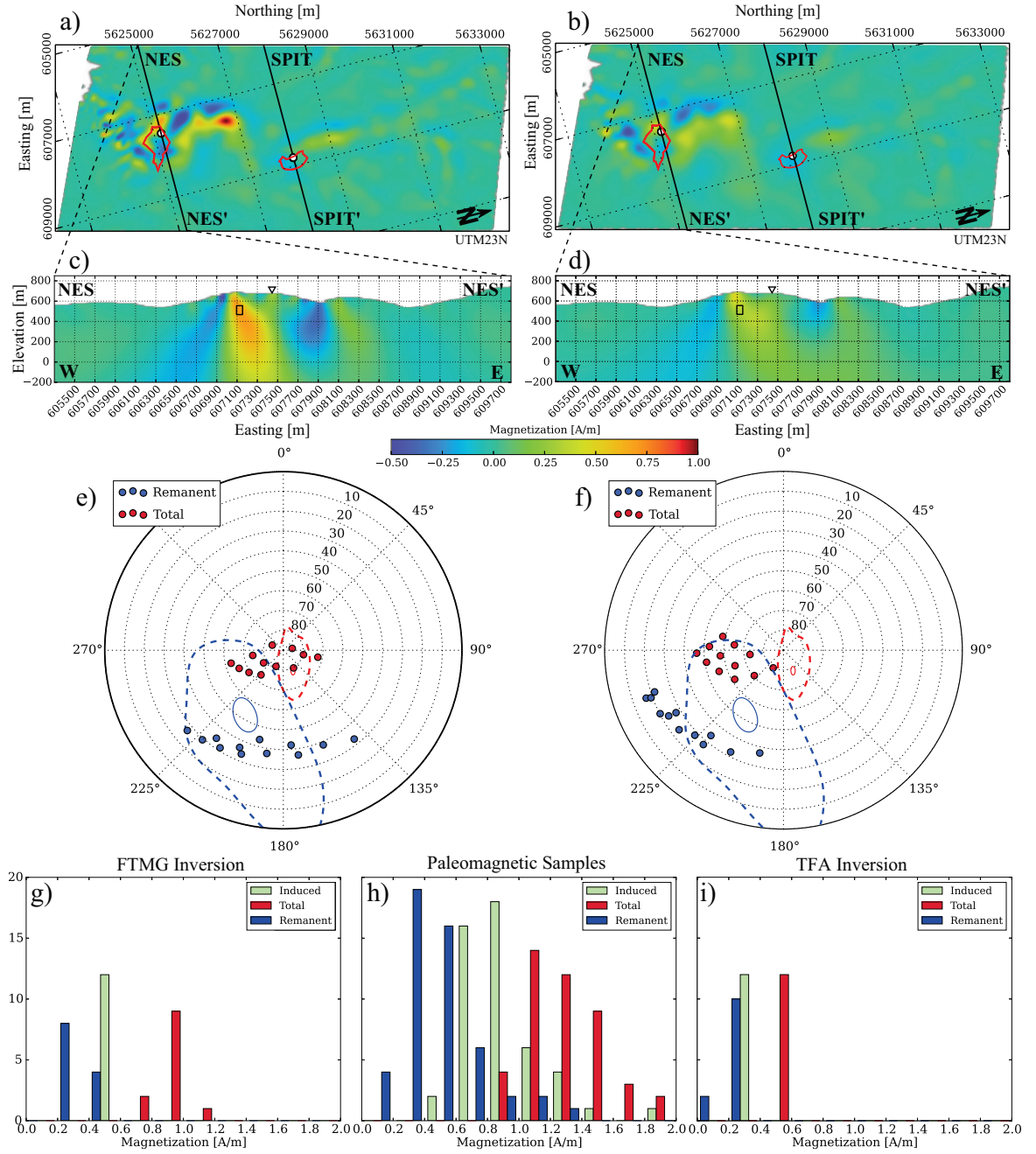


Figure A.16: Comparison of FTMG and TFA inversion results with measured paleomagnetic data. The upper row shows horizontal slices of the downward magnetization at an elevation of 400 m through the final model of the FTMG inversion (a) and TFA inversion (b). The red polygons mark the location of the *Nesselgrund* quarry (south) and *Spittergrund* quarry (north). Paleomagnetic sampling locations are noted by white dots within the quarries. c) and d) show vertical slices along the profile NES-NES'. The paleomagnetic sampling site at the *Nesselgrund* quarry is marked here by the white triangle at the surface. Slices of the second profile SPIT-SPIT' and the other magnetization components of both models are shown in Fig. A. The magnetization direction within the black boxes in c) and d) are shown in the polar plots e) and f) using the polar azimuthal equidistant projection, and their appropriate magnetization in the histograms g) and i). The blue and red isolines in e) and f) refer to the probability density function of the measured magnetization directions of the paleomagnetic samples shown in Fig. 5.9. The dashed isolines encircle 95 % of the data and is the solid isoline representing the median. Each bin in the histograms g), h) and i) includes a range of 0.2 A/m. Coordinates in a-d) are given in the UTM32N projection.

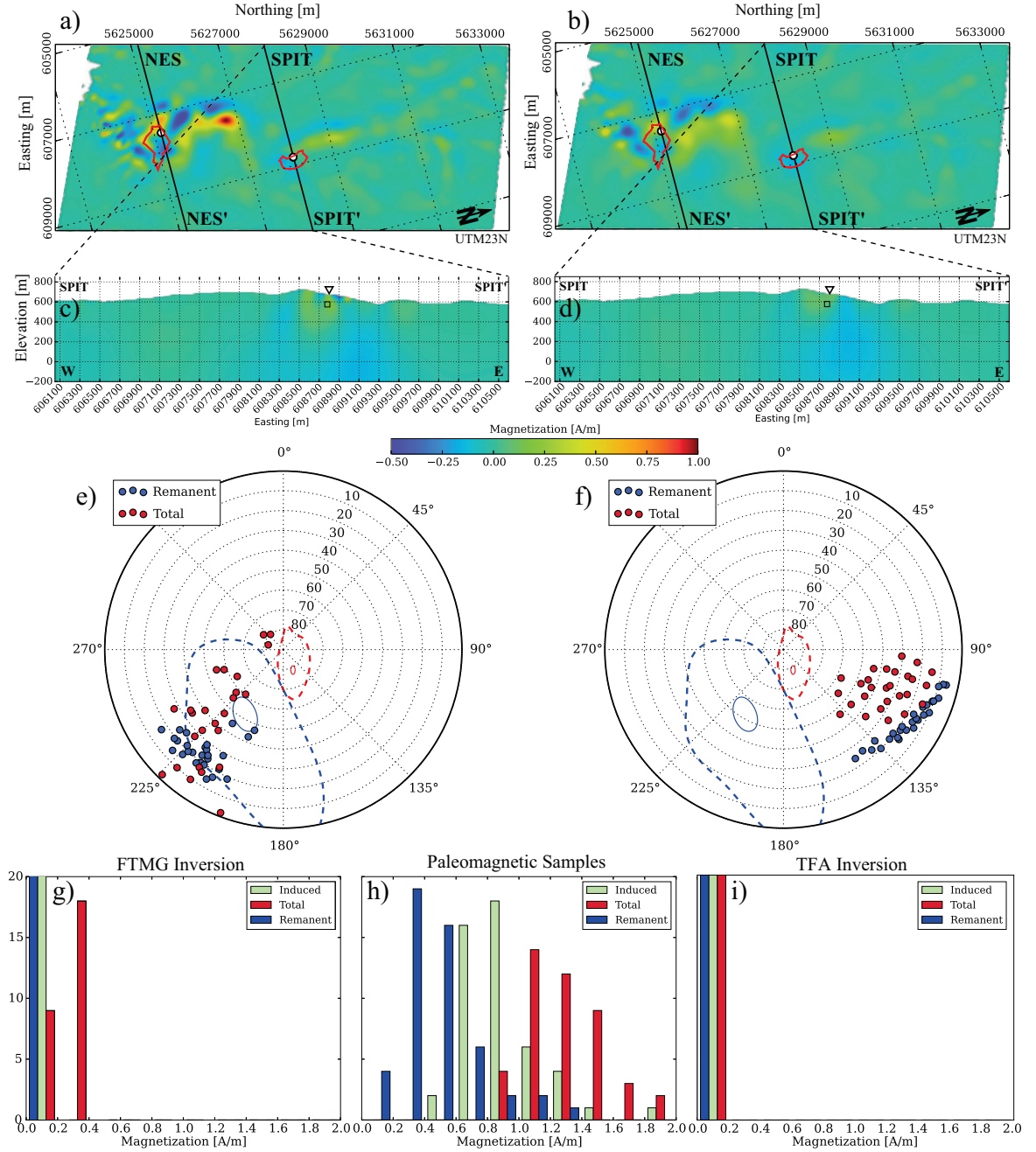


Figure A.17: Comparison of FTMG and TFA inversion results with measured paleomagnetic data. The upper row shows horizontal slices of the downward magnetization at an elevation of 400 m through the final model of the FTMG inversion (a) and TFA inversion (b). The red polygons mark the location of the *Nesselgrund* quarry (south) and *Spittergrund* quarry (north). Paleomagnetic sampling locations are noted by white dots within the quarries. c) and d) show vertical slices along the profile SPIT-SPIT'. The paleomagnetic sampling site at the *Spittergrund* quarry is marked here by the white triangle at the surface. The magnetization direction within the black boxes in c) and d) are shown in the polar plots e) and f) using the polar azimuthal equidistant projection, and their appropriate magnetization in the histograms g) and i). The blue and red isolines in e) and f) refer to the probability density function of the measured magnetization directions of the paleomagnetic samples shown in Fig. 5.9. The dashed isolines encircle 95 % of the data and is the solid isoline representing the median. Each bin in the histograms g), h) and i) includes a range of 0.2 A/m. Coordinates in a-d) are given in the UTM32N projection.

B Appendix: FTMG data and inversion results of the "Ohrdruf" area

Here, the acquired magnetic gradient tensor maps of the "Ohrdruf" area are shown. Two additional maps of the calculated total field anomaly and the topography with flight lines are presented as well. Histograms of the residual magnetic gradient tensor components after the magnetization vector inversion are depicted in Fig. B.10 and slices along the N-S plane through the "Siebleben" magnetization model are given in Fig. B.11.

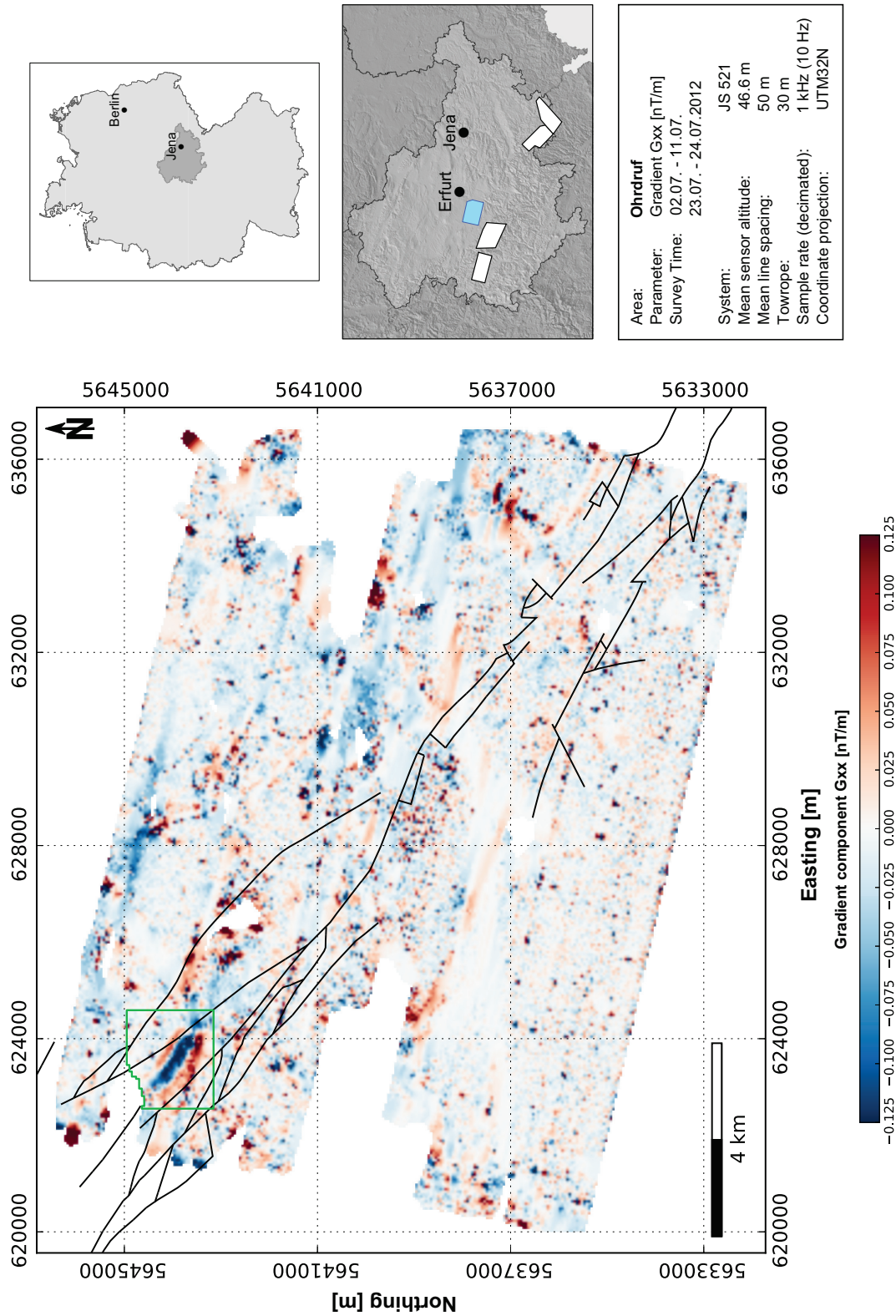


Figure B.1: Mapped magnetic gradient tensor component Gxx of the "Ohrdruf" area. The black lines indicate the published location of the EGSFZ. The green box marks the outline of the "Siebleben" study site.

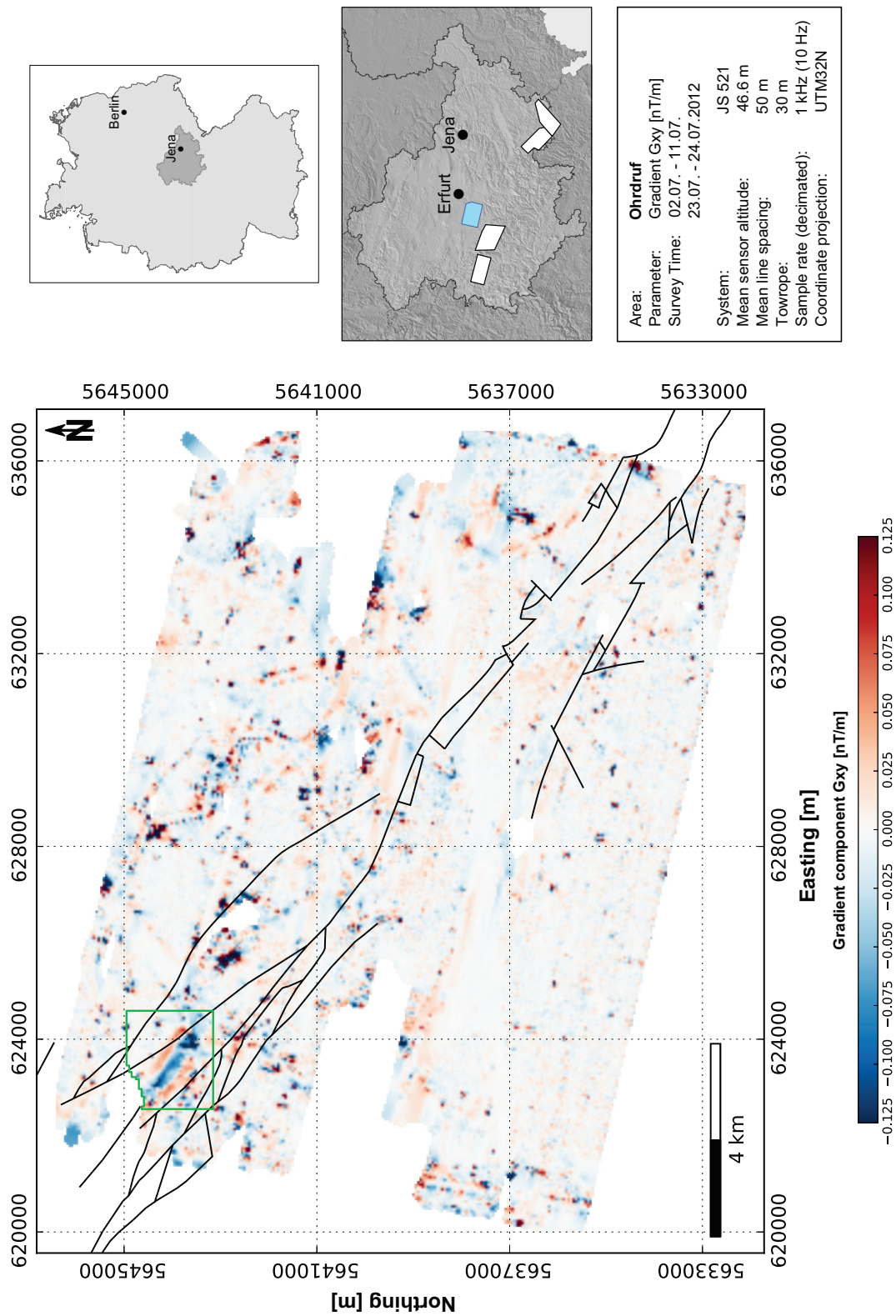


Figure B.2: Mapped magnetic gradient tensor component G_{xy} of the "Ohrdruf" area. The black lines indicate the published location of the EGSFZ. The green box marks the outline of the "Siebleben" study site.

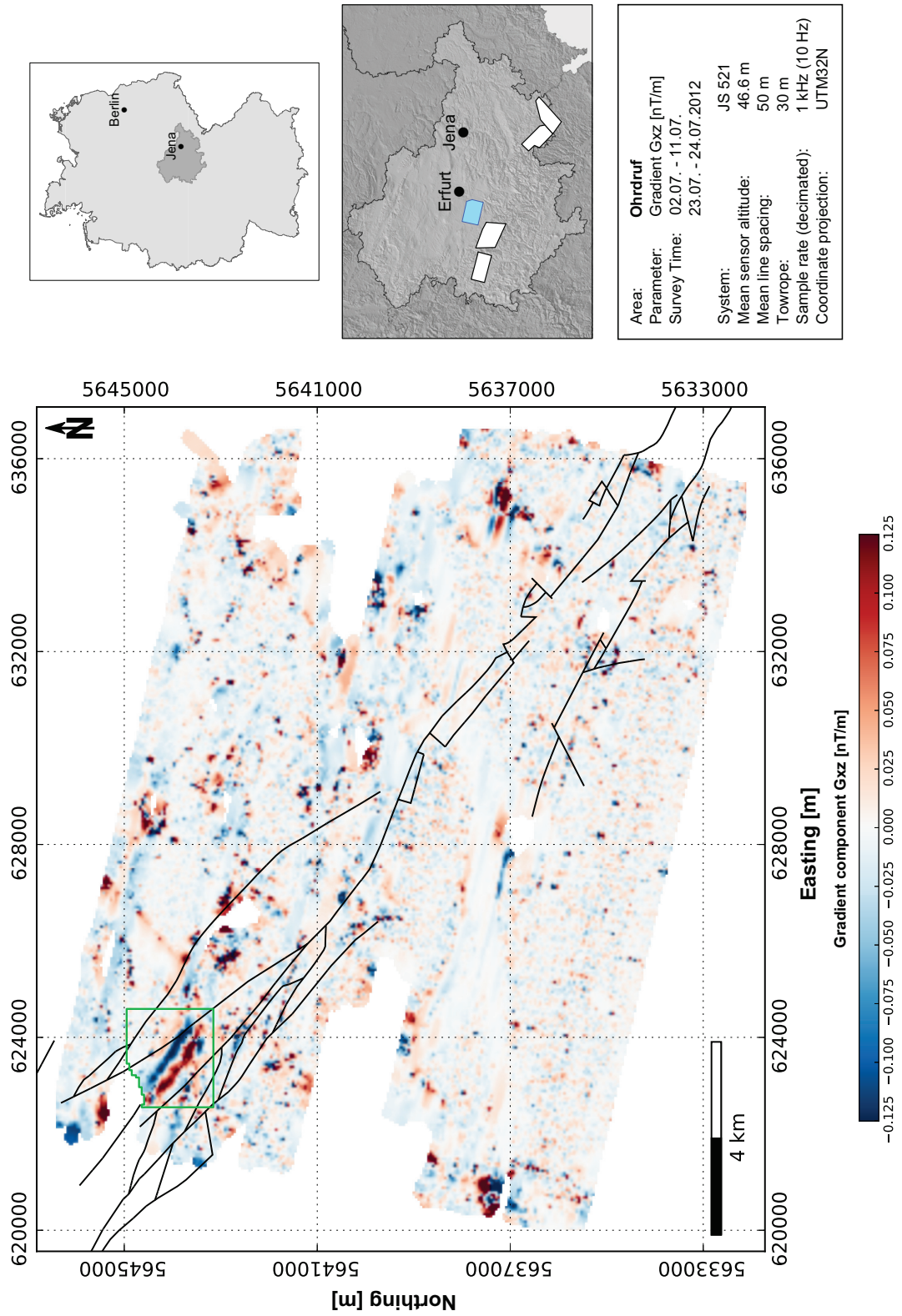


Figure B.3: Mapped magnetic gradient tensor component G_{xz} of the "Ohrdruf" area. The black lines indicate the published location of the EGSFZ. The green box marks the outline of the "Siebleben" study site.

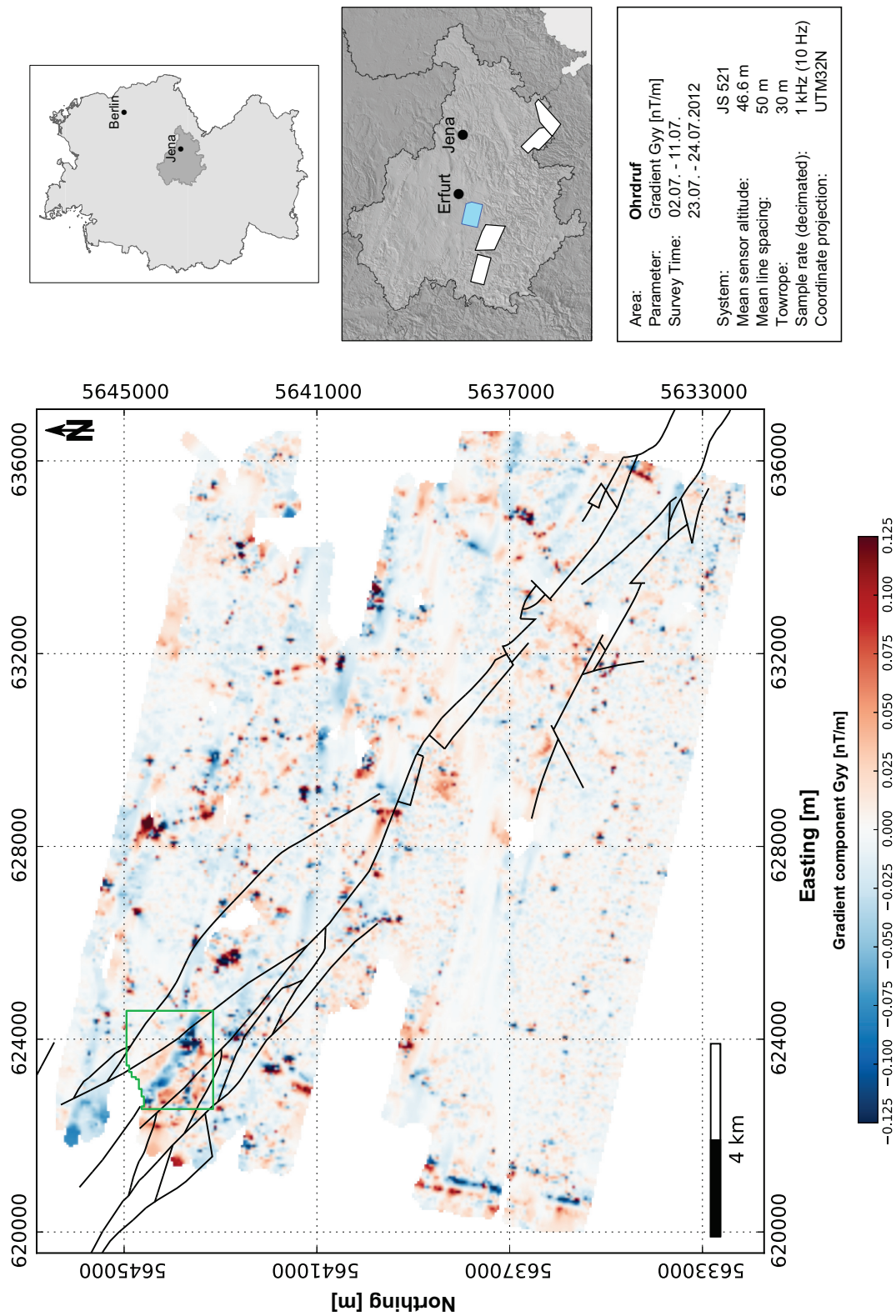


Figure B.4: Mapped magnetic gradient tensor component Gyy of the "Ohrdruf" area. The black lines indicate the published location of the EGSFZ. The green box marks the outline of the "Siebleben" study site.

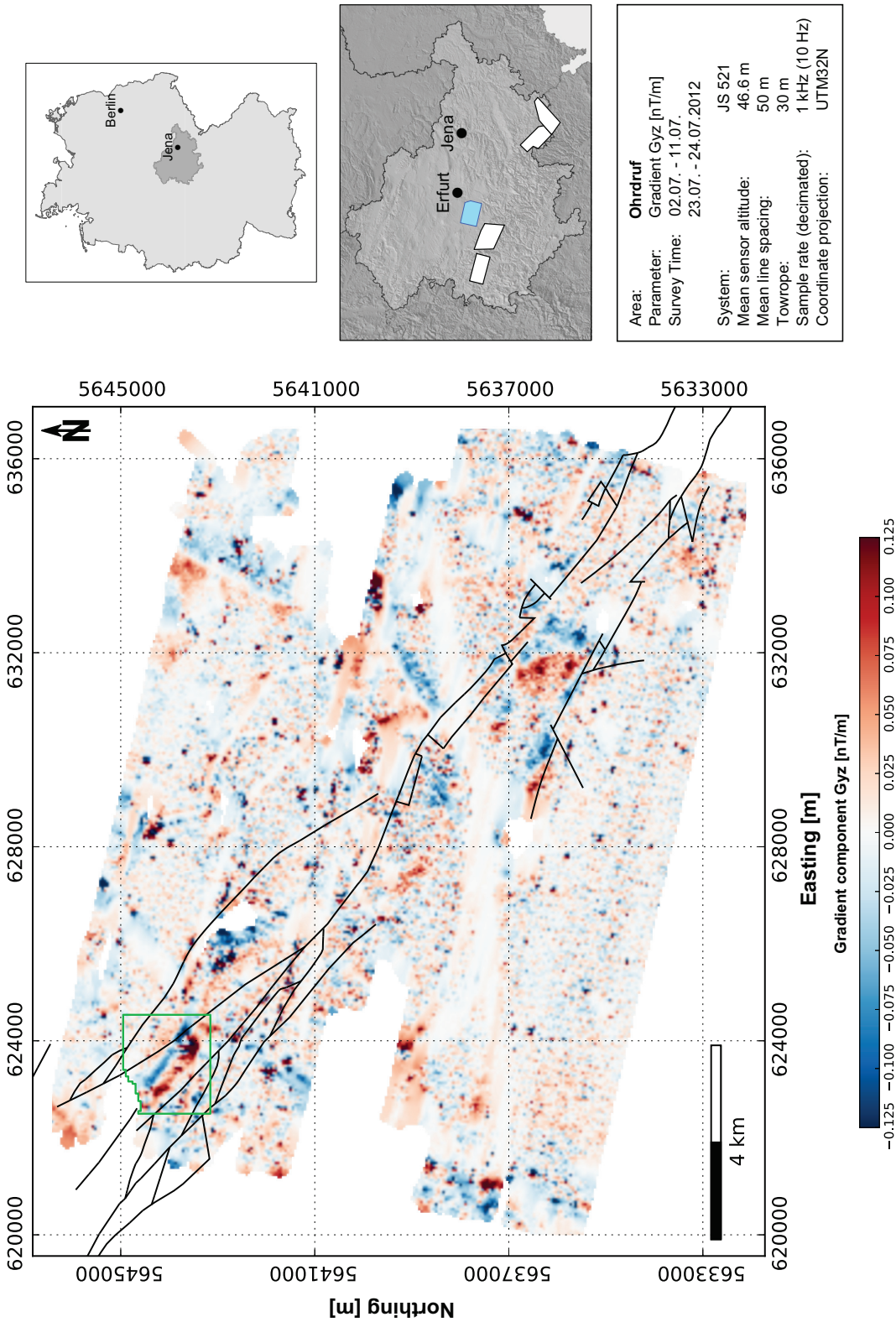


Figure B.5: Mapped magnetic gradient tensor component G_{yz} of the "Ohrdruf" area. The black lines indicate the published location of the EGSFZ. The green box marks the outline of the "Siebleben" study site.

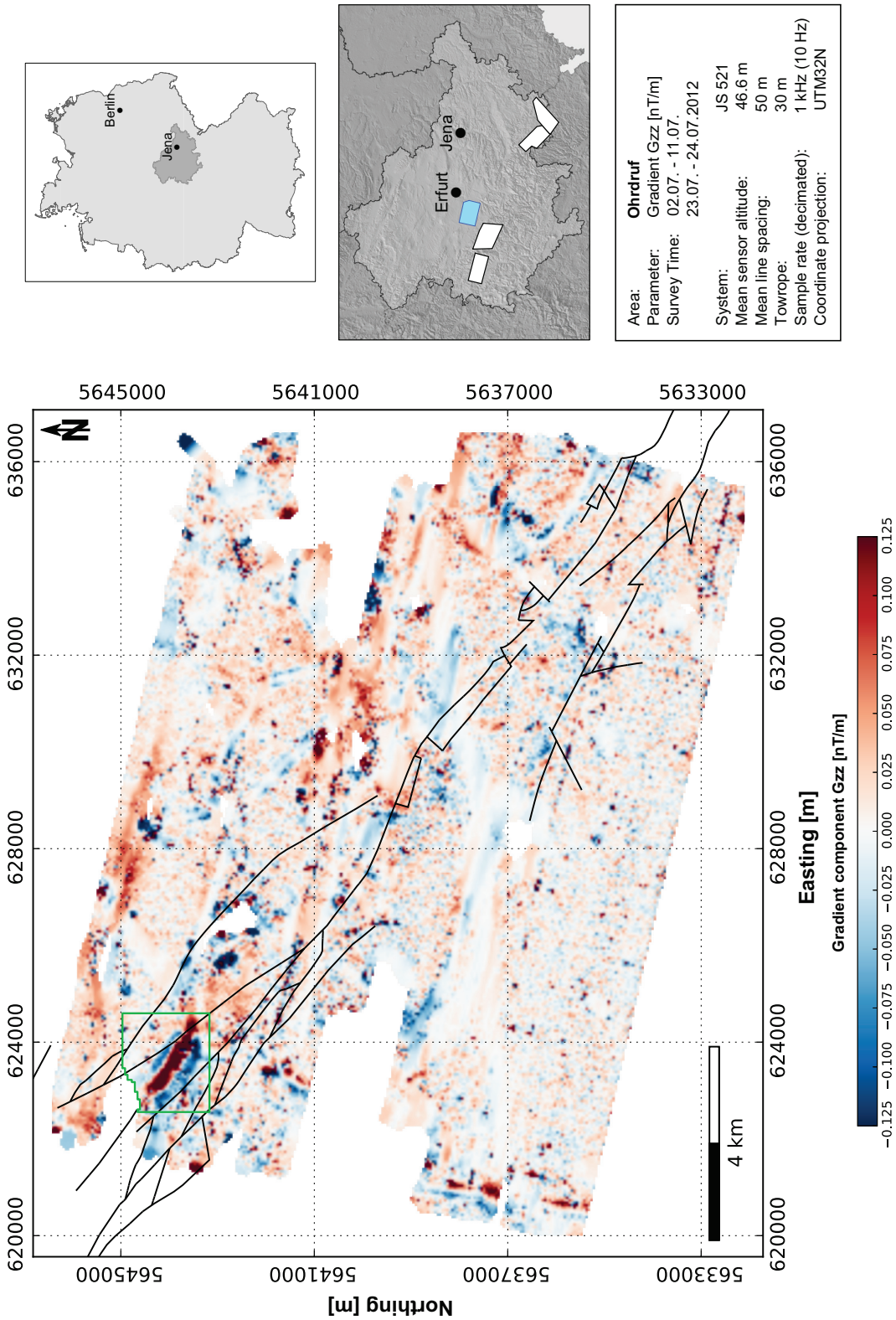


Figure B.6: Mapped magnetic gradient tensor component G_{zz} of the "Ohrdruf" area. The black lines indicate the published location of the EGSFZ. The green box marks the outline of the "Siebleben" study site.

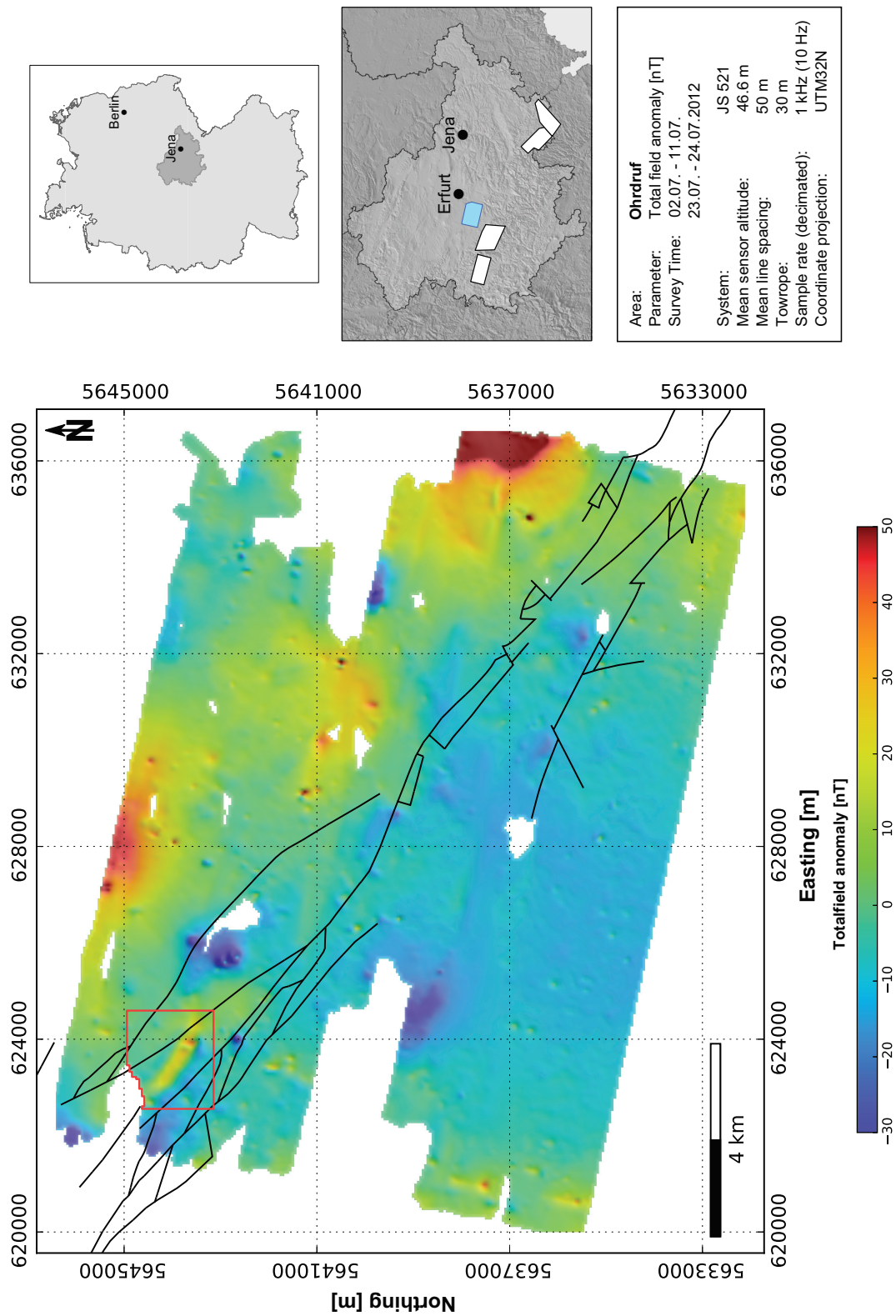


Figure B.7: Mapped total magnetic field anomaly of the "Ohrdruf" area. The black lines indicate the published location of the EGSFZ. The red box marks the outline of the "Siebleben" study site.

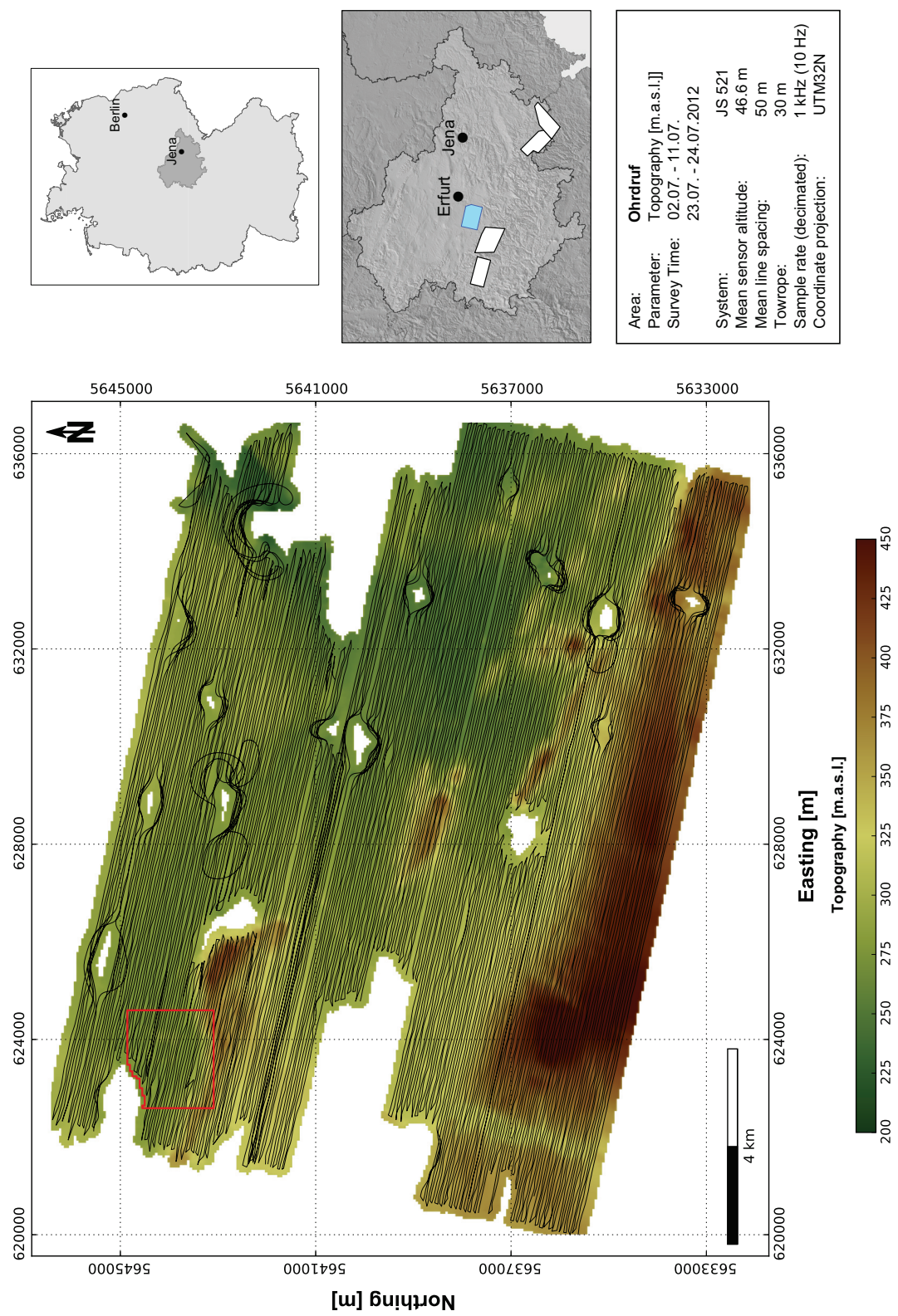


Figure B.8: Topography and flight track of the "Ohrdruf" area. The red box marks the outline of the "Siebleben" study site.

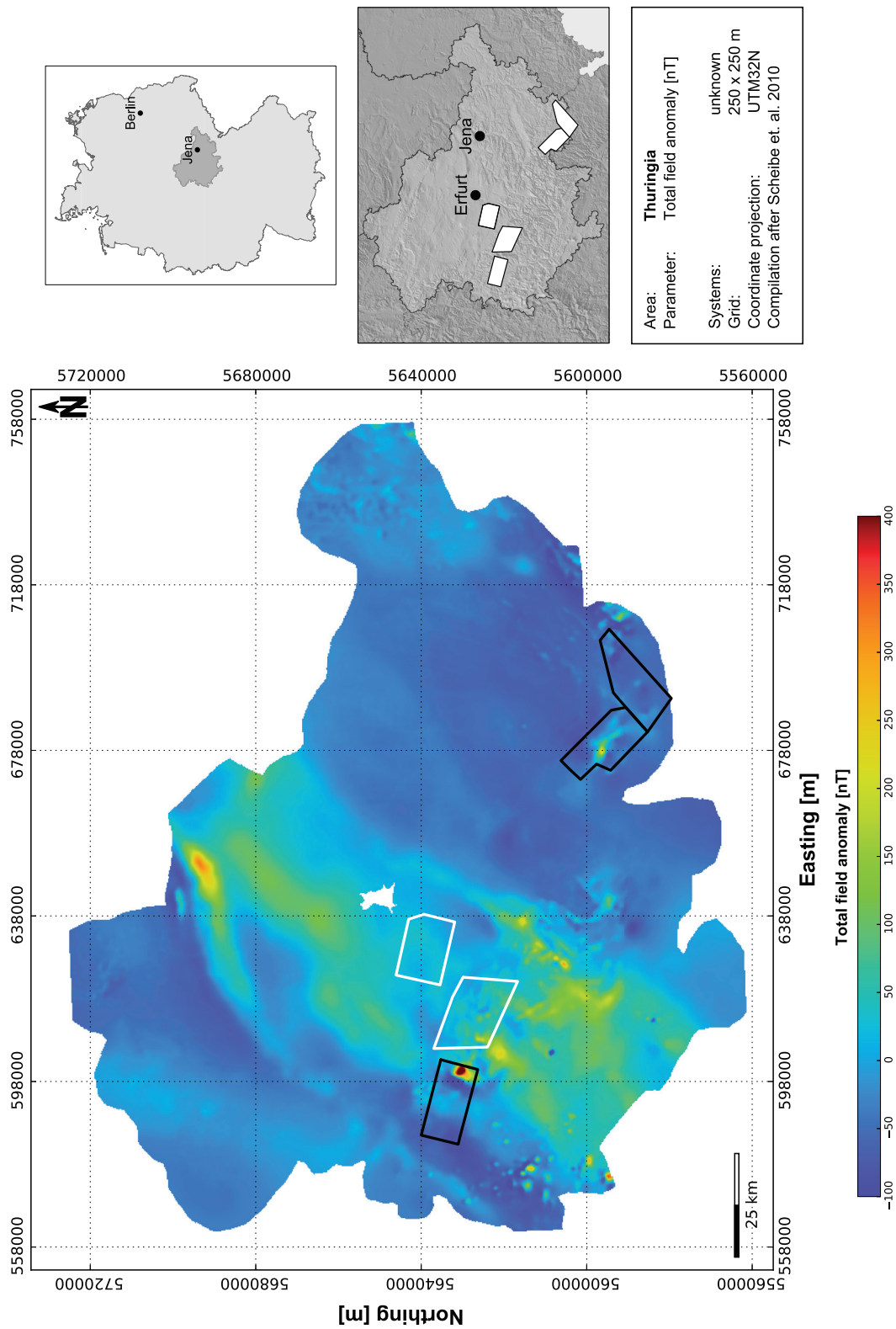


Figure B.9: Mapped total magnetic field anomaly of Thuringia. The different survey areas are denoted by the black and white boxes. Data compilation by *Scheibe et al.* (2010).

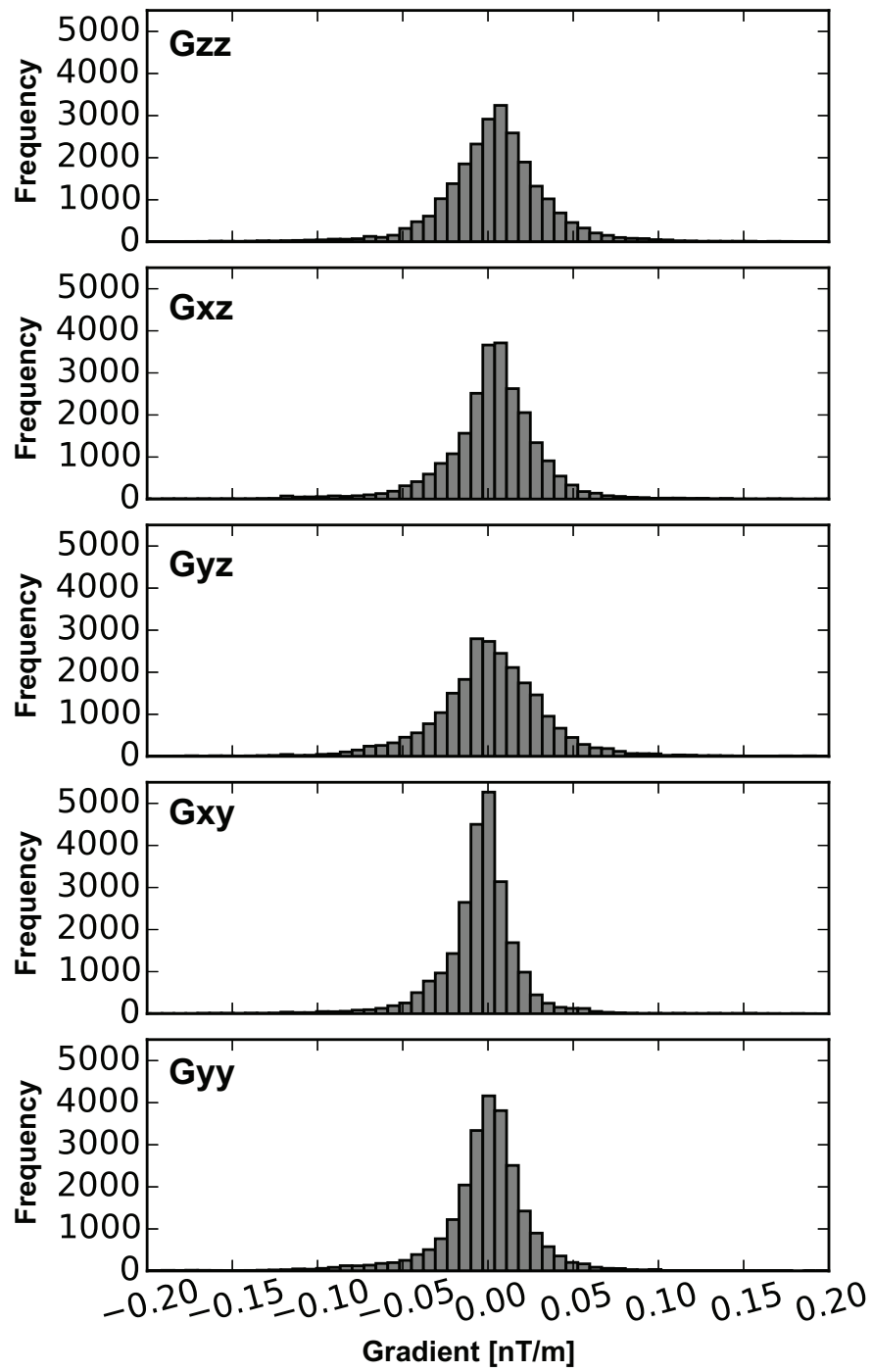


Figure B.10: Histogram plots of the residual between calculated gradient tensor of the final model and observed gradient tensor.

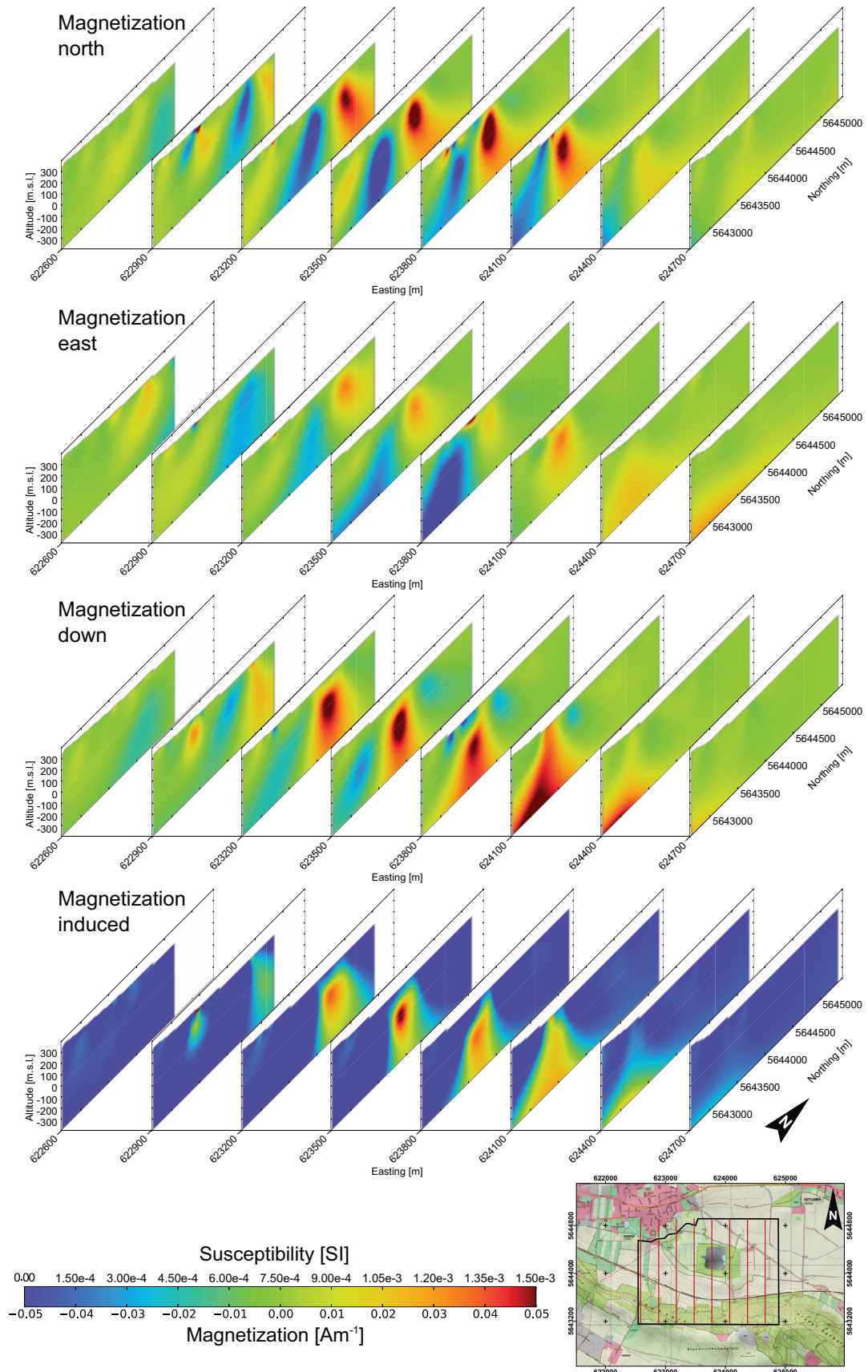


Figure B.11: Slices in NS-direction through the final model. The color scale is clipped to $\pm 0.05 \text{ A/m}$ and 0 to $15 \times 10^{-3} \text{ SI}$ units for the calculated induced magnetization. Coordinates are given in the UTM32N projection.

C Appendix: Susceptibility and Paleomagnetic Measurements

In this study susceptibility measurements were performed on various outcrops in Thuringia. The locations of these measurements are shown in Fig. 5.11. The results are compiled in Table 3. The map also includes the outlines of the five survey areas and the locations of the two quarries *Spittergrund* and *Nesselgrund*. At these two quarries paleomagnetic samples were collected. The results of the paleomagnetic analysis are shown in Table 4.

Site	Abbrev.	Easting	Northing	N	Geol. unit	Min.	Max.	Average [SI]	Median [SI]	σ [SI]
Burgwenden	BGW	660783	5677727	15	muWU	0.00	4.00×10^{-5}	2.47×10^{-5}	2.00×10^{-5}	2.87×10^{-5}
Burgwenden	BGW	660783	5677727	7	muO	2.00×10^{-5}	8.00×10^{-5}	5.00×10^{-5}	5.00×10^{-5}	1.90×10^{-5}
Burgwenden	BGW	660783	5677727	13	muWM	0.00	7.00×10^{-5}	4.46×10^{-5}	5.00×10^{-5}	2.06×10^{-5}
Burgwenden	BGW	660783	5677727	7	muT	2.00×10^{-5}	6.00×10^{-5}	4.00×10^{-5}	4.00×10^{-5}	1.20×10^{-5}
Burgwenden	BGW	660783	5677727	14	muWO	4.00×10^{-5}	8.00×10^{-5}	5.93×10^{-5}	6.00×10^{-5}	1.16×10^{-5}
Burgwenden	BGW	660783	5677727	14	mm	1.00×10^{-5}	1.40×10^{-4}	8.07×10^{-5}	8.50×10^{-5}	3.28×10^{-5}
Großmonra	GM	658931	5676358	25	kmS	1.20×10^{-4}	2.40×10^{-4}	1.66×10^{-4}	1.60×10^{-4}	2.84×10^{-5}
Auerstedt	AU	681086	5665100	7	mu	2.00×10^{-5}	7.00×10^{-5}	5.10×10^{-5}	6.00×10^{-5}	1.80×10^{-5}
Großheringen	GH	686641	5665329	7	mm	5.00×10^{-5}	1.10×10^{-4}	8.40×10^{-5}	9.00×10^{-5}	1.80×10^{-5}
Gösen	GOE	702335	5652372	11	smV	2.00×10^{-5}	9.00×10^{-5}	4.30×10^{-5}	3.00×10^{-5}	2.30×10^{-5}
Seeborgen	SB	622046	5643446	40	kmSM	0.00	2.20×10^{-4}	5.19×10^{-5}	4.00×10^{-5}	4.70×10^{-5}
Burg Gleichen	BG	629287	5638024	10	kmSM	3.00×10^{-5}	1.10×10^{-4}	7.60×10^{-5}	8.50×10^{-5}	2.80×10^{-5}
Wachsenburg	WB	631716	5635637	11	kmGOG	0.00	5.00×10^{-5}	1.90×10^{-5}	1.00×10^{-5}	1.60×10^{-5}
Haarhausen	HH	633295	5635968	16	mo	2.00×10^{-5}	6.00×10^{-5}	3.81×10^{-5}	4.00×10^{-5}	1.24×10^{-5}
Haarhausen	HH	633295	5635968	9	mm	3.00×10^{-5}	9.00×10^{-5}	5.60×10^{-5}	5.00×10^{-5}	2.10×10^{-5}
Haarhausen	HH	633295	5635968	11	ku	2.00×10^{-4}	3.40×10^{-4}	2.72×10^{-4}	2.80×10^{-4}	4.00×10^{-5}
Plaue	PL	632744	5628502	16	mm	1.00×10^{-5}	5.00×10^{-5}	3.13×10^{-5}	3.00×10^{-5}	1.36×10^{-5}
Plaue	PL	632744	5628502	11	muS	3.00×10^{-5}	7.00×10^{-5}	4.10×10^{-5}	4.00×10^{-5}	1.30×10^{-5}
Plaue	PL	632744	5628502	38	muWO	1.00×10^{-5}	7.00×10^{-5}	3.99×10^{-5}	4.00×10^{-5}	1.85×10^{-5}
Plaue	PL	632744	5628502	9	muT	2.00×10^{-5}	5.00×10^{-5}	3.80×10^{-5}	4.00×10^{-5}	1.00×10^{-5}
Plaue	PL	632744	5628502	9	muWM	3.00×10^{-5}	7.00×10^{-5}	5.70×10^{-5}	6.00×10^{-5}	1.40×10^{-5}
Reisdorf	RD	678822	5663692	11	ku	2.20×10^{-4}	1.03×10^{-3}	7.59×10^{-4}	7.90×10^{-4}	1.85×10^{-4}
Nesselgrund†	NES	607266	5624827	10	ruROGb	1.00×10^{-2}	9.58×10^{-2}	3.66×10^{-2}	2.18×10^{-2}	2.63×10^{-2}
Spittergrund†	SPIT	608769	5627751	43	ruROGb	1.20×10^{-2}	3.77×10^{-2}	2.28×10^{-2}	2.19×10^{-2}	5.61×10^{-3}

Table 3: Compilation of sampling sites of susceptibility measurements. All measurements were performed on outcrop walls using a hand-held kappameter (section 3.4) except the entries marked with †. Samples from these locations (†) were analyzed at the magnetic laboratory in Grubenhagen, Germany (LIAG). The locations of all sampling sites are marked in Fig. 5.11 using the abbreviations in the second column. The coordinates are given in UTM32N projection. Geological Units: muWU - Lower Wellenkalk; muO - Oolithzone; muWM - Middle Wellenkalk; muT - Terebratelzone; muWO - Upper Wellenkalk; mm - Middle Muschelkalk; kmS - Middle Keuper (Schilfsandstone); mu - Lower Muschelkalk; smV - Middle Buntsandstone (Volpriehausen); kmSM - Steinmergelkeuper; kmGOG - Middle Keuper upper gypsum zone; mo - Upper Muschelkalk; muS - Schaumkalkzone; ku - Lower Keuper; ruROGb - Lower Rotliegend (Höhenberger dolerite).

Table 4: Results of the susceptibility and NRM measurements of all samples collected at *Spittergrund* (SPIT) and *Nesselgrund* (NES) quarry.

Name	Susceptibility [SI]	NRM [mA/m]	Inclination [°]	Declination [°]	Q-ratio
NES1-a	4.94×10^{-2}	553.0	48.0	195.5	0.29
NES2-a	6.97×10^{-2}	997.7	48.9	222.4	0.37
NES2-b	9.58×10^{-2}	1290.0	59.9	218.8	0.35
NES3-a	1.87×10^{-2}	664.2	47.2	182.4	0.91
NES3-b	2.28×10^{-2}	572.0	37.7	184.3	0.64
NES4-a	1.88×10^{-2}	450.3	63.7	209.2	0.61
NES5-a	2.08×10^{-2}	398.3	73.1	73.3	0.49
NES5-b	1.82×10^{-2}	461.3	75.5	309.2	0.65
SPIT1-a	2.58×10^{-2}	1056.0	7.4	174.3	1.05
SPIT1-b	2.50×10^{-2}	1091.0	-3.8	178.2	1.12
SPIT1-1	2.85×10^{-2}	392.1	37.5	175.0	0.35
SPIT1-2	2.37×10^{-2}	238.7	62.9	238.0	0.26
SPIT1-3	3.12×10^{-2}	423.4	30.8	171.8	0.35
SPIT1-4	2.84×10^{-2}	293.8	2.1	149.3	0.27
SPIT1-5	1.80×10^{-2}	170.6	13.8	190.2	0.24
SPIT1-6	1.73×10^{-2}	164.0	33.4	223.2	0.24
SPIT1-7	2.47×10^{-2}	166.4	23.4	172.8	0.17
SPIT2-1	3.54×10^{-2}	564.0	7.3	290.5	0.41
SPIT2-2	3.29×10^{-2}	577.1	40.9	214.0	0.45
SPIT2-3	3.13×10^{-2}	208.9	30.4	184.4	0.17
SPIT2-4	2.87×10^{-2}	435.7	25.3	227.6	0.39
SPIT2-5	2.50×10^{-2}	486.8	19.2	212.7	0.50
SPIT2-6	2.74×10^{-2}	153.8	9.7	290.4	0.14
SPIT2-7	2.77×10^{-2}	225.2	50.1	194.0	0.21
SPIT2-8	3.77×10^{-2}	595.3	35.1	182.9	0.40
SPIT4-1	2.50×10^{-2}	370.7	54.2	211.7	0.38
SPIT4-2	2.10×10^{-2}	295.8	46.4	220.0	0.36
SPIT4-3	2.33×10^{-2}	382.3	59.7	195.5	0.42
SPIT4-4	2.32×10^{-2}	392.0	61.5	224.6	0.43
SPIT4-5	1.95×10^{-2}	295.7	57.9	235.5	0.39
SPIT4-6	1.96×10^{-2}	346.2	52.6	217.9	0.45
SPIT4-7	2.16×10^{-2}	416.9	60.4	219.8	0.49
SPIT4-8	2.07×10^{-2}	372.8	55.3	232.1	0.46
SPIT4-9	2.22×10^{-2}	364.5	74.3	245.6	0.42
SPIT4-10	2.23×10^{-2}	306.5	45.2	220.4	0.35
SPIT4-11	1.94×10^{-2}	312.5	64.3	217.6	0.41
SPIT4-12	2.07×10^{-2}	323.2	59.7	198.0	0.40
SPIT4-13	2.31×10^{-2}	410.1	48.8	252.1	0.46
SPIT5-1	2.13×10^{-2}	821.4	26.7	195.9	0.99
SPIT5-2	2.19×10^{-2}	795.6	20.9	180.6	0.93
SPIT5-3	1.98×10^{-2}	733.7	19.8	191.4	0.95
SPIT5-4	1.75×10^{-2}	614.5	31.1	194.5	0.90
SPIT5-5	1.91×10^{-2}	786.7	16.1	175.6	1.06
SPIT5-6	1.79×10^{-2}	776.7	11.0	184.2	1.11
SPIT5-7	1.20×10^{-2}	480.1	16.6	183.8	1.03
SPIT6-1	1.90×10^{-2}	459.5	43.5	220.8	0.62
SPIT6-2	1.72×10^{-2}	357.4	38.2	204.0	0.53
SPIT6-3	1.77×10^{-2}	459.5	46.1	218.6	0.67
SPIT6-4	1.78×10^{-2}	422.6	37.5	197.9	0.61
SPIT6-5	1.49×10^{-2}	333.7	38.6	212.7	0.57

D Appendix: Color maps

Here, the color maps used in this study are depicted using a simple color perception validation after *Kovesi* (2015). This shows, that the applied color maps have a fairly constant color perception across the complete range.

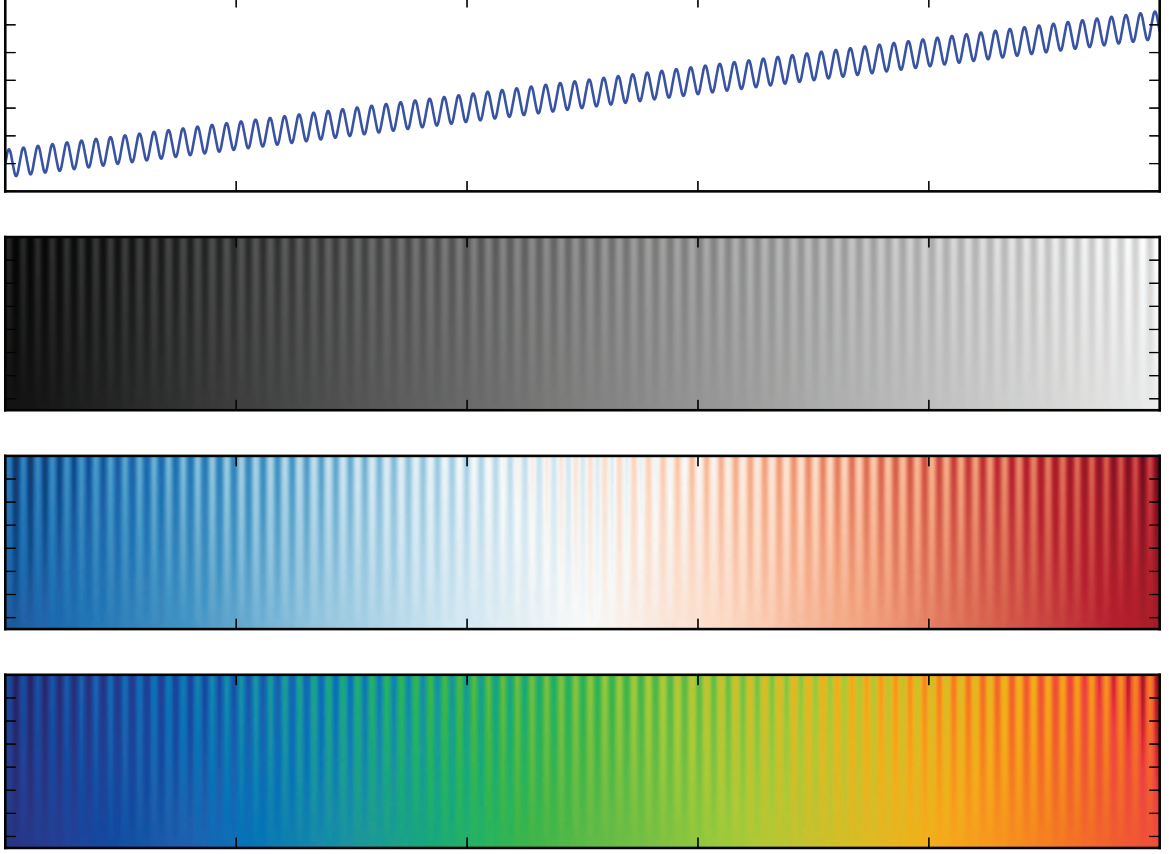


Figure D.1: Color perception test after *Kovesi* (2015) of the three color maps used in this work. At the top a linear function with a sine wave with an amplitude variation of 10 % of the maximum signal is used to illustrate the color perception. The three color maps are gray scale from black to white, a diverging color map from red to blue, and a rainbow color map, sampled from the CIELab color space. Note that the representation of the 10 % sine signal is constant across the complete color spectrum in these three examples.

Acknowledgements

First of all I want to thank my supervisor Prof. Dr. Nina Kukowski for giving me the opportunity to write my PhD thesis and for her constructive comments on various different aspects throughout my entire work. Special thanks to goes to Dr. Ronny Stolz for his support throughout the last four years. I especially want to thank him for his trust during the organization of the different surveys and for the endless discussions and proofreading of my manuscript and abstracts in the last years.

I want to thank Markus Schiffler, who was responsible in our group for the development of the inversion algorithm and processing of the airborne FTMG data. Many thanks to Dr. Andreas Goepel, who supported us in the selection of the airborne survey areas and provided help during acquisition and interpretation of the different data sets.

Special thanks are going to Dr. Uwe Meyer, Dr. Bernhard Siemon, Carsten Plath and Hans-Ulrich Balzer of the Federal Geological Survey of Germany (BGR), who provided the helicopter and supported us during installation of several crucial systems. Without them the multiple survey campaigns in 2012 and 2013 would not have been possible. I also want to thank our pilots Bernhard Stooss and Martin Klenke, who had to learn how to fly with this unusual external load and challenging flight pattern. Their willingness to fly exactly along the predefined flight lines and produce only little offsets is gratefully acknowledged. I also want to thank Stefan Dunkel, Torsten Krause (Supracon AG), Dr. Matthias Schmelz and Thomas Schönau (IPHT), who sacrificed some of their time and helped as ground crew during the airborne surveys. The support of Andreas Chwala (IPHT) and Marco Schulz (Supracon AG), especially in the initial phase of the survey and for the preparation of the airborne system, is gratefully acknowledged.

Many thanks to Dr. Christian Rolf and Kathrin Worm of the Leibniz-Institute of Applied Geophysics (LIAG) for their help collecting the orientated rock samples and for performing the paleomagnetic analysis at their laboratory in Grubenhagen. I also want to thank Dr. Thomas Günther and Wolfgang Südekum, also at the LIAG in Hannover, for their help during the acquisition of the geoelectrical data sets at the "Siebleben" site.

My deepest thanks goes to my fellow colleagues Dr. Martin Krause and Dr. Alexander Malz for numerous interesting discussions about our project and our work. The support and help of Michael Warsitzka, Pascal Methe, Dr. Daniel Beyer, and Cindy Kunkel is also gratefully acknowledged. Thanks to Raphael Rochlitz and Felix Halpaap, who helped me collecting susceptibility values in Thuringia and who performed additional electromagnetic surveys in other areas.

This work was done within the framework of the multidisciplinary project INFLUINS, funded by the German Federal Ministry of Education and Research (BMBF), under grant no. 03 IS 2001 A. I thank the BMBF for financial support during my study.

Selbständigkeitserklärung

Ich erkläre, dass ich die vorliegende Arbeit selbständig und unter Verwendung der angegebenen Hilfsmittel, persönlichen Mitteilungen und Quellen angefertigt habe.

Ort, Datum

Unterschrift des Verfassers